Durham University

# Durham E-Theses

## *The Search For Pulsar Wind Nebulae in the Very High Energy Gamma-ray Regime*

KEOGH, DOMINIC,ROBERT

**How to cite:**

KEOGH, DOMINIC,ROBERT (2010) *The Search For Pulsar Wind Nebulae in the Very High Energy Gamma-ray Regime*, Durham theses, Durham University. Available at Durham E-Theses Online: http://etheses.dur.ac.uk/776/

**Use policy**

The full-text may be used and/or reproduced, and given to third parties in any format or medium, without prior permission or charge, for personal research or study, educational, or not-for-profit purposes provided that:

- a full bibliographic reference is made to the original source
- a link is made to the metadata record in Durham E-Theses
- the full-text is not changed in any way

The full-text must not be sold in any format or medium without the formal permission of the copyright holders.

Please consult the full Durham E-Theses policy for further details.

Academic Support Office, Durham University, University Office, Old Elvet, Durham DH1 3HP
e-mail: e-theses.admin@dur.ac.uk Tel: +44 0191 334 6107
http://etheses.dur.ac.uk

# The Search For Pulsar Wind Nebulae in the Very High Energy $\gamma$-ray Regime

**Dominic Robert Keogh MSci FRAS**

A Thesis presented for the degree of
Doctor of Philosophy


Very High Energy $\gamma$-ray Astronomy Group
Department of Physics
University of Durham
England

September 2010

# The Search for Pulsar Wind Nebulae in the Very High Energy $\gamma$-ray Regime

**Dominic Robert Keogh MSci FRAS**

Submitted for the degree of Doctor of Philosophy
September 2010

## Abstract

The aim of this Thesis is to study the development of pulsar wind nebulae in the TeV regime and in doing so uncover more sources which have as yet not been observed at these wavelengths. It is found that the extent of pulsar wind nebula in the TeV $\gamma$-ray increases with its age while no developmental relationship is seen concerning the luminosity or spectral index of the nebulae when observed in the TeV $\gamma$-ray regime due to uncertainties in the measurements available.

TeV $\gamma$-ray upper limits are calculated for several nebulae observed in the X-ray regime allowing the strength of their magnetic fields to be constrained but only one new source, which was previously confused with its companion, was discovered, the Eel Nebula.

Predictions of the fluxes of many of the sources for which upper limits are derived in this work have been calculated from observations of their emission in X-rays and some of these sources should be uncovered with the next generation CTA instrument.

# Declaration

The work in this thesis is based on research carried out in the very high energy $\gamma$-ray astronomy group of the department of physics at the university of Durham, England. No part of this thesis has been submitted elsewhere for any other degree or qualification and it is all my own work unless referenced to the contrary in the text.

**Copyright © 2010 by Dominic Robert Keogh**.

"The copyright of this thesis rests with the author. No quotations from it should be published without the author's prior written consent and information derived from it should be acknowledged".

# Acknowledgements

The work presented in this thesis would not have been possible for the help and support of a great many friends, colleagues and family; they are too numerous to mention individually but all have my deepest respect and thanks.

First of all I must thank my parents who have always been supportive of all of my pursuits from the start of my life and encouraged me to reach for all my goals in life and I would never have got as far as I have in life without their help.

During my 4 years in the Durham $\gamma$-ray group I have learnt a great deal about astrophysics and science in general thanks to both my fellow students and my supervisors; Dr Paula Chadwick, Dr John Osborne and Dr Lowry McComb. I must also give a big thank you to my friend Dr Hugh Dickinson for taking so much time out of his work to help me with mine and being an excellent travelling companion on my first trip to Namibia.

Lastly I must thank my fiancée Heather for her constant support and encouragement without whom I would never have been able to complete this work, at least not on time, and so I dedicate this thesis to her.

# Contents

# List of Figures

# List of Tables

# Chapter 1

# The Production and Detection of Very High Energy $\gamma$-rays

The emission from pulsar wind nebulae on which this thesis focuses is dominated by non-thermal particle acceleration processes. In order to study the processes by which particles are accelerated it is necessary to understand the radiation that they produce at the extremes of the electromagnetic spectrum. This chapter focuses on the mechanisms by which highly energetic radiation is produced and the methods by which it can be detected.

## 1.1 Observing the Non-Thermal Universe

Historically astronomy has been dominated by the observation of thermal radiation sources. Any object with a temperature greater than absolute zero will emit radiation due to the movement of its internal particles. If an object is in thermal equilibrium with its surrounding environment (not an unreasonable assumption when one is dealing with astronomical timescales) it will emit blackbody radiation in accordance with Wien's displacement law:

$$\lambda_{max} = \frac{2.9 \times 10^{-3}}{\mathrm{T}} \tag{1.1}$$

Where $\lambda_{max}$ is the wavelength in metres at which the radiation is at its maximum and T is the temperature of the black body in Kelvin. Thermal radiation has been

observed more readily than other varieties of radiation primarily because nature has equipped us to view only a very small band of the electromagnetic spectrum directly. As a result all astronomical observations until the modern age focused on the narrow range of light with wavelengths between 380 to 750 nm which is visible to the naked eye. The Earth's atmosphere is transparent at only a few wavelength bands (See Figure 1.1), limiting the observations that we can make. However, as the atmosphere is transparent in the visible waveband it is this band that we have evolved the ability to observe directly, thus affording us easy access to this portion of the electromagnetic spectrum.

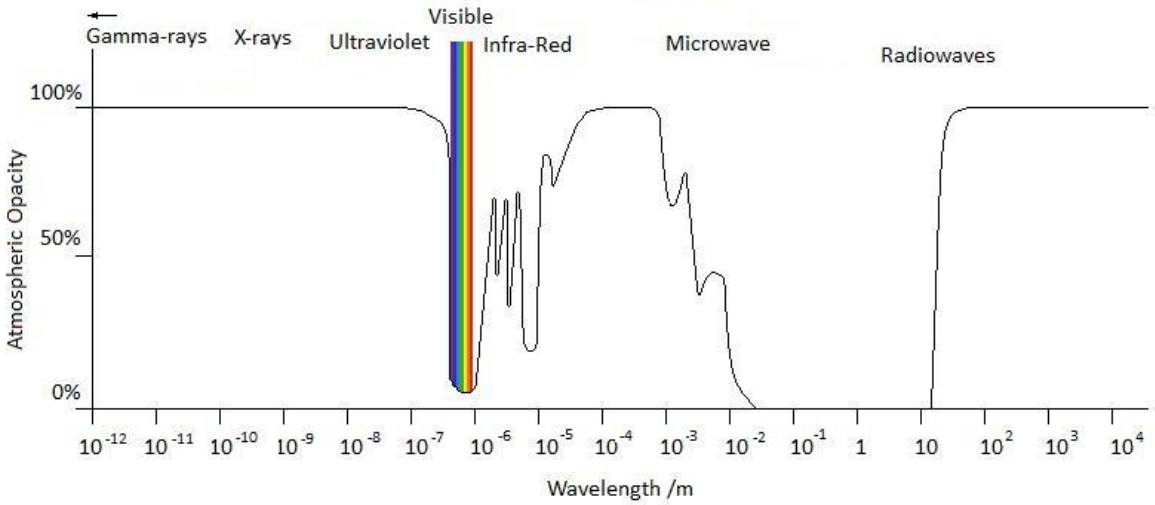


Figure 1.1: The areas of the spectrum in which the Earth's atmosphere is transparent; the most significant portions are the visible (380 to 750nm) and the radio portion between 10mm and 10m [51].

Most visible light is generated in a broad spectrum by thermal processes and observations of a thermal spectrum in conjunction with Wien's law can be used to infer temperature. This is complemented by characteristic emission lines which show the presence of certain elements (see Section 1.3.4). These details allow a large amount of information to be inferred about the nature of distant bodies in the universe. Atomic transition lines can show the chemical makeup of distant objects and Doppler shifting of these lines means that this can also be used to infer the speed of motion of astronomical objects relative to the observer along the line of

sight. However, these are not the only processes at work in distant stars and if we limit ourselves to only these, then we limit the interesting astronomical phenomena that we can observe.

Non-thermal radiation allows us to observe and measure many more astrophysical properties such as magnetic fields and particle acceleration. It is emitted in all parts of the spectrum; however, it is not easily observed in central wavelengths where it gets overwhelmed by thermal emission. As the atmosphere is opaque at most wavelengths, the earliest systematic observations of non-thermal radiation were taken in the radio, which includes the largest range of wavelengths visible through the Earth's atmosphere (see Figure 1.1). The first radio observations took place purely by chance when Karl Jansky, a telephone engineer working for Bell laboratories, was investigating interference with transatlantic radio observations. Jansky noticed a repeating signal with a period of 23 hours and 56 minutes corresponding to the Earth's sidereal period and hence implying an extraterrestrial origin and leading to the development of a whole new astronomical field [123]. From these early observations radio astronomy has developed into a large field with telescopes and arrays of telescopes that are able to observe radiation across several orders of magnitude with great sensitivity.

Radio observations have the advantage of the transparency of the atmosphere (see Figure 1.1); to observe many other components of the non-thermal spectrum it is necessary to get above the atmosphere and as a result these were first observed much later. X-rays, which can be thermal or non-thermal, have been observed since the 1960s using satellites as well as balloon-based instruments. The first imaging X-ray satellite, the *Einstein* observatory [89] was launched in 1978, allowing us to map the X-ray sky for the first time. Since then great improvements have been made in the field of X-ray astronomy; the current generation of space based X-ray telescopes are each best adapted to a specialist area of observation. *Swift* [46] and *RXTE* [122] are able to manoeuvre into position quickly and are as such useful for observing transient phenomena such as $\gamma$-ray bursts and flaring AGN. For long term planned observations of steady sources *XMM-Newton* [91] has the greatest spectral resolution in the X-ray regime while morphology is best observed with the *Chandra*

observatory [196] which has the greatest angular resolution at X-ray wavelengths.

However, even at these energies, many interesting astronomical phenomena are not observable, such as the inverse Compton process which emits most of its radiation in the $\gamma$-ray regime. It is necessary to go to high energies (GeV - TeV energies), to see these phenomena, and this is our main motivation for undertaking $\gamma$-ray astronomy.

### 1.1.1 The History of $\gamma$-ray Observations

In order to consider the difference between X-ray and $\gamma$-ray astronomy it is first necessary to determine the difference between an X-ray and a $\gamma$-ray. Historically, the two types of radiation were discovered separately as the products of two different types of source. While $\gamma$-rays were first observed as the products of certain radioactive decay processes [190], X-rays were discovered coming from the acceleration of electrons [175].

When astronomical sources are observed, the production mechanism of the radiation is not usually known and so it is more convenient to define the boundary between X-ray and $\gamma$-ray sources by their energy rather than the method by which they are produced. It would be unwise to define a photon with the same properties by two differing designations. In some cases the production mechanism or even the mechanism by which they are detected is used to demarcate the boundary between X-rays and $\gamma$-rays. However, for the purposes of this thesis I will define any photon with an energy greater than the rest mass of an electron (511 keV) as a $\gamma$-ray; in this way any photon created by electron positron annihilation will fall within this definition.

At the lower end of the $\gamma$-ray spectrum (up to about 50 GeV), observations are best made by space-based observatories as is the case in X-rays. The current leading telescope observing in the lower end of the $\gamma$-ray regime is the *Fermi* satellite (see Section 1.2.1).

### 1.1.2 Very High Energy $\gamma$-rays

When we get to the highest energy $\gamma$-rays (energies above 100 GeV) the flux coming from even the brightest sources is very low indeed. For example, the Crab Nebula, the brightest constant source in the gamma-ray sky, has a flux of only $2.26 \times 10^{-11}$ photons/cm$^2$/s above 1 TeV [17]. At this rate a camera the the size of the LAT on the *Fermi* satellite, which has a detector area of 2.5m$^2$ [153], would observe only $2 \times 10^{-7}$ photons per year if it were constantly observing this nebula.

The low flux which would result from direct detection of VHE $\gamma$-rays is avoided by utilizing the Cherenkov effect which allows the whole atmosphere to be used as a detector and hence ground based $\gamma$-ray observations can then be made. This technique, from which most of the data for this thesis comes, is discussed in Section 1.2.2.

In the past ten years the current generation of ground based Cherenkov telescopes has led to a massive expansion in the number of, and indeed the number of classes of, very high energy (VHE) $\gamma$-ray sources. At the turn of the millennium only six sources which have been confirmed using current instruments were known to emit in the TeV waveband [110], with the majority being variable sources which were only observed at the height of their activity. These sources represented only three classes of object with only one pulsar wind nebula (the Crab Nebula [193]) and one supernova remnant (RXJ 1713.7-3946 [155]) known. There are, as of August 2010, more than 100 known very high energy (VHE) $\gamma$-ray sources [116] with additional sources being discovered all the time by the current generation of Cherenkov telescopes. These telescopes, HESS and CANGAROO III in the southern hemisphere and VERITAS and MAGIC in the northern hemisphere, have made VHE $\gamma$-ray astronomy into a viable astronomical field in its own right, uncovering many new source types in the process.

In addition, there are now more than twice the number of *classes* of VHE $\gamma$-ray source than were known ten years ago, as well as many sources which have yet to be identified [28] which may represent unique source classes of their own. Of the sources that we can positively identify, by far the most numerous sources are pulsar wind nebulae, which are the subject of this thesis. The majority of these were discovered

during the HESS Galactic Plane scan which has surveyed the central portion of the Galaxy between Galactic latitudes of -3° and +3° and Galactic longitudes of -100° and 60° [23]. About ten of the sources discovered in the survey are supernova remnants which are, like pulsar wind nebulae, a product of supernovae.

In some cases both a supernova remnant and a pulsar wind nebula are seen together as the products of the same supernova and in this case the system is known as a plerion. In some cases, such as that of the Crab Nebula, the adjacent PWN and SNR are visible at other wavelengths but we are yet to distinguish any such objects in the TeV regime due to the limited angular resolution available with the current generation of TeV $\gamma$-ray telescopes. While we are unable to distinguish between the emission from different parts of the system based on their position it is possible to see a pulsed component of emission from the central pulsar which can, as a result, be distinguished from the constant emission from the other parts of the PWN/SNR system. This pulsed component has so far only been seen in the Crab nebula.

While these objects are the most numerous, there are a number of other Galactic source classes visible in the VHE $\gamma$-ray regime. These include the centre of our own Galaxy [9], young stellar clusters such as Westerlund 2 [24] as well as a number of gamma-ray binaries such as LS 5039 [18].

The new generation of VHE $\gamma$-ray telescopes has also led to a large number of new observations of extragalactic sources. As a result new VHE $\gamma$-ray emitting active galactic nuclei (AGN) have been discovered, which has allowed many interesting aspects of fundamental physics to be investigated. Most of the observed galaxies are blazars (such as PKS 2155-304 [53]) with the exception of the radio galaxies M87 [21] and Centaurus A [30] and the starburst galaxies NGC 253 [8] and M82 [189].

### 1.1.3 Cosmic Rays

Another motivation for the observation of VHE $\gamma$-rays is to research the origin of galactic cosmic rays. In 1912 Victor Hess, after whom the HESS telescope array is named, took a balloon ride to investigate the origin of atmospheric ionizing radiation. At the time this was thought to be the product of nuclear decay processes occurring in rocks on the Earth's surface. If this were the case the amount of radiation observed

would decrease as altitude decreased; in reality, the flux was observed to increase at high altitudes, and so Hess concluded that this radiation must be coming from a source of cosmic origin [102]. Magnetic fields usually cause disruption to the path of charged particles such as cosmic rays and so the origin of these particles is unknown; however the processes by which cosmic rays are produced also produce VHE $\gamma$-rays and so by studying the origin of VHE $\gamma$-rays we can understand where cosmic rays are produced.

We have been able to measure the cosmic ray spectrum accurately at energies below about $10^{18}$ eV (See Figure 1.2). It can be described as a pure power law with a spectral index in the range -2.5 to -2.7 up to a few PeV where it steepens slightly at a feature known as the knee. This part of the spectrum is assumed to be the product of Fermi shock front acceleration in supernova remnants (see Section 2.4.1) although this has yet to be conclusively proven; if this is indeed the case then $\gamma$-ray emission is expected from these particles in the 100s of TeV range and $\gamma$-ray observations are needed to confirm that such acceleration is taking place.

After the knee, a spectral index of approximately -3.0 is seen until energies in the region of 1 EeV ($10^{18}$eV) where the spectrum flattens slightly at a feature known as the ankle. Unlike their lower energy cousins, the highest energy cosmic rays are less affected by magnetic fields due to their higher magnetic rigidity. In principle we should thus be able to find out the origin of these particles. However, their flux is very low and so determining their origin requires a large area detector; the Auger experiment [162] aims to detect the directional origin of these particles.

## 1.2 Current $\gamma$-ray Observatories

As has already been discussed the current generation of VHE $\gamma$-ray telescopes has led to at least a tenfold increase in the number of observed sources in this waveband. Recent advances in instrumentation have also led to better observations of lower energy $\gamma$-ray sources.

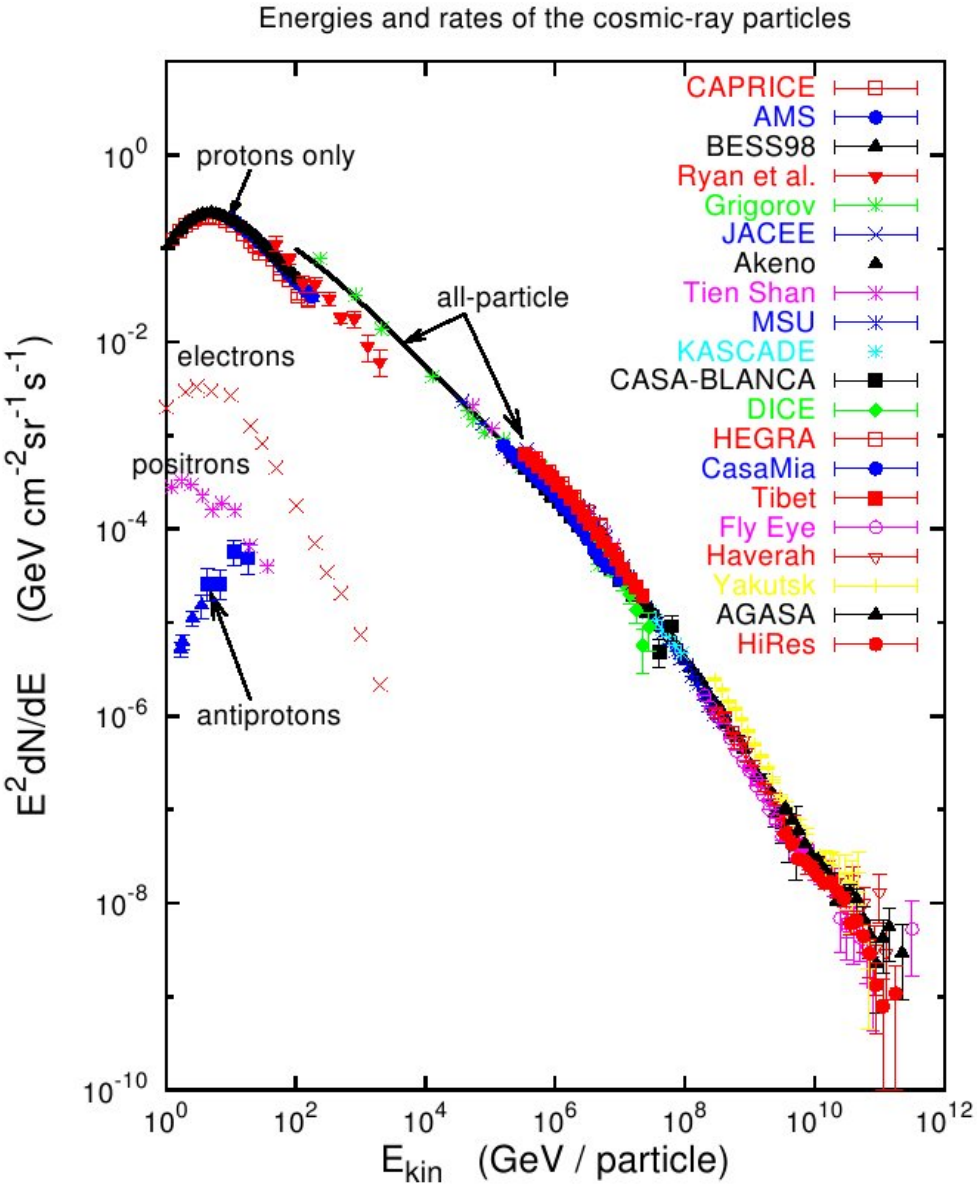


Figure 1.2: The cosmic ray spectrum as presented in [109] showing the features of the cosmic ray spectrum as measured by a number of experiments. It also shows the relative intensities of different types of cosmic rays at low energy.

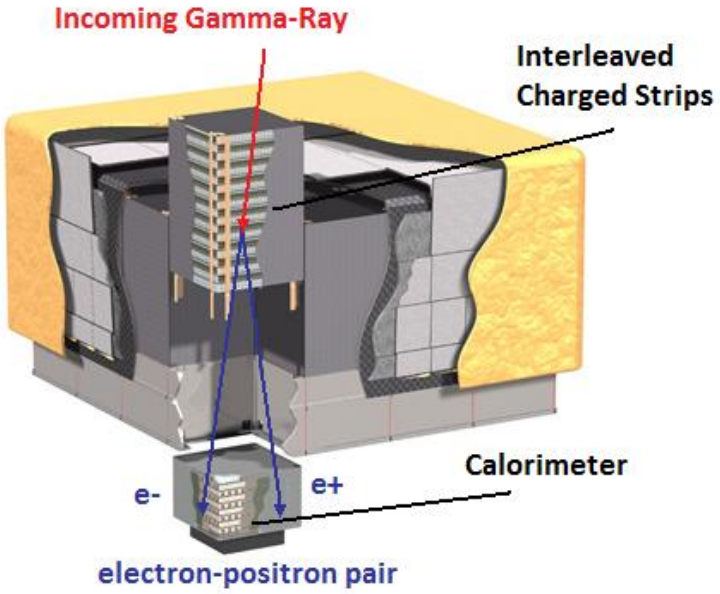


Figure 1.3: The large area telescope of the *Fermi* satellite [36], showing a stack of interleaved charged strips and a calorimeter at the bottom; charged particles enter from the top of the detector. 16 of these stacks form the Fermi LAT.

### 1.2.1 Space based observations

At the lower end of the $\gamma$-ray spectrum (typically below 50 GeV) observations are made using satellite-based instruments. Currently, the most advanced satellite in operation in this waveband is the *Fermi* observatory, named in honour of Italian physicist Enrico Fermi. *Fermi* was launched on the 11th of June 2008 by an international team with support from the governments of the United States, France, Italy, Sweden and Japan [183], prior to its launch it was known as the *GLAST* observatory.

The main instrument of the *Fermi* satellite, the large area telescope (LAT), was built to observe $\gamma$-rays with energies between 20 MeV and 300 GeV [183]. However, although there is sensitivity up to 300 GeV, the rarity of events at such high energies means that events above about 50 GeV are unlikely to be observed with any frequency and so spectral measurements above this value are not claimed for most sources [35]. The highest energy photons observed with the Fermi LAT are more energetic than those observed with previous satellite-based $\gamma$-ray observatories;

this gives us the first opportunity to overlap with existing Cherenkov observatories allowing us to map a complete $\gamma$-ray spectrum from 30 MeV to 10 TeV for the first time.

The LAT employs a system of silicon strip detectors (see Figure 1.3) [36]. When a $\gamma$-ray passes through the detector it will ionize the silicon layers; the charged silicon ions and electrons produced will move towards the charged strips at the end of the silicon, creating a measurable charge. By interleaving these strips it is possible to track the movement of a particle through the detector and hence determine its origin. These detectors are complemented by a caesium iodide calorimeter. When a $\gamma$-ray passes into a caesium iodide crystal, it scintillates, creating a flash of light, the brightness of which depends on the energy of the progenitor photon. As a result, the position and the energy of the incoming $\gamma$-ray can be obtained; *Fermi* is able to localize a point source to 0.3-2 arcminutes, with energy resolution varying between 4% at 5 GeV and 2% at 196 GeV [35].

*Fermi* works in a sky survey mode whereby it takes a full sweep of the sky every three hours [126]. This means that variable sources can be monitored as well as allowing us to view every object in the sky. Even in its first 11 months of monitoring the sky the *Fermi* collaboration compiled a list of 1451 sources [80].

Some of the most interesting of these discoveries relate to its observations of pulsars. One such discovery is the pulsar at the centre of the supernova remnant CTA1 [2]. The Geminga pulsar was thought to be visible only in the $\gamma$-ray regime, but has since been observed at other wavelengths. As a result CTA1 is currently the only pulsar that is radio-quiet and X-ray quiet but visible in $\gamma$-rays. The discovery of CTA1, along with several other observations of $\gamma$-ray pulsars by *Fermi* [3], has led to a better understanding of the emission mechanisms of pulsars and to the discovery that outer magnetosphere models are favoured as the cause of pulsar emission rather than polar cap models where gamma-rays are generated closer to the pulsar surface [3].

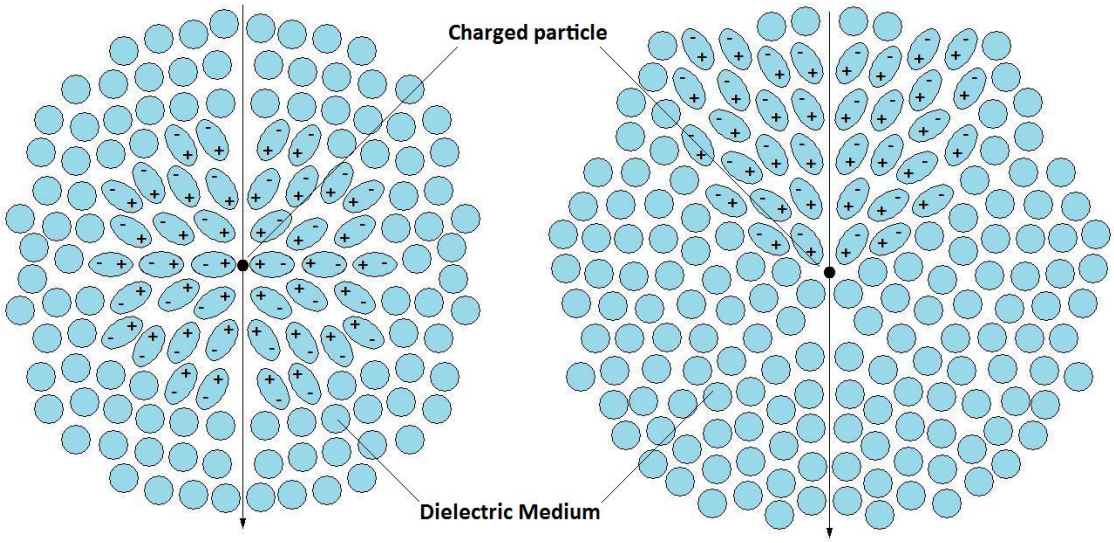


Figure 1.4: The movement of a negatively charged particle downwards through a dielectric medium with subluminal (left) and superluminal (right) velocities.

### 1.2.2 The Cherenkov Effect

When a charged particle travels through a dielectric medium at a speed greater than the phase velocity of light in that medium it produces a bright flash of light, known as Cherenkov radiation. As a charged particle passes through a medium it induces an electric field in the medium by inducing dipoles in the surrounding particles. At low particle velocities (see Figure 1.4) the creation of dipoles around the moving charge will be symmetrical and so not be visible at long distances. However, if the particle velocity is comparable to the velocity of light in the medium, then the overall charge of the dipoles will no longer be symmetrical in the line of movement of the electron (see Figure 1.4). This force slows down the incoming electron, causing it to produce radiation [124].

As the light produced is moving more slowly than the particle that is producing it, the wavefronts of the generated waves will interfere constructively (see Figure 1.5) to produce a flash of light. This will be seen at an angle of $\theta$ where:

$$\theta = arccos\frac{c}{nv} \tag{1.2}$$

where $n$ is the refractive index of the medium and $v$ is the velocity of the particle.

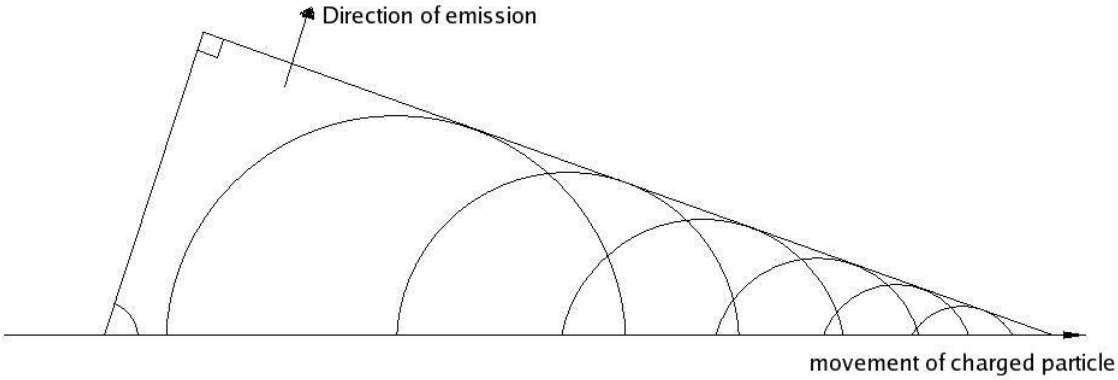


Figure 1.5: A Huygens construction showing that the Cherenkov radiation generated by a particle moving through a dielectric medium will interfere constructively

When a VHE gamma-ray strikes the Earth's upper atmosphere it will interact to produce an electron positron pair. These in turn will slow down and produce photons via bremsstrahlung (see Section 1.3.3) which will in turn create more electron positron pairs. As a result a large shower of electrons is produced (see Figure 1.6), all of which produce Cherenkov light by the process described above until the point at which the light produced no longer has sufficient energy to produce electron positron pairs. In a typical 1 TeV air shower 100s of electron positron pairs are produced which leads to the creation of a cone of light of half angle $\theta \approx 1^{\circ}$ (see Figure 1.7). This can be observed from the ground as an ellipse with its long axis pointing towards the source of the photon. The shape and size can be used to determine the energy of the incoming photon [108]; a typical 1 TeV photon will produce an ellipse of major axis 150 m. The size of the observed ellipse will increase with distance from its origin and so a more accurate estimate of the direction of the air shower can be made by placing the detector at a lower altitude. However, the ellipse observed will be less bright at lower altitudes and indeed much of its energy will be absorbed by the atmosphere so in practice most Cherenkov telescopes are located at altitudes of about 2 km as a compromise between atmospheric absorption and positional estimation.

A significant source of background noise is caused by incoming cosmic rays which

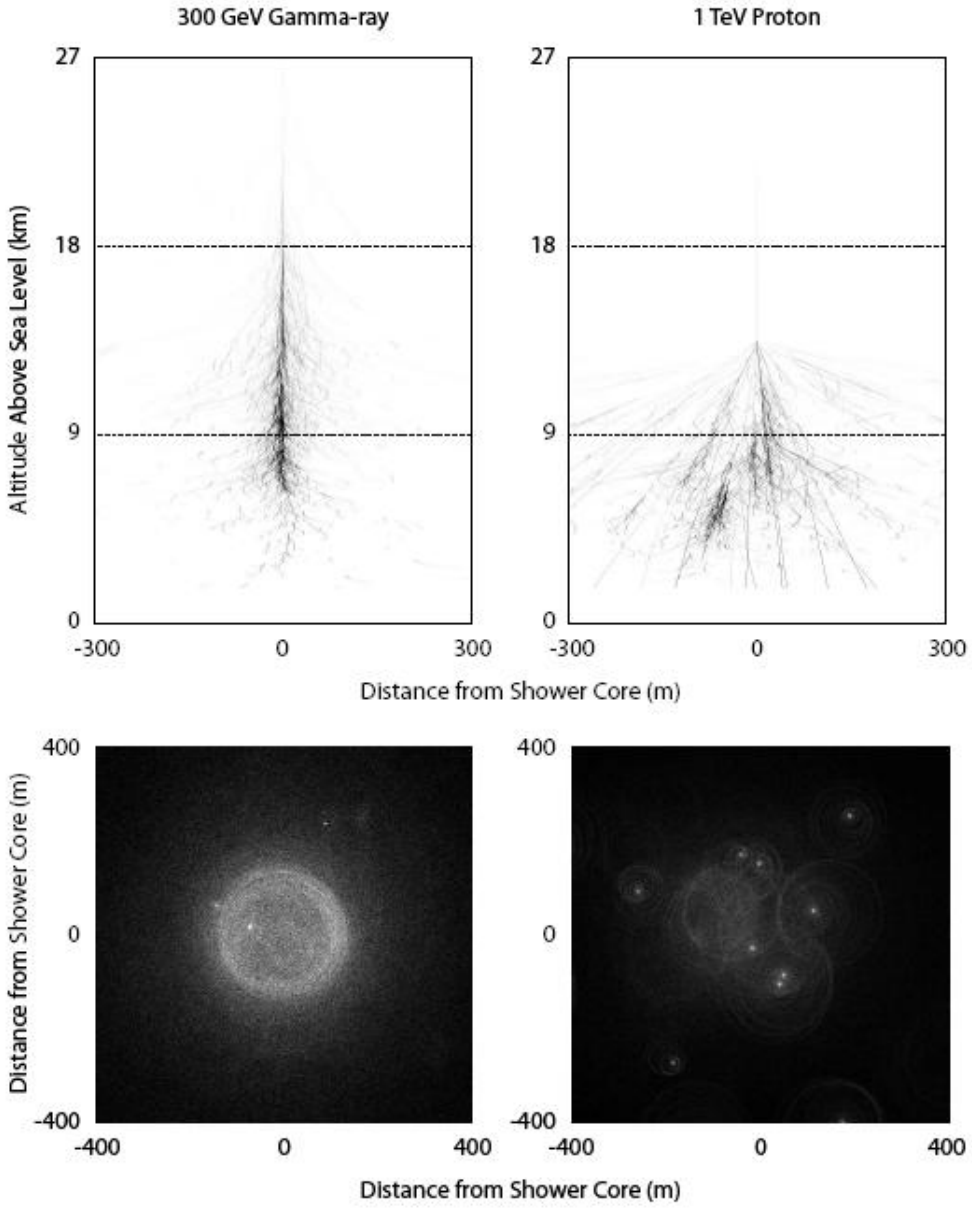


Figure 1.6: The air showers produced by the interaction of a $\gamma$-ray (left) and a cosmic ray (right) with the Earth's atmosphere [39].

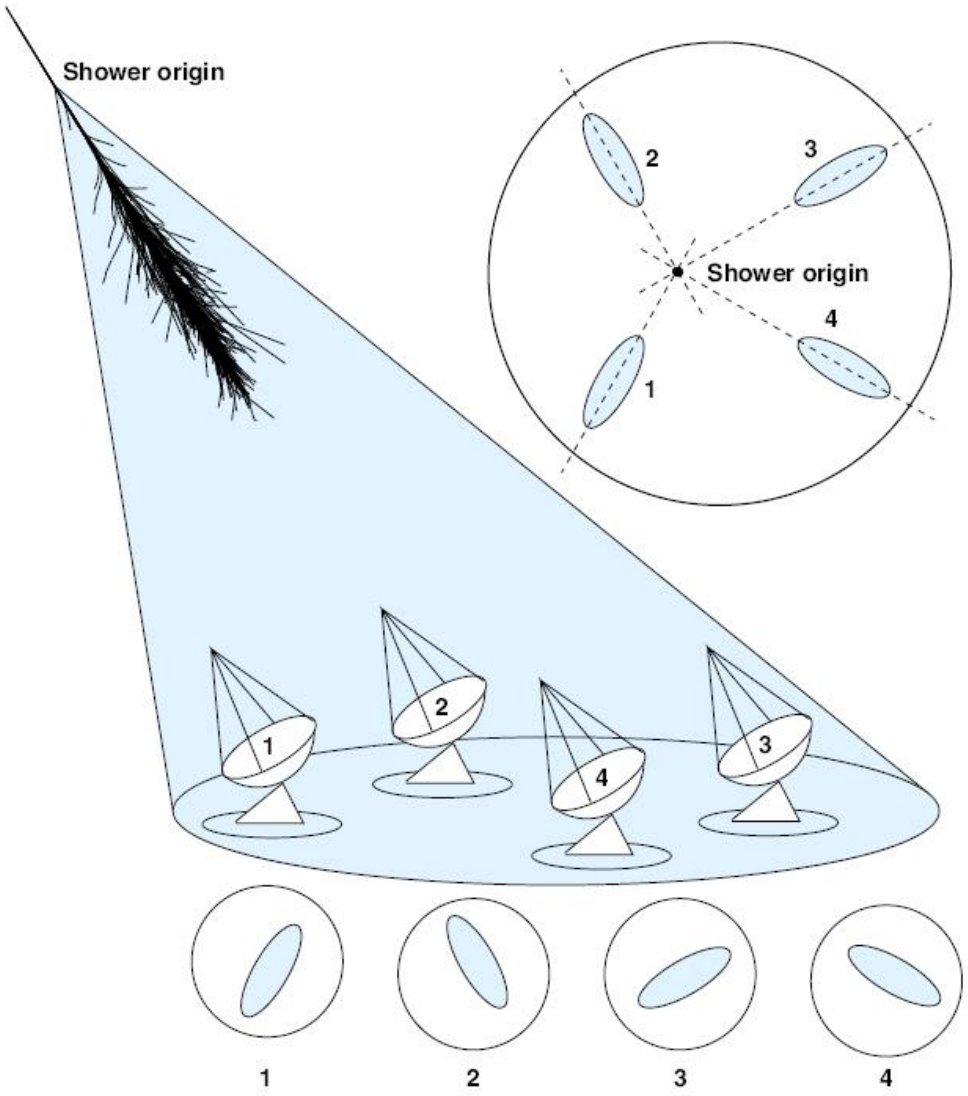


Figure 1.7: An incoming $\gamma$-ray interacting with the Earth's atmosphere, it produces a cone of Cherenkov light which forms an ellipse on the ground. The axis of each shower image points towards the origin of the shower [70].

also produce particle air showers and corresponding flashes of Cherenkov light. However, the shower produced by the interaction of a cosmic ray has hadronic and muon components which causes the air shower to have a broader and more irregular shape, as can be seen in Figure 1.6. The shape of an air shower can thus be used to determine the type of particle that created it, more detail of this process is given in Chapter 3.

### 1.2.3 Stereoscopic Observations

Single Cherenkov telescopes suffer from a number of significant problems which prevent accurate calculations of energy and position from being made. When an observation of a Cherenkov light shower is used to infer its properties, both the angle of arrival and the energy of the incoming particle will affect the size of the shower ellipse as seen from the ground. Due to the error in the orientation of the image and the position of its centre there is a large intrinsic error in the position of the source using this method.

Ideally, observations of the shower must be made with several telescopes to get a much more accurate estimate of position and energy of the source. If multiple images of the shower are used then it is not necessary to use the shape of the ellipse to estimate the position of the incoming air shower as the point of intersection of the images observed can be used instead. As the position derived in this method is more accurate the energy of the air shower can be estimated using this positional calculation and so it too can be determined more accurately. Multiple telescopes also allow background muons present in the local environment of the telescope, which could pass through the camera of a single telescope and trigger it, to be eliminated by requiring that more than one telescope responds for an event to be recorded. More detail on this process is given in Chapter 3.

The use of multiple telescopes has allowed the current generation of Cherenkov telescopes to greatly expand the number of observed VHE gamma-ray sources. There are currently four leading Cherenkov observatories; with two located in each hemisphere, the whole sky can be observed. In the northern hemisphere the VERITAS array, located in Arizona, consists of four telescopes each with a reflecting area of

Table 1.1: The parameters of the Current Generation of TeV $\gamma$-ray observatories. $\star$ CANGAROO III consists of 4 telescopes but not all of these are currently operational.

| Observatory | Location | Energy Threshold GeV | $N_{tels}$ | Area $m^2$ | Field of View $^\circ$ |
|---|---|---|---|---|---|
| CANGAROO III [76] | Australia | 250 | 4$\star$ | 79 | 4 |
| HESS [17] | Namibia | 100 | 4 | 107 | 5 |
| MAGIC [140] | La Palma | 25 | 2 | 300 | 3.5 |
| VERITAS [194] | Arizona | 100 | 4 | 110 | 3.5 |

approximately 110 $m^2$ and was completed in 2007 [194]. It is primarily used to make observations of active galactic nuclei and other extragalactic sources as fewer galactic sources are visible from its northern hemisphere location.

The other major northern hemisphere observatory is the MAGIC observatory on the Canary Island of La Palma. It consists of two large telescopes, each with a reflecting area of about 300 $m^2$ [140]. This increased area allows MAGIC to observe photons down to an energy of 25 GeV at zenith, much lower than its competitors which have a typical energy threshold of 100-200 GeV. This allows it to view phenomena such as the pulsed emission from the Crab nebula which is not possible at the higher energy thresholds of its competitors [34]. Its northern hemisphere location does however mean that it is unable to view the region around the Galactic Centre where most Galactic Sources are located and so, like VERITAS, most of its sources are AGN.

In the southern hemisphere there are two observatories which were designed with four telescopes similar to VERITAS. The Australian-based CANGAROO telescope has discovered fewer sources than any of its main competitors and is now running only two telescopes due to technical problems [76]. The Namibian-based HESS telescopes have been used to discover over sixty sources as of the start of 2010 and are described in more detail below. Details of the current generation of Cherenkov observatories are given in Table 1.1.


Figure 1.8: Namibia showing the position of the HESS site.

### 1.2.4 The HESS Telescopes

The High Energy Stereoscopic System (HESS) telescopes are located in the Khomas highlands of Namibia (23°16′18″ South, 16°30′00″ East) near the Gamsberg mountain (see Figure 1.8). The array was constructed by a consortium of European and African universities and has been in operation as a full array since 2004 [17]. In that time it has made a large number of discoveries, particularly of supernova remnants and pulsar wind nebulae (PWNe), which as Galactic objects are more likely to be observed from the southern hemisphere as they are more numerous in this portion of the sky.

The observatory consists of four telescopes which are arranged in a square of side 120 m [17] (Figure 1.9), which allows for maximum sensitivity to photons with energies of around 100 GeV at zenith; while this was the initial energy threshold of the telescopes this is slowly increasing as the reflectivity of the mirrors gradually degrades with a current energy threshold of about 200 GeV. However, this degradation should be reduced by the mirror replacement work currently (August 2010)

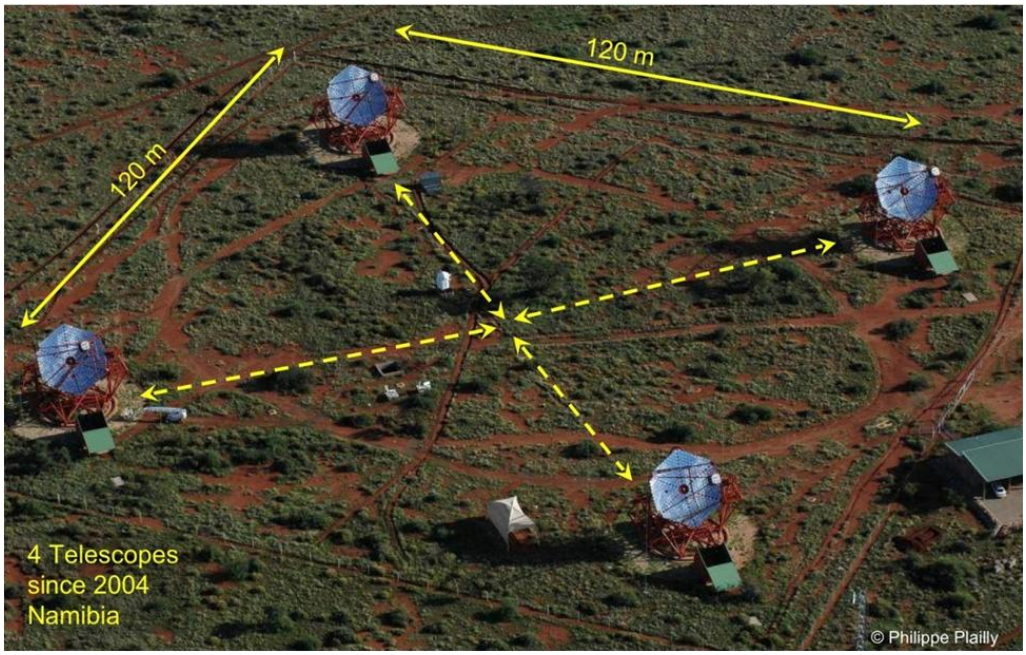


Figure 1.9: An aerial photo showing the position of the HESS telescopes at the corners of a square of side 120m [163].

underway on the telescopes. Each telescope has a diameter of 13m and consists of 382 round mirrors, each with a diameter of 60 cm, giving a total reflecting area of 107 $m^2$ [17]. The mirrors are placed in a Davis-Cotton arrangement [64]. In this design a spherical telescope structure is used with its mirror segments, which are also spherical, each having a focal length twice that of the telescope itself. At the focal point of the telescope, the camera consists of an array of 960 photomultiplier tubes which each observe an area of sky 0.16° across giving a field of view for the detector of 5° [17].

The Cherenkov light which is used by the HESS telescopes to observe VHE $\gamma$-rays peaks in intensity in the ultraviolet, but due to atmospheric absorption the light observed peaks in the blue end of the visible spectrum (at a wavelength of about 300 nm) when it is observed from the ground. It is thus necessary to use the short duration of the Cherenkov light flashes to distinguish them from the night sky background. A large amount of this background radiation is removed by HESS by only recording data when it is triggered by a fast flash of light, which usually corresponds to a Cherenkov event. The background (this time the product of cosmic

ray events) is further reduced by performing cuts on these events so that only those recorded events that are thought to be generated by TeV $\gamma$-rays are used in analysis. The method by which these cuts are applied and the energy of the events is calculated is described in Chapter 3.

## 1.3 Mechanisms for the production of non-thermal radiation

As we have seen, in order to understand the extraterrestrial bodies which generate VHE $\gamma$-rays we must first understand the processes by which these $\gamma$-rays are produced. The understanding of these mechanisms gives an insight into the inner workings of distant astronomical objects and also allows us to form a better understanding of the fundamental physical systems underlying these processes.

### 1.3.1 Synchrotron Radiation

One of the main sources of non-thermal radiation is the interaction of charged particles with magnetic fields. When a moving charged particle enters a magnetic field it will be deflected by it and, if the magnetic field is strong enough, it will move in a helical orbit spiralling around the magnetic field lines (see Figure 1.10). In this case, the movement of the particle in the magnetic field can be expressed in terms of two components, which correspond to the components of the magnetic field parallel and perpendicular to the magnetic field. The parallel component of this motion will not be affected by the magnetic field and this will represent the speed at which the particle will travel along the magnetic field. The perpendicular component of the incoming particle will determine the radius of its motion around the magnetic field and thus determine the frequency of the radiation emitted.

The acceleration of a charged particle in a magnetic field is given by:

$$a = \frac{v^2}{r} = \frac{q}{\gamma m}\mathbf{v} \times \mathbf{B} \tag{1.3}$$

Where $\mathbf{v}$ is the velocity of the charged particle and $\mathbf{B}$ is the strength of the

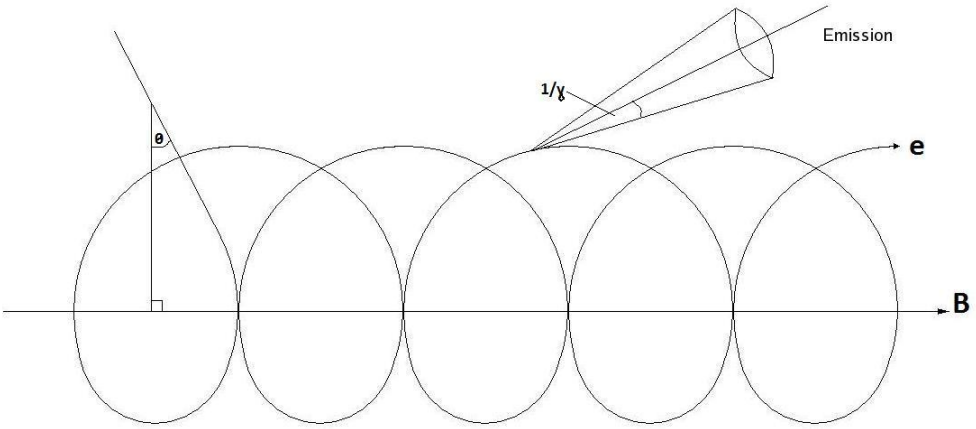


Figure 1.10: Synchrotron emission. A particle with an electric charge (e) enters a magnetic field at an angle $\theta$ to it. The particle begins to orbit around the magnetic field lines following a helical path and emits radiation in a cone tangential to its path of movement with a half angle equal to $1/\gamma$.

magnetic field in which it is moving, $\gamma$ is the Lorentz factor, and $r$, $m$ and $q$ represent the radius of curvature, mass and charge of the particle respectively. In order to calculate the energy of the radiation that is produced in this process we also need to know the energy loss rate of an accelerated charged particle:

$$-\left(\frac{dE}{dt}\right)_{rad} = \frac{q^2|a|^2}{6\pi\epsilon_0 c^3} \tag{1.4}$$

where $\epsilon_0$ is the permittivity of free space and c is the speed of light in a vacuum. For an electron this gives:

$$-\left(\frac{dE}{dt}\right)_{rad} = \frac{q^4 v^2 B^2 sin^2\theta}{6\pi\epsilon_0 c^3} = \sigma_T c \frac{B^2}{\mu_0}\left(\frac{v}{c}\right)^2 \gamma^2 \sin^2\theta \tag{1.5}$$

Where $\sigma_T$ is the Thompson cross section, $\mu_0$ is the vacuum permeability and $\theta$ is the angle of incidence of the charged particle. This expression can be averaged over all pitch angles to give:

$$-\left(\frac{dE}{dt}\right)_{rad} = \frac{2}{3}\sigma_T c \frac{B^2}{\mu_0}\left(\frac{v}{c}\right)^2 \gamma^2 \tag{1.6}$$

In the case of non-relativistic cyclotron radiation, the characteristic frequency of

the radiation emitted is given by the gyration frequency. This can be derived by taking the acceleration equation above and equating the frequency with $\nu = \frac{v}{2\pi r}$ to give:

$$\nu_g = \frac{qB}{2\pi m} \tag{1.7}$$

In the case of electrons moving at relativistic speeds, synchrotron radiation is produced. This radiation is concentrated in the forward direction (see Figure 1.10), lying entirely within a cone of angular width $\theta = 1/\gamma$ and projecting a conical annulus on the sky. This beaming results in a spreading of the spectrum with most of the energy peaking at a frequency $\nu_c = \gamma^2 \nu_g$ which gives:

$$\nu_c = \gamma^2 \frac{qB}{2\pi m} \tag{1.8}$$

It also results in polarization of the radiation perpendicular to the magnetic field. As $\gamma$ is related to the energy of the electrons, the observed spectrum of the synchrotron radiation will be directly related to energy spectrum of the electrons by the factor $\alpha = \frac{x-1}{2}$, where $\alpha$ is the spectral index of the radiation and $x$ is the spectral index of the electron energies. Observation of this radiation can therefore not only show the presence of relativistic electrons but also of the magnetic field necessary for their production.

At lower frequencies, when the brightness temperature of the photons released becomes greater than the kinetic temperature of the radiating electrons, the radiation is absorbed and so a spectral index of $\nu = 5/2$ is observed with a turnover at the point where the brightness and kinetic temperatures are equal (see figure 1.11). The brightness temperature is defined as [69]:

$$T_b = \frac{c^2 I_\nu}{2\nu^2 k_B} \tag{1.9}$$

where $c$ is the speed of light in a vacuum, $k_B$ is Boltzmann's constant, $\nu$ is the frequency and $I_\nu$ is the intensity of the radiation at the given frequency. The radiation produced in this procedure is observed at a range of frequencies from the radio to the X-ray regime but it is not observed in VHE $\gamma$-rays because source

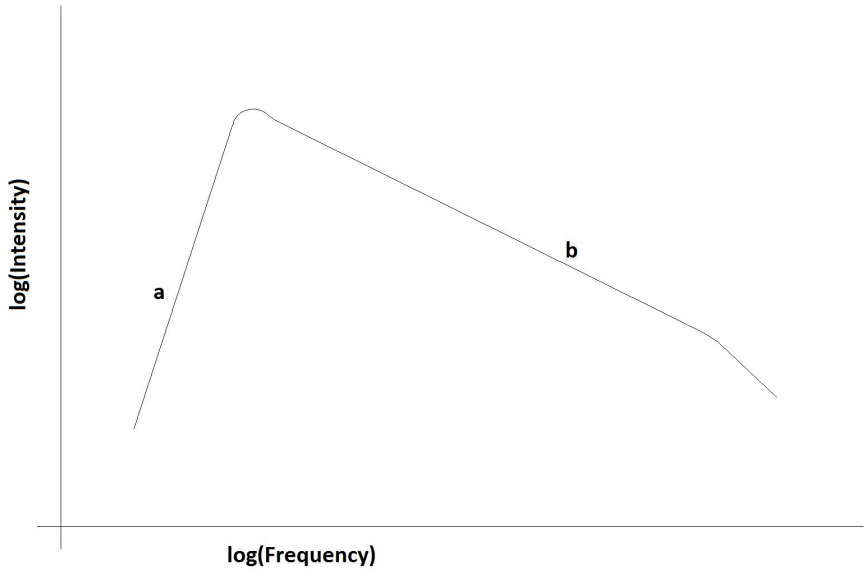


Figure 1.11: The spectral turnover expected in a synchrotron spectrum. a and b represent the areas of the spectrum, which are absorption and emission dominated respectively.

electrons of the energies required to generate synchrotron photons have yet to be observed; energies of the order of $10^{11}$ TeV are required to generate TeV $\gamma$-ray synchrotron photons. It is however important in the understanding of VHE $\gamma$-ray sources as it is in some cases the source of lower energy photons which can act as seed photons for the inverse Compton boosting described in Section 1.3.5.

### 1.3.2 Curvature Radiation

Curvature radiation is closely related to synchrotron radiation as it is also caused by the movement of a charged particle in a magnetic field. However, while synchrotron radiation is derived from the component of movement perpendicular to the magnetic field, curvature radiation is caused by the component parallel to the field. In this case the charged particle will follow the magnetic field lines and experience acceleration due to the curvature of these lines. This will emit radiation with a characteristic frequency of [139]:

$$\nu_c = \frac{\gamma^3}{r_c} \tag{1.10}$$

Where $r_c$ is the radius of curvature along which a particle is travelling. It is only observed in environments with strong magnetic fields ($> 10^8$ G) with a large amount of curvature, such as pulsar magnetospheres. For Crab-like young pulsars this results in a typical frequencies of $10^{18}$ Hz (keV energies) and thus emission in the X-ray regime. Meanwhile millisecond pulsars will typically emit at frequencies of about $10^{22}$ Hz (10 MeV energies) and so emit at the lower end of the $\gamma$-ray regime [59].

### 1.3.3 Bremsstrahlung

Bremsstrahlung, named for the German expression for braking radiation, is another form of non-thermal radiation produced by the acceleration (or more specifically deceleration) of charged particles, atoms or molecules. In this case, the deceleration is caused by the proximity of a travelling particle to the electric fields of nuclei lying in its path. A fast-moving charged particle will slow and be deflected on its interaction with another charged particle and thus radiation is produced (see Figure 1.12). It is useful in astronomy as it shows areas where relativistic electron winds are propagating through dense material.

The energy spectrum of the radiation produced in this process will be a power law of the same form as the electron energy spectrum by which it is produced. The average energy of the photon produced in this process will be $\frac{1}{3}$ of the initial energy of the incident electron with the maximum energy of the photon matching the energy of the electron from which it is generated [139]. As a result it is possible to generate VHE $\gamma$-rays by this process if the electrons involved are energetic enough but it is more commonly observed at lower energies (around 100 MeV) where more progenitor electrons are available.

### 1.3.4 Nuclear And Atomic Transition Emission

Bremsstrahlung is produced by the interaction of a passing electron with an ion and so is also known as free-free emission, a form of atomic transition which emits a continuous spectrum of radiation. Similar emission is created by electrons that are atomically bound to the nucleus with which they are interacting; this is known as

bound-bound emission. When an electron is present in an excited atomic orbital it will drop down to its most stable state and in doing so emit radiation of a specific wavelength. Nuclear transition lines are seen at higher energies than atomic transition lines (in the MeV regime) and allow the nickel and cobalt produced in SNRs to be observed. A similar process of excitation and decay occurs with the nucleons in an atomic nucleus.

### 1.3.5 Comptonisation

As we have seen, many types of non-thermal radiation are created by acceleration processes related to magnetic fields. Not all non-thermal photons are generated in this way and indeed perhaps the most relevant production mechanism in terms of VHE $\gamma$-ray astronomy is instead the interaction of existing photons with particles.

In 1923, while investigating the effect of bombarding atoms with X-ray radiation, Arthur Compton noted that the X-ray radiation, as well as being deflected (as would be expected from classic electromagnetic theory), was shifted to a higher wavelength

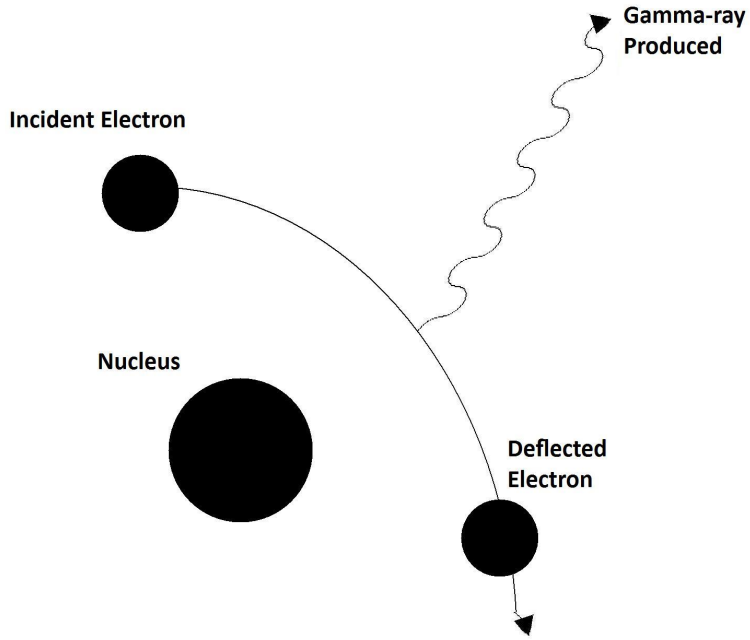


Figure 1.12: The bremsstrahlung emission mechanism.

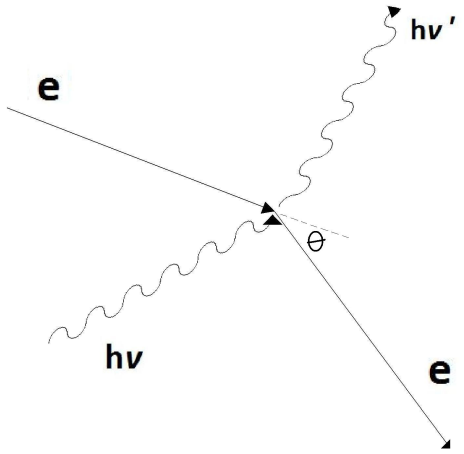


Figure 1.13: Compton scattering of a photon by an energetic electron.

because it had lost energy to the electrons present in the bombarded atom (See figure 1.13). He observed the relation:

$$\lambda_1 - \lambda = \frac{h}{m_e c}(1 - \cos\theta) \tag{1.11}$$

where $\lambda$ and $\lambda_1$ are the wavelengths of the photons before and after scattering respectively and $\theta$ is the angle by which the radiation is scattered (See Figure 1.13). This can be expressed in energy terms as:

$$\epsilon_1 = \frac{\epsilon}{1 + \frac{\epsilon}{mc^2}\cos\theta} \tag{1.12}$$

where $\epsilon$ and $\epsilon_1$ are the energies of the photon before and after scattering respectively. However, if the electron is moving relativistically, the momentum transfer will not result in a net energy gain for the electron; instead, the photon will gain energy from the electron. This is easiest to understand if we consider the interaction in terms of the reference frame of the electron. In this case the energy of the incident and product photons are shifted by:

$$\epsilon' = \gamma\epsilon[1 + (v/c)\cos\theta] \tag{1.13}$$

$$\epsilon_1 = \gamma\epsilon_1'[1 + (v/c)\cos\theta] \tag{1.14}$$

where $\epsilon'$ is the energy of the photon in the frame of reference of the electron and $\epsilon$ is the energy of the photon in the laboratory frame. It can be shown that the energy of the product photon is shifted by:

$$\epsilon_1 = \gamma^2\epsilon \tag{1.15}$$

in the relativistic case. As a result, observation of this radiation can be used to determine the energy spectrum of relativistic electrons. Consequently, by comparison with synchrotron emission from the same source, it can be used to infer the strength of the magnetic field in which the electrons are moving. In some cases the synchrotron electrons which generate the photons are also responsible for shifting them to higher energies via the inverse Compton process; this is known as the synchrotron self Compton (SSC) mechanism and results in a much larger TeV flux than when background radiation seed photons, such as the cosmic microwave background and ambient starlight, are responsible for the Compton scattering. In the TeV regime the inverse Compton process is the main emission process by which pulsar wind nebulae emit and as lower energy electrons can produce this emission than are required for synchrotron emission larger pulsar wind nebulae are seen in this regime than at lower photon energies, this is discussed in more detail in Section 2.6.

### 1.3.6 Pion Decay

In the high energy interactions that take place in stars many secondary particles are produced. By looking at the decay products of these particles we can get an indication of the nuclear interactions that are taking place. When a proton travelling at a high energy interacts with a nucleus, high energy pions of all types are produced. By observing the decay products of these energetic pions we can thus infer the presence of energetic protons, which theoretically could allow us to distinguish between leptonic and hadronic particle populations, although this is difficult

in practice. Charged pions have a typical lifetime of $2.6\times10^{-8}$ s and decay in the following fashion:

$$\pi^+ \rightarrow \mu^+ + \nu_m^u \tag{1.16}$$

$$\pi^- \rightarrow \mu^- + \overline{\nu_m^u} \tag{1.17}$$

The muons produced will quickly decay further into electrons and additional neutrinos. As neutrinos have only ever been observed in limited quantities from two astronomical sources (the Sun [159] and supernova 1987a [40] [112]) and these only at lower energies than the neutrinos produced in this process, the most productive method of observing pion decay at present is by looking for the energetic photons produced by neutral pions.

Neutral pions typically have a shorter lifetime than charged pions (typically $1.8 \times 10^{-16}$ s) and decay as follows:

$$\pi^0 \rightarrow 2\gamma \tag{1.18}$$

As the rest mass of a neutral pion is 139.6 MeV, the energy of the photons created will be no less than half of this value (69.2 MeV). However, due to the velocity of the pion the energy of the photons observed may be much greater, and can also be used to infer the energy of the protons involved in the original collision. The presence of pion decay emission will thus imply the presence of energetic protons in a system. However it is difficult to distinguish these photons from those produced by the inverse Compton process as they emit at similar energies and with similar spectra.

### 1.3.7 Electron-Positron Annihilation

Another particle process that is known to generate non-thermal radiation is the annihilation of electrons and positrons, the inverse of the process described in Section 1.4.1. However, as the energy of the interacting leptons is usually split evenly

between the two interacting photons, two 511 keV photons are produced if the interacting particles are at rest; such emission is not seen at TeV wavelengths.

### 1.3.8 Dark Matter Annihilation

Dark matter is the material which is present in the universe but is not directly observed. It is predicted to make up about 20% of the mass of the universe compared to only 4% made up of observable baryonic matter (the remaining 76% is accounted for by dark energy) [81]. Many theoretical particle physics predictions point to the existence of a weakly interacting massive particle or WIMP as the most likely candidate to account for this unobserved matter. It is a potential source of non-thermal radiation that has not, as yet, been observed.

Many of the predicted varieties of WIMPs are expected to annihilate with themselves as they are supersymmetric and hence are their own antiparticle. Depending on the mass of the dark matter particle this may produce non thermal radiation at TeV energies. However, no dark matter candidate source has so far been identified; in the TeV regime this is not surprising as the current generation of instruments are not expected to be sensitive enough to observe the fluxes predicted by current models. The most likely source for observation of this emission is the Galactic Centre; observation of annihilation flux in this region is difficult because of the strong astrophysical source present in this region which may hide any annihilation signal [81].

## 1.4 Absorption Mechanisms of VHE $\gamma$-rays

While understanding the mechanisms by which VHE $\gamma$-ray radiation is produced is important, it is also necessary to know the mechanisms by which they can be absorbed prior to observation in order to fully understand the spectra that are observed. Mechanisms that absorb thermal radiation will also absorb non-thermal radiation of similar wavelengths and so there are a large number of mechanisms such as atomic excitation to consider. However, most of these do not absorb VHE $\gamma$-rays. At these energies only two absorption mechanisms are important. One is the atmospheric interaction by which Cherenkov light is generated and VHE $\gamma$-rays

are observed (see Section 1.2.2) while the other is the interaction with background light via pair production.

### 1.4.1 Pair production and VHE photons

If a photon has a sufficient energy it will interact with background photons to produce an electron positron pair:

$$2\gamma \rightarrow e^- + e^+ \tag{1.19}$$

As energy must be conserved in this interaction it can only occur if the combined energies of the interacting photons in the centre of momentum frame exceed twice the rest mass energy:

$$\epsilon_1 \epsilon_2 (1 - cos\theta) > 2m_e^2 c^4 \tag{1.20}$$

where $\epsilon_1$ and $\epsilon_2$ are the energies of the two incident photons and $\theta$ is the angle between them. A major source of such absorption for VHE $\gamma$-rays is the extragalactic background light (EBL). The EBL is the sum of all starlight emitted in the history of the universe which has not been absorbed. As we can see from Equation 1.20, TeV photons will interact with infrared, visible and ultraviolet photons; this is not much of a problem in the observation of Galactic sources as the distance the $\gamma$-rays have to travel is less than 30 kpc and the interaction cross-section is small, typically $1.5 \times 10^{-23}$ cm $^2$ for a 1 TeV photon [184]. However, the probability of interaction is much greater over the 120 Mpc distance to the nearest VHE emitting blazars, Markarian 421 and Markarian 501 and becomes more important for more distant objects such as PKS 2155-304, which has a redshift of z= 0.117 [31]. This limits the maximum distance from which VHE $\gamma$-rays can be detected; the most distant source that has been observed so far in the VHE gamma-ray regime is 3C279 which has a redshift of z$\approx$0.5 [142].

The absorption signature may be used to infer upper limits to the EBL provided that the distance to the AGN in known. However, the assumptions which must at present be made regarding absorption intrinsic to the source limit the usefulness of

this approach.

# Chapter 2

# Pulsar Wind Nebulae

A pulsar wind nebula is formed by the interaction of the relativistic electrons which are streaming out from the magnetic poles of a pulsar into the surrounding medium of a supernova remnant. The interaction of these electrons with ambient photons causes VHE $\gamma$-ray photons to be produced.

In this Chapter, the processes by which supernovae occur are discussed along with the mechanisms by which they pro duce supernova remnants and pulsars. This is followed by more detail as to how the emission of relativistic electrons into the surrounding medium generated by the supernova forms a pulsar wind nebula.

## 2.1 The End of a Star

For most of their lives stars generate energy in a fusion reaction in which four hydrogen nuclei are fused together to form a helium nucleus releasing 26.71 MeV in the process. This interaction requires a temperature of about $10^7$ K which can be derived using the quantum mechanical formula:

$$T_{\text{quantum}} = \frac{4}{3}\frac{\mu_m Z_1^2 Z_2^2 e^4}{kh^2} \tag{2.1}$$

where $T_{\text{quantum}}$ is the temperature necessary for fusion to occur if we include quantum mechanical tunnelling effects; if a classical Coulomb barrier approach was used the necessary temperature would be much larger, and indeed nuclear fusion in our own Sun would be impossible. $Z_1$ and $Z_2$ are the numbers of protons in each

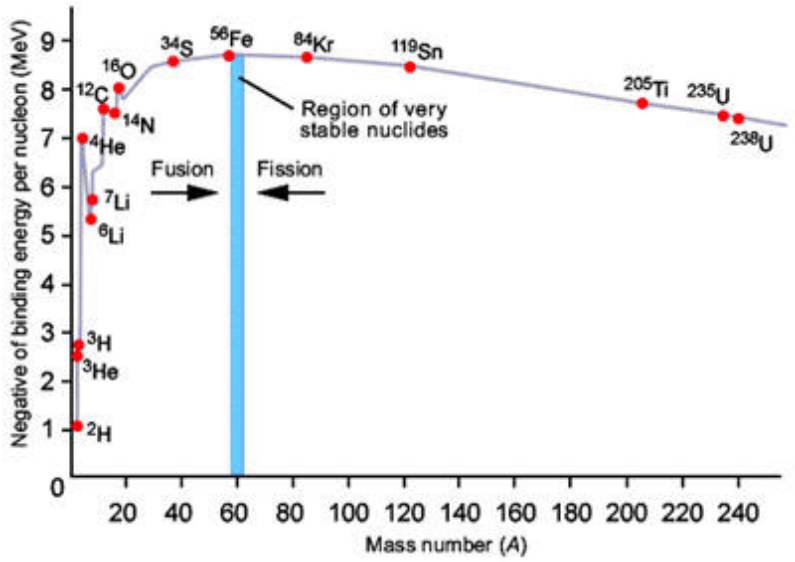


Figure 2.1: The binding energy per nucleon of known isotopes taken from [62] showing a number of common isotopes. It also shows the mass numbers at which fusion and fission reactions are energetically favourable.

nucleus which in the case of hydrogen fusion are both equal to one; $\mu_m$ is the reduced mass of the colliding particles. As the internal pressure and temperature which a star can reach are dependent on the mass, this reaction only occurs in stars which have a mass of at least 10% of the mass of the Sun.

Once this hydrogen fuel has run out, fusion processes begin with other elements, starting with helium and building up to heavier nuclei. As the temperature required for nuclear fusion increases with the mass and charge of the particles involved, only larger stars are capable of fusing many of the heavier elements. In the largest stars this process produces many shells of progressively more massive nuclei, with fusion continuing in each layer. This will include layers of carbon, oxygen and silicon which progressively release less and less energy until iron is produced, which has the highest binding energy per nucleon of any atom (See Figure 2.1). As a result fusion processes for nuclei heavier than iron are no longer exothermic.

At this point high temperatures of the order of $10^9$ K are present in the core of the star and the photons present are sufficiently energetic to initiate a process known as photodisintegration, where large elements are broken down into smaller

ones by interaction with photons. A high energy photon will strike nuclei in the iron core and reduce them to smaller nuclei, which can be summarised by the following:

$$^{56}\mathrm{Fe}_{26} + \gamma \rightarrow 13^{4}\mathrm{He}_{2} + 4\mathrm{n} \tag{2.2}$$

$$^{4}\mathrm{He}_{2} + \gamma \rightarrow 2\mathrm{p}^{+} + 2\mathrm{n} \tag{2.3}$$

Due to the much lower binding energy of the products than the progenitors of these interactions, this process is highly endothermic and so the temperature and hence the pressure in the core of the star begins to decrease rapidly. The process occurs at a high rate and so fusion processes, which are much slower, are unable to balance this process by the creation of heavier nuclei. In these circumstances the electrons in the star start to combine with the protons present to create more neutrons:

$$p + e^{-} \rightarrow n + \nu_{e} \tag{2.4}$$

In most circumstances the neutrons generated in such processes would decay back to a proton and an electron; however, in the central core of a dying star electrons are degenerate and so an electron cannot be released. Additionally, the neutrinos generated in this process will be capable of escaping the stars core rapidly due to their small interaction cross-section and cause an even greater drop in the temperature and pressure of the core with $\approx 90\%$ of the energy released in the supernova lost via this neutrino release. Observations of the neutrinos produced in this interaction were observed from the supernova 1987A [40] [112].

## 2.2 Supernovae

The rapid decrease in pressure in the core of the star removes the mechanism for supporting the star and the outer layers will fall towards its centre. This will continue until the density of the stellar core reaches about three times that of an atomic nucleus; at this point the Pauli exclusion principle starts to affect the neutrons in the core. As neutrons are Fermions, they cannot inhabit the same state as one

another and so at high densities (of the order of $8 \times 10^{17}$ kg/m$^3$) the neutrons are subject to degeneracy pressure which stabilizes the star and creates an outward force of repulsion from its centre. This process is extremely rapid, taking about only one fiftieth of a second; while the core is collapsing the outer layers remain almost motionless. The pressure in the core creates an outward pressure wave which causes the outer layers to be thrown off at high speeds of the order of $10^4$ km/s.

Perhaps 30-50 percent of the mass of the star is thrown off in the above process at high temperature ($\approx 10^6$ K) and pressure. As a result elements heavier than iron which are not generated in the cores of stars (as their production processes are endothermic) can be generated in the initial supernova explosion in a process known as rapid neutron capture. Heavy nuclei can capture neutrons easily but usually the larger nuclei created in this process decay back to their component elements as they are unstable. However, when rapid neutron capture exists many additional neutrons can be captured and thus a stable nucleus of a heavier element is achieved. As the stars which produce such emission are typically more than eight times the mass of the Sun, several solar masses of material are blown off in the explosion carrying of the order of $10^{51}$ ergs ($10^{46}$ Joules) of kinetic energy. This results in an expanding shock wave travelling at initial speeds of the order of $10^4$ km/s creating a supernova remnant (SNR).

When the outer layers of the star have been blown away a core remains. If the mass of the core is below about three times the mass of the Sun (corresponding to an initial main sequence stellar mass of twenty solar masses) it will stabilize and form a pulsar; if the mass is greater than this it will collapse to form a black hole. The mass threshold below which a star forms a neutron star rather than a black hole is highly debatable and no firm limit has been established [82] although most current models predict that progenitor stars above about 20 solar masses will form black holes when they collapse.

This kind of supernova, the product of a massive star at the end of its life is known as a type II supernova and is identified by the presence of Hydrogen emission lines in its observed spectrum. If the outer layers of the star have been removed by the time the supernova occurs no Hydrogen emission is seen and the supernova is known as a

type Ia (which contains an aditional strong Silicon absorbtion line) or Ib supernova (which does not contain an additional Silicon absorbtion line). Type Ia supernovae are the result of the accretion of mass onto a white dwarf from its companion star in a binary system; when the white dwarf has accreted enough mass to exceed the Chandrasekhar limit it cannot support its own mass and so will implode in a type Ia supernova. Type Ib supernovae are also the products of binary systems, in this case the strong stellar winds of the companion to a large main sequence star strip it of its outer layers resulting in a heavy element rich star devoid of Hydrogen emission, the supernova process of a type Ib supernova is otherwise similar to that of a type II supernova.

## 2.3 Pulsars

While working on the Cambridge radio telescope making observations of quasars Jocelyn Bell, a PhD student at the time, noted a recurring signal which was deduced to be of extraterrestrial origin as the time at which it was observed advanced by 4 minutes every night, consistent with sidereal time. This signal consisted of a series of regularly spaced pulses with a period of 1.337 s, and was identified as originating from the first pulsar, PSR B1919+21, a rapidly rotating and compact neutron star [107]. The existence of such objects was first postulated in 1934, only a year after the discovery of the neutron. Walter Baade and Fritz Zwicky were attempting to explain the cause of supernovae and proposed that the energy released was created by the binding together of material from a progenitor star together to form a dense core of neutrons [37].

Today over 1800 pulsars are known [143]; they consist of the compact core of neutrons that is left behind at the centre of a supernova explosion when the outer layers of the star are blown off. They are rapidly rotating (a typical period of a few seconds) extremely dense (about $6.65\times10^{17}$ kg/m$^3$), and measure only about 12 km across with a strong magnetic field (typically $10^{14}$ G).

The strong magnetic fields and the rapid rotation (the average rotation period is of the order of 1 s but approaches 1 ms in the most rapidly rotating cases) for

which they are known is a result of the conservation of magnetic field and angular momentum during this process. In a contracting fluid or gas magnetic field lines will remain frozen in and so as the supernova progenitor collapses the total magnetic flux present will be conserved. As this flux is spread over a much smaller area than in the progenitor star (a pulsar will have a typical diameter of about 12 km compared to a $10^6$ km diameter for a typical star) a much stronger magnetic field will be observed; typical pulsars have magnetic fields of the order of $10^{14}$ G compared to the at most $10^3$ G in a main sequence star. Similarly angular momentum is conserved in the collapsing star and so angular velocity is greatly increased. Typically the rotation period of a pulsar is around 1 s compared to 25 days for a main sequence star such as the Sun.

### 2.3.1 Pulsar Rotation

The high density, strong magnetic field and rapid rotation of pulsars result in the rapid, frequent and precise pulses that are seen in pulsars. The magnetic and rotational poles of a pulsar are usually offset from one another (see Figure 2.2), as the magnetic field of the pulsar rotates and induces an electromagnetic field in the surrounding interstellar medium. Particles in the outer layers of the pulsar are accelerated to relativistic speeds by the strong electromagnetic field; these follow the magnetic field lines away from the pulsar. The particles' acceleration along these magnetic field lines results in the emission of curvature radiation (see Section 1.3.2) which is seen when the emitting pole passes a distant observer, creating the pulsed emission for which these objects are known. Some relativistic electrons which are accelerated away from the surface of the neutron star escape at the magnetic poles where the field lines are not closed; these electrons enter the surrounding supernova remnant and their interaction with this creates a pulsar wind nebula.

One of the most important characteristics of the pulsed emission observed in pulsars is the stability of duration of each pulse. The pulse has been measured to one part in $10^{15}$ s in some cases and as such pulsars are the most accurate clocks known in the universe. The precision expected from pulsars along with the strong gravitational fields present have been used to test the principle of general relativity.

In 1974 Russell Hulse and Joseph Taylor discovered the binary pulsar system PSR B1913+16 consisting of a pulsar and its companion star which is also a neutron star but is not observed as a pulsar [120]; they travel around their common centre of gravity in elliptical orbits once every 7.75 hours. When the pulsar and its companion are at their closest point to each other the pulses appear to a distant observer to take longer to arrive. This is a result of the strong gravitational field present in the companion star which distorts space time around it and causes time to progress more slowly in this region of space. The accurate measurement of the pulse allows the precession of periastron to be measured confirming the predictions of general relativity. Hulse and Taylor were awarded the Nobel prize in prize for physics for

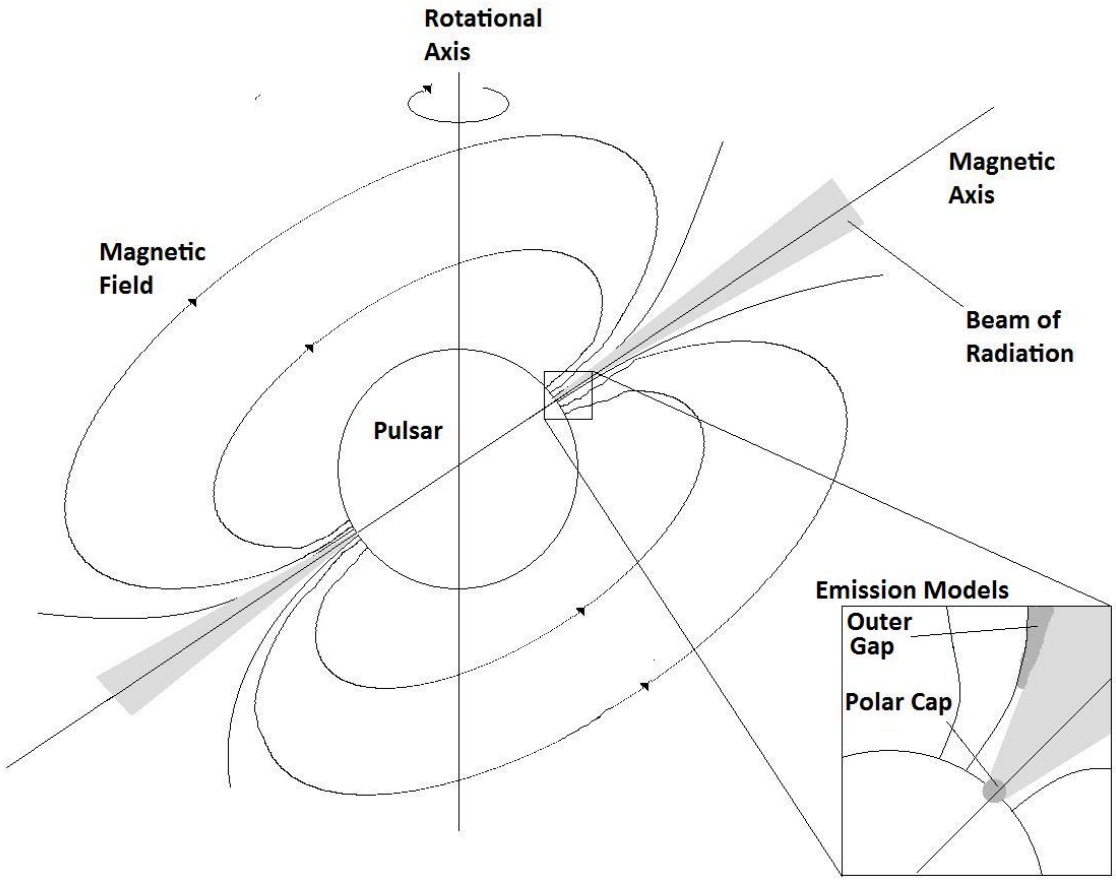


Figure 2.2: The offset magnetic and rotational axis of a pulsar along with the direction of emission of the radiation beam. The emission regions proposed by most emission mechanisms are shown the polar cap and the outer gap mechanisms, recent *Fermi* observations [5] exclude the possibility of polar cap emission.

this discovery in 1993.

### 2.3.2 Pulsar Spindown

As pulsars are emitting energy their rotation will gradually slow down at a typical rate of up to $10^{-15} - 10^{-13}$ s/s; due to the precision with which a pulsar period can be measured this slowdown can also be precisely observed. However, occasionally a pulsar will sharply increase its rotational velocity, creating a "glitch". This is the result of movement in the solid neutron crust that forms on the surface of the pulsar. When a pulsar loses angular momentum it will become less oblate; however the solid crust will usually preserve its shape until the whole surface is rearranged in one jolt, rearranging the pulsar's angular momentum and causing a small, sharp increase in its angular velocity.

The spindown of a pulsar is important in the study of pulsar wind nebulae as it will allow us to calculate the rate at which energy is lost by the pulsar. This can then be used to infer the energy that is input into the surrounding nebula. The rate at which the pulsar loses energy is given by its spindown luminosity $\dot{E}$:

$$\dot{E} = 4\pi^2 I \frac{\dot{P}}{P^3} \tag{2.5}$$

where $I$ is the moment of inertia of the pulsar, $P$ is its period and $\dot{P}$ is the period derivative which measures the rate of change of the pulsar's period. $P_0$ is the period of the pulsar at its birth and $n$ is its breaking index. These values are used to work out the characteristic age of the pulsar:

$$\tau_c = \frac{P}{(n-1)\dot{(P)}} \left(1 - \left(\frac{P_0}{P}\right)^{n-1}\right) \approx \frac{P}{2\dot{P}} \tag{2.6}$$

which can be used to determine the age of the pulsar wind nebula produced. The first term gives a more accurate estimate of the age of the system but requires the braking index and initial period of the pulsar to be known. The braking index is the power to which the slowdown in angular velocity occurs, and is defined as:

$$n = \frac{P\ddot{P}}{\dot{P}} + 2 \tag{2.7}$$

where $P$, $\dot{P}$ and $\ddot{P}$ are the period and its first and second derivatives respectively. The default assumption is generally $n$=3, but values as low as $n$=2 have been observed. The second term is more approximate but can be calculated for any known pulsar. However, this approximate equation often overestimates the age of young pulsars as it assumes that the current period of pulsar is much lower that its initial period and that it has a braking index of $n = 3$, which is not necessarily the case.

This is well illustrated by the pulsars associated with historically observed supernovae such as the Crab nebula pulsar and the pulsar associated with G21.5-0.9 which are both discussed in Chapter 4. The Crab nebula pulsar has a characteristic age of almost 300 years more than its historically observed age while the G21.5-0.9 pulsars characteristic age is more than twice its real age if it is indeed associated with the supernova of 386 AD. This discrepancy is important in the context of pulsars which are currently producing pulsar wind nebulae as they are in general young pulsars (see Section 4.1).

The characteristic age calculation also falls down for older pulsars where an additional decay in the spindown rate occurs as a result in the decay of the magnetic dipole moment; this results in the characteristic age overestimating the age of pulsars which should show ages of the order of $10^6 - 10^7$ years but are observed as being of ages of the order of $10^8 - 10^9$ years. This is less important in the study of pulsar wind nebulae.

## 2.4 Supernova Remnant Formation and Development

As we have seen, the material thrown off in a pulsar explosion will expand at high velocity into the surrounding interstellar medium forming a supernova remnant (SNR). This consists of the outer layers of the supernova which are heated to a high temperature by the explosion and ejected at velocities of the order of $10^4$ km/s into the surrounding medium. In the early stages of its evolution, the development of the remnant is dominated by the initial conditions of the supernova and so will expand adiabatically as a ball of hot gas until the matter swept up from the surrounding

medium forms a significant percentage of the matter present in the remnant. As the initial velocity is supersonic, a shock wave will form at the front of the expanding SNR.

When the remnant has swept up more mass than it initially contained it enters what is known as the Sedov-Taylor phase. At this stage the dynamics of the expanding remnant are dominated by both the total mass of the remnant and the initial energy released by the supernova explosion which will expand following the relation [168]:

$$r \propto \left(\frac{\mathrm{E_{SN}}}{\rho_0}\right)^{1/5} t^{2/5} \tag{2.8}$$

where $r$ is the radius of the expanding remnant, $\mathrm{E_{SN}}$ is the energy released into the remnant in the initial supernova explosion, $\rho_0$ is the initial density of the medium into which it is expanding and $t$ is time since the supernova. The deceleration of the expanding sphere occurs firstly in the outer layers of the nebula and so the inner layers will catch up, thus increasing the density of the outer layers. As the expanding shock wave continues to decelerate, the flow of gas into the outer layer becomes supersonic relative to the shell, creating a second inner shock wave which heats the material in the outer shell. As the material approaching the edge of the shell builds up, this internal wave will propagate back, heating up the nebula and converting the kinetic energy of the shock wave into thermal energy. This reverse shock will travel back to the centre of the nebula where it interacts with the central pulsar wind nebula which has been created.

### 2.4.1 Shock Front Acceleration

The particles which are observed in the shells of supernova remnants are accelerated to relativistic speeds across the shock wave which develops at its edge. This was first postulated by Enrico Fermi in 1949 and is known as first order Fermi acceleration as it depends linearly on the velocity of the shock [79]. Additional acceleration occurs due to the reflection of particles by the shock, it is known as second order Fermi acceleration as the acceleration is dependent on the square of the velocity of the

shock, unlike first order Fermi acceleration it is not as important to the acceleration taking place in SNR shocks and so is not discussed here.

In the vicinity of a shock wave, such as that present at the edge of a supernova, there are particles of relativistic energies present on both sides of the shock travelling at a much higher velocity than the shock, which they are able to pass through without difficulty. The mass of material is conserved through the shock front and so:

$$\rho_1 \mu_1 = \rho_2 \mu_2 \tag{2.9}$$

where $\rho$ and $\mu$ are the density and velocity of the material before (1) and after (2) the shock (see Figure 2.3). The shock front is assumed to be non-relativistic and expanding with a velocity $U$ and as the gas is assumed to be fully ionised the density ratio can be shown to be $\frac{\rho_1}{\rho_2} = \frac{1}{4}$ [139]. In their own frame of reference the particles on both sides of the shock move stochastically. These particles will sometimes pass over the shock front where the particles will interact with a flow of particles travelling at $\frac{3}{4}$ of the velocity of the shock. This results in an increase in velocity of $\sim U/c$ when the particle crosses the shock front. Magnetic inhomogeneity in the vicinity of the shock front can cause the direction of the particle to be reversed causing this crossing of the schok to occur many times, each resulting in an increase in energy. As a result the energy of the particle will greatly increase. The particle will thus gain energy each time it crosses the shock front as it passes in either direction:

$$\frac{\Delta E}{E} = \frac{U}{c} cos\theta \tag{2.10}$$

where $\Delta E$ is the energy change of the particle as it crosses the shock, $E$ is the energy of the particle before it crosses the shock and $\theta$ is the angle at which particles approach the shock front. The number of particles which approach the shock front at each angle is proportional to $sin\theta \mathrm{d}\theta$ while the rate at which particles cross the shock is proportional to the portion of their velocity perpendicular to it, $cos\theta$. As a result, the probability of a particle crossing the shock is proportional to $2sin\theta cos\theta \mathrm{d}\theta$ when averaged over all angles of approach. Thus the average energy gained on crossing the shock is:

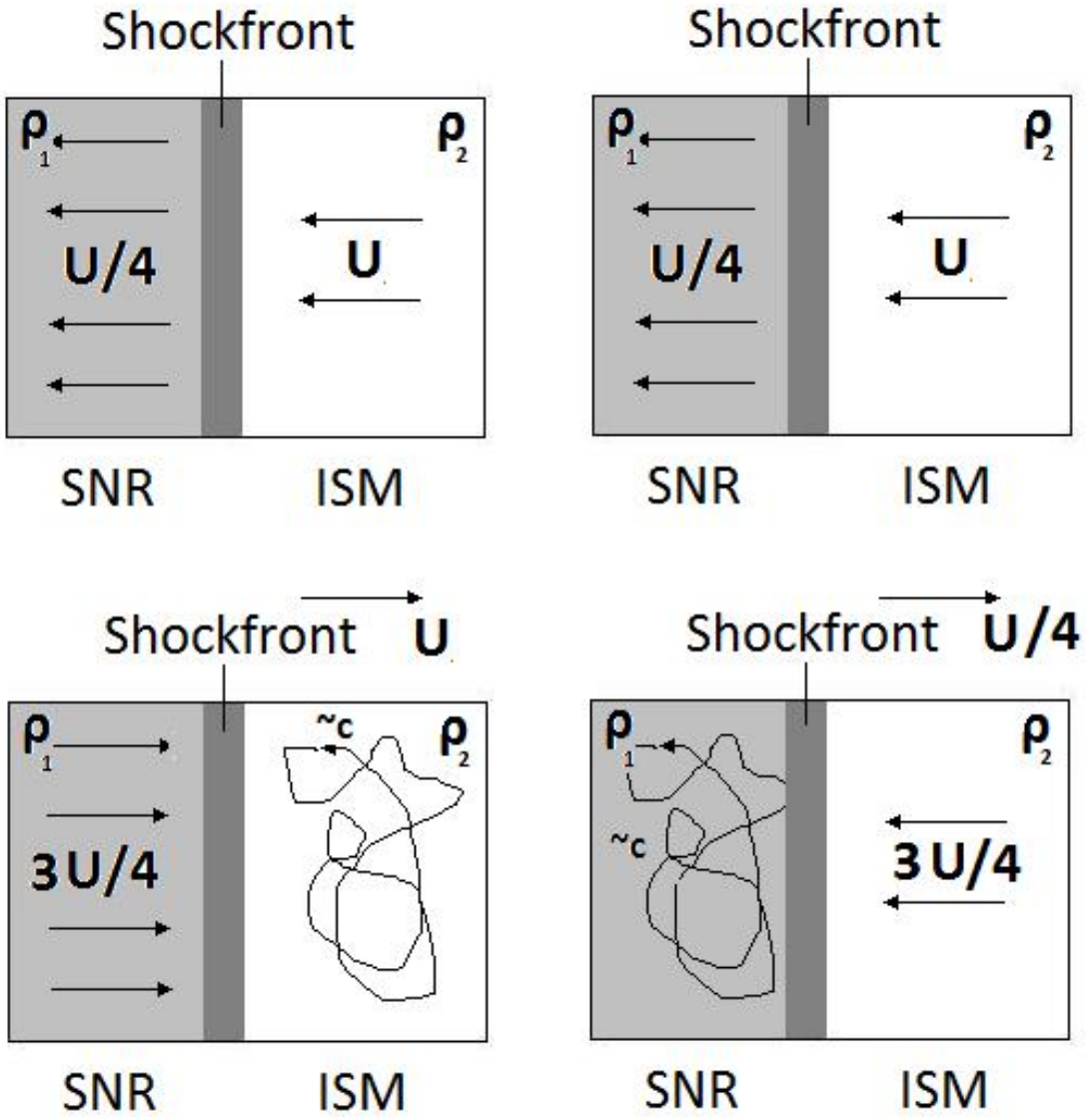


Figure 2.3: The first order Fermi acceleration mechanism. The top row shows the velocity of particles in the frame of reference of the shock while the bottom shows the shock front in the frame of the particle distribution in the shocked material (right) and the interstellar medium (left) respectively. After moving stochastically on its own side of the shock in its own frame of reference a particle may cross the shock front in either direction and will interact with a flow travelling at 3/4 of the shock velocity. This results in an increase of $\sim U/c$ in either direction when it crosses the shock front [79] [139].

$$\left\langle \frac{\Delta E}{E} \right\rangle = \frac{U}{c} 2cos^2\theta sin\theta d\theta = \frac{2}{3}\frac{U}{c} \tag{2.11}$$

If the probability of the particles escaping the magnetic field is calculated based on kinetic theory [139] then a power law with a spectral index of 2 is expected for the output:

$$N(E > E_0) = constant \times \int_{E_0}^{\infty} E^{-2} dE \tag{2.12}$$

where $N(E > E_0)$ is the number of particles which escape with energy greater than $E_0$. This gives a power-law distribution of high energy particles. However, in the case of a supernova remnant a steeper power law is observed with a spectral index closer to -2.6. This is usually explained by the containment of particles within the SNR [139]. The high energy particles produced diffuse freely within the remnant but may also escape from it. The higher the energy of the particles, the more likely they are to escape from the remnant; this is more likely to leave behind lower energy particles and hence causes the spectrum to steepen [139]. However, this is the topic of ongoing research.

## 2.5 Pulsar Wind Nebulae: Production and Development

As pulsars are generated in supernovae they will initially be surrounded by an expanding supernova remnant. The central pulsar in the nebula will initially be highly energetic and so will pump accelerated high energy electrons into the surrounding medium. Concurrently, it will rotate with a period of less than 1 s (see Section 2.3.1) and as a result will sweep out a strong magnetic field into the surrounding medium. The interaction of these electrons with the supernova remnant and the magnetic field swept out by the pulsar will form a highly magnetic environment where the electrons present will emit radiation via the inverse Compton and synchrotron mechanisms.

### 2.5.1 Expansion into unshocked medium

Just after the supernova explosion in which a pulsar is created, the surrounding supernova remnant is still moving freely out into the interstellar medium at a velocity of $10^4$ km/s. As the pulsar itself will be moving much more slowly, typically of the order of 500 km/s, this will be embedded in the expanding SNR (while the PWN is expanding into unshocked ejecta), close to its centre. The pulsar wind nebula has a much higher pressure than the surrounding remnant and so will expand rapidly into it. At this stage the expansion of the pulsar wind nebula is nearly symmetrical and so will evolve as [56]:

$$R_{PWN} \propto \frac{\dot{E}_0^{1/5} E_{SN}^{3/10} t^{6/5}}{M_{ejecta}^{1/2}} \tag{2.13}$$

where $R_{PWN}$ is the radius of the pulsar wind nebula, $\dot{E}_0$ is the energy output of the pulsar while $E_{SN}$ and $M_{ejecta}$ are respectively the energy and mass of the supernova remnant into which it is expanding. As the power output in the early stages of a pulsar's lifetime is basically constant, $\dot{E} \approx \dot{E}_0$. This creates a rapidly expanding and nearly symmetric nebula in the centre of the expanding SNR.

### 2.5.2 Reverse Shock

After about 1000 years, the supernova remnant into which the pulsar wind nebula is expanding enters the Sedov-Taylor Phase (see Section 2.4). In the outer layers of the SNR a reverse shock develops which will initially travel outwards with the expanding SNR, but eventually will start to move inward. The reverse shock would reach the nebula in less than [168]:

$$T_{Sedov}(years) = \frac{3.25 \times 10^{28} M_{ejecta}\ n_0}{E_{SN}} \tag{2.14}$$

where $n_0$ is the number density of the ambient gas surrounding the remnant in $\mathrm{cm}^{-3}$, $M_{ejecta}$ is the mass of the supernova remnant in solar masses and $E_{SN}$ is the energy ejected in the supernova explosion in ergs. The collision of the incoming shock front and the expanding pulsar wind nebula will typically occur after a few thousand years. The reverse shock will then compress the central pulsar wind nebula by a

large factor, greatly increasing its temperature and pressure, leading to an oscillation in the size of the nebula lasting for a few thousand years as the relative pressures of the nebula and the surrounding supernova remnant stabilise.

The original 'kick' with which a pulsar exits the supernova in which it was created ($\approx 500$ km/s) is usually less that the initial expansion speed of the supernova remnant ($\approx 10^4$ km/s). As a result the pulsar will generally be at the centre of the nebula for the first thousand years of its life. However, once the nebula has been subject to a reverse shock, the pulsar will usually move away from the centre of the nebula towards its edge where the pulsar wind nebula will either starts to expand again into the crushed medium (as discussed in Section 2.5.3) or in some cases will escape it entirely; this leads to the creation of a bow shock nebula (discussed in Section 2.5.4) around the escaped pulsar and leaves behind a relic pulsar wind nebula of older relativistic electrons.

### 2.5.3 Expansion into a Crushed Medium

Once the pressure differential between the supernova remnant and the pulsar wind nebula has stabilised, the pulsar wind nebula will continue to expand into the shocked material of the SNR. The expansion will not accelerate but occur at a constant rate, which is dependent on the rate of energy output from the pulsar. If this rate is approximately constant, as it is in the earlier years of the pulsar's lifetime, then the radius of the pulsar wind nebula will evolve as $R_{PWN} \propto t^{\frac{11}{15}}$ [168]. As the rate of pulsar output diminishes this falls to $R_{PWN} \propto t^{\frac{3}{10}}$ after time $\tau_0$ [168]:

$$\tau_0 = \frac{P_0}{(n-1)\dot{P}_0} \tag{2.15}$$

where $P_0$ and $\dot{P}_0$ are the initial period and period derivative of the pulsar in question and $n$ is its braking index.

### 2.5.4 Bow Shock Nebulae

In cases where the pulsar has a high velocity it can escape the original pulsar wind nebula and form a new bow shock nebula around itself. This will form behind the

moving pulsar wind nebula with a bridge of emission linking it to the main nebula.

As the central pulsar moves away from the centre of the SNR towards its edge, its speed relative to the sound speed in the remnant will increase (the sound speed in the outer layers of the nebula is lower due to its lower density) and so the pulsar will begin to move supersonically. This results in a small (less than 1 parsec across), tightly confined PWN with a shape similar to a comet, such as the Mouse [87].

## 2.6 Emission From Pulsar Wind Nebulae

As we have seen, electrons are accelerated to relativistic energies in the outer layers of a pulsar and escape into the surrounding medium of the supernova remnant. This wind interacts with a shock front downstream of the wind to further acelerate the particles to energies of about $10^15$eV. Concurrently, the pulsar will sweep out a magnetic field into the nebula. The relativistic electrons downstream of the shock will then orbit around the magnetic field lines running through the nebula and radiate synchrotron emission (see Section 1.3.1). This emission is seen over a broad range of frequencies from radio to X-ray, with the highest energies of X-ray emission corresponding to the highest energy electrons injected into the system (see Equation 1.8).

The pressure of this radiation pushes particles away from the area immediately surrounding the pulsar so that only the relativistic wind is present, terminating in the shock front at the point where the pressure of the wind balances the internal pressure of the pulsar wind nebula. This expands as [86]:

$$R = \sqrt{\frac{\dot{E}}{4\pi\omega c P}} \tag{2.16}$$

Where $R$ is the radius of the wind termination, $P$ is the pressure of the nebula interior and $\omega$ is the equivalent filling factor (the fraction of the wind volume occupied) for an isotropic wind. Before this shock is passed the particles will travel parallel to and along the magnetic field and so will not interact with it. After they pass this barrier, the electrons are further accelerated and scattered by their passage accross the shock front and are no longer parallel to the magnetic field lines

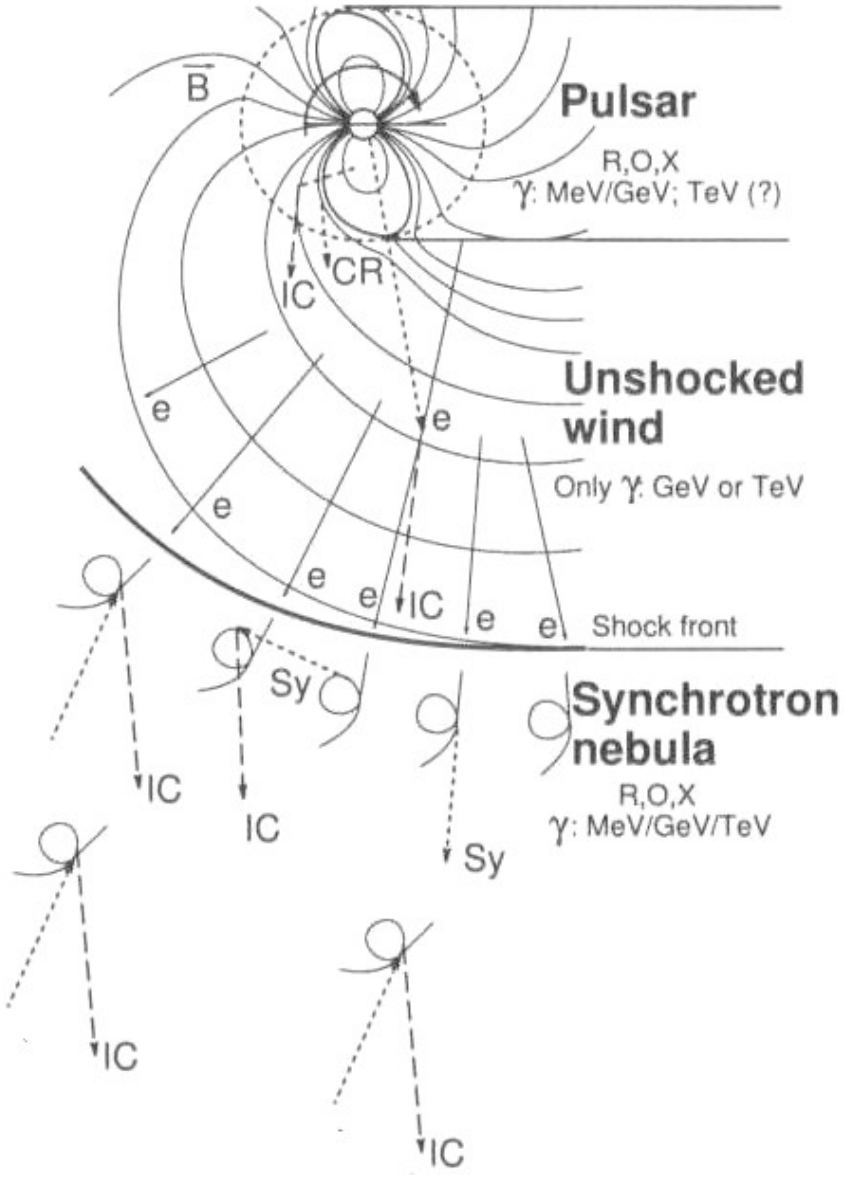


Figure 2.4: Emission from a pulsar wind nebula, showing the synchrotron nebula which is visible in all wavelengths compared to the unshocked wind in which only inverse Compton emission is observed. In older pulsar wind nebulae only inverse Compton emission is seen at the furthest portions of the "synchrotron nebula" as the more energetic electrons required to emit in the synchrotron regime have cooled at these distances. Figure adapted from Aharonian [32].

and so synchrotron emission can occur beyond this point. This results in an area immediately adjacent to the pulsar where no synchrotron emission is observed (see Figure 2.6).

Characteristically, the synchrotron emission observed from most pulsar wind nebulae has a flat power law spectrum at radio wavelengths with a spectral index of about -0.3. This steepens in the X-ray regime to about -2. The cause of this spectrum is not well understood; if a simple power law was assumed for the input electron spectrum then the photon spectrum expected would show a broken power law with a spectral break at frequency [90]:

$$\nu_b = 10^{24} \frac{t}{2\ (B_{PWN})^3} \tag{2.17}$$

where $B_{PWN}$ is the magnetic field strength of the pulsar wind nebula in Gauss and $t$ the age of the electrons producing the radiation in years. As the frequency at which the break occurs is inversely proportional to the age of the source photons, the nebula will be larger at lower energies and so larger synchrotron nebulae will be seen in radiowaves than in X-rays. The largest nebulae are observed in the VHE $\gamma$-ray regime where lower energy electrons are emitting via the inverse Compton process.

As has been discussed, pulsar wind nebulae are prominent sources of very high energy $\gamma$-rays. At these wavelengths, emission is caused by inverse Compton acceleration of seed photons by the relativistic electrons present in the nebula (see Section 1.3.5). As the electron energies needed to boost photons to these energies are not as large as that required for synchrotron emission to occur, inverse Compton emission is seen at the extremes of the nebula where synchrotron emission can no longer be observed and as such older pulsar wind nebulae are observed to be much larger in VHE $\gamma$-rays than their X-ray counterparts. In addition to this, inverse Compton emission is seen in the unshocked wind area of the PWN as the electrons present are energetic enough to produce inverse Compton radiation even if they are unable to produce synchroton radiation.

The brightness of the observed inverse Compton nebula is dependent on the availability of seed photons. The Crab nebula has a large supply of synchrotron-

generated photons and so these are accelerated to TeV energies by Compton scattering. However, in most cases background light (typically Galactic starlight or light from the cosmic microwave background) is boosted in this process and so lower rates of emission are seen.

# Chapter 3

# The Analysis Of VHE $\gamma$-rays

In this Chapter we discuss the analysis procedures undertaken when carrying out HESS analysis in order to define sources and to calculate upper limits when no signal is detected. It will begin with details on how observation of an air-shower is used to calculate the origin and energy of an incoming VHE $\gamma$-ray in both a single telescope and the stereoscopic case before going on to discuss the intricacies of the HESS analysis process.

## 3.1 Reconstruction of the Origin of a TeV Event

When an observation of a Cherenkov light shower is used to infer its properties, both the angle of arrival and the energy of the incoming particle will affect the size of the shower ellipse as seen from the ground. This is shown in Figure 3.1 in which the major axis of the observed image approximates the axis of the shower along which the $\gamma$-ray source is located. The size and shape of the image is used to estimate the distance to the event. There is a large intrinsic error in the position of the source derived using this method due to difficulty in estimating the core distance to the shower location from the position of the air shower.

Ideally, observations of a shower must be made simultaneously with several telescopes to accurately measure the shower's point of origin and its energy. Intersecting the image axes gives a much more accurate estimation of the position of the source (see Figure 3.2), and once this is known, a much more accurate estimation of the

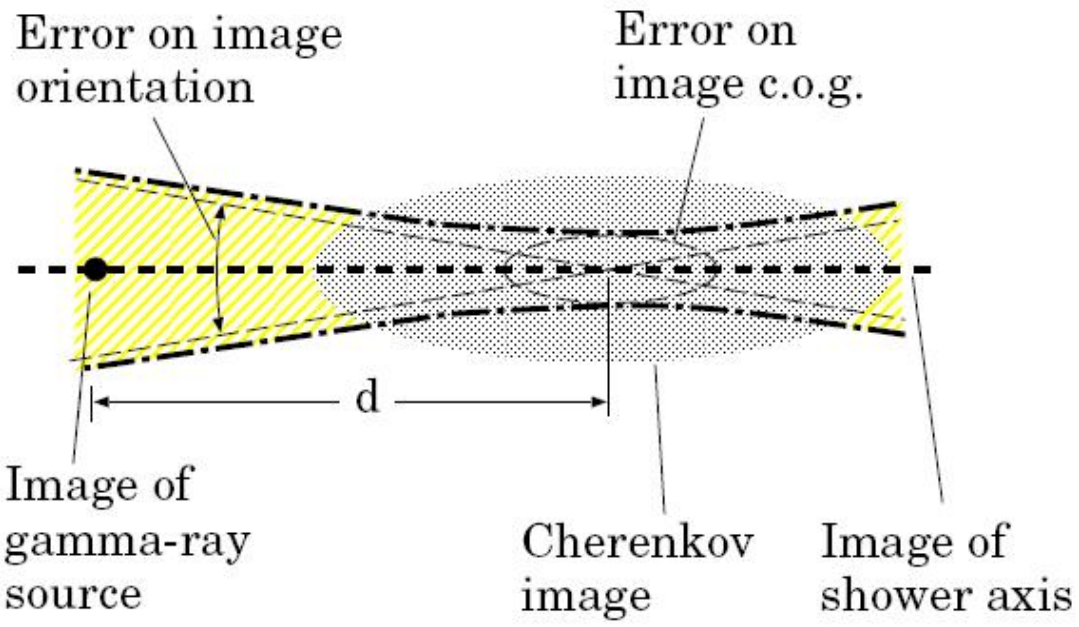


Figure 3.1: The image reconstruction of an event from a single Cherenkov telescope showing the margin of error in the position [114].

energy of the source. Multiple telescopes also allow background muons present in the local environment of the telescope, which could pass through the camera of a single telescope and trigger it, to be eliminated by requiring that more than one telescope responds for an event to be recorded.

## 3.2 The HESS Trigger System and Event Cuts

As well as allowing background muons to be eliminated the HESS trigger system reduces the background of cosmic ray events observed. Additionally, as the trigger only records when a fast flash of light is observed it allows the observed night sky background to be reduced improving the signal to noise ratio. The trigger system employed by HESS uses a series of overlapping 64 pixel sectors. The recording system is triggered when a brief flash of light (a few ns) is seen in a certain number of pixels within a sector and the resulting signal contains more than a preset number of photoelectrons. These thresholds are programmable and are typically set to a few photoelectrons viewed across a minimum of 2 to 4 pixels [83]. Additionally

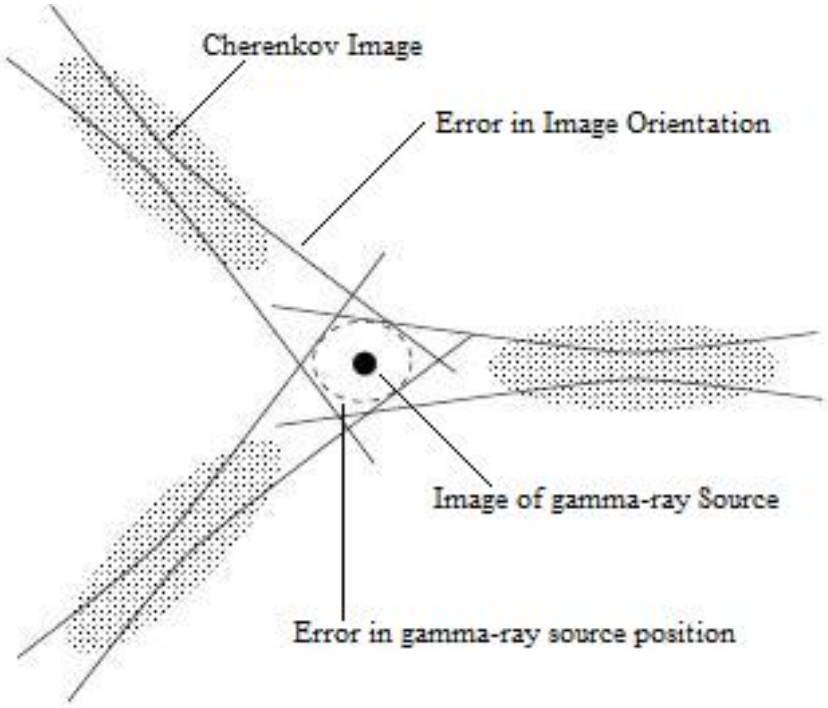


Figure 3.2: The image reconstruction of an event for three Cherenkov telescopes showing the more accurate position obtained [114].

the central recording system of the HESS array will only trigger if more than one telescope triggers simultaneously.

The size and shape of the events observed is used to distinguish the events from cosmic ray induced air showers which are typically smaller and more irregularly shaped than those produced by $\gamma$-rays of the same energy (see Figure 1.6). This is done with a series of data selection cuts. Some of these cuts used are shown in Figure 3.3. HESS has three default sets of cuts: hard, standard and loose [83]. The harder cuts will typically exclude some genuine $\gamma$-ray events but as a result a much greater percentage of the unwanted hadronic events is excluded. This increases the ratio of wanted $\gamma$-ray events to unwanted hadronic events and as a result increases the precision of event pointing. This makes the hard cuts good for analysis of target morphology. Looser cuts allow more data to be acquired and so are good for the production of spectra as all possible data are utilized. The standard cuts provide a compromise between the pointing accuracy needed to produce a good morphology

| Cuts | MRSW max | MRSL max | PE min | $\theta^2$ (°) max | All $\gamma$ % | All BG % |
|---|---|---|---|---|---|---|
| Hard | 0.7 | 2.0 | 0.01 | 200 | 13 | 8e-4 |
| Standard | 0.9 | 2.0 | 0.0125 | 80 | 35 | 9e-3 |
| Loose | 1.2 | 2.0 | 0.04 | 40 | 68 | 0.11 |

Table 3.1: Selection cuts for standard HESS observations. Hard cuts exclude the most events and are the best for morphological study as they have the best positional accuracy while loose cuts exclude the least and are useful for investigating spectra as the greatest number of events are included in the spectrum observed. Standard cuts are a compromise between these two extremes. Cuts are applied on the number of photoelectrons (PE) generated, MRSW, MRSL and the distance of the shower position to the source ($\theta$). [17]

and the amount of data needed to estimate an energy spectrum and are used to establish the presence of a source.

The cuts allow hadronic cosmic ray events to be removed in a number of ways, which depend on their size, shape and the accuracy with which their position can be determined. The number of photoelectrons recorded is used as $\gamma$-rays are usually brighter than the hadronically created air showers in the upper atmosphere. An important cut is the mean-reduced-scale-width (MRSW) of the recorded events [17]. This parameter is defined as the mean of the difference in standard deviation for each telescope from the width observed in the image from that which is expected from $\gamma$-ray simulations based on image intensity. Its value is given by:

$$MRSW = \frac{1}{N_{tel}} \sum_{i=0}^{N_{tel}} \frac{w_i - < w_e >}{\sigma_i} \tag{3.1}$$

where $N_{tel}$ is the number of telescopes used in the observation, $w_i$ and $< w_e >$ are respectively the observed width of the shower and the shower width expected from simulations and $\sigma_i$ is the standard deviation of the simulated width. MRSW is based on the mean scaled width (MSW) parameter developed by the HEGRA collaboration for this purpose [165], and also takes into account the use of multiple telescopes in the HESS array. The cuts applied remove non-$\gamma$-ray events based on their size, shape and the accuracy with which their position can be determined are

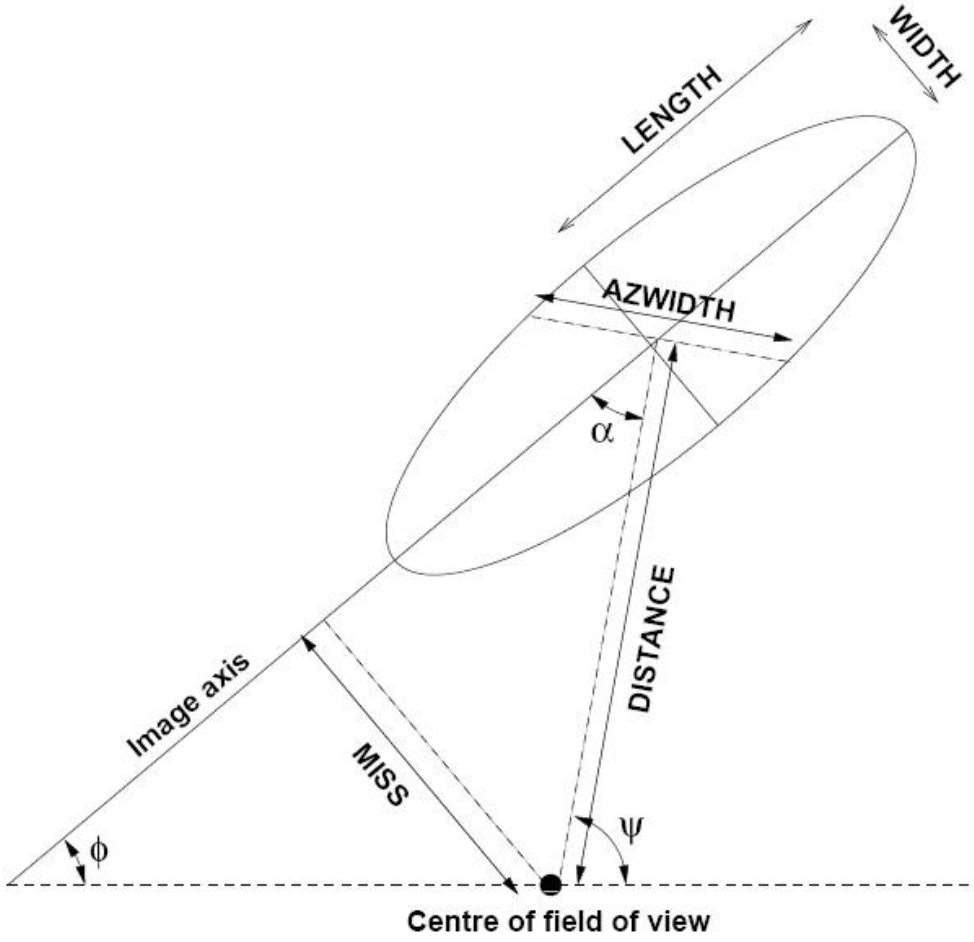


Figure 3.3: Parameters for the analysis of Cherenkov air showers as defined by [108]. Figure taken from [70].

shown in Table 3.1.

These cuts are applied at various points in the analysis chain process to balance the needs of the user to customise the analysis with the data storage capacity of the HESS analysis systems. Initially the individual HESS telescopes capture raw air shower images and these are recorded by the central HESS control system if more than one telescope is triggered simultaneously. These raw images are later corrected for by comparison with calibration data to adjust for systematic biases caused by factors such as variance in efficiency of the telescope photomultiplier tubes. These events are then subject to two levels of event selection to distinguish between genuine $\gamma$-ray events and cosmic ray events. Primary event selection takes place centrally

before the distribution of data to the end users. In this process the image is cleaned so that only pixels with more than 5 photoelectrons recorded are kept and then only if they are part of a larger cluster of pixels. The air shower parameters are derived for the remaining events by the end user who can select the cuts discussed above to optimise their analysis and calculate the properties of the incoming air shower.

## 3.3 Significance Calculation

Even after these cuts have been applied a significant amount of background remains in the dataset. For this reason, it is necessary to calculate the statistical significance of the source detection. It is based on the method described in Li and Ma [138] and is given by:

$$S = \frac{N_{on} - \alpha N_{off}}{\sqrt{\alpha(N_{on} + N_{off})}} \tag{3.2}$$

where S is the statistical significance, $N_{on}$ and $N_{off}$ are the number of on and off counts respectively and $\alpha$ is the ratio between the effective exposure time of on-axis and off-axis counts and so takes into account the difference in the on-axis and off-axis areas observed. The off-axis counts used are based on a background derived from a different portion of the telescope's field of view. In the case of HESS a reflected (where the background is offset from the centre of the camera by the same distance as the source [38]) or ring background (where the background is taken from a ring surrounding the source [38]) is used; these are shown in Figure 3.3. The ring background assumes that there is a steady decay in the camera acceptance with distance from its centre, as in this case the average acceptance obtained should be the same as that seen in the on-region, and the size of the ring can be adjusted to avoid any contaminating sources. It is used whenever a region map is produced. The reflected region background takes its off counts from areas the same distance from the centre of the camera as the on-region, consequently any decay in camera acceptance with distance from its centre does not matter. It is used whenever a spectral or significance calculation is made. A third background method exists where background regions are specified by the user for the analysis of sources in

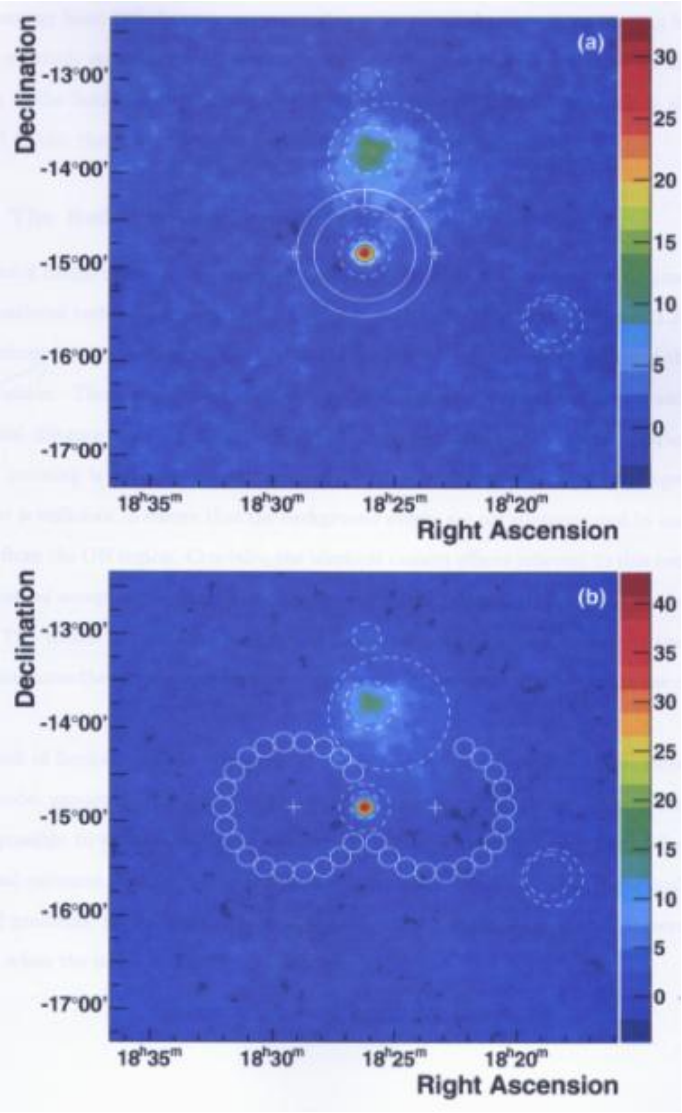


Figure 3.4: The regions from which on and off counts are taken in the ring (a - top) and reflected region (b - bottom) background methods as shown for the binary source LS5039 by Dickinson [70]. The observed target is seen in the centre of the diagram in each case while other known $\gamma$-ray sources seen (which are excluded in the analysis background) are also surrounded by dashed lines. The background regions, from which the off-axis counts are taken are shown surrounded by solid lines. The observation positions of the HESS telescopes are denoted by the white crosses.

crowded regions of the sky. Its use is not recommended as it does not take into account changes in acceptance across the camera.

## 3.4 Flux calculation

Once a source has been detected the flux of the source can then be calculated in order to compare it to the emission observed at other wavelengths.

In the HESS observations presented in this thesis the flux is estimated from the number of excess events compared to background [17]. The integral flux is calculated by assuming the functional form of the $\gamma$-ray flux. Usually for a basic analysis a decreasing power law is assumed and so the integral flux (I) above a given energy threshold ($E_t$) can be expressed as:

$$I = \int_{E_t}^{E_{max}} I_0 \left(\frac{E}{E_0}\right)^{-\Gamma} dE \tag{3.3}$$

where $E_{max}$ is the nominal upper cut-off energy, $\Gamma$ is the assumed spectral index and $I_0$ is the flux normalisation value at energy $E_0$. The value of $I_0$ is derived from the measured $\gamma$-ray excess ($\Delta$) which can be expressed as:

$$\Delta = \int_{0}^{E_{max}} \int_{t_{start}}^{t_{stop}} I_0 \left(\frac{E}{E_0}\right)^{-\Gamma} A_{eff} dt dE \tag{3.4}$$

where $t_{stop}$ and $t_{start}$ are the stop and start times of the observation respectively and $A_{eff}$ is its effective area. The effective area is the area over which an incoming $\gamma$-ray will trigger the telescope and survive event selection. It is dependent on the particle energy (E), the offset of the target from the pointing direction of the telescopes and the zenith angle of the observation and is calculated as:

$$A_{eff} = \frac{N_T}{N_S} \times \pi r^2 \tag{3.5}$$

where $N_T$ is the number of triggered events, $N_S$ is the number of simulated events and $\pi r^2$ is the area over which Cherenkov light can be detected. The Flux ($F_i$) of each energy bin is given by [13]:

$$F_i = \frac{O_i - B_i}{\Delta E_i t_i} \tag{3.6}$$

where $O_i$ and $B_i$ are the sum of on and off source events calculated from the effective area, $t_i$ is the exposure time and $\Delta E_i$ is the energy width for the bin concerned. The spectrum is calculated iteratively; an initial value of the spectral index $\Gamma = 2.0$ is assumed and this is used to calculated the value of the effective area for each bin from which the spectral index can be recalculated in turn. When this deviates from the hypothesis the process is repeated using the new spectral index until the numbers converge.

## 3.5 Upper Limit Calculation

In many of the observations presented in this thesis no source was seen and so an upper limit to the flux is given in the place of a flux measurement. For this purpose we use a method derived from the Feldman and Cousins approach developed for the analysis of neutrino signals which like TeV $\gamma$-ray signals deal with low signal data [78]. The Feldman and Cousins approach unifies in its consideration the treatment of upper limits for a non-detection and the upper confidence limit for the detection of a source, meaning a choice between the two does not have to be made in the case of a borderline detection or in the presentation of a limit when the measured flux is contaminated by a brighter overlapping source.

A Feldman Cousins upper limit is thus calculated similarly to calculating the error on a flux measurement but with an assumed spectral index taking the place of that calculated for an observed source. When a measurement is calculated an estimate of the upper and lower error is made by calculating the probability distribution function given such that the values for the upper ($x_1$) and lower ($x_2$) limits have the same likelihood and that [78]:

$$\int_{x_2}^{x_1} P(x|\mu)dx = \alpha \tag{3.7}$$

where $P(x|\mu)$ is the probability function of obtaining $x$ for a given value of $\mu$ where $\mu$ is the true value of $x$ and is obtained from a direct measurement of the flux; $\alpha$ is the confidence level required from the limits. As only non-negative values of $x$ are allowed in cases where the value of $x$ is low the lower limit ($x_2$) becomes zero

and hence the upper limit $x_1$ is quoted in place of the measurment with error band. In the analysis presented here a Gaussian probability distribution is used along with a 99% confidence limit.

# Chapter 4

# A Survey of Known VHE $\gamma$-ray Pulsar Wind Nebulae

As of August 2010 there were ten known sources of very high energy (VHE) $\gamma$-rays that have been confirmed as pulsar wind nebulae as well as approximately fifteen others which are suspected to be pulsar wind nebulae (PWN). In addition, the HESS dark sources may represent relic pulsar wind nebulae which have reached the end of their life and emit in the very high energy $\gamma$-ray regime but have yet to be observed at other wavelengths. The observed nebulae represent a broad range of ages and show a range of characteristics. This Chapter focuses on the different properties of the known pulsar wind nebulae as well as aiming to discuss why very high energy $\gamma$-ray emission is seen from some pulsar wind nebulae and not others.

This Chapter begins with a discussion of the properties of young pulsar wind nebulae (Section 4.1), which are defined as those have not yet been the subject of a reverse shock crush detailed in Section 2.5.2, before moving on to discuss middle aged nebulae (Section 4.2) and finally old and relic nebulae where no new output from a central pulsar is still present (Section 4.3). It is concluded with a population study analysing the development of the observable properties of known pulsar wind nebulae (Section 4.4).

## 4.1 Young Pulsar Wind Nebulae

As we have seen in Section 2.5 at the beginning of their lives pulsar wind nebula are expanding rapidly into a surrounding supernova remnant. This results in the small highly energetic nebulae that we observe in the VHE $\gamma$-ray regime. In this Section the properties of all confirmed young pulsar wind nebulae are discussed with most attention given to the TeV $\gamma$-ray emission from these nebulae and the emission from their associated X-ray nebulae. The X-ray and $\gamma$-ray properties of each nebula discussed along with additional suspected young pulsar wind nebulae are summarised in Table 4.1 along with details of the progenitor associated with each listed in Table 4.2.

### 4.1.1 The Crab Nebula

The Crab Nebula was the first steady source of VHE $\gamma$-rays to be discovered and so was considered the archetype of young $\gamma$-ray pulsar wind nebulae. However, after

Figure 4.1: A Hubble image showing the shell part of the Crab Nebula [105].

the observation of other young pulsar wind nebulae in this regime, it could now be considered something of a unique source. It is brighter that all other constant sources in the TeV regime and generates $\gamma$-rays in non-typical way.

In 1054 Chinese and Japanese astronomers made an observation of a bright temporary star, visible in the daylight for 23 days gradually diminishing over time. It disappeared after being visible to the naked eye for almost two years [185], it wasn't observed again until the eighteenth century.

Observations of this extended nebula have been made in every available wave-band and reveal a shell type supernova remnant with filamentary outer layers expanding into the surrounding interstellar medium at a velocity of 700 - 1800 km/s [57]; this can be used to infer a distance to the nebula of 2 kpc. The supernova remnant surrounds a central pulsar wind nebula powered by the progenitor pulsar PSR B0531+21.

The most detailed optical images are from the Hubble space telescope (see Figures 4.1 and 4.2). These show the filamentary structure of the outer supernova remnant (Figure 4.1) and the structure of the central pulsar wind nebula (Figure 4.2). This shows much brighter supernova shell than the central pulsar wind nebula in the optical regime.

X-ray observations of the source have also been made using the latest X-ray satellites such as Chandra [178]. In this case there is no evidence for emission in the outer SNR shell. The difference in relative brightness of the SNR shell and central nebula between the optical and X-ray regimes is explained by the nature of emission in these two components of the source. Synchrotron emission is produced by the central pulsar wind nebula at wavelengths from radio to $\gamma$-ray regimes and by inverse Compton emission in the TeV $\gamma$-ray regime; however, this is not the case in the SNR shell where much of the emission is thermal, or the result of emission line transitions in the filaments of the shell. This makes X-rays a useful tool for observing the shape of the central pulsar wind nebula because at these wavelengths it can be easily distinguished from its shell.

Both optical and X-ray images of the central pulsar wind nebula provide us with information about the morphology of this source. It is seen as an ellipsoid

Figure 4.2: A Hubble image showing the central pulsar wind nebula of the Crab Nebula [106].

with major axis 4.4 pc and minor axis 2.9 pc filling a volume of $\approx 30$ pc$^3$ [104]. The area immediately adjacent to the pulsar can be seen to emit less radiation than the nebula around it; this is because in this area the wind is not shocked and hence does not emit synchrotron radiation. The total synchrotron luminosity of the nebula integrated across all wavelengths (synchrotron emission is visible from the radio regime to energies of about 1 GeV) is about $1.3 \times 10^{38}$ ergs/s corresponding to about a quarter of the spindown energy being lost by the pulsar into its surroundings.

Another important feature of the Crab is the central progenitor pulsar powering the emission of its central nebula. This is also seen energy bands from the radio up to 27 GeV [34]. The pulsar has a period of $\approx 33$ ms and a period derivative of $\dot{P} \approx 4.21 \times 10^{-13}$s/s. From this a spindown luminosity of $L_{spin} \approx 5 \times 10^{38}$ ergs/s can be calculated.

The Crab Nebula has been the subject of observations by almost all the ob-

servatories operating in the VHE $\gamma$-ray waveband. The earliest detections of this nebula in this waveband were made by the 10m telescope at the Whipple observatory on Mount Hopkins in Arizona while the imaging atmospheric Cherenkov technique was being developed [77]. This eventually gave a confirmed detection with a statistical significance of 9.0 $\sigma$ in 1988 with an observed integral flux of $1.8 \times 10^{-11}$ photons /cm$^2$/s above 0.7 TeV. Later observations such as those by the HEGRA experiment [193] allowed the spectrum of the Crab to be determined. As this is the brightest known constant source of VHE $\gamma$-rays in the sky, it is used as a "standard candle" for $\gamma$-ray measurements with many published results being

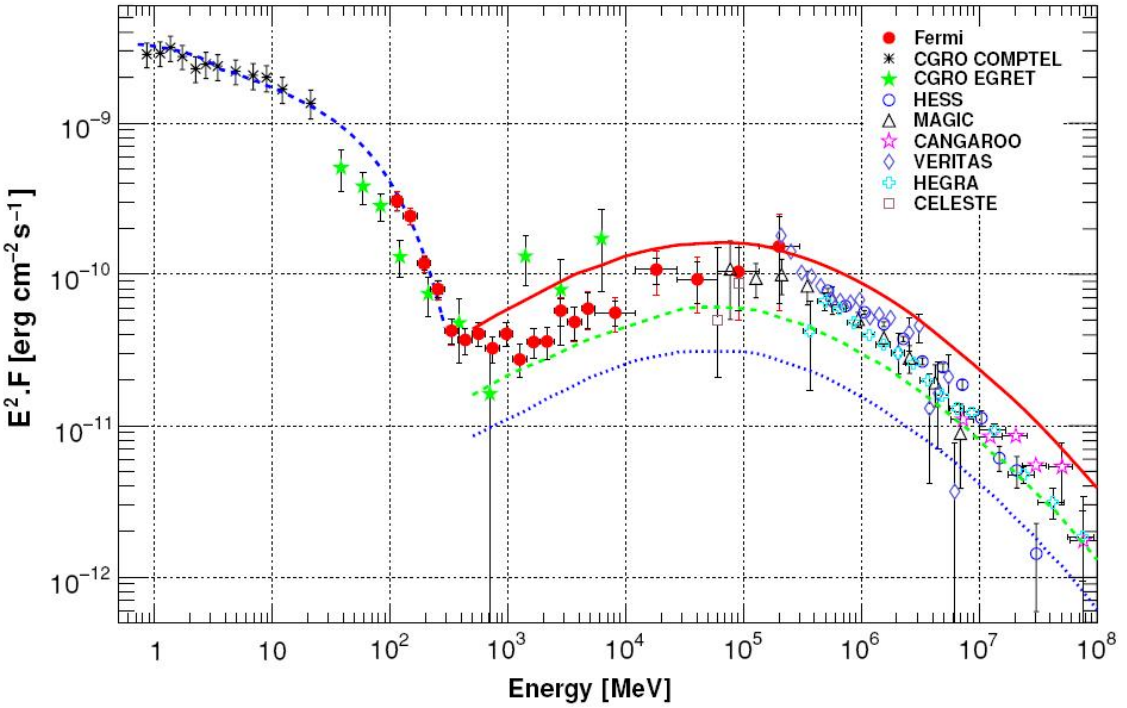


Figure 4.3: The spectral energy distribution of the Crab Nebula across the $\gamma$-ray regime taken from [5] with data from VERITAS [52], MAGIC [34], HESS [17], *Fermi* [5], CANGAROO [186], *CGRO* [134] (A satellite observing lower energy $\gamma$-rays), HEGRA [10], Whipple [193] and CELESTE [181] (earlier ground-based Cherenkov observatories) and show consistency between these different observations. An inverse Compton peak is observed in $\gamma$-rays as well as the decline in the synchrotron emission observed at MeV energies. IC spectra are plotted with an assumed magnetic field of 100 $\mu$G (solid red line), 200 $\mu$G (dashed green line) and 300 $\mu$G (dotted blue line).

expressed in terms of a percentage of the Crab flux.

The current generation of TeV Cherenkov telescopes have allowed the spectrum of the central pulsar wind nebula in the Crab to be more accurately assessed, first by HESS [17] and more recently by the VERITAS [52] and MAGIC [34] observatories. As HESS is a southern hemisphere observatory and the Crab is a northern hemisphere object (at a declination of 22.01°) HESS has the highest energy threshold for its observation while MAGIC, with its larger detector and northern hemisphere location, has the lowest. However, as can be seen in Figure 4.3, the spectra in each case are comparable and show a decaying power law with a spectral index of -2.31 $\pm$ 0.2 and a turnover at 90 GeV. This is consistent with the spectrum observed with the Fermi LAT in which the spectral turnover for this source at $\approx$ 80 GeV is observed [5] (see Figure 4.3). A luminosity above 1 TeV is (3.23 $\pm$ 0.42) $\times$ $10^{34}$ erg/s was observed for this source by HESS.

Due to the brightness of the source only 23 hours of data were needed to produce the published HESS spectrum [17]. As of April 2010 an additional 38 hours of observations of the Crab nebula have been made. Analysis of these data was used to give the spectrum and skymap for the source seen in Figure 4.4 and Figure 4.5, a description of how HESS analysis is carried out is found in Chapter 3. The results obtained agree with those obtained in the published HESS paper when a smaller dataset was used.

This spectrum is a result of synchrotron self Compton emission in the pulsar wind nebula whereby the relativistic electrons present in the nebula generate synchrotron photons (see Section 1.3.1) and then accelerate them to TeV $\gamma$-ray energies though the inverse Compton mechanism (see Section 1.3.5). Emission of this kind is not observed in most known pulsar wind nebulae making the Crab Nebula a very interesting object and explaining why it is much brighter than other pulsar wind nebulae in the TeV regime, where the inverse Compton seed photons are taken from other sources such as galactic background light and microwave background radiation.

Comparison of the spectrum seen in X-rays and that seen in the gamma-ray regime allows the energy of the electron spectrum and magnetic field of the nebula to be calculated. The magnetic field is inferred to be 100-300 $\mu$G [5] which is

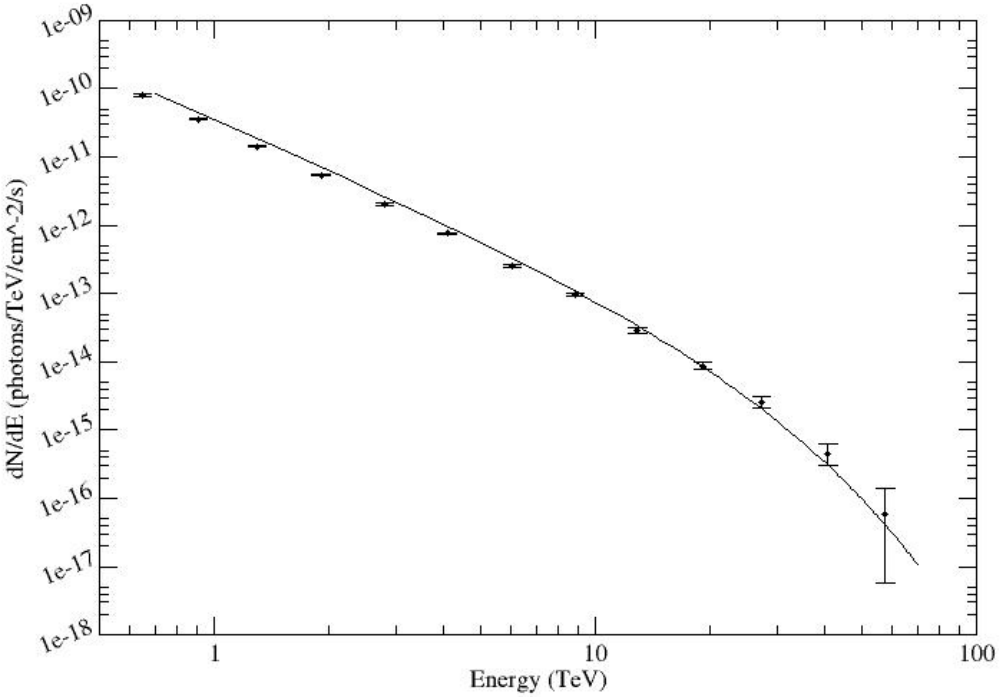


Figure 4.4: A new analysis showing the spectrum of the Crab Nebula with HESS using all 61 hours of available data (points) compared to the exponential cut-off power law derived in published HESS observations using a smaller dataset [17] (line) which has the form $\mathrm{dN/dE}=3.76\times10^{2.39}\mathrm{e}^{-E/14.3}$.

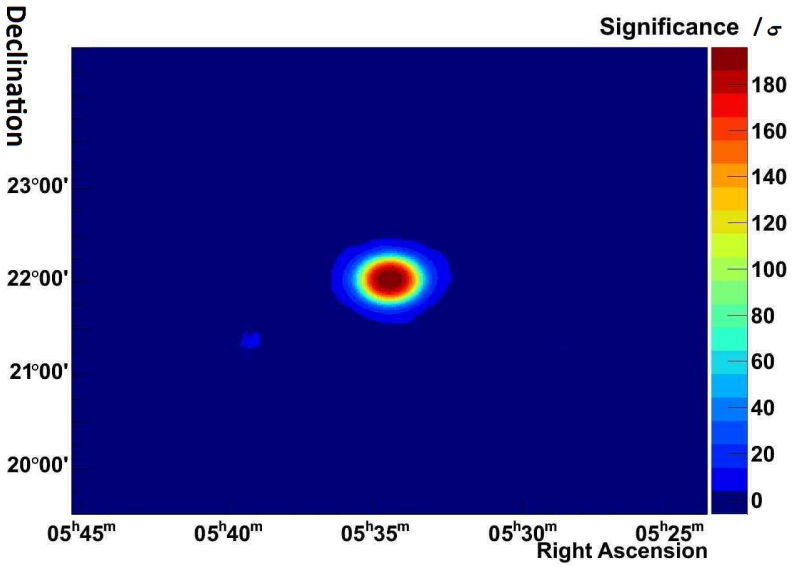


Figure 4.5: A new analysis showing emission from the Crab nebula with HESS using all 61 hours of available data, the source is seen in a characteristic fashion for a point source observed with HESS and a significance of $195\sigma$ is seen. The extension shown corresponds to that expected for a point source seen through the HESS point spread function (PSF).

higher than most nebulae of this type. This has the effect of confining the electrons present for longer than usual and thus allows the synchrotron self Compton emission described above to occur. However, the reason for this unusually strong magnetic field has yet to be explained but may be due to a higher than average density of the nebula.

Recent $\gamma$-ray observations by the MAGIC collaboration [34] and using the *Fermi* satellite [5] have observed the pulsations from the central pulsar powering the nebula. Pulsations are seen at energies up to 27 GeV. At $\gamma$-ray energies the period of these pulsations is the same 33 ms that is seen at other wavelengths [34]. While the *Fermi* results [5], in common with optical and radio observations, show a very large on-pulse and a much smaller interpulse, in the MAGIC observations the two pulses (corresponding to emission from the two poles of the pulsar) show roughly similar intensities (see Figure 4.6). A difference is also seen in the width of the observed pulses at different wavelengths with much broader pulses seen in the X-ray and lowest energy $\gamma$-ray regimes.

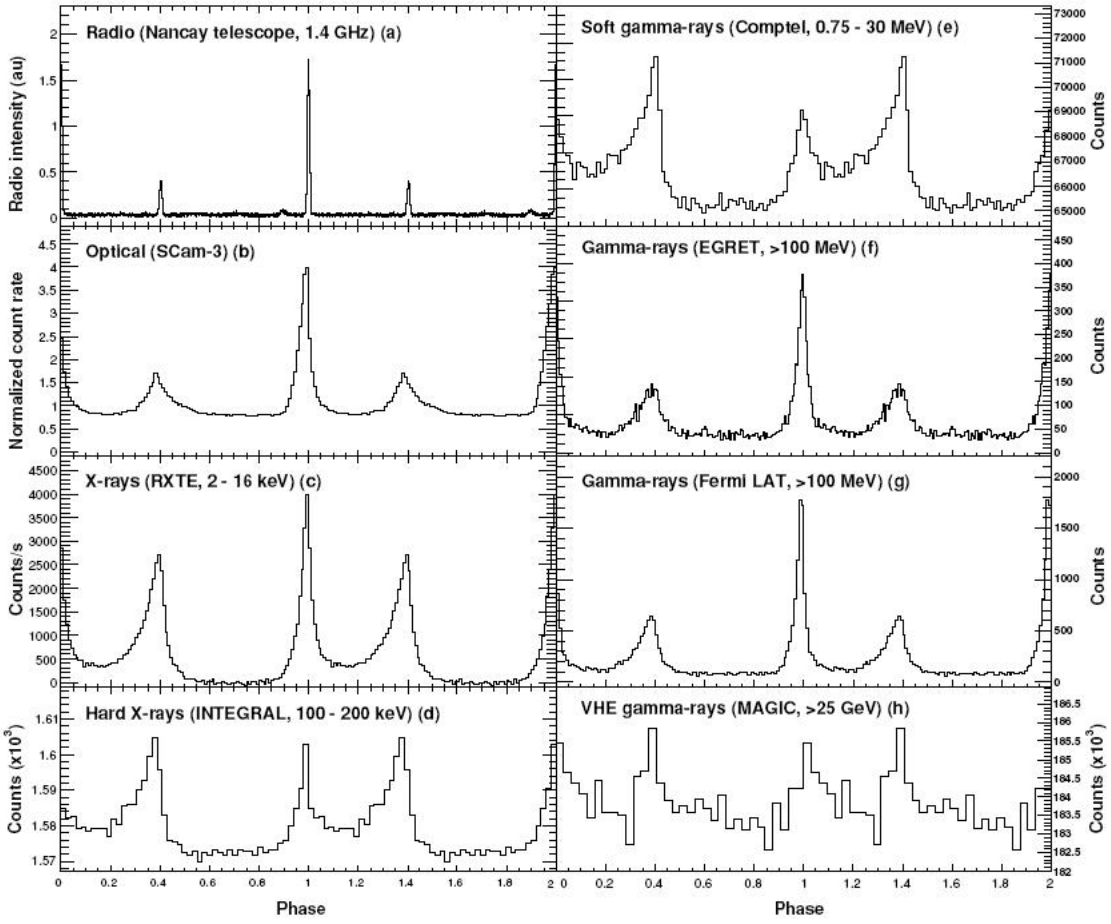


Figure 4.6: Pulsation diagram for the Crab Nebula in radio (a) [158], optical (b) [158] X-ray (c) [176] (d) [151],and a number of $\gamma$-ray wavebands (e) [134] (g) [5] (h) [34] taken from [5].

These latest high-energy observations of the Crab pulsar pulsations have allowed the site of emission to be constrained. Prior to these observations two main types of model were proposed; polar cap models where the emission takes place near the magnetic pole of the neutron star (such as [63]) and the outer gap models where emission takes place further from the pulsar's surface [55]. Predictions of the emission from outer gap models predict that a simple exponential cut-off should be seen in the pulsed emission while polar cap models predict that the highest energy $\gamma$-rays produced will interact with virtual photons of the strong magnetic field immediately adjacent to the pulsar by a process of pair production and so a steeper cut-off will be seen. If the strength of the pulsars magnetic field is known then the observed cut-off energy of the pulsed emission can be used to estimate the minimum height above the pulsar surface at which emission can occur without the $\gamma$-rays produced interacting with the surrounding magnetic field. For the crab nebula emissions observed by Fermi a radius of more than 3.7 times that of the pulsar is calculated for the emission height in the Crab Nebula and hence polar cap models which emit close to the surface are excluded by this result [5].

### 4.1.2 Kes 75

As the first observations of inverse Compton emission from a pulsar wind nebula were of the Crab Nebula, this was assumed to represent the emission mechanism of all young pulsar wind nebulae. If this were the case, similar emission would be expected from other young pulsar wind nebulae such as Kes 75. Kes 75 is a bright X-ray and radio PWN observed around the energetic pulsar PSR J1846-0258 [100] [135]. The most recent analysis of Chandra X-ray observatory data from this source showed a shell type remnant with a high-powered pulsar wind nebula in the centre [156]. This detail will not be visible in the $\gamma$-ray regime as the point spread function of the HESS telescopes does not have the necessary resolution to distinguish between the two objects.

PSR J1846-0258 at the centre of this nebula is one of the youngest and most energetic pulsars in the Galaxy with a spindown luminosity of $\dot{E} = 8.3 \times 10^{36}$erg/s and a characteristic age of $\tau_c = 723$ years [100] [135]. However, as with many young

Figure 4.7: An X-ray image of the Kes 75 complex taken using the Chandra X-ray telescope [88]. Low energy X-rays are coloured red and high energy X-rays are coloured blue. In the centre of the nebula high energy X-rays dominate while only lower energy X-rays are seen in the SNR shell.

pulsars, this may not represent the actual age of the system in question due to changes in the value of $\dot{P}$ which are expected in young pulsars. Indeed the Kes 75 system has never been identified with a known historical supernova contrary to the normal expectation for such a young nebula. It has one of the largest magnetic fields of all young pulsars, B = $4.9 \times 10^{13}$ G [135].

The most recent distance measurements estimate the distance to this nebula to be between 5.1 - 7.5 kpc [137] giving the supernova remnant shell a diameter of 2.80 pc. Unlike the SNR shell associated with the Crab nebula, which is of a similar age to Kes 75, this remnant can be seen in many wavebands. X-ray observations clearly show the shell of the nebula which implies the presence of shocked material typical of a SNR entering its Sedov phase [187].

The central pulsar wind nebula of this remnant is also well observed in the X-

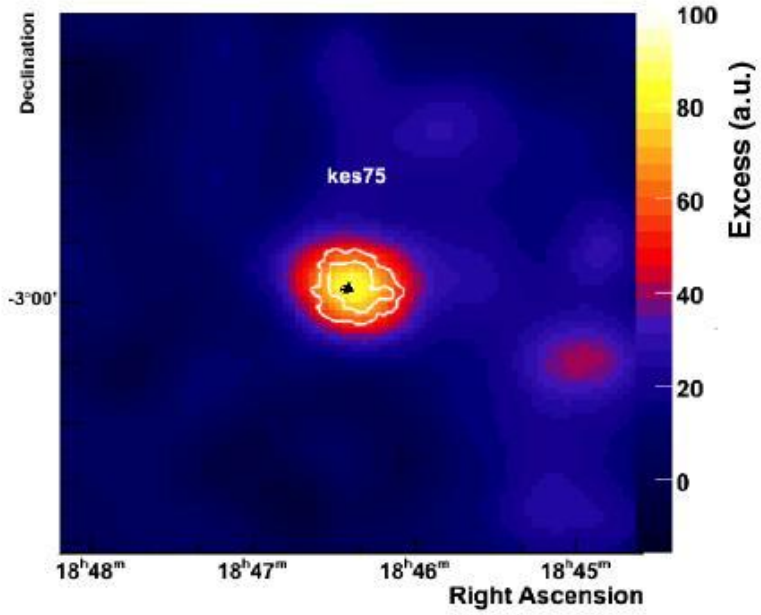


Figure 4.8: Kes 75 as viewed in the VHE $\gamma$-ray regime taken from [187]. It is seen as a point like source within the PSF of the HESS telescope array, and so the central nebula and shell elements of emission cannot be distinguished from each other.

ray regime. It measures 0.6 pc across [156] and the morphology of the nebula is well studied. The X-ray nebula is shown in Figure 4.7 and shows a symmetrical form similar in morphology to the Crab. It is extended symmetrically along the northeast-southwest axis; deep observations also show a jet along this axis. It has a power law spectrum with an index of -1.93 $\pm$ 0.03, although this is steeper in the central jet where an index of -1.7 $\pm$ 0.2 is seen [156]. Its total luminosity between 0.5 and 10 keV is $L_X = 1.4 \times 10^{35}$erg/s which accounts for $\sim$ 2% of its spindown luminosity [156].

Kes 75 was first seen in the VHE $\gamma$-ray regime in the HESS Galactic Plane survey [23]. It is a good example of a young pulsar wind nebula which, like the Crab, is point-like when compared to the point spread function of the HESS array. As a result, it is not possible to distinguish between VHE $\gamma$-rays from the central pulsar wind nebula and the surrounding supernova remnant (See Figure 4.8). The most comprehensive published results for this source in the TeV $\gamma$-ray regime [187] show a power law with spectral index of -2.26 $\pm$ 0.15 and a luminosity above 1 TeV

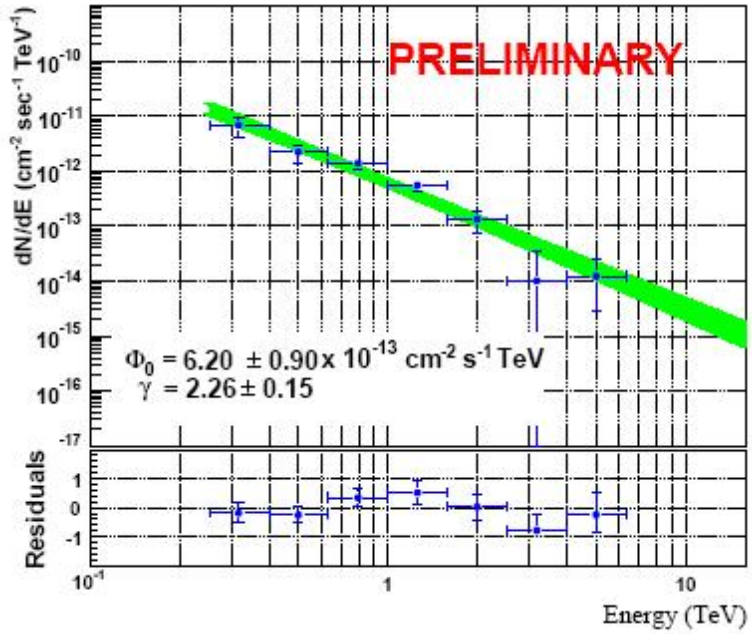


Figure 4.9: The spectrum of the nebula Kes 75 in the VHE $\gamma$-ray regime taken from [96] using the HESS telescopes.

of $(7.4 \pm 1.4) \times 10^{33}$ erg/s, this spectrum is shown in Figure 4.9.

Most of the emission from this nebula is expected to come from the central pulsar wind nebula; however, a contribution of up to 13% from the shell cannot be ruled out [187]. Even so, comparison of the X-ray and $\gamma$-ray fluxes of the central pulsar wind nebula can be used to calculate the magnetic field strength of the nebula to be about 15 $\mu$G [187] which is much lower than the similarly aged Crab Nebula and indeed lower than the value expected if the nebula was in equipartition. As a consequence of the lower magnetic field strength, the flux expected is lower than that observed in the Crab Nebula. This is because a stronger magnetic field, such as that of the Crab Nebula, allows synchrotron photons generated in the nebula to be maintained and boosted via the synchrotron self Compton mechanism. If the magnetic field is weaker then these photons do not interact with the electrons present in the nebula and will escape; thus only ambient photons are available for inverse Compton boosting, resulting in a lower observed VHE $\gamma$-ray flux.

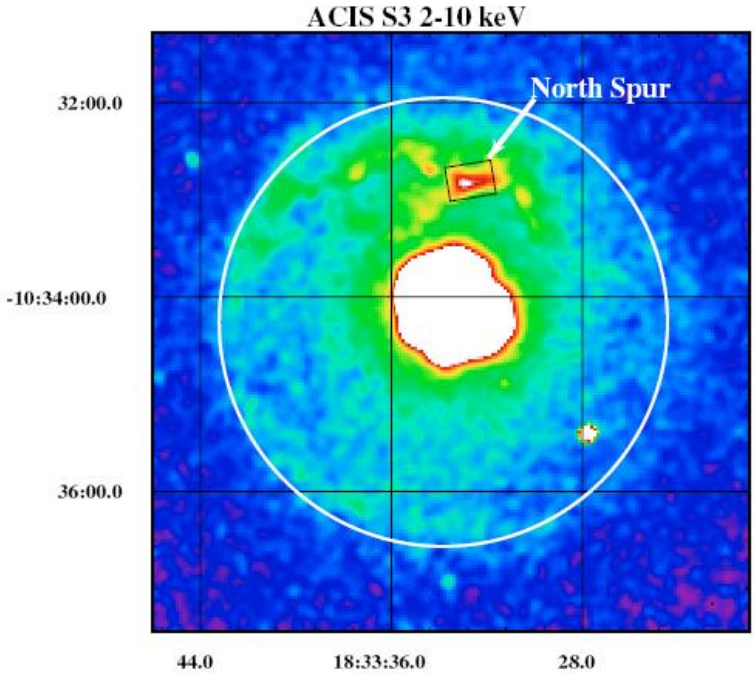


Figure 4.10: A Chandra image of the nebula G21.5-0.9 taken from [43], showing a strong source corresponding to the pulsar wind nebula in its centre with diffuse emission corresponding to the surrounding supernova remnant material. Shell type emission is only seen in a small portion of the source, the "North Spur".

### 4.1.3 G21.5-0.9

Another important example of a young pulsar wind nebula which has been described as similar to the Crab nebula is G21.5-0.9, which has been more extensively studied than Kes 75 at radio [166] and X-ray wavelengths [43]. The most comprehensive recent observations of this source were made using the Chandra and XMM-Newton satellites [43].

The nebula is located around the recently discovered pulsar PSR J1833-1034 [50]. It has a measured period and period derivative of 61.86 ms and $2.0 \times 10^{-13}$ s/s respectively implying a spindown luminosity of $3.3 \times 10^{37}$ erg/s and a characteristic age of 4900 years. However, as with many young pulsars, the characteristic age is thought to overestimate the age of the system as the period of the pulsar at its birth is probably not too dissimilar to its current period. Study of the nebula itself leads to an estimated age of the system of approximately 1000 years, giving the nebula a

similar age to the Crab and Kes 75 nebulae; it may be associated with the recorded historical supernova of 386 AD [95].

Chandra observations show a bright central pulsar wind nebula surrounded by a halo of diffuse emission [43]. This halo contains two bright features which may correspond to shockfront heating in the supernova remnant. The halo itself is caused by the scattering of dust originating from the central pulsar wind nebula. The central nebula shows a power law spectrum of index -1.89 ± 0.02 and a luminosity of $2.29 \times 10^{35}$ ergs/s between 0.5 and 8 keV. This may be compared to emission in the VHE $\gamma$-ray regime where a power law spectrum of -2.08 ± 0.22 is observed and a luminosity above 1 TeV of $(4.3 \pm 0.1) \times 10^{33}$ ergs/s. From these results, a magnetic field strength of the nebula of 15 $\mu$G is derived.

The VHE $\gamma$-ray emission and the magnetic field observed for this source are similar to those observed in the case of Kes 75 and indeed are the product of the same emission mechanism in which background photons are inverse Compton boosted by relativistic electrons in the energetic nebula. The spectrum and morphology obtained in HESS observations of this object are shown in Figure 4.11 and Figure

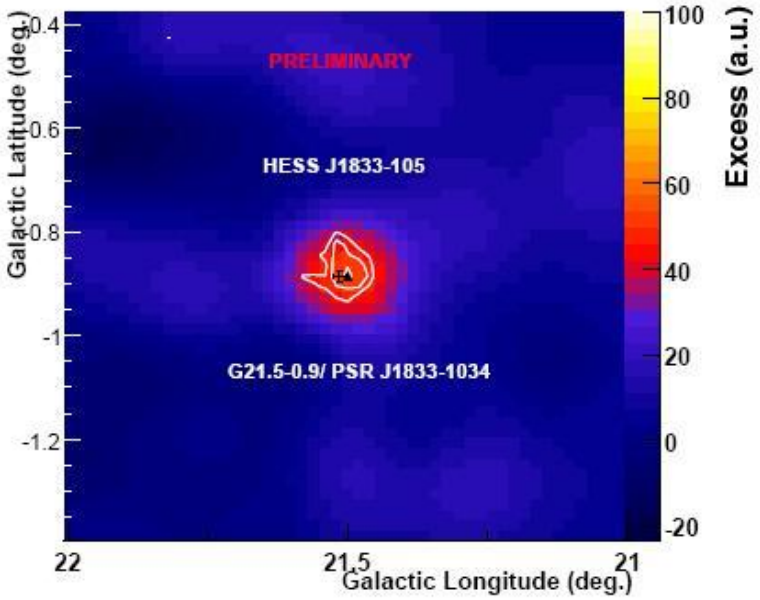


Figure 4.11: G21.5-0.9 as viewed in the VHE $\gamma$-ray regime taken from [96]. It is seen as a point like source within the PSF of the HESS telescope array.

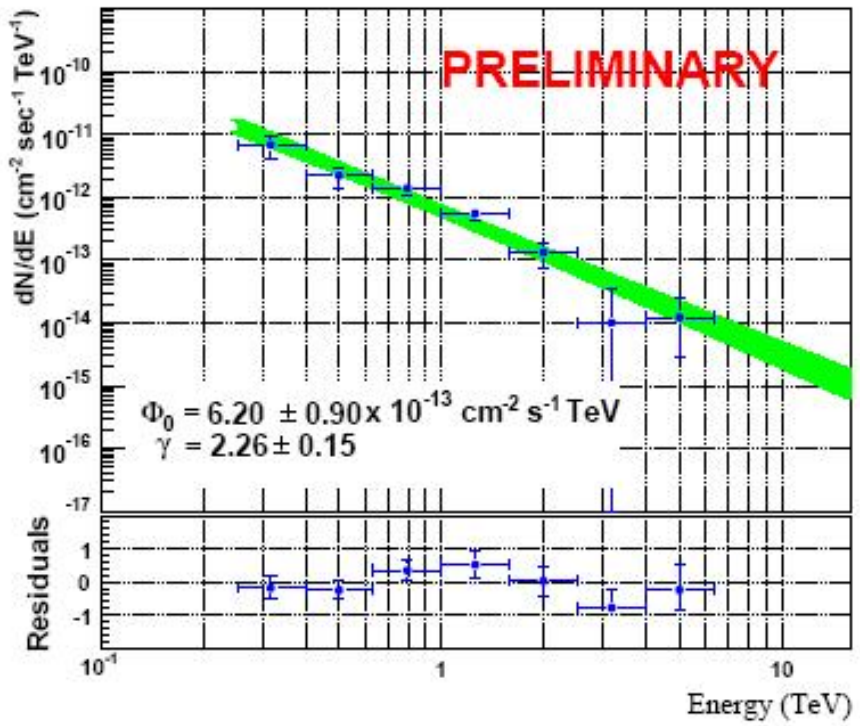


Figure 4.12: The spectrum of the nebula G21.5-0.9 in the VHE $\gamma$-ray regime taken from [96] observed using the HESS telescopes.

4.12 respectively.

### 4.1.4 G0.9+0.1

The Galactic Centre object G0.9+0.1 is another young pulsar wind nebula which emits in the TeV $\gamma$-ray regime. Like G21.5-0.9 the progenitor pulsar was discovered after the observation of this source with HESS. Radio observations of its progenitor pulsar, PSR J1747-2809 [49] give a period of 52 ms and a period derivative of $1.56 \times 10^{37}$ s/s implying a spindown luminosity of $\dot{E} = 4.3 \times 10^{37}$ erg/s and a characteristic age of 5,300 years [49]. However, as with many young pulsars, this is thought to be an overestimate compared to the age derived from analysis of the nebula. Observations of the surrounding nebula have allowed its true age to be estimated as no more than 2 - 3 kyr [180] making the nebula somewhat similar to G21.5-0.9.

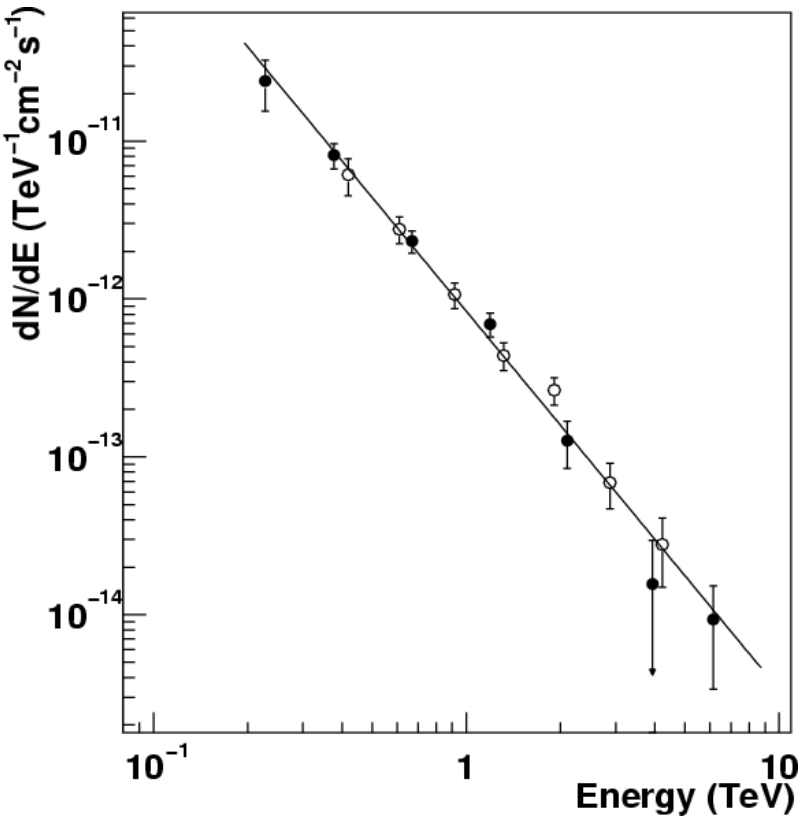


Figure 4.13: The spectrum observed by HESS of the galactic centre nebula G0.9+0.1 [180], open circles denote datapoints obtained using hard cuts while standard cuts are denoted by filled circles.

As G0.9+0.1 is located very close to the Galactic Centre region it is difficult to observe in most wavelengths due to source confusion and galactic absorption in this area. This meant that the central PWN was not detected conclusively in X-rays until *BeppoSAX* [180] made observations of the region. The most recent observations in X-rays by the *XMM-Newton* observatory show a power-law with index -1.99 $\pm$ 0.19 and a luminosity of $5 \times 10^{34}$ erg/s between 2 - 10 keV.

Due to the low angular resolution of the current generation of Cherenkov $\gamma$-ray instruments it was also difficult to make observations in this regime of objects in the Galactic Centre. It was detected by HESS and has a spectrum with spectral index of -2.40 $\pm$ 0.29 and a luminosity above 1 TeV of $1.1 \pm 0.1 \times 10^{32}$ erg/s [15], this spectrum is shown in Figure 4.13. Its Galactic Centre location results in its brightness as a TeV $\gamma$-ray emitting source as more ambient starlight is available

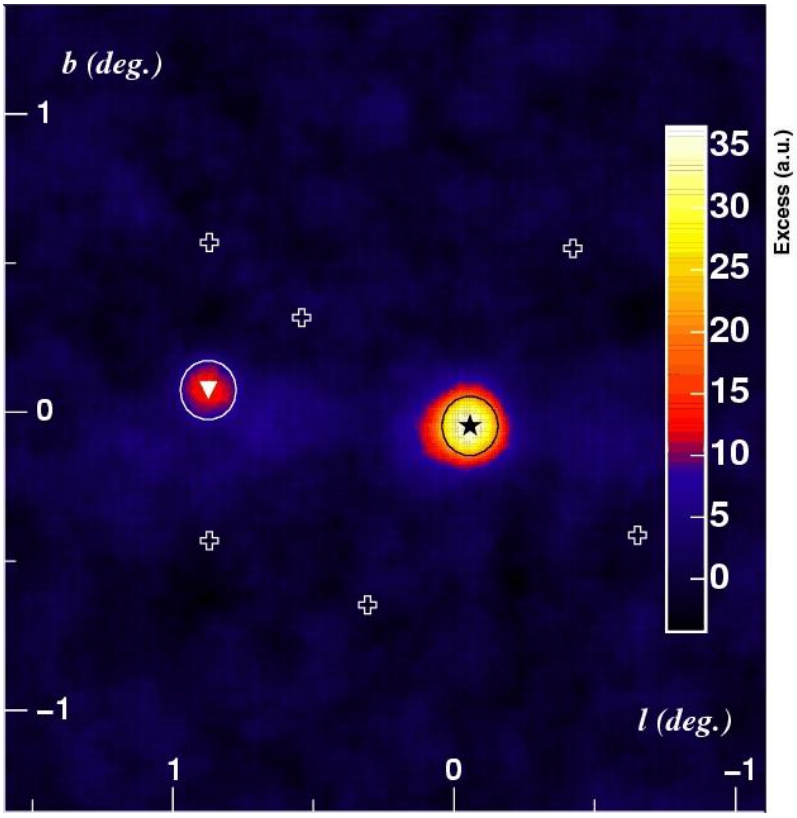


Figure 4.14: The galactic centre region as viewed in the TeV $\gamma$-ray regime. G0.9+0.1 is marked by a white triangle while the neighbouring Sagittarius A* is marked with a black star [180].

in the Galactic Centre for inverse Compton boosting than would be in the further reaches of the Galaxy, an image of this region is shown in Figure 4.14.

### 4.1.5 MSH 15-52

MSH 15-52 is perhaps the most interesting of the young pulsar wind nebulae that have been observed in the VHE $\gamma$-ray regime because unlike other young PWN that have been observed at these wavelengths it is observed as an extended nebula. The nebula is at a distance of 5.2 $\pm$ 1.4 kpc [84] similar to many other known young PWNe which implies that its large angular size has a physical explanation (see Figure 4.15). This physical explanation may be either due to the age of the nebula or the lower than average density of the surrounding ISM or a combination of both.

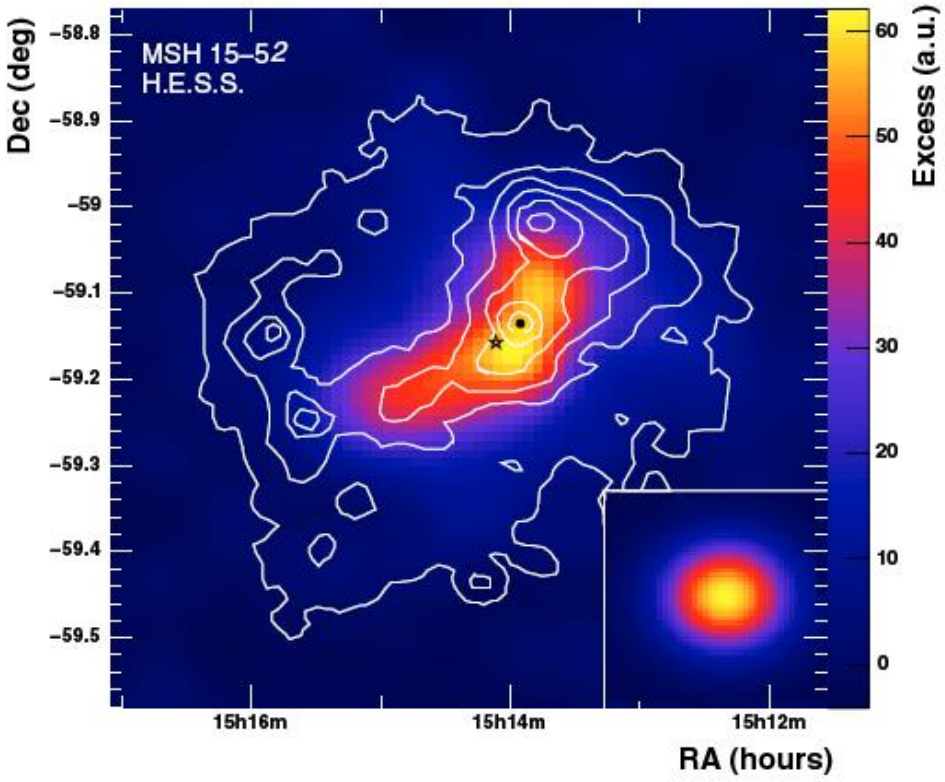


Figure 4.15: VHE $\gamma$-ray emission from the pulsar wind nebula MSH15-52 [12], with X-ray emission overlaid (white contours); it shows extension towards the northwest and southeast directions in both $\gamma$-ray and X-ray wavelengths. The point spread function of the HESS array is shown in the box in the bottom right hand corner.

Its supernova remnant was also only the third to be associated with a progenitor pulsar, in this case PSR B 1509-58. The pulsar has a period of 155 ms and a period derivative of $1.8{\times}10^{-12}$ s/s which are used to calculate its spindown luminosity of $\dot{E} = 1.8 \times 10^{37}$ erg/s and characteristic age of 1,700 years [132] [179]. Unlike many of the other young pulsars discussed in this Chapter this may be close to the actual age of the pulsar and hence the nebula which surrounds, which goes some way to explain its large size relative to the other young pulsar wind nebulae discussed.

X-ray observation of this nebula shows an extension in the northern and eastern directions (see Figure 4.15) [75]. Like most of the young PWNe it again shows a power law, in this case with a spectral index of -1.65 $\pm$ 0.05. Its luminosity between 0.5 and 10 keV is $3.98 \times 10^{34}$erg/s [75]. The unusual size of the nebula is due to a

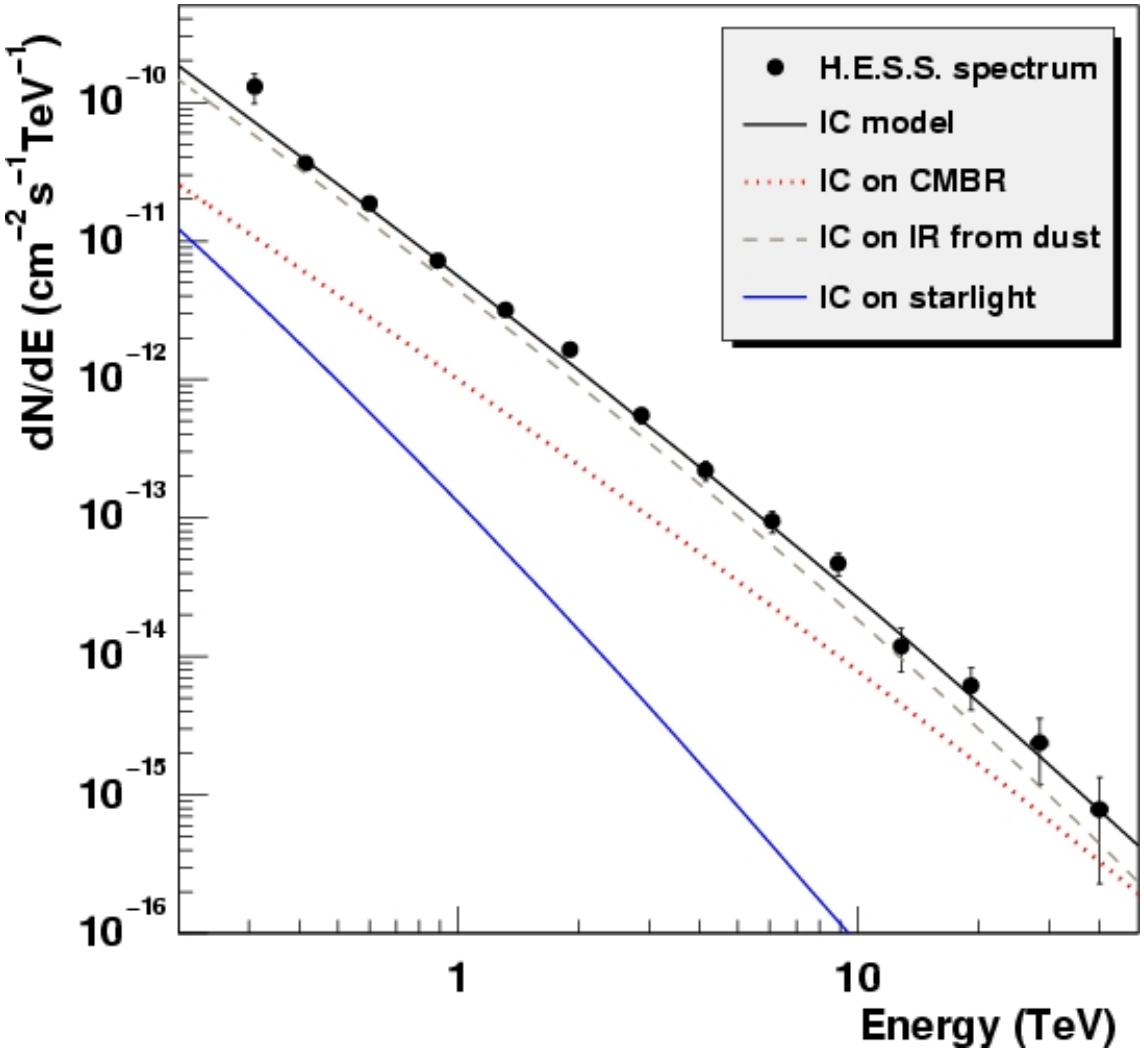


Figure 4.16: The spectrum of MSH15-52 as observed by HESS in the TeV regime [12]. The observed spectrum is compared to an inverse Compton model of emission expected from background starlight and the cosmic microwave background as discussed in [12]. As can be seen here, the inverse Compton emission observed cannot be explained by either starlight alone and so some infra red emission from dust reflection must be present in the vicinity of the nebula.

lower than average ISM density in the vicinity of this pulsar.

MSH15-52 was the first extended pulsar wind nebula to be observed in the VHE $\gamma$-ray regime [12]. The HESS observations confirm the observation of an extended nebula seen in the X-ray regime (see Figure 4.15), and the PWN shows a power law spectrum with index -2.27 and a luminosity above 1 TeV of $7.24\times10^{34}$ erg/s (15%

Crab); the spectrum for this object is shown in Figure 4.16. From these values the magnetic field strength of this nebula can be inferred to be 17 $\mu$G.

### 4.1.6 Properties of Young PWNe

As we have seen, for many years the central nebula of the Crab was considered as the archetype of a young pulsar wind nebula, although we can now see that this is not strictly the case. While the Crab is compact and visible as a point source in the TeV $\gamma$-ray regime and has a similar spectrum to other young pulsar wind nebulae, it is much brighter than otherwise expected and its spectral index of -2.63 $\pm$ 0.2 is the highest known for a young pulsar wind nebula in the VHE $\gamma$-ray regime (compared to a mean value of -2.2 $\pm$ 0.1).

The observed properties of young pulsars in the TeV $\gamma$-ray regime can vary quite considerably from case to case and this is attributable to many factors even within this small group of targets at a similar evolutionary point.

Perhaps the greatest influence is the material into which the pulsar wind nebula and its surrounding supernova remnant is expanding. Some of the nebulae discussed in this section are surrounded by a visible non-thermal shell-type supernova remnant (such as G21.5-0.9 and G0.9+0.1) while others are not (such as the Crab) and this is a result of the interaction of the expanding supernova remnant with dense material in the surrounding medium, creating a shock front. The density of this material also determines the expansion speed of the PWN into the material surrounding it and so it is possible to expand faster into the surrounding material if it is of a low density, as is seen in the most extended young pulsar wind nebula MSH15-52.

Position is also relevant for the flux of source photons for inverse Compton boosting, as has been seen in G0.9+0.1, which is brighter than the otherwise comparable object G21.5-0.9. G0.9+0.1 is in the direction of the Galactic Centre and so much more ambient starlight is available for inverse Compton boosting.

Another critical factor in determining the difference in TeV $\gamma$-ray flux from observed pulsar wind nebulae is the strength of the magnetic field present in the nebula as this is responsible for the synchrotron self Compton boosting of the ambient photons. This is dependent on the strength of the magnetic field of the progenitor

pulsar from which it is derived as well as the properties of the material with which it interacts such as the density of the surrounding material.

## 4.2 Middle aged Pulsar Wind Nebulae

After it has swept up an appreciable fraction of its original mass from material in the surrounding interstellar medium, a supernova remnant will produce an inverse shock front moving inwards towards the pulsar wind nebula at its centre. The incoming shockwave interacts with the central pulsar wind nebula after about 10,000 years; nebulae soon after this interaction are referred to as middle-aged pulsar wind nebulae. Like the discussion of young pulsar wind nebulae, this discussion focuses on the comparison between the pulsar wind nebulae seen in VHE $\gamma$-rays and their X-ray companions. Discussion focuses on the most well-established sources while detail of all known middle aged pulsar wind nebulae are given in Table 4.3, and details of their progenitor pulsars are given in Table 4.4.

### 4.2.1 Vela X

Vela X, one of the most famous pulsar wind nebulae after the Crab, is visible through the entire spectrum from radio to TeV $\gamma$-rays, where it is one of the few extended sources of this type visible. It is an important source in the study of pulsar wind nebulae as it was the first middle-aged pulsar wind nebula to be observed [195]; this allowed the concept of pulsar wind nebula evolution to develop. It was also the first PWN to be observed to have its progenitor pulsar significantly offset from its centre [148], thus leading to the study of PWN expansion in an inhomogeneous medium. It is at a distance of only 290 pc [74] allowing its extended morphology to be studied in great detail.

The progenitor pulsar for this nebula has been identified as PSR B0833-45 which, as expected for an extended pulsar wind nebula, is much older than the pulsars discussed so far. It has a period of 89 ms and a period derivative of $1.25\times10^{-13}$s/s which implies a spin down luminosity of $\dot{E} = 6.9 \times 10^{36}$ergs/s and a characteristic age of 11,000 years [136]. However it is still young when compared to the general

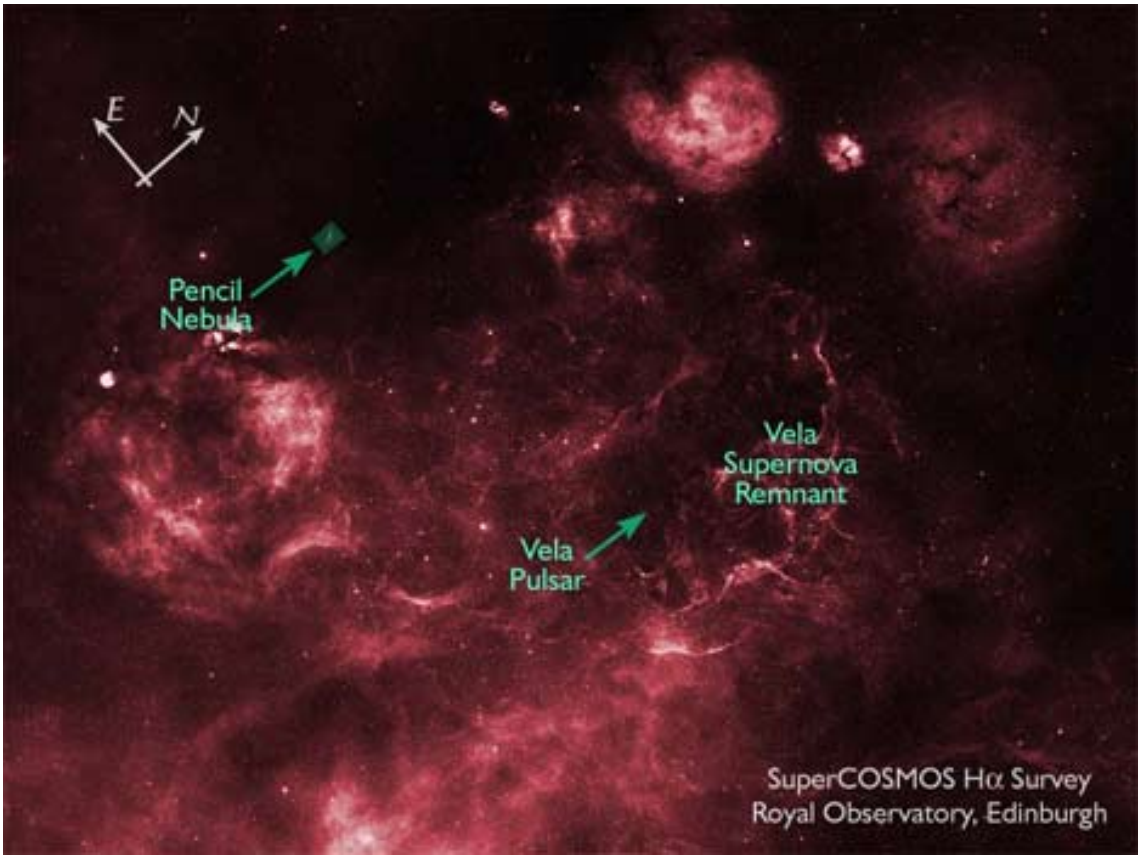


Figure 4.17: The Vela complex as seen in the H-alpha optical band showing its filamentary structure [160].

pulsar population as many pulsars have ages of the order of $10^6$ or $10^7$ years [182]. Unlike the characteristic ages calculated for the progenitors of young PWNe the characteristic age of this object is closer to the true age of the nebula.

Early observations of this source in the radio regime identified three components of non-thermal emission which were designated Vela X, Y and Z respectively [195]. The Y and Z components correspond to elements of the supernova remnant shell while the central pulsar wind nebula, the brightest element of the system, corresponds to Vela X.

The supernova remnant shell is also visible in the optical regime (see Figure 4.17) where it shows a fine filamentary structure similar to that seen in younger SNR such as the one associated with the Crab nebula.

In the X-ray regime, Vela X shows a strong central source around the pulsar

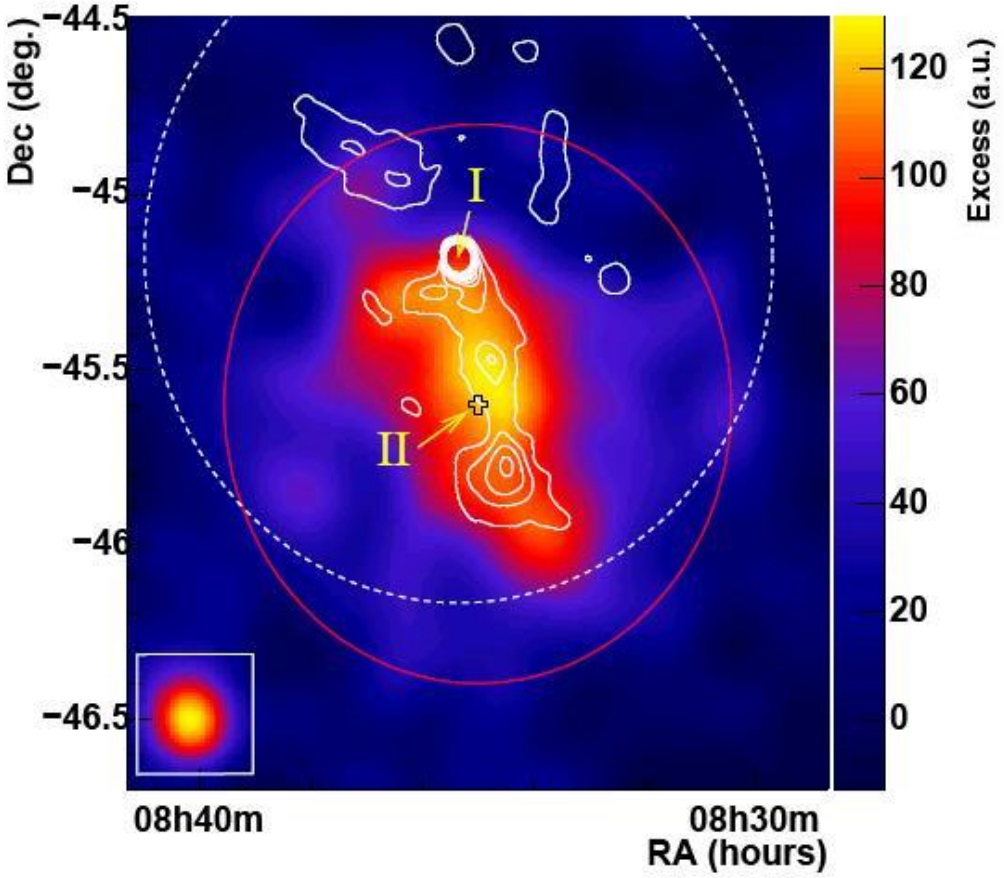


Figure 4.18: The Vela X nebula as seen in the TeV $\gamma$-ray regime [22]. The pulsar position is marked I while the centre of the $\gamma$-ray nebula is marked II.

position [148] with morphology similar to that seen in young pulsar wind nebulae such as the Crab. However, the X-ray nebula observed is much smaller than the Crab's, measuring only 0.1 pc [146] across compared to the 1.0 - 1.3 pc diameter of the Crab PWN. This is due to the reduced energy output of the older pulsar powering it with a spindown luminosity two orders of magnitude smaller than the younger nebula. The central nebula shows a broken power law spectrum in the X-ray regime showing a spectrum of -1.66 $\pm$ 0.1 below 12.5 keV and -2.01 $\pm$ 0.1 above this value [146]. The central nebula has a luminosity of $5.5 \times 10^{33}$erg/s between 0.1 and 200 keV. Additionally, weaker emission in the X-ray is seen extending to the south of the nebula [148].

The nebula has also been well observed in the VHE $\gamma$-ray regime [22] and shows

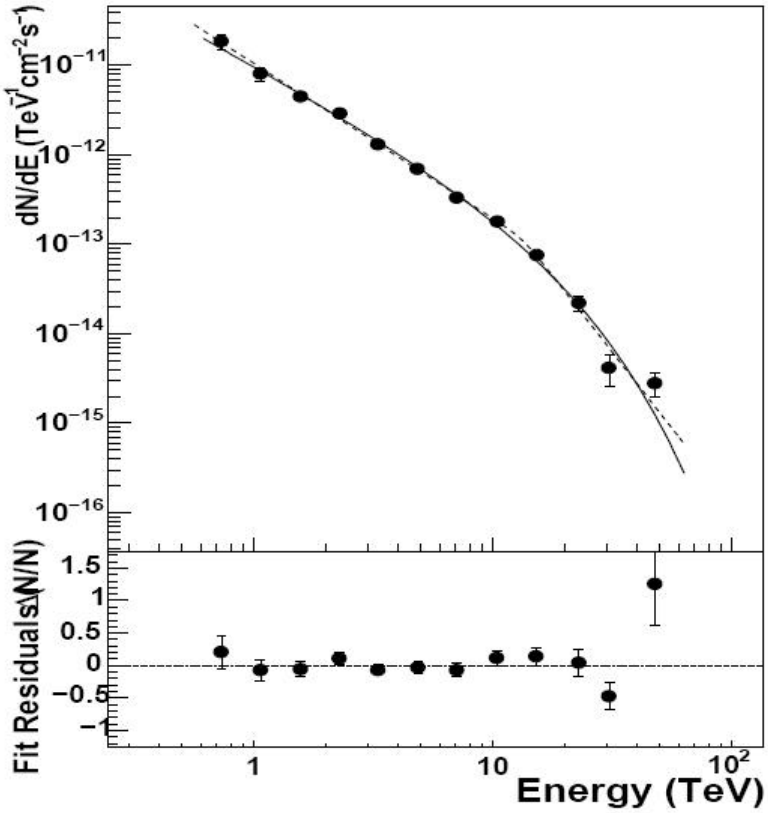


Figure 4.19: The energy spectrum of $\gamma$-ray emission from the Vela X nebula [22].

greatly extended emission to the south of the pulsar position corresponding to the extended emission seen in [148]. These observations show that much of the emission from the nebula is offset from the central pulsar position with a measured centre of gravity of the observed VHE $\gamma$-ray excess centred on a right ascension of 129° and a declination of -45.6° (J2000) [22], compared to a pulsar position of right ascension 128.84° and declination -45.17° (J2000); the difference between these positions is shown in Figure 4.18.

An offset of pulsar wind nebula emission such as this is not seen in younger pulsar wind nebulae (with the exception of MSH15-52 where a small offset is seen) or indeed in X-rays where emission is centred around the progenitor pulsar. The offset observed is the result of expansion into an inhomogeneous medium [42] which allows the nebula to expand faster in some directions than in others (in this case the density of the surrounding material is lower to the south of the pulsar). This is compounded by the effects of the inverse shock which will arrive earlier on the side

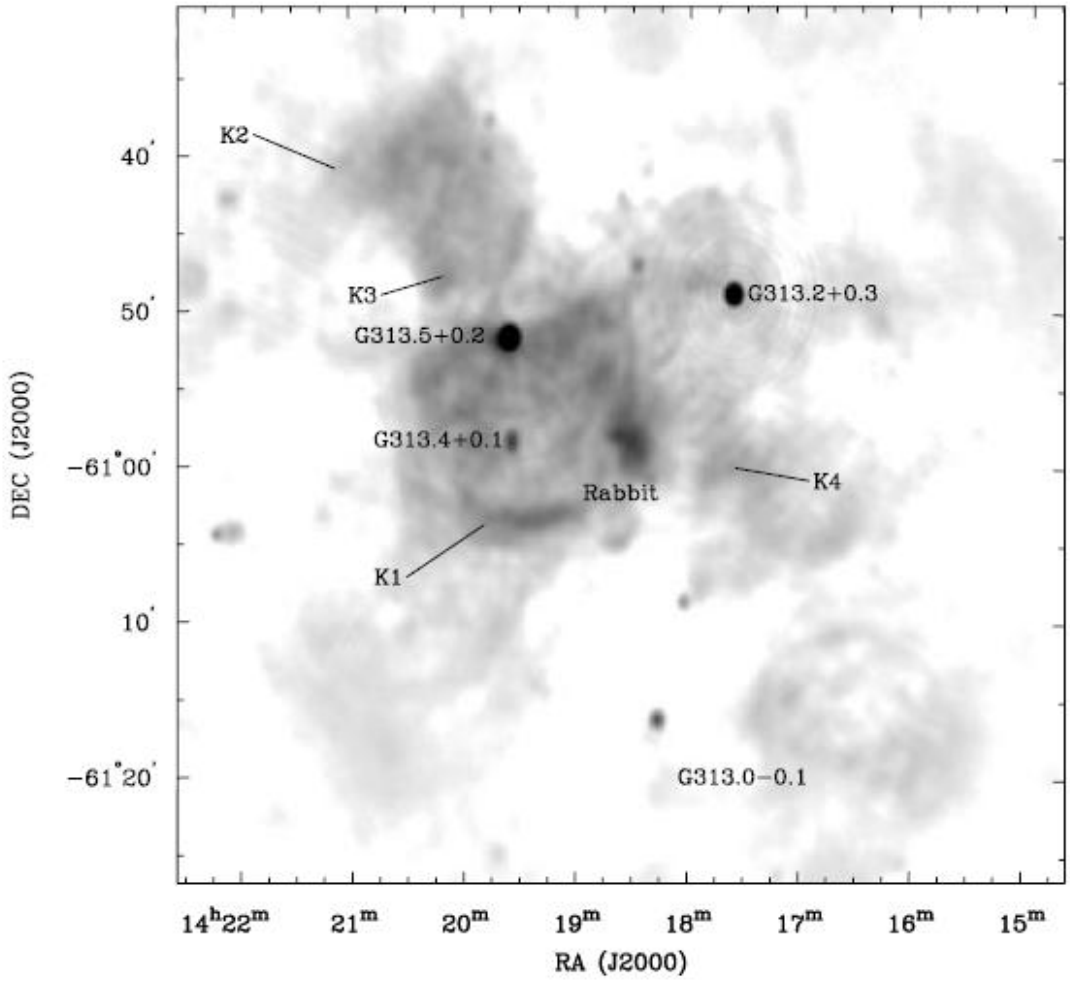


Figure 4.20: A 20cm radio image of the Kookaburra complex taken using ATCA [171] showing the shape of the complex from which it derives its name.

of the nebula where more material is present causing the pulsar itself to be close to the edge of the observed $\gamma$-ray nebula observed here.

The HESS observations of this nebula show a broken power law emission like that observed in the X-ray regime, this shows the highest point at which electrons are present in the nebula and producing inverse Compton photons. It has a spectral index of -1.45 $\pm$ 0.22 below 13.4 TeV and an index of -3.4 above this value. The luminosity above 1 TeV is observed to be $(1.38 \pm 0.55 \times 10^{36}$ erg/s.

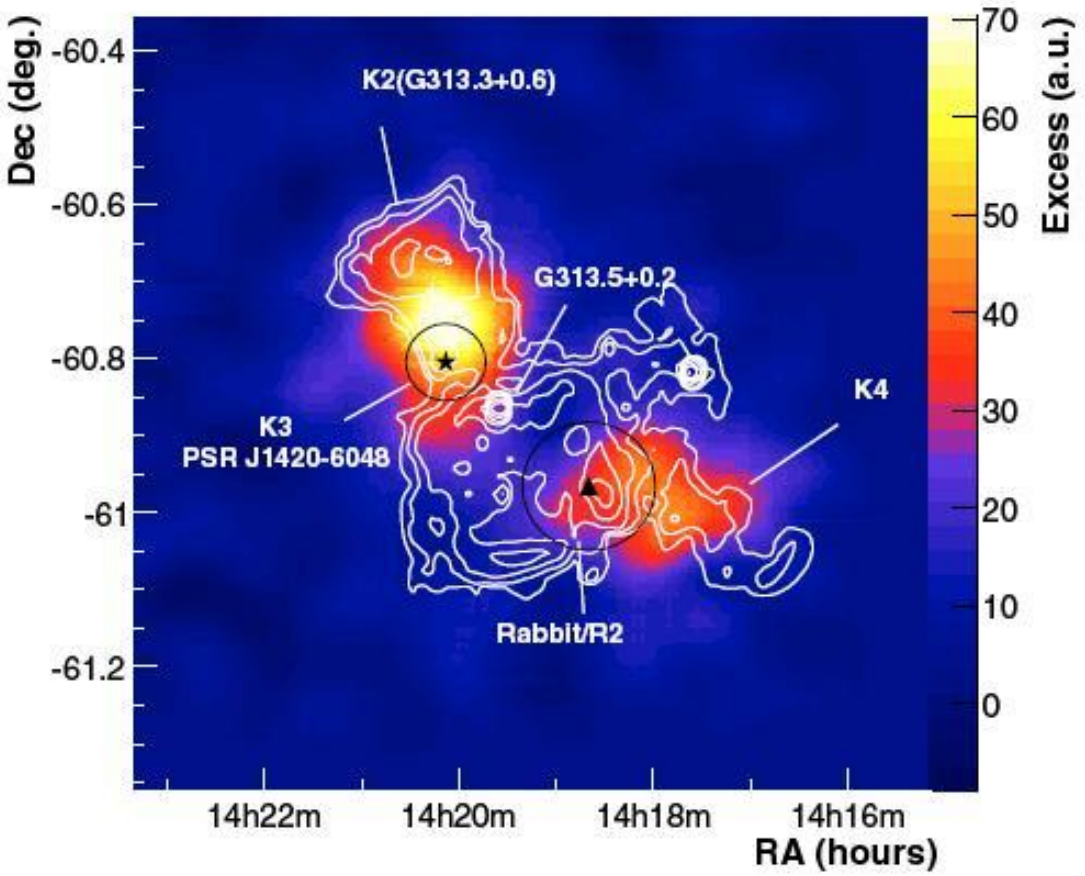


Figure 4.21: VHE $\gamma$-ray observation of the Kookaburra complex showing two nebulae corresponding to the K3 (Kookaburra) and Rabbit Nebulae which are seen on the "wings" of the radio source (white contours from ATCA 20cm data) [19].

### 4.2.2 Kookaburra and Rabbit

The Kookaburra complex was discovered to be a VHE $\gamma$-ray emitting source in the HESS Galactic Plane survey [23] and corresponds to a region well observed at all wavelengths from radio to VHE $\gamma$-ray. Its name is derived from the emission observed in the radio regime, where a strong central source is observed with two "wings" at its extremes (see Figure 4.20). These wings correspond to the two nebulae observed in the TeV $\gamma$-ray regime, which are both pulsar wind nebulae. The progenitor pulsar of the north-easterly wing was known before TeV $\gamma$-ray emission was observed and the nebula created by this pulsar has been designated as the Kookaburra Nebula, by which nomenclature we shall refer to it in this section.

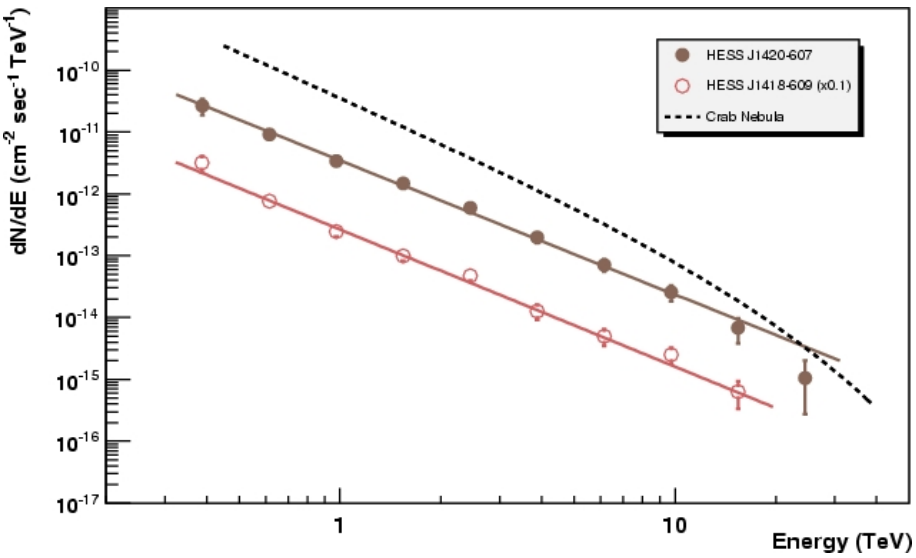


Figure 4.22: The spectra of the Kookaburra (HESSJ1420-607) and Rabbit (HESSJ1418-609) nebulae as seen in the TeV $\gamma$-ray regime [19].

At the southern edge of the Kookaburra nebula lies the pulsar PSR J1420-6048 which has been positively identified as the progenitor of the system. It has a period of 68 ms and a spindown rate of $8.28 \times 10^{-14}$ s/s [61], which is used to calculate the characteristic age of 13,000 years and the spindown luminosity of $\dot{E} = 1.0 \times 10^{37}$ erg/s, typical of a middle-aged pulsar wind nebula such as this. It is at a distance of 5.6 kpc [61].

Surrounding this pulsar is a small X-ray pulsar wind nebula [188] showing a luminosity of $1.6 \times 10^{35}$ erg/s between 2 and 10 keV and a spectral index of -2.03 and showing a faint northerly extension consistent with the $\gamma$-ray emission region observed. The corresponding $\gamma$-ray region, shown in Figure 4.21, has a luminosity above 1 TeV of $5.9 \times 10^{33}$ ergs/s and a spectral index of -2.17 $\pm$ 0.12 [19]; this spectrum is shown in Figure 4.22.

The other wing of the Kookaburra complex, generally referred to as the Rabbit nebula, lies on the eastern edge of the complex. It is brighter and has a greater angular extent than its companion in the X-ray regime with a luminosity of $3.5 \times 10^{33}$ ergs/s between 0.5 and 8 keV, and a power law spectral index of -1.7 $\pm$ 0.1. It is however less bright in the TeV $\gamma$-ray regime when compared to its neighbour with a luminosity of $8.1 \times 10^{33}$ ergs/s above 1 TeV and a spectral index of -2.22 $\pm$ 0.12,

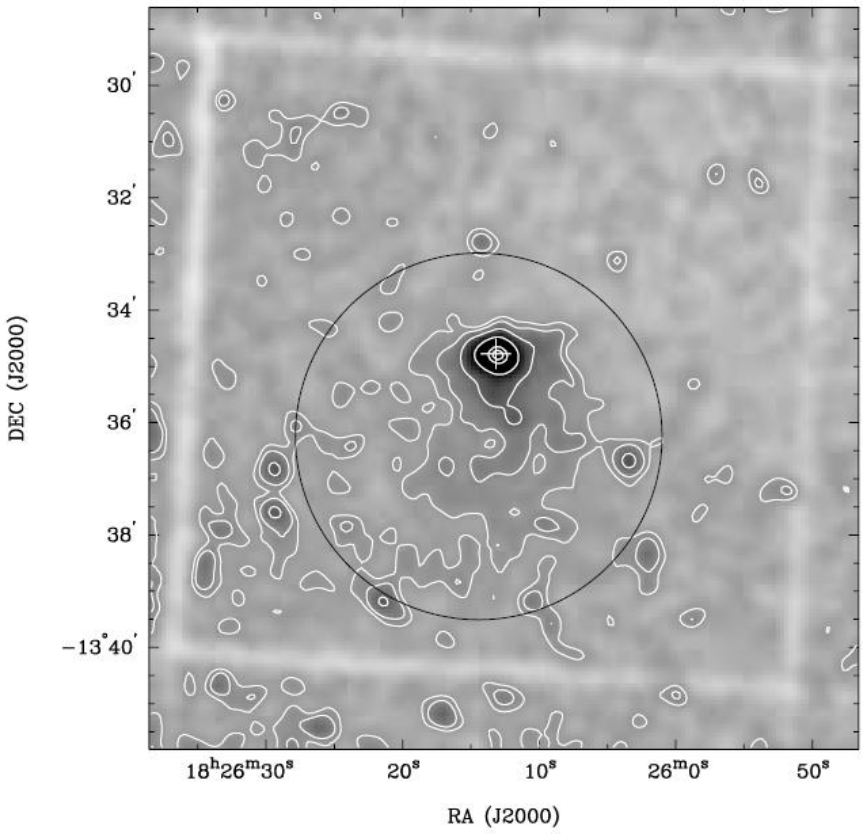


Figure 4.23: An XMM-Newton image of the HESS J1825-137 nebula showing an extended trail of emission towards the south of the pulsar (white cross) [85].

this spectrum is shown in Figure 4.22.

Its progenitor pulsar J1418-6058 was only recently discovered by the *Fermi* collaboration [3] allowing its properties to be investigated. J1418-6058 has a period of 111ms and a period derivative of $1.70\times10^{-13}$ s/s giving a spindown luminosity of $\dot{E} = 5.0 \times 10^{36}$ erg/s and a characteristic age of 10,300 years making it younger than its companion. Distance estimates based on Possenti et al [164] give the distance to this nebula of approximately 5 kpc [19], similar to its companion.

### 4.2.3 HESS J1825-137

HESS J1825-137 is the oldest known TeV $\gamma$-ray emitting pulsar wind nebula and, like the other known middle-aged pulsar wind nebulae, is offset from the progenitor pulsar B1823-13 which produced it. It is also one of the most interesting known TeV

$\gamma$-ray emitting pulsar wind nebulae as it has been used to show the cooling of the electron spectrum in a pulsar wind nebula with distance from the central nebula. It is at a distance of 4.12 kpc [58]

The progenitor pulsar B1823-13 has a period of 101ms and a period derivative of $7.5 \times 10^{-14}$ s/s which gives a spindown luminosity of $\dot{E} = 2.8 \times 10^{36}$erg/s and a characteristic age of 21,400 years. Surrounding this pulsar is a small X-ray pulsar wind nebula with a luminosity of $3.16 \times 10^{32}$ ergs/s and a spectral index of -1.3. It is much smaller (measuring only 0.2 pc across) than the X-ray nebula observed in other middle aged pulsar wind nebulae due to the less energetic pulsar at its centre. A trail of emission in the nebula is seen to its south (see Figure 4.23) heading towards the direction of $\gamma$-ray emission seen in this source [85].

In the TeV $\gamma$-ray regime the source is highly extended to the south of its progenitor pulsar [20] (see Figure 4.24). It shows extension over 1.5° from the pulsar which, given the distance of 4 kpc to this source, gives it a physical extent of 100 pc making it the largest known pulsar wind nebula in the TeV regime.

When the spectrum of the entire emission of this nebula is observed it is well described by a number of models including that of a broken power law, under which circumstance it shows a spectral index below 2.7 TeV of -2.26 $\pm$ 0.2 and an index of -2.63 $\pm$ 0.2 above 2.7 TeV, with an luminosity of $1.12 \pm 0.23 \times 10^{35}$ erg/s above 1 TeV [20]. What is more notable about the TeV $\gamma$-ray observation of this source is that the source shows a softening of its spectrum with distance from the pulsar, which demonstrates the cooling of the electron population responsible for inverse Compton emission as they move away from their source (see Figure 4.25).

It also shows that the size of the nebula observed is dependent on the energy at which we observe it; at higher energies the nebula will be smaller as it corresponds to only the highest energies of electrons. Typically, inverse Compton photons produced by the boosting of microwave background radiation will have energies of approximately 50 TeV from an interaction with a 100 TeV electron or 5 TeV if they are the product of an interaction with a 1 TeV electron. This corresponds to the much smaller nebula seen in X-rays which is caused by emission from the newly ejected electrons near the pulsar. The electrons needed to generate X-ray synchrotron emis-

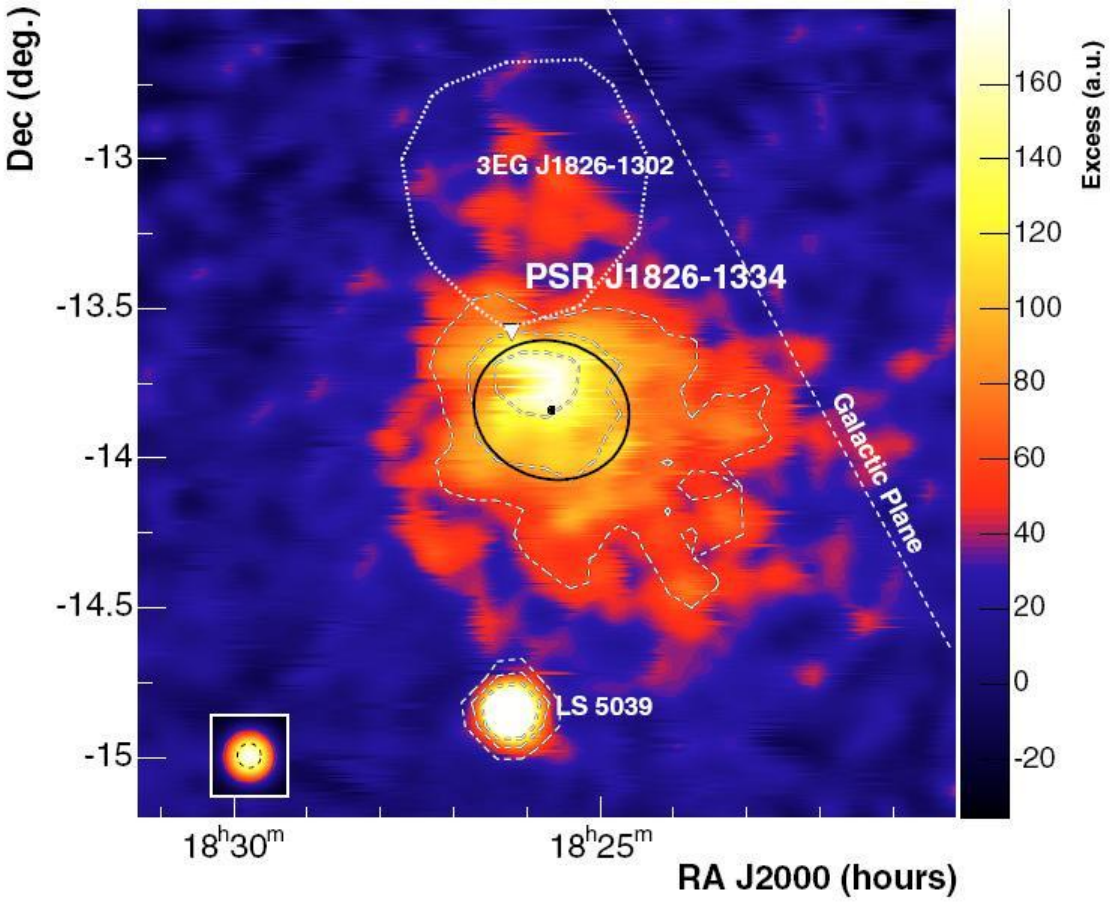


Figure 4.24: HESS observation of the HESS J1825-137 nebula showing it's extension to the south of the pulsar (white triangle). The binary source LS 5039 is also indicated. The square to the bottom left indicates the PSF of the HESS system [20].

sion are much more energetic with 10 TeV electrons required to produce $\approx$ 1 keV photons, this explains the smaller pulsar wind nebula compared with that seen in the TeV $\gamma$-ray regime.

### 4.2.4 Properties of Middle Aged Pulsar Wind Nebulae

As we have seen, middle aged pulsar wind nebulae are much larger than their younger companions when observed in the VHE $\gamma$-ray regime, while middle aged pulsar wind nebulae are smaller than young PWN in X-rays. As these pulsar wind nebulae have been the subject of the reverse shock crushing as discussed in Section 2.5.2, the pulsar becomes offset from the centre of the VHE $\gamma$-ray nebula. The progenitor

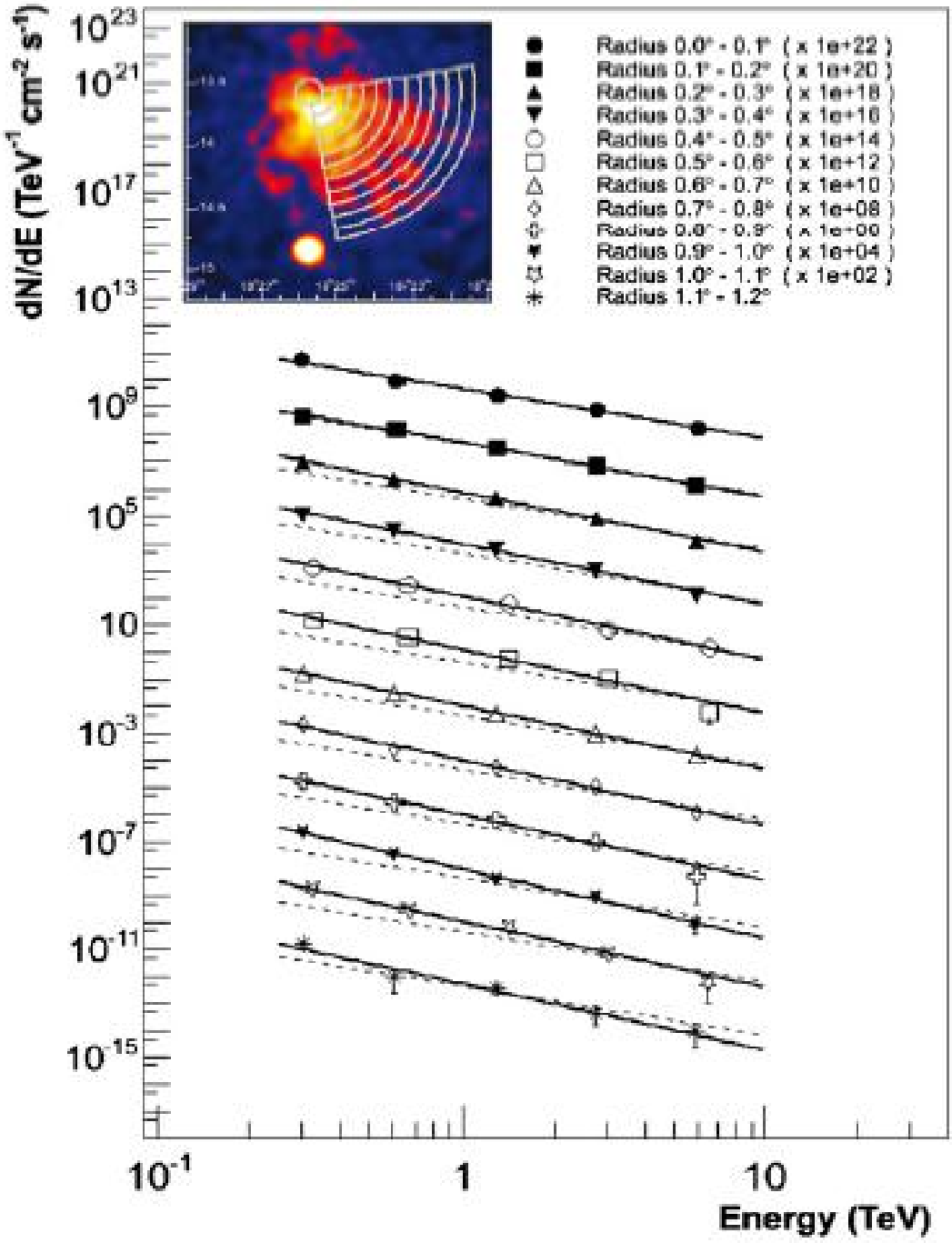


Figure 4.25: The softening of the spectrum of HESS J1825-137 with distance from the pulsar. The spectra shown correspond to those taken in 1.0° intervals centred on the suspected progenitor PSR B1823-13. They are each compared to the spectral slope of the inner circle (dotted line) to show the softening of the spectrum [20] and show a statistically significant increase in the spectral index of the nebula out to 0.6°.

pulsars of all known middle aged TeV $\gamma$-ray pulsar wind nebulae are located towards their edge. As the X-ray nebulae are the product of the youngest, most energetic electrons they are not offset in the same way as their VHE $\gamma$-ray counterparts and form symmetrical nebulae around their progenitor pulsars. Some of the older nebulae do however show faint tails of X-ray emission in the direction of the $\gamma$-ray emission; this is seen in both the Vela X and HESS J1825-137 nebulae.

The spectra of such nebulae appear somewhat evolved from that seen in the younger pulsar wind nebulae as a cut off begins to be observed as in the case of the Vela X (see section 4.2.1) and HESS J1825-137, nebulae which exhibit cutoffs in their spectra at 13.4 TeV and 2.7 TeV, respectively. The spectra seen in these sources are also less steep than their younger counterparts, with spectral indices ranging from -1.7 to -2.26 before the observed cut-offs in spectrum. It is however difficult to discuss the spectra of such objects because, as has been observed in the case of HESS J1825-137, the observed spectrum changes throughout the nebula. This is due to changes in the underlying electron and photon populations throughout the nebula which are responsible for the inverse Compton emission.

## 4.3 Old and Relic Pulsar Wind Nebulae

As we have seen, all the pulsar wind nebulae that are known to emit VHE $\gamma$-ray photons are associated with young, highly energetic progenitor pulsars and are also observed as pulsar wind nebulae in the X-ray regime. As pulsars age, the particle population that is injected into the surrounding nebula becomes less energetic. In addition, the particles injected earlier in the life of the pulsar have cooled because of the synchrotron emission which results in the production of the X-ray nebula. These more energetic electrons are responsible for the synchrotron emission observed in the X-ray regime and so are visible only close to the progenitor pulsar. In contrast, such energetic electrons are not needed for inverse Compton emission to occur in the TeV $\gamma$-ray regime and so the cooled electrons which are seen over a much greater area can create a larger nebula, as we have seen in the case of middle-aged pulsar wind nebulae.

In much older nebulae the young energetic electrons are no longer being replenished by a central progenitor pulsar and indeed, as the nebula may be offset during the process of inverse shock crushing discussed in Section 2.5.2, may not be present in the centre of the nebula. As a result of this, only the older electron population will be present and the oldest pulsar wind nebulae will only be visible through the inverse Compton emission in the TeV regime and so will not be seen in X-rays.

As a result these older or "relic" pulsar wind nebulae will be visible in the TeV $\gamma$-ray regime and many may be associated with unidentified "dark" sources from the HESS galactic plane survey [23]. Many of the sources discovered in this survey are as yet unidentified but have similar spectra (with a spectral index of between 2.1 and 2.5) and extension to known VHE $\gamma$-ray pulsar wind nebulae. However, they are not currently associated with known pulsar wind nebulae at other wavelengths and so it is possible that they represent "relic" pulsar wind nebulae consisting of an older electron population which is not being replenished by its progenitor pulsar.

One possible candidate "relic" pulsar wind nebula is the HESS dark source HESS J1614-518 [23] which is extended and has a power law spectral index of -2.46 which may be expected for a pulsar wind nebula which is no longer being replenished by its progenitor pulsar.

## 4.4 The Development of Known Pulsar Wind Nebulae

As we have seen, the emission seen in the VHE $\gamma$-ray regime from pulsar wind nebulae is characterised by a decaying power law and corresponds to inverse Compton emission of the relativistic electrons produced in the outer layers of the pulsar when they interact with ambient photons. As we now have knowledge of 23 confirmed and suspected pulsar wind nebulae, these nebulae can be studied in terms of the development of their spectra, size and luminosity.

It is also interesting to study the corresponding Synchrotron emission from these sources which, like the inverse Compton emission, is dependent on the underlying electron population of the nebula under investigation. In this Section the inverse

Compton emission generated in the TeV $\gamma$-ray regime has been compared to the 0.5 - 8 keV X-ray emission in each case. The drawback to this approach is that the X-ray emission is not produced by the same electron population as the VHE $\gamma$-ray emission as X-ray Synchrotron photons of $\approx$ keV energies are produced by electrons with typical energies of 10 TeV whereas 1 TeV photons generated by the inverse Compton process have typical progenitor electrons with energies closer to 5 TeV. In ideal circumstances a somewhat lower portion of the X-ray spectrum would thus be monitored (corresponding to electron energies of $\approx$100MeV); however, the 0.5 - 8 keV band is observed by both the Chandra and XMM-Newton satellites and so is the best synchrotron comparison available to the inverse Compton TeV $\gamma$-ray data.

### 4.4.1 Spectral Index

By studying the development of the spectral indices of these nebulae in the X-ray and VHE $\gamma$-ray regimes we can investigate the development of the underlying spectrum of the progenitor electron population. Theory suggests that the spectrum of the synchrotron emission observed in the X-ray will be related to the underlying spectrum of the electron population by the factor $\alpha = \frac{x-1}{2}$, where $\alpha$ is the spectral index of the radiation and $x$ is the spectral index of the electron energies (see Equation 1.8). This is because the energy of the photon produced is proportional to the square of the electron energy. The spectrum of the inverse Compton emission observed is also proportional to the square of the electron energy and so should be similarly dependent on the spectral index of the electron population. As a result, the energy spectrum observed in the TeV $\gamma$-ray regime should correlate with that seen in X-rays. A comparison of the spectral indices seen in X-rays and TeV $\gamma$-rays can be seen in Figure 4.26.

As we can see in Figure 4.26, no relationship is seen between the spectral indices seen in X-rays and TeV $\gamma$-rays, however due to the size of the error bars in the majority of the sources a link cannot be ruled out. The figure also shows that the spectral indices of TeV $\gamma$-ray observations do not vary much from a mean value of $2.2 \pm 0.1$. A direct relation of $\Gamma_X = \Gamma_\gamma$ which may be expected due to both inverse Compton and synchrotron radiation being dependent on a factor of $\gamma^2$ is not observed

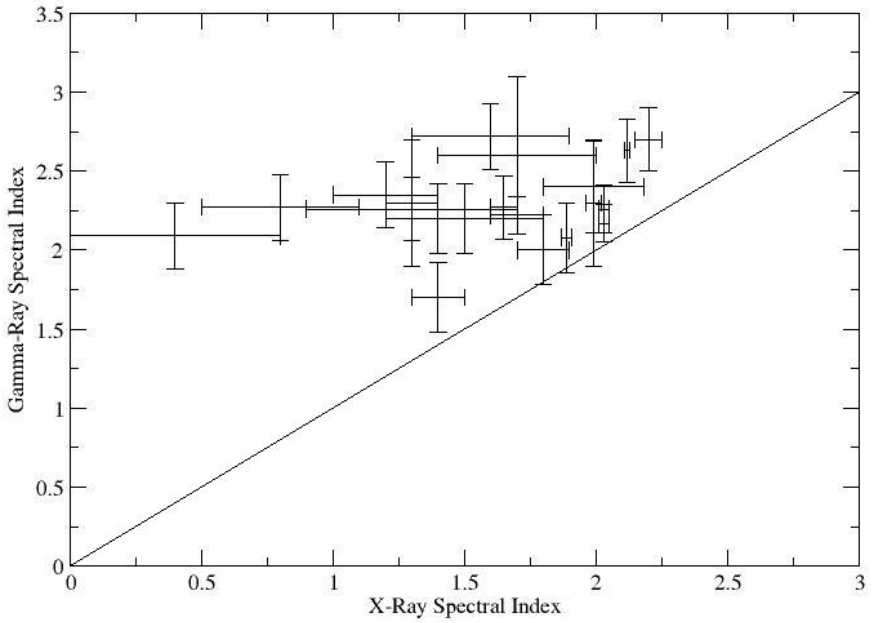


Figure 4.26: A comparison of the spectral indices of known pulsar wind nebulae that have been observed in the TeV $\gamma$-ray regime with the spectral indices of their X-ray counterparts. An expected direct correlation is overlaid on this plot but no such relation is seen.

with a reduced chi-squared for this relation of 13.8/18, which implies a good fit but the uncertainties observed in the spectral indices are too large to exclude other fits to the data. This is due to two factors dependent on the way in which each spectrum is measured. Firstly, the spectra calculated in the TeV $\gamma$-ray regime are taken over a much greater area than their X-ray counterparts due to the extension of many of the older pulsar wind nebulae in the TeV $\gamma$-ray regime. However, as most of the observed flux still comes from the central portion of the nebula, this will dominate the spectrum which obviates the effect. As a result, the other factor is much more important; the difference in energies of the underlying electron population, this means that the spectrum of the electron population observed in the TeV $\gamma$-ray regime is of lower energy than that observed in the X-ray regime. However, in all cases the the spectral index observed in $\gamma$-rays is greater than that observed in X-

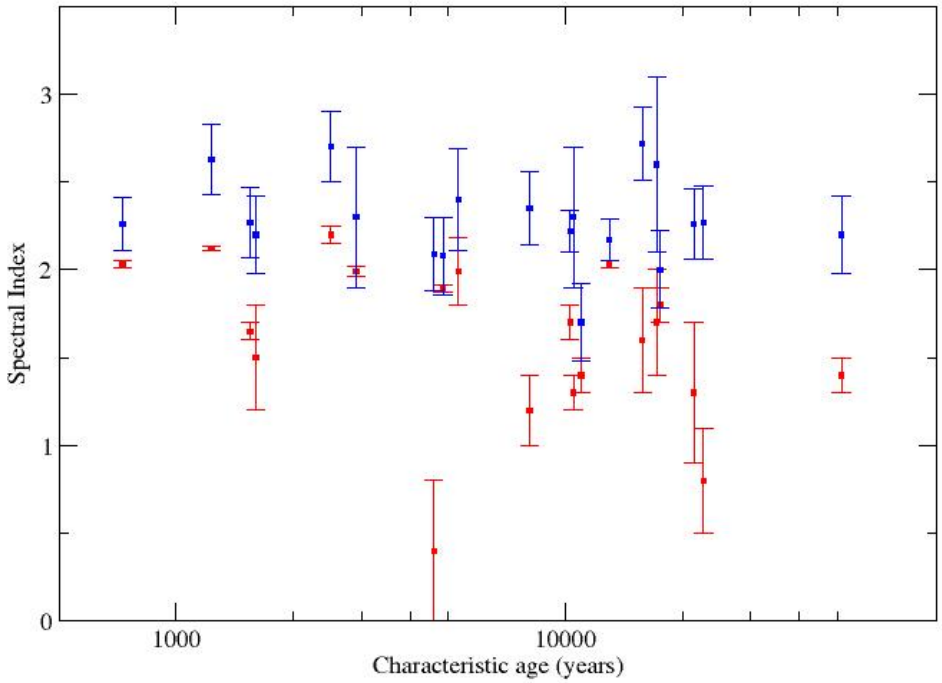


Figure 4.27: The development of spectral indices of known TeV pulsar wind nebulae (blue) and their X-ray counterparts (red) when compared to the characteristic age of their progenitor pulsars

rays. This implies a spectral break in the electron energy spectrum between the X-ray and TeV $\gamma$-ray populations.

It is also interesting to understand how these indices change with time. At the centre of the nebula adjacent to its progenitor pulsar the electron population of a PWN is being constantly replenished, as a result the observed spectrum in the central portion of the nebula is not expected to change. This should be seen in the X-ray regime as the only part of the pulsar wind nebula observed is in the central portion near the pulsar; the spectral index observed in this regime should not change significantly with time.

In the VHE $\gamma$-ray regime however the picture is more complex; when we observe in this regime we are looking at a lower energy electron population (typically of the

order of TeV rather than 10s of TeV), these electrons lose their energy more slowly than their higher energy counterparts they can be seen at a larger distance from the progenitor pulsar and so as we have seen a much larger pulsar wind nebula is seen in VHE $\gamma$-rays than is seen in X-rays. The aging electron population also results in a steepening in the power law observed in these nebulae as we move away from the progenitor pulsar as is seen in HESS J1825-137 [20] (see Section 4.2.3). Figure 4.27 shows the development of the spectral indices of known pulsar wind nebulae in order to assess the development of spectral index with time.

As we see in Figure 4.27, there is no dependence of spectral index with age in either regime with a reduced chi-squared around the mean of 4.45/20 and 2.46/22 in the X-ray and TeV $\gamma$-ray respectively; this is expected in X-rays for the reasons discussed earlier; the constant spectrum in the VHE $\gamma$-ray is probably due to the dominance of the luminosity of the more energetic younger portion of the nebula at its centre when compared to the older cooled electron population in its outskirts. This effect overwhelms any steepening of emission in the outer reaches of the nebula, this cannot be seen in most cases due to a lack of statistics, with the exception of HESS J1825-137 which is discussed in Section 4.2.3.

### 4.4.2 Size

As the pulsar wind nebulae observed in X-rays and VHE $\gamma$-rays are the products of different components of the electron population, it is reasonable to assume that the evolution of their size will not necessarily follow the same path. We expect the most energetic electrons to cool more quickly than their lower energy counterparts and so it can be reasonably expected that at ages greater than this cooling time the VHE $\gamma$-ray nebula will become larger than its X-ray counterpart.

As the lower energy electrons are less likely to be affected by cooling, the VHE $\gamma$-ray emission will continue to expand away from their progenitors into the surrounding medium. Analysis of the size of pulsar wind nebulae when compared to the characteristic age of its progenitor in this regime should reveal a positive correlation of expansion with age, at least for the timescales of known VHE $\gamma$-ray pulsar wind nebulae (which have ages of up to 50,000 years). A break in this increasing

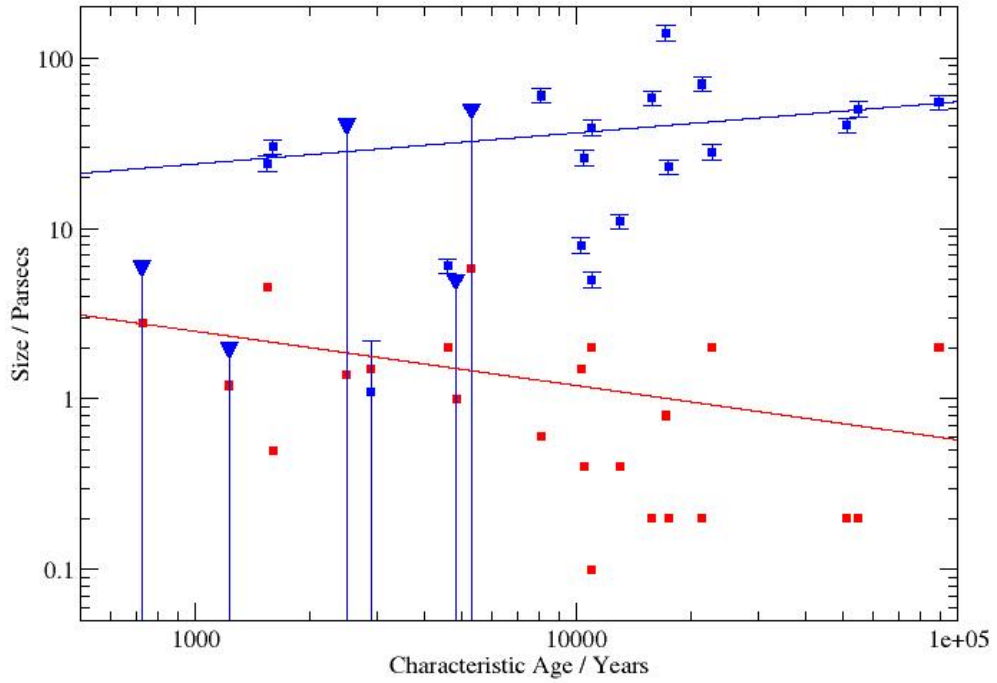


Figure 4.28: The development of the size of pulsar wind nebulae in the X-ray (red) and VHE $\gamma$-ray regimes (blue) when compared to their characteristic age. A best fit line of the form $Ax^B$ is given in each case and shows the expansion of the nebula in the $\gamma$-ray regime and a shrinking in the X-ray regime. Points denoted by triangles are upper limits to the extent of younger PWN observed in the TeV $\gamma$-ray regime where the nebulae appear as point sources to current instruments. The contraction observed in the X-ray follows the relation $L_X = 22.4 \text{ x } ^{-0.32\pm0.1}$ while in the VHE $\gamma$-ray regime a trend of $L_\gamma = 6.3 \text{ x } ^{0.36\pm0.1}$ is obtained.

trend is however expected to occur after a few thousand years when the reverse shock of the supernova remnant interacts with and crushes the central nebula (see Section 2.5.2). Once this has occurred expansion is expected to resume.

In contrast, the higher energy electrons which create the X-ray nebula will cool more rapidly and a smaller nebula is thus expected. If the level of energy injected into the nebula by the pulsar remained constant the nebula would soon expand to

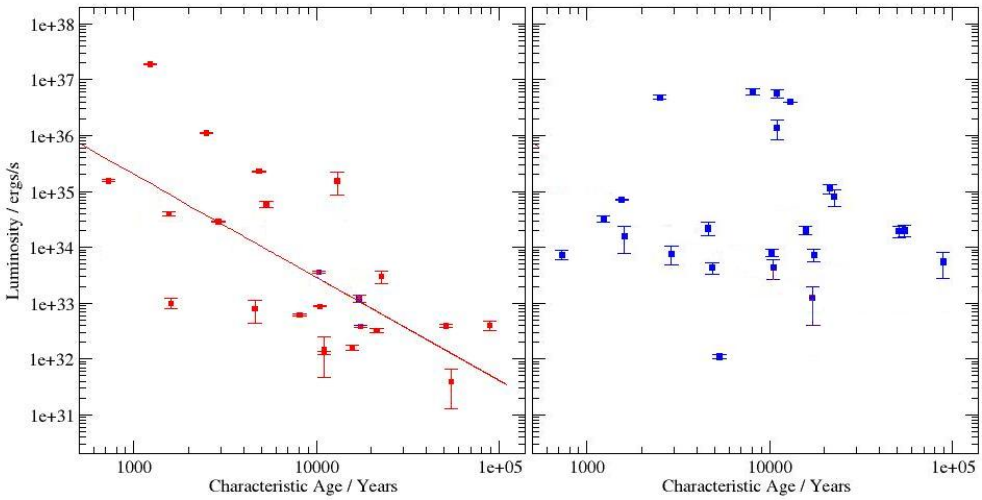


Figure 4.29: The development of the luminosity of pulsar wind nebulae in X-ray (red, left) and TeV $\gamma$-rays (blue, right) when compared to the characteristic ages of known pulsar wind nebulae observed in the TeV $\gamma$-ray regime. A power law fit is shown for the X-ray observations; no clear relationship is seen in the TeV $\gamma$-ray regime.

a equilibrium size. However, as a pulsar slows down the amount of energy that it injects into the surrounding nebula will also be reduced and this in turn will cause a reduction in the size of the pulsar wind nebula produced. The development of the pulsar wind nebulae in both X-rays and VHE $\gamma$-rays is seen in Figure 4.28.

As can be seen in Figure 4.28 the size of a pulsar wind nebula does indeed increase with age in the VHE $\gamma$-ray regime while decreasing in X-rays as expected. Both have been fit with a power law of the form L = A x $^{B}$ where A and B are variable constants, L is the luminosity of the source and x is the extent of the source, taken as the distance across its major axis. The contraction observed in the X-ray follows the relation $L_X$ = 22.4 x $^{-0.32\pm0.1}$ and shows a good fit with $\chi^2 = 28.3/21$. In the VHE $\gamma$-ray regime a trend of $L_\gamma$ = 6.3 x $^{0.36\pm0.1}$ is obtained which also shows a good fit with $\chi^2 = 18.7/21$.

### 4.4.3 Luminosity

Perhaps one of the most interesting factors to consider when investigating the evolutionary properties of a pulsar wind nebula is its luminosity. As was discussed in the previous section, the amount of energy input into the pulsar wind nebula by its progenitor pulsar decreases with age; this results in the contraction in size of the X-ray pulsar wind nebula but should also show a decrease in total luminosity as the amount of relativistic electrons producing synchrotron emission decreases. In the TeV $\gamma$-ray regime we expect the electrons which produce inverse Compton radiation to be more long lasting and so the reduction of power from the pulsar is compensated for by the accumulation of electrons over the life of the pulsar. A comparison of the characteristic age of the pulsar with the luminosities of known pulsar wind nebulae in X-rays and TeV $\gamma$-rays is given in Figure 4.29.

As can be seen in Figure 4.29 there is no clear relationship between the luminosity and characteristic age in the TeV $\gamma$-ray regime. In the X-ray regime however a power law relationship of the form $L = 7\times10^{40}t_c^{-1.8}$ is observed indicating a link between the age and the observed luminosity of X-ray pulsar wind nebulae with a correlation coefficient of 0.47. These results show the expected relationship also seen by similar observations by Mattana [150] which found an relationship between the luminosity of these PWN in the X-ray and their characteristic age while observing no relationship between the $\gamma$-ray luminosity and this parameter.

### 4.4.4 The Development of Pulsar Wind Nebulae in TeV $\gamma$-rays and X-rays

In this section I have attempted to study the development of pulsar wind nebulae which are observed in the TeV $\gamma$-ray regime by analysis of their observable properties, specifically their luminosity, size and spectral indices. Analysis of these properties in the TeV $\gamma$-ray regime shows that only the size of the observed nebula varies with time as the nebulae will continue to expand into their surrounding medium throughout their lifetime; the luminosity and spectral indices of the observed sources do not vary with time due to the dominance of the bright central portion of these nebulae

in determining these observed characteristics of the source.

In the X-ray regime an inverse dependence is seen between the characteristic age of the progenitor pulsar and both the luminosity and size of the nebula. This is because only young energetic electrons which have just been emitted by the progenitor pulsar are seen in this regime and so the loss of power with age of the pulsar is reflected in the observed properties of the pulsar wind nebula at these wavelengths.

Table 4.1: X-ray and TeV $\gamma$-ray properties of all known young pulsar wind nebulae seen in the TeV $\gamma$-ray regime. Some data taken from [128]

| Name | X-ray Luminosity ergs/s $\times 10^{34}$ | X-ray Spectral Index | X-ray Extent pc | $\gamma$-ray Luminosity ergs/s $\times 10^{34}$ | $\gamma$-ray Spectral Index | $\gamma$-ray Extent pc | ref |
|---|---|---|---|---|---|---|---|
| Crab | 1910 ± 43 | 2.12 ± 0.01 | 1.2 | 3.23 ± 0.42 | 2.31 ± 0.2 | < 2 | [17] |
| N157B | 112 ± 3 | 2.20 ± 0.05 | 1.4 | 490 ± 40 | 2.7 ± 0.2 | < 41 | [54] |
| G292.2-0.5 | 0.1 ± 0.02 | 1.5 ± 0.3 | 0.5 | 1.58 ± 0.79 | <2.2 | 30 | [177] |
| MSH15-52 | 3.98 ± 0.27 | 1.65 ± 0.05 | 4.5 | 7.24 ± 0.18 | 2.27 ± 0.2 | 24 | [12] [75] |
| G0.9+0.1 | 6.0 ± 0.8 | 1.99 ± 0.19 | 5.8 | 0.011 ± 0.001 | 2.40 ± 0.29 | <50 | [49] [15] |
| G12.8-0.0 | 0.079 ± 0.035 | 0.4 ± 0.4 | 2 | 2.18 ± 0.60 | 2.09 ± 0.21 | 6 | [23] [101] |
| G21.5-0.9 | 22.9 ± 0.52 | 1.89 ± 0.02 | 1 | 0.43 ± 0.10 | 2.08 ± 0.22 | <5 | [43] [72] |
| Kes 75 | 15.5 ± 0.7 | 2.03 ± 0.02 | 2.8 | 0.74 ± 0.14 | 2.26 ± 0.15 | <6 | [187] [156] |
| G54.1+0.3 | 2.88 ± 0.066 | 1.99 ± 0.03 | 1.5 | 0.76 ± 0.28 | 2.3 ± 0.4 | <11 | [141] [6] |

Table 4.2: Properties of the progenitor pulsars of all known young pulsar wind nebulae observed in the TeV $\gamma$-ray regime [144].

| PWN | Associated Pulsar | Right Ascension $^\circ$ | Declination $^\circ$ | Distance kpc | Period ms | Period Derivative s/s $\times 10^{-14}$ | Char Age years | Spindown Luminosity ergs/s $\times 10^{36}$ | Surface B field TG | |
|---|---|---|---|---|---|---|---|---|---|---|
| Crab | B0531+21 | 83.83 | 22.01 | 2.00 | 33 | 42.1 | 1,230 | 457 | 3.78 | [151] [34] |
| N157B | J0537-6910 | 84.45 | -69.17 | 48 | 16 | 5.18 | 2,500 | 470 | 92.5 | [192] [149] |
| G292.2-0.5 | J1119-6127 | 169.81 | -61.46 | 8.40 | 408 | 402 | 1,600 | 2.3 | 0.41 | [47] [145] |
| MSH15-52 | B1509-58 | 228.48 | -59.14 | 5 | 155 | 180 | 1,550 | 18 | 0.15 | [132] [179] |
| G0.9+0.1 | J1747-2809 | 266.84 | -28.12 | 17.55 | 52 | 15.6 | 5,310 | 43 | 2.88 | [49] |
| G12.8-0.0 | J1813-1749 | 273.40 | -17.83 | | 44.7 | 15.0 | 4,600 | 68.0 | 2.65 | [94] |
| G21.5-0.9 | J1833-1034 | 278.39 | -10.57 | | 61.9 | 20.0 | 4,850 | 34.0 | 3.58 | [50] |
| Kes 75 | J1846-0258 | 281.60 | -2.98 | | 326 | 708 | 728 | 8.12 | 4.86 | [100] [135] |
| G54.1+0.3 | J1930+1852 | 292.63 | 18.87 | 5 | 137 | 75.1 | 2,900 | 12.0 | 1.03 | [48] [141] |

Table 4.3: The X-ray and TeV $\gamma$-ray properties of all known middle aged pulsar wind nebulae observed in the TeV $\gamma$-ray regime. Some data taken from [128]

| Name | X-ray Luminosity ergs/s $\times 10^{34}$ | X-ray Spectral Index | X-ray Extent pc | $\gamma$-ray Luminosity ergs/s $\times 10^{34}$ | $\gamma$-ray Spectral Index | $\gamma$-ray Extent pc | ref |
|---|---|---|---|---|---|---|---|
| Vela X | 0.0129 ± 0.00086 | 1.4 ± 0.1 | 0.1 | 138 ± 55 | 1.45 ± 0.22 | 5 | [146] [22] |
| G304.6+0.1 | 0.0145 ± 0.0099 | | 2 | 575 ± 97 | 2.44 ± 0.21 | 39 | [14] |
| Rabbit | 0.355 ± 0.016 | 1.7 ± 0.1 | 1.5 | 0.81 ± 0.12 | 2.22 ± 0.12 | 8 | [19] |
| Kookaburra | 15.5 ± 7.0 | 2.03 ± 0.02 | 0.4 | 398 ± 0.59 | 2.17 ± 0.12 | 11 | [188] [19] |
| G332.5-0.3 | 0.0617 ± 0.0028 | 1.2 ± 0.2 | 0.6 | 603 ± 78 | 2.35 ± 0.21 | 60 | [129] [23] |
| G344.7-0.1 | 0.00398 ± 0.00272 | | 0.2 | 2.00 ± 0.45 | 2.31 ± 0.23 | 50 | [23] |
| G343.1-2.3 | 0.0380 ± 0.0017 | 1.8 ± 0.1 | 0.2 | 0.74 ± 0.19 | 2 ± 0.22 | 23 | [174] [115] |
| G349.0-0.4 | 0.0398 ± 0.0082 | 1.9 ± 0.2 | 2 | 0.55 ± 0.27 | 0.7 ± 0.6 | 7 | [111] [25] |
| HESSJ1804-216 | 0.016 ± 0.002 | 1.6 ± 0.3 | 0.2 | 2.00 ± 0.34 | 2.72 ± 0.21 | 58 | [23] |
| G11.1-1.0 | 0.039 ± 0.003 | 1.4 ± 0.1 | 0.2 | 1.95 ± 0.44 | 2.2 ± 0.22 | 40 | [127] [25] |
| HESSJ1825-137 | 0.032 ± 0.003 | 1.3 ± 0.4 | 0.2 | 11.2 ± 2.3 | 2.26 ± 0.2 | 70 | [85] [16] |
| HESSJ1837-069 | 0.30 ± 0.08 | 0.8 ± 0.3 | 2 | 8.13 ± 2.76 | 2.27 ± 0.21 | 28 | [93] [147] |
| G75.2+0.1 | 0.12 ± 0.018 | 1.7 ± 0.3 | 0.8 | 0.12 ± 0.08 | 2.6 | 140 | [103] [1] |
| G106.6+2.9 | 0.087 ± 0.002 | 1.3 ± 0.1 | 0.4 | 0.43 ± 0.16 | 2.3 ± 0.4 | 26 | [97] [121] |

Table 4.4: The properties of the progenitor pulsars of all known middle aged pulsar wind nebulae observed in the TeV $\gamma$-ray regime. [144]

| PWN | Associated Pulsar | Right Ascension $^\circ$ | Declination $^\circ$ | Distance kpc | Period ms | Period Derivative s/s $\times 10^{-14}$ | Char Age years | Spindown Luminosity ergs/s $\times 10^{36}$ | Surface B field TG | |
|---|---|---|---|---|---|---|---|---|---|---|
| Vela | B0833-45 | 128.84 | -45.17 | 0.29 | 89 | 12.5 | 11,000 | 6.9 | 3.38 | [136] [73] |
| G304.6+0.1 | J1301-6305 | 195.44 | -63.08 | 15.84 | 185 | 26.7 | 11,000 | 1.7 | 7.10 | [145] |
| Rabbit | J1418-6058 | 214.68 | -60.97 | | 111 | 17.0 | 10,300 | 5.0 | 4.38 | [3] |
| Kookaburra | J1420-6048 | 215.03 | -60.80 | 7.69 | 68 | 8.32 | 13,000 | 10 | 2.41 | [61] |
| G332.5+0.3 | J1617-5055 | 244.37 | -50.92 | 6.46 | 69 | 13.5 | 8100 | 16.0 | 3.10 | [130] |
| G344.7-0.1 | J1702-4128 | 255.72 | -41.47 | 5.18 | 182 | 5.23 | 55,000 | 0.34 | 3.12 | [133] |
| G343.1+2.3 | B1706-44 | 257.4 | -44.48 | 1.82 | 102 | 9.30 | 17,500 | 3.4 | 3.12 | [125] [191] |
| G349.0+0.4 | J1718-3825 | 259.56 | -38.42 | 4.24 | 75 | 1.32 | 89,500 | 1.3 | 1.01 | [145] |
| HESSJ1804-216 | B1800-21 | 270.96 | -21.62 | 3.94 | 134 | 13.4 | 15,800 | 2.2 | 4.29 | [113] [58] |
| G11.1-1.0 | J1809-1917 | 272.43 | -19.29 | 3.71 | 83 | 2.55 | 51,300 | 1.8 | 1.47 | [154] |
| HESSJ1825-137 | B1823-13 | 276.56 | -13.57 | 4.12 | 101 | 5.51 | 21,400 | 2.8 | 2.80 | [58] [113] |
| HESSJ1837-069 | J1838-0655 | 279.51 | -6.92 | ? | 70 | 4.93 | 22,700 | 5.5 | 1.89 | [93] |
| G75.2+0.1 | J2021+3651 | 305.27 | 36.85 | 18.88 | 104 | 9.5 | 17,200 | 3.4 | 3.19 | [4] [103] |
| G106.6+2.9 | J2229+6114 | 337.27 | 61.23 | 12 | 52 | 7.83 | 10,500 | 22.0 | 2.03 | [97] |

# Chapter 5

# $\gamma$-ray Upper Limits of X-ray Selected Pulsar Wind Nebulae

As has been seen, all known pulsar wind nebulae that emit in the TeV $\gamma$-ray regime are also seen as X-ray sources. Many other pulsar wind nebulae have been observed in X-rays and it is expected that all pulsar wind nebulae that are observed in the X-ray regime will be associated with inverse Compton emission of some kind and so are expected to be seen as VHE $\gamma$-ray sources. In this Chapter I used archival HESS data to study X-ray observed pulsar wind nebulae to investigate if it was possible to detect any new sources in the VHE $\gamma$-ray regime. The sources were not detected as distinct objects and so limits on their parameters using the data obtained.

## 5.1 X-ray selection of targets

As has been discussed previously after a few thousand years of expansion, pulsar wind nebulae consist mostly of older, less energetic electrons with younger electron populations only being present near the source pulsar where they are replenished. The young electrons create a small synchrotron nebula around the pulsar which is visible in X-rays. In contrast, a much larger nebula is revealed in the TeV regime. This nebula is thought to be generated by inverse Compton boosting of the cosmic microwave background [19] as there is no longer a source of synchrotron electrons to allow synchrotron self Compton photons to be created, such as occurs in some of

the younger nebulae such as the Crab [17].

As X-ray pulsar wind nebulae are in general quite small it is necessary to use an X-ray instrument of good angular resolution to resolve them and properly distinguish them from point sources which may appear to be extended as a result of the PSF of an instrument. Of the current generation of X-ray satellites the *Chandra* observatory has the best angular resolution and so I have chosen this instrument to identify pulsar wind nebulae for which upper limits will be calculated. Kargaltsev and Pavlov [128] provides a catalogue of known PWNe that have been detected by *Chandra* which are shown in Tables 5.1 and 5.2; however, some additional nebulae (The Eel [169] and G7.4-2.0 [45]) have been observed using *Chandra* but were not included in Kargaltsev and Pavlov [128] and so have been added to the target list and marked where appropriate.

The combination of Kargaltsev and Pavlov [128] and the additional targets into Tables 5.1 and 5.2 provides a catalogue of 56 nebulae that have been observed by *Chandra*, of which all but 17 have identified progenitor pulsars associated with them. Of these, ten (see Tables 5.1 and 5.2) have been confirmed as pulsar wind nebulae in the TeV waveband and are the subject of previous publications, while a further 13 (see Tables 5.1 and 5.2) of the sources have been associated with known TeV gamma-ray objects, although this emission has not been conclusively proven as being associated with the pulsar wind nebulae, these 23 sources were used to investigate the development of pulsar wind nebulae in Section 4.4. Ten of the targets currently have no usable HESS observations; the majority of the unobserved sources are located in the northern hemisphere and are too far north for observation with HESS. Some of the sources, such as IC443 [7] have not been observed as pulsar wind nebulae but as supernova remnants whose emission would be indistingushable in the TeV $\gamma$-ray regime and so have not been included in this analysis.

This Chapter provides analyses for the remaining seventeen PWNe in the catalogue for which archival HESS data are available, with a total observation time of over 450 hours. As the size of PWN varies depending on their age, in this work upper limits have been calculated for a point like source ($\theta = 0.1$) coincident with the X-ray position of the pulsar as well as an extended source ($\theta = 0.22$) to allow for

Table 5.1: Known X-ray PWNe as observed by Chandra taken from [128] with the exception of the objects marked ⋆. Where an object has been the subject of previous TeV observations the reference for these observations is given, otherwise the table indicates if these objects have had upper limits calculated for them in this paper or if they are the subject of another HESS campaign. Some of the sources are too far north to be observed, declinations of above about 20° are difficult to see from the position of the HESS site. D⋆ is the distance to the nebula under investigation in kPc. Part 1 - PWN with 0 < RA < 250, continued in table 5.2.

| Name | Pulsar | RA ° | Dec ° | D⋆ | status |
|---|---|---|---|---|---|
| CTA1 | | 1.76 | 73.05 | 1.4 | Too Far North |
| 3C58 | J0205+6449 | 31.41 | 64.83 | | Too Far North |
| Mushroom | B0355+54 | 59.72 | 54.22 | 1.04 | Too Far North |
| Crab | B0531+21 | 83.63 | 22.01 | 2 | Confirmed PWN [17] |
| N157B | J0537-6910 | 84.45 | -69.17 | 50 | Suspected PWN |
| N158A | B0540-69 | 85.05 | -69.33 | 50 | - |
| G180.0-1.7 | J0538+2817 | 84.6 | 28.29 | 1.47 | Upper Limit |
| IC443 | | 94.52 | 22.46 | 1.5 | Observed as SNR [33] |
| Geminga | J0633+1746 | 98.48 | 17.77 | 0.25 | Upper Limit |
| G230.39-1.42 | J0729-1448 | 112.32 | -14.81 | 4 | - |
| Vela X | B0833-45 | 128.84 | -45.18 | 0.29 | Confirmed PWN [22] |
| G287.4+0.6 | B1046-58 | 162.05 | -58.53 | 3 | Upper Limit |
| MSH11-62 | | 167.95 | -60.66 | 1 | Upper Limit |
| G284.3-1.8 | J1016-585 | 154.09 | -58.95 | 3 | - |
| G292.2-0.5 | J1119-6127 | 169.81 | -61.46 | 8.4 | Candidate PWN [177] |
| MSH11-54 | J1124-5916 | 171.16 | -59.27 | 6 | Upper Limit |
| G293.8+0.6 | | 173.75 | -60.9 | 2 | Upper Limit |
| G304.6+0.1 | J1303-6305 | 195.44 | -63.09 | 7 | Candidate PWN [14] |
| G309.92-2.51 | J1357-6429 | 209.26 | -64.49 | 2.5 | Candidate PWN [167] |
| Rabbit | | 214.68 | -60.97 | 5 | Confirmed PWN [19] |
| Kookaburra | J1420-6048 | 215.03 | -60.8 | 5.6 | Confirmed PWN [19] |
| G319.97-0.62 | J1509-5850 | 227.36 | -58.85 | 4 | Observed as FVW |
| MSH15-52 | B1509-58 | 228.48 | -59.14 | 5 | Confirmed PWN [12] |
| MSH15-56 | | 238.25 | -56.2 | 4 | Upper Limit |
| G327.1-1.1 | | 238.6 | -55 09 | 7 | Upper Limit |
| G332.5-0.3 | J1617-5055 | 244.37 | -50.92 | 6.5 | Candidate PWN [11] |

Table 5.2: A continuation of Table 5.1. Part 2 - PWNN with 250 < RA < 360.

| Name | Pulsar | RA ° | Dec ° | D⋆ | status |
|---|---|---|---|---|---|
| G344.7-0.1 | J1702-4128 | 255.72 | -41.48 | 5 | Candidate PWN [28] [23] |
| G343.1-2.3 | B1706-44 | 257.43 | -44.49 | 2 | Candidate PWN [115] |
| G349.0-0.4 | J1718-385 | 259.56 | -38.42 | 4 | Candidate PWN [25] |
| G34.01+20.27 | J1740+1000 | 265.11 | 10 | | Upper Limit |
| Mouse | J1747-2958 | 266.82 | -29.97 | 5 | - |
| G0.9+0.1 | | 266.85 | -28.15 | 10 | Confirmed PWN [15] |
| Duck | B1757-24 | 270 | -24.86 | 5 | Upper Limit |
| G8.40+0.15 | B1800-21 | 270.96 | -21.62 | 4 | Candidate PWN [23] |
| G11.1-1.0 | J1809-1917 | 272.43 | -19.29 | 3.5 | Candidate PWN [25] |
| G7.4-2.0 ⋆ | | 272.45 | -32.2 | 1.7 | Upper Limit |
| G11.2-0.3 | J1811-1925 | 272.87 | -19.42 | 5 | Upper Limit |
| G12.8-0.0 | | 273.37 | -17.84 | 4.5 | Candidate PWN [11] |
| G16.7+0.1 | | 275.24 | -14.34 | 10 | Upper Limit |
| Eel ⋆ | | 276.54 | -12.95 | | Upper Limit |
| HESSJ1825-137 | B1823-13 | 276.55 | -13.58 | 4 | Confirmed PWN [20] |
| G21.5-0.9 | J1833-1034 | 278.39 | -10.57 | 4.7 | Confirmed PWN [65] |
| G25.24-0.19 | | 279.5 | -6.93 | 10 | Candidate PWN [11] |
| Kes75 | J1846-0258 | 281.6 | -2.98 | 19 | Confirmed PWN [187] |
| G34.7-0.4 | B1853+01 | 284.04 | 1.23 | 3 | - |
| G39.2-0.3 | | 286.02 | 5.45 | | Upper Limit |
| G54.1+0.3 | J1930+1852 | 292.63 | 18.87 | 5 | Candidate PWN [6] |
| G47.38-3.88 | B1929+10 | 293.06 | 10.99 | 0.36 | Upper Limit |
| DA495 | | 298.08 | 29.43 | 1.5 | To Far North |
| CTB80 | B1951+32 | 298.24 | 32.88 | 2.5 | Upper Limit |
| G59.20-4.70 | B1957+20 | 299.9 | 20.8 | 2.5 | - |
| CTB87 | | 304.01 | 37.2 | 6 | To Far North |
| G75.23+0.12 | J2021+3651 | 305.27 | 36.86 | 4 | Candidate PWN [1] |
| G10.93-45.44 | J2124-3358 | 321.18 | -33.98 | 0.25 | Upper Limit |
| Guitar | B2224+65 | 336.47 | 65.59 | 1 | To Far North |
| G106.3+2.7 | J2229+6114 | 337.27 | 61.24 | 3 | Candidate PWN [121] |

the investigation of both old and young PWN as both source types appear as compact nebulae surrounding the central progenitor pulsar in X-rays (although their age could be estimated from observations of the pulsar where these exist). Where observations in each individual case indicate that an older or younger pulsar wind nebula should be expected this is discussed along with analysis of that target. Although an offset is expected for older extended pulsar wind nebulae this is not accounted for in this analysis, as the direction in which this offset will occur is unknown. In addition, a point-like cut will allow a direct comparison between the smaller X-ray source and the $\gamma$-ray emission generated by the same particle population.

## 5.2 HESS significances and Upper Limits

The standard HESS analysis (as discussed in Chapter 3) [17] was used to calculate the significance and flux upper limits for the PWN listed (see Tables 5.1 and 5.2) which had not been the subject of previous HESS publications and for which archival data were available. The statistical significances are calculated using the method detailed in Li and Ma [138] while the upper limits use the Feldman-Cousins method [78] (these methods are covered in more detail in Chapter 3). These values are presented in Table 5.3 for a point source analysis and in Table 5.4 for an extended region analysis. To obtain upper limits an assumed spectrum of $E^{-2.2}$ was used, which is the mean spectrum for the confirmed TeV emitting pulsar wind nebulae of all ages listed in Tables 5.1 and 5.2.

Most of the observed nebulae show no significant VHE $\gamma$-ray signal. The highest statistical significances are from sources which can be shown as being contaminated by adjacent sources which are discussed in more detail below; the distribution of significances of the remaining targets is shown in Figure 5.1 for a point-like region analysis and for an extended region analysis. This shows a distribution of significance around zero for the sources for which upper limits have been calculated with an average of 0.6 $\sigma$ for a point-like analysis. A broader distribution is seen in the case of extended analysis with a average of -0.2 $\sigma$. If we use the on and off axis counts to calculate the significance for all runs, taking into account for the longer

Table 5.3: Upper limits and the statistical significances for unpublished PWNe in the catalogue for which HESS data is available derived assuming a point source around the central target ($\theta^2$=0.01). Upper limits are given above a 1 TeV threshold for each source with the exception of G180.0-1.7 (marked †) which was observed at a high zenith angle, giving an energy threshold of 1.26 TeV. All calculations assume an $E^{-2.2}$ spectrum. The targets marked ⋆ overlap other extended $\gamma$-ray sources and as such any emission present cannot be distinguished from those sources.

| Name | time hours | $N_{on}$ | $N_{off}$ | alpha | Upper Limit ($10^{-13}$/cm$^2$/s) | $\sigma$ |
|---|---|---|---|---|---|---|
| G180.0-1.7 † | 3.6 | 44 | 813 | 0.053 | 5.16 | 0.10 |
| Geminga | 9.3 | 83 | 1944 | 0.043 | 3.03 | -0.11 |
| G287.4+0.6 | 24.5 | 140 | 3093 | 0.041 | 3.35 | 1.13 |
| MSH11-62 | 25.5 | 195 | 5989 | 0.032 | 2.84 | 0.19 |
| MSH11-54 | 23.3 | 174 | 4962 | 0.030 | 5.18 | 1.80 |
| G293.8+0.6 | 12.9 | 95 | 4549 | 0.023 | 2.56 | -1.11 |
| MSH15-56 | 15.4 | 53 | 2115 | 0.024 | 4.75 | 0.27 |
| G327.1-1.1 | 7.3 | 56 | 1035 | | 4.08 | 0.25 |
| G34.01+20.27 | 4.5 | 45 | 825 | 0.053 | 4.94 | 0.16 |
| Duck | 53.41 | 194 | 7879 | 0.027 | 1.09 | -1.46 |
| G7.4-2.0 | 2.19 | 8 | 310 | 0.014 | 38.20 | 1.49 |
| G11.2-0.3 ⋆ | 50.9 | 257 | 5177 | 0.039 | 3.55 | 3.49 |
| G16.7+0.1 ⋆ | 62.0 | 295 | 6236 | 0.042 | 2.12 | 1.93 |
| G18.5-0.4 ⋆ | 94.0 | 424 | 14169 | 0.021 | 5.88 | 6.55 |
| G39.2-0.32 | 51.9 | 355 | 9038 | 0.034 | 2.96 | 2.74 |
| G47.38-3.88 | 1.77 | 14 | 304 | 0.043 | 7.89 | 0.21 |
| G10.93-45.44 | 4.40 | 28 | 476 | 0.053 | 5.68 | 0.50 |

Table 5.4: Upper limits and the statistical significances for unpublished PWNe in the catalogue for which HESS data is available derived assuming an extended analysis region around the central X-ray target ($\theta^2$=0.0484) . Upper limits are given above a 1 TeV threshold for each source with the exception of G180.0-1.7 (marked †) which was observed at a high zenith angle, giving an energy threshold of 1.26 TeV. All calculations assume an $E^{-2.2}$ spectrum. The targets marked ⋆ overlap other extended $\gamma$-ray sources and as such any emission present cannot be distinguished from those sources.

| Name | time hours | $N_{on}$ | $N_{off}$ | alpha | Upper Limit ($10^{-13}$/cm$^2$/s) | $\sigma$ |
|---|---|---|---|---|---|---|
| G180.0-1.7 † | 3.6 | 226 | 1456 | 0.144 | 16.47 | 1.07 |
| Geminga | 9.3 | 399 | 3927 | 0.103 | 6.27 | -0.34 |
| G287.4+0.6 | 22.8 | 666 | 5592 | 0.114 | 7.65 | 1.14 |
| MSH11-62 | 24.6 | 906 | 12014 | 0.077 | 4.95 | -0.52 |
| MSH11-54 | 23.3 | 756 | 9747 | 0.081 | 5.18 | 1.80 |
| G293.8+0.6 | 12.9 | 477 | 9186 | 0.062 | 2.39 | -3.73 |
| MSH15-56 | 11.5 | 236 | 4418 | 0.061 | 3.93 | -1.97 |
| G327.1-1.1 | 7.3 | 271 | 2155 | 0.112 | 10.94 | 0.77 |
| G34.01+20.27 | 4.5 | 221 | 1490 | 0.144 | 12.61 | 0.44 |
| Duck | 50.8 | 938 | 15601 | 0.068 | 1.13 | -3.94 |
| G7.4-2.0 | 2.19 | 31 | 705 | 0.031 | 66.28 | 1.77 |
| G11.2-0.3 ⋆ | 48.32 | 1142 | 10368 | 0.091 | 11.37 | 6.04 |
| G16.7+0.1 ⋆ | 61.6 | 1397 | 11975 | 0.106 | 6.45 | 3.48 |
| G18.5-0.4 ⋆ | 93.1 | 1869 | 28836 | 0.057 | 11.39 | 5.38 |
| G39.2-0.32 | 51.9 | 1611 | 17985 | 0.083 | 6.90 | 3.03 |
| G47.38-3.88 | 1.77 | 65 | 659 | 0.098 | 16.70 | 0.08 |
| G10.93-45.44 | 4.40 | 123 | 837 | 0.144 | 11.41 | 0.23 |

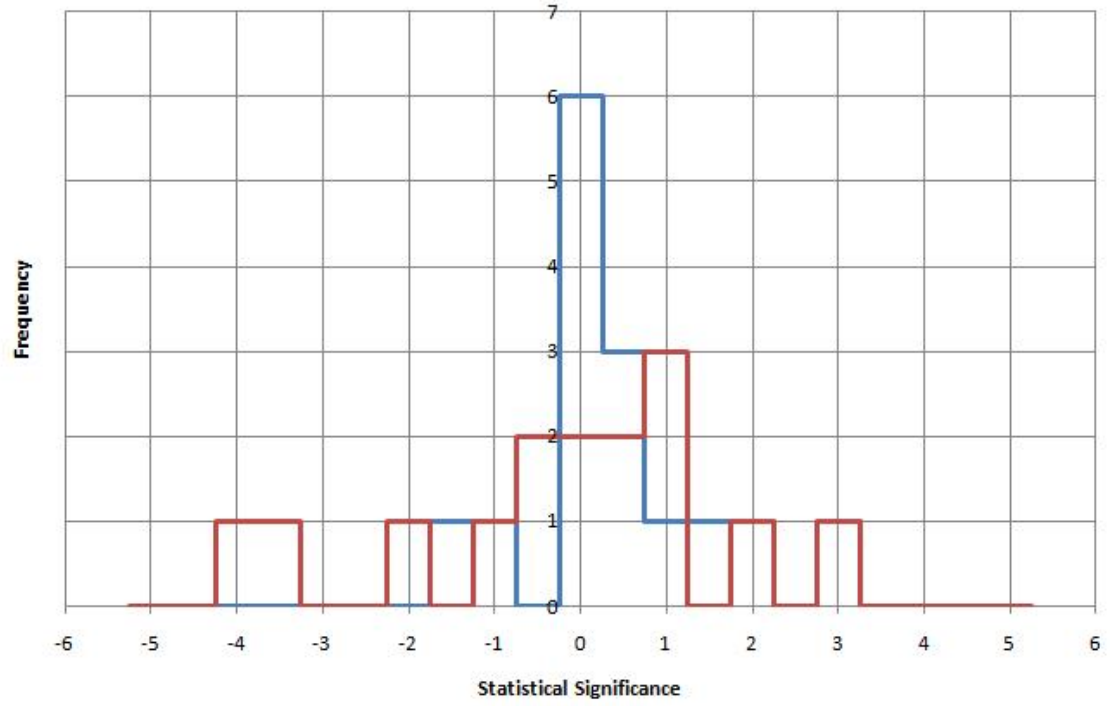


Figure 5.1: The significance distribution for the PWNe for which Upper Limits have been obtained for a pointlike (blue) and extended (red) analysis. Most of the targets have significances clustered around 0, a broader distribution is seen for the extended analysis.

observation times of some of the sources, we obtain significances of 2.2 $\sigma$ and 2.3 $\sigma$ for an extended and point-like analysis respectively. This shows no conclusive proof for a positive bias in the significance of this group of sources.

No significant outlier is observed in this dataset and due to its discrete nature it is entirely consistent with a distribution centred around 0. The highest significance comes from the analysis of G39.2-0.3 which has a statistical significance of $\approx 3\ \sigma$ in both a pointlike and extended analysis. Each of the objects analysed is discussed in Section 5.5 below and where appropriate compared to predictions made later in this Chapter.

## 5.3 Relation of X-ray flux to $\gamma$-ray flux

X-ray observations of the target pulsar wind nebulae have been used in conjunction with the method presented by de Jager [67] to obtain predictions of $\gamma$-ray flux.

Where a magnetic field strength estimate is provided in the relevant X-ray observation paper, this value is used; otherwise the equipartition method of [67] is used to estimate the value of the magnetic field strength. The $\gamma$-ray flux predictions are then compared to the derived upper limit for a point source calculated above 1 TeV (the point source limit is used in this case so that it can be compared directly to the area of the sky viewed in the X-ray regime). This approach was taken as it allows the flux in the $\gamma$-ray to be predicted from X-ray observations rather than from the parameters of the assumed progenitor pulsar wind nebula. As a result, the PWN which have not been associated with a progenitor can be included in the analysis and thus a consistent analysis can be applied across all of the sources observed. These predictions are shown in Table 5.5. The derived fluxes are given above an energy threshold of 1 TeV. As many of the most well established X-ray pulsar wind nebula have now been observed in the TeV $\gamma$-ray regime many of the sources under investigation in this Chapter are less well observed and as such less likely to be associated with a known progenitor.

The de Jager model [67] uses the X-ray spectrum to predict the electron energy spectrum from which the $\gamma$-ray spectrum can be obtained. However, the X-ray synchrotron emission is also dependent on the strength of the magnetic field in the nebula while the inverse Compton emission is dependent on the level of background photons present. As a result, if the strength of the magnetic field and the X-ray flux are known we can calculate the minimum $\gamma$-ray flux if the X-ray flux is known by using the following equation [67]:

$$F_{1TeV} = \frac{6.6 \times 10^{-17}(1.4 \times 10^{-5})^{a_x} e^{2.2a_x - 0.126a_x^2} F_{1keV}}{B^{a_x+1}} \tag{5.1}$$

Where $F_{1TeV}$ and $F_{1keV}$ are the monochromatic fluxes in photons/cm$^2$/s at 1 TeV and 1 keV respectively, $B$ is the magnetic field strength in the nebula and $a_x$ is the spectral index of the X-ray nebula. This value is a minimum because it assumes that the only source of photons for inverse Compton boosting is the microwave background radiation. In reality the $\gamma$-ray flux may be much larger than this as there may be twice as many background photons present in the synchrotron nebula, even without requiring synchrotron self Compton effects such as those seen in the

Crab Nebula. This is due to the presence of other sources of background radiation such as ambient starlight.

By inverting the synchrotron spectrum and using it to predict the inverse Compton spectrum observed de Jager [67] shows that the observed TeV $\gamma$-ray flux ($S_\gamma$) scales as $S_\gamma \propto B^{-\Gamma}$ where $\Gamma$ is the spectral index of the observed X-ray emission and B is the magnetic field strength of the nebula. As we can see, the magnetic field strength is very important to the calculation of the $\gamma$-ray flux from the observed X-ray flux.

However, in many cases the magnetic field strength is not known and so it has to be assumed that the nebula is in equipartition close to the progenitor pulsar. This assumes that the energy in the system is split equally between its magnetic field and the thermal energy in its particle population, which in this case can be calculated from the observed X-ray flux using the relation:

$$B_{eq} = 1.8 \times 10^{-4} \left( \frac{0.038^{a_x} F_{1keV} k}{\theta d \alpha (2a_x - 1)} \right)^{\frac{2}{7}} \tag{5.2}$$

Where $B_{eq}$ is the strength of the magnetic field assuming equipartition, $\theta$ is half the diameter of the pulsar wind nebula seen in X-rays in arcminutes and $d$ is the distance to the nebula. The factor $k = E_{min}^{\frac{1-2a_x}{2}} - E_{max}^{\frac{1-2a_x}{2}}$ where $E_{min}$ and $E_{max}$ are the minimum and maximum energies for which the X-ray energy spectrum is valid. The factor

$$\alpha = 2^{a_x - 1} \frac{a_x + 5/3}{a_x + 1} \Gamma\left(\frac{3a_x + 1}{6}\right) \Gamma\left(\frac{3a_x + 2}{6}\right) \tag{5.3}$$

is based on the kinetic energy spectrum and is used to describe the underlying electron population. In assuming that the nebula is in equipartition in the area immediately surrounding the pulsar which corresponds to the X-ray nebula we make the assumption that energy can be transferred between the magnetic field and the particle population and that enough time has elapsed for these values to equalize. This is not unreasonable for the older nebulae under investigation; in these cases the area immediately surrounding the nebula has had time to form a stable equilibrium. Predicted fluxes for the nebulae based on both published estimates for the magnetic

field strength and the equipartition calculated values are given in Table 5.5 and are compared to the upper limits derived in each case.

As we can see, for most of the sources observed the predicted values of integrated flux above 1 TeV are of the order of $10^{-15}$ or $10^{-16}$ ergs/cm$^2$/s which is well below the $10^{-13}$ ergs/cm$^2$/s typical of observed pulsar wind nebulae in the TeV regime and below the upper limits calculated from available HESS data. As a result it is unlikely that the majority of these nebulae will be seen with the current generation of TeV Cherenkov telescopes without a significant investment of time. However, these sources may be detectable with the next generation Cherenkov instrument which is currently in the planning stages, CTA.

A number of the sources are however predicted to have integrated fluxes of the order of $10^{-13}$ ergs/cm$^2$/s and so may be viable targets for observation with the current generation of TeV Cherenkov instruments; these are discussed in more detail in Section 5.5. The largest predicted flux was calculated for the nebula G7.4-2.0. Two of the other sources with large predicted fluxes based on the above equations are the nebulae G16.7+0.1 and G11.2-0.3 which have predicted fluxes of $1.46 \times 10^{-13}$ ergs/cm$^2$/s and $2.95 \times 10^{-14}$ ergs/cm$^2$/s respectively. However as has been discussed previously both of these nebulae are difficult to detect due to contamination by brighter neighbouring sources. They are discussed in more detail in Chapter 6.

### 5.3.1 Application to known TeV Pulsar Wind Nebulae

To assess the value of this model, it is necessary to apply it to nebulae which have already been observed in the TeV $\gamma$-ray regime to see if the predictions made will tally with the observations of this nebula. Here we calculate the parameters expected for two well-observed sources discussed in Chapter 4, G21.5-0.9 and the Kookaburra, as examples of young and middle aged pulsar wind nebulae respectively. Additional targets were not used in this analysis due to a lack of data available from which to calculate a prediction. The predicted and observed TeV $\gamma$-ray fluxes for these nebulae are shown in Table 5.6.

Also shown in Table 5.6 are predictions of the TeV $\gamma$-ray flux, calculated for both an observationally-derived and a equipartition-calculated magnetic field, which is

Table 5.5: Predicted $\gamma$-ray flux above 1 TeV from the known X-ray flux for targets for which this is available and comparison with the derived upper limits for these targets. Where they are available the magnetic fields quoted in the X-ray observations are given and used to calculate predicted flux values, in each case these are given second in the table.

| | $d$ | X-ray flux at 1 keV | $a$ | $\theta$' | B | Pred. $\gamma$-ray flux above 1 TeV | $\gamma$-ray flux UL above 1 TeV |
|---|---|---|---|---|---|---|---|
| | kPc | /cm$^2$/s $\times 10^{-5}$ | | arcmin | $\mu$G | /cm$^2$/s $\times 10^{-15}$ | /cm$^2$/s $\times 10^{-15}$ |
| Geminga [161] | 0.25 | 0.746 | 1.84 | 0.83 | 21.2 | 5.60 | 303 |
| G287.4+0.6 [92] | 2.7 | 4.37 | 1.7 | 0.18 | 70.0 | 0.150 | 335 |
| | | | | | 23.8 | 2.76 | |
| MSH11-62 [98] | 6 | 194 | 2 | 2.5 | 70.0 | 7.42 | 284 |
| | | | | | 36.0 | 54.5 | |
| MSH11-54 [117] | 4.8 | 14.4 | 1.72 | 0.018 | 55.8 | 0.924 | 518 |
| MSH15-56 [118] | 17 | 37.5 | 2.9 | 1.0 | 220.0 | 0.0200 | 475 |
| | | | | | 51.9 | 5.60 | |
| G327.1-1.1 [127] | 3.6 | 1.12 | 1.4 | 0.66 | 7.4 | 7.43 | 408 |
| Duck [131] | 5 | 33.7 | 1.6 | 0.16 | 33.0 | 7.85 | 109 |
| G7.4-2.0 [45] | 1.8 | 225 | 2.09 | 0.5 | 20.0 | 425 | 38.2 |
| | | | | | 92.0 | 3.81 | |
| G11.2-0.3 [173] | - | 277 | 1.73 | 0.66 | 46.5 | 29.5 | 355 |
| G16.7+0.1 [99] | 10 | 119 | 1.17 | 0.5 | 12 | 146 | 212 |
| | | | | | 17.6 | 63.4 | |
| G39.2-0.32 [157] | 8 | 101 | 1.5 | 0.3 | 28.6 | 29.9 | 296 |
| G47.38-3.88 [152] | 0.36 | 2.87 | 1.35 | 0.08 | 33.0 | 0.494 | 789 |
| G10.93-45.44 [119] | 0.25 | 0.746 | 2.2 | 0.5 | 30 | 0.459 | 568 |
| | | | | | 35.3 | 0.273 | |

Table 5.6: Predicted $\gamma$-ray fluxes of two pulsar wind nebulae using the de Jager method for both an equipartition derived magnetic field (given second in each case) and the magnetic field strength derived from other methods quoted in published material.

| | $d$ | X-ray flux at 1keV | $a$ | $\theta$' | B | Pred. $\gamma$-ray flux above 1TeV | $\gamma$-ray flux above 1TeV |
|---|---|---|---|---|---|---|---|
| | kPc | /cm$^2$/s $\times 10^{-5}$ | | arcmin | $\mu$G | /cm$^2$/s $\times 10^{-15}$ | /cm$^2$/s $\times 10^{-15}$ |
| G21.5-0.9 [65] [43] | 4.30 | 6870 | 1.89 | 0.80 | 25 | 4970 | 1300 |
| | | | | | 135 | 38.0 | |
| Kookaburra [188] [19] | 7.69 | 81.1 | 2.03 | 0.18 | 8.0 | 3180 | 2640 |
| | | | | | 65.8 | 4.00 | |

compared to the observational flux. As can be seen by these results in both cases, the observed value is close to the prediction calculated using the de Jager model [67] when an observationally-derived magnetic field but not when an equipartition-derived value is used. This shows that the model works well in its calculation of flux from a known magnetic field strength. However, the calculation of magnetic field strength in this model does not work particularly well as is seen here by the discrepancy of equipartition predicted magnetic field strengths with observed values. This is acknowledged by the authors of the model who state "the purpose of this paper us not to give accurate estimates of B" [67]. As a result the predicted fluxes in this Chapter will be accurate only when the magnetic field strength is known.

The fluxes calculated for observationally derived magnetic field strength are however lower than the observed $\gamma$-ray flux. This is due to the de Jager model [67] only taking into account CMB photons as seed photons for the inverse Compton process. In reality many other sources of radiation will be available as seed photons and so the true $\gamma$-ray flux will be somewhat higher as seen in Table 5.6 ($\approx$ 3 - 4 times in the case of G21.5-0.9 and $\approx$ 1.5 times in the case of the Kookaburra).

## 5.4 Magnetic Field Lower Limits

As we have shown that the method of flux calculation from a known magnetic field from the de Jager model [67] provides accurate predictions it is possible to invert this

Table 5.7: Magnetic field lower limits for the nebulae for which X-ray data are available.

| Nebula | B Field Lower Limit ($\mu$G) | B(Eq) ($\mu$G) | B(pub) ($\mu$G) |
|---|---|---|---|
| Geminga | 2.62 | 21.2 | - |
| G287.4+0.6 | 4.03 | 23.8 | 70.0 |
| MSH11-62 | 20.8 | 36.0 | 70.0 |
| MSH11-54 | 5.45 | 55.8 | - |
| MSH15-56 | 16.6 | 51.9 | 220.0 |
| G327.1-1.1 | 1.39 | 7.4 | - |
| Duck | 12.00 | 33.0 | - |
| G7.4-2.0 | 9.83 | 20.0 | 92.0 |
| G11.2-0.3 | 18.68 | 46.5 | - |
| G16.7+0.1 | 10.10 | 17.6 | 12 |
| G39.2-0.32 | 11.43 | 28.6 | - |
| G47.38-3.88 | 1.43 | 33.0 | - |
| G10.93-45.44 | 3.24 | 35.3 | 30 |

calculation and use the upper limit and the X-ray flux measurement to calculate a lower limit to the magnetic field present in the nebula, using the following equation:

$$B_{LL} = \left( \frac{1.5 \times 10^{16} F_{1TeV} e^{\left(0.16 a_x^2 - 2.2 a_x\right)}}{F_{1keV} (1.4 \times 10^{-5})^{a_x}} \right)^{\frac{1}{a_x + 1}} \tag{5.4}$$

Where $B_{LL}$ is the lower limit of the magnetic field, $F_{1TeV}$ and $F_{1keV}$ are the differential fluxes or flux upper limits of the nebula at 1 TeV and 1 keV respectively and $a_x$ is the spectral index of the nebula in the X-ray regime. This has been done for the nebulae for which usable published X-ray observations exist and these are shown in Table 5.7.

All the limits calculated are lower than the equipartition values calculated and the published values from their respective papers and so do not rule out any of these previously derived values. In a few cases the calculated lower limits are close to the derived and published values, however, not surprisingly these are generally in cases where the predicted fluxes also lie close to the calculated flux upper limits, such as in the case of G16.7+0.1 which is subject to source confusion and is discussed in more detail in Chapter 6.

## 5.5 Discussion of Individual Sources

In this Chapter, we have calculated the upper limits on the fluxes of 17 sources and then used X-ray data where it was available to calculate predicted fluxes for these. This Section gives details about the individual observations and compares them to the predictions made using the de Jager model [67]. All of the nebulae observed are discussed, but those which are adjacent to a larger source are discussed in more detail in Chapter 6. TeV $\gamma$-ray flux predictions of individual sources are only discussed when independent magnetic field strengths are available due to the uncertainty in predicting these using an equipartition assumption; in these cases the predictions will be compared to the point-source upper limits so that they can be directly compared to the X-ray flux as discussed in Section 5.3.

### 5.5.1 Nebulae Adjacent to a Larger $\gamma$-ray Source

In the X-ray regime pulsar wind nebulae are small and located close to the central pulsar, unlike the VHE $\gamma$-ray regime where older nebulae are in general extended. As a result, many nebulae which are distinct in the X-ray regime are part of the same extended complex of emission in the TeV $\gamma$-ray regime. Consequently, analysis of the region around the nebula incorporates emission from the extended complex, and upper limits are unlikely to correspond solely to emission from the source under investigation. This is observed in three cases listed in Table 5.3 which are discussed in more detail in Chapter 6. Two of the nebulae under consideration in this case are in the vicinity of the most extended known pulsar wind nebula in the TeV $\gamma$-ray regime, HESS J1825-137 which is discussed in Section 4.2.3. They are G18.5-0.4, also known as the Eel, which is located in the north of the nebula and G16.7+0.1 which is located in its west.

As we can see in Table 5.3 the region corresponding to the nebula G18.5-0.4 (the Eel Nebula) in the northern extension of HESS J1825-137 has a high statistical significance of 6.55 $\sigma$ for a point source and 5.38 $\sigma$ for an extended source. If it were not located close to the extended nebula this would be considered adequate evidence for TeV emission from this source, and indeed this emission has been proposed as coming from the separate northern source [170] as the movement of the progenitor pulsar PSR B1823-13 away from the emission of the HESS J1825-137 implies that emission should be concentrated towards the south and west of this source. However, while the brightest emission from HESS J1825-137 is seen in this southwesterly direction, substantial emission is seen to its north, corresponding to the location of the Eel nebula G18.5-0.4. No break in emission between the main nebula and this northern extension has been observed and an attempt to distinguish this nebula from its brighter neighbour is made in Section 6.2.

In contrast to the emission from the G18.5-0.4, the other source overlapping with HESS J1825-137 is located southwest of the progenitor pulsar in the outer reaches in its emission, beyond the area analysed in [20] (see 4.2.3) as part of the softening of the spectra of this source. Less emission is seen in this area than to the north and the point source analysis results in a chance significance of 1.93 $\sigma$, which does

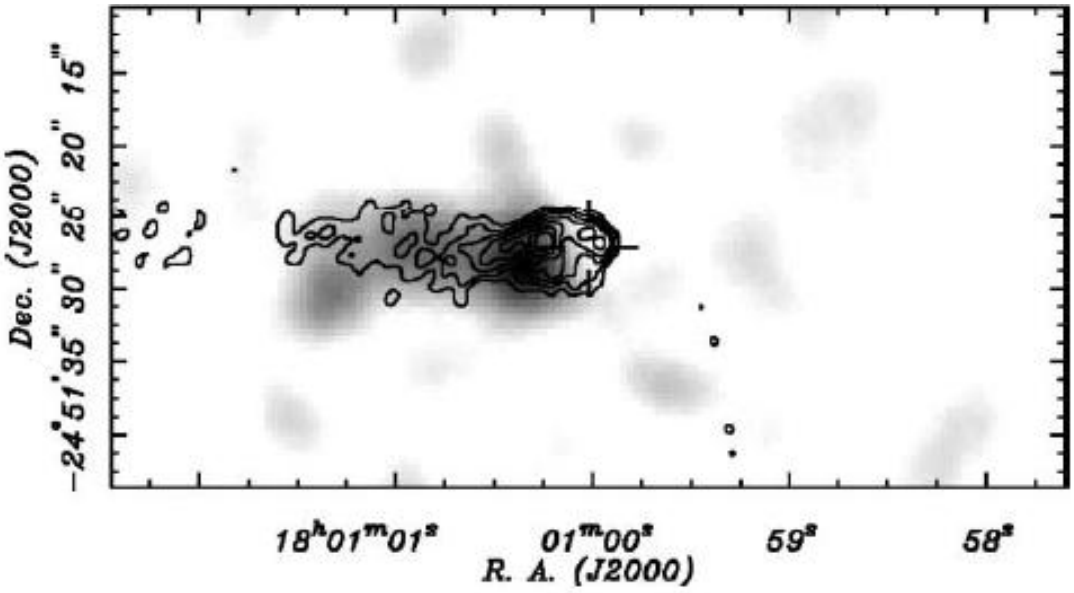


Figure 5.2: The Duck Nebula as seen by Chandra in X-rays shown in greyscale. It is overlayed with 4.9GHz radio data and both show emission to the east of the central pulsar (marked with crosshairs [131].

not constitute evidence for a detection. G18.6-0.4 corresponds to the X-ray source observed in [99].

G11.2-0.3 is the third source surrounding the young pulsar PSR J1811-1925; point source analysis centred on its X-ray position shows a large significance due to its location in the outer reaches of another extended nebula. In this case it is located in the outer edge of the HESS source HESS J1809-193 corresponding to the PWN G11.1-1.0 observed in both the X-ray and $\gamma$-ray regimes [127] [25]. It is further discussed in Section 6.1 where we attempt to disentangle it from its larger neighbour.

### 5.5.2 The Duck

Another source which is located close to another known HESS source is the Duck Nebula, also known as G5.4-1.2, which is located $\approx$ 1° from the complex HESS J1800-240 [27]. In this case, a point source analysis centred on the X-ray position does not show any evidence for a signal , and so contamination of this region by HESS J1800-240 is not apparent and nor is there any evidence of emission from the

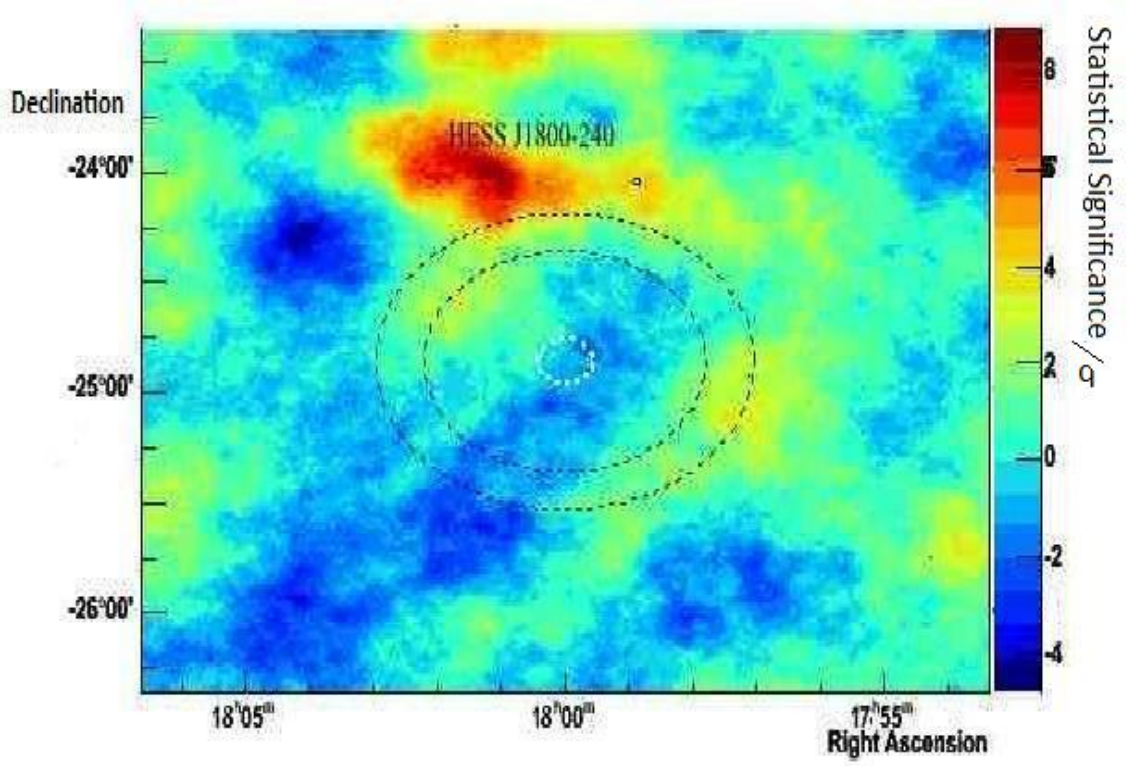


Figure 5.3: A $\gamma$-ray skymap using a ring background for a pointlike emission region surrounding the Duck nebula. No emission corresponding to the Duck is seen.

Duck Nebula.

The Duck nebula received its name after its appearance in some radio wavelengths were a large extended supernova remnant with a small protruding pulsar wind nebula at its edge is seen [41]; this is thought to resemble the head of a Duck with the protruding pulsar wind nebula under investigation here corresponding to its beak. In the X-ray regime, only the beak, corresponding to the pulsar wind nebula created by the pulsar PSR B1757-24, is seen as a point source with a faint tail extending 20" towards the East in the direction fo the supernova remnant [131], this is shown in Figure 5.2. The progenitor pulsar of this nebula has a characteristic age of 16,000 years and a spindown luminosity of $\dot{E} = 2.6 \times 10^{36}$ergs/s making it much older than most known TeV $\gamma$-ray emitting pulsar wind nebulae. This is consistent with the small, faint nebula. The protrusion of the pulsar wind nebula from the central SNR means that this source may be regarded as a bow-shock pulsar wind nebula as discussed in Section 2.5.4.

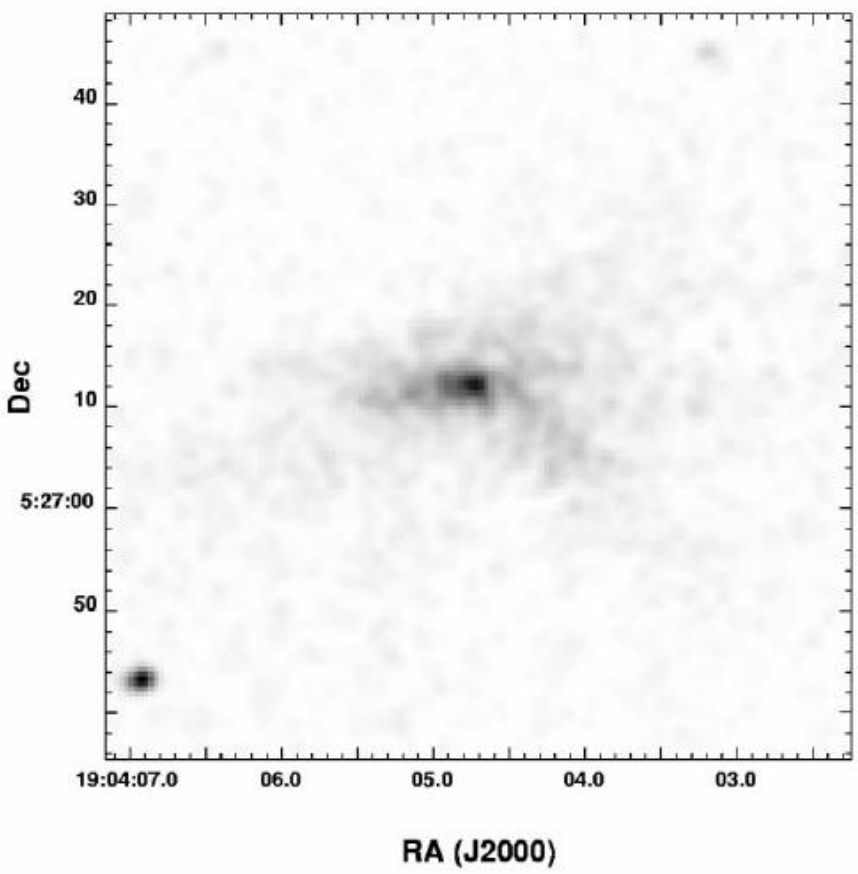


Figure 5.4: A X-ray image of G39.2-0.3 taken using Chandra in the 3.0 - 8.0 keV frequency band taken from [157] showing extended emission to the east and southwest of the centre of the nebula.

With a statistical significance of 1.09 $\sigma$ when analysed as a point source and 1.13 $\sigma$ when analysed as an extended source this source was not detected above a level consistent with background noise, as shown in the skymap of the region seen in the TeV $\gamma$-ray regime which is shown in Figure 5.3. If this nebula were to be observed in the $\gamma$-ray regime it would probably be seen as an extended nebula due to the age of the source or indeed a relic $\gamma$-ray pulsar wind nebula at some distance from the X-ray nebula due to the escape of the progenitor pulsar from the nebula.

### 5.5.3 G39.2-0.3

G39.2-0.3 also appears in a crowded region of sky with the nearby source HESS J1908+063 [29] clearly visible in the $\gamma$-ray skymap (see Figure 5.5) of this source.

The X-ray nebula is one of the most distant under investigation in this Section at a distance of $\approx 8$ kpc it is seen as a faint nebula which as yet has not been associated with a progenitor pulsar [157], this is shown in Figure 5.4.

This nebula shows the highest statistical significance of any of the sources observed in this section which are not the subject of overlap with an adjacent nebula. However, as the significances seen are 2.74 $\sigma$ and 3.03 $\sigma$ for a pointlike and extended analyses respectively these do not represent detections and indeed may just be the result of fluctuations in background in a crowded region as is seen in Figure 5.5. The $\approx 3$ $\sigma$ significance detected for this source was initially detected after just 30 hours of observations and so an additional 20 hours of observations were taken as a result of an observation proposal by the author of this thesis in order to confirm detection of this source, however, the significance did not increase as can be seen in Figure 5.6.

### 5.5.4 G7.4-2.0

The source with the highest predicted TeV $\gamma$-ray flux is G7.4-2.0 if we assume the CO line observation derived value for its magnetic field of 20 $\mu$G given in the discovery paper [45] which results in a predicted significance of $4.25\times10^{-13}$ ergs/cm$^2$/s. However, the source is not very well observed and has the least constraining value for an upper limit of all of the sources presented due to a short observation time of only 2.19 hours with runs taken at the edge of the camera field of view (2.37° off axis); these observations are shown in Figure 5.7. As the source is located in the southern hemisphere sky it is in a position easily observable by HESS and so could be observed with another 20-30 hours of observations if it does indeed have a magnetic field of 20 $\mu$G as calculated by Braje [45]. However, its location is in a crowded RA band and so it will not be a high priority for further observations.

### 5.5.5 G287.4+0.6

G287.4+0.6 is another source for which an accurate magnetic field strength (70 $\mu$G) is known and as such the $\gamma$-ray flux can be predicted from the X-ray observations. In

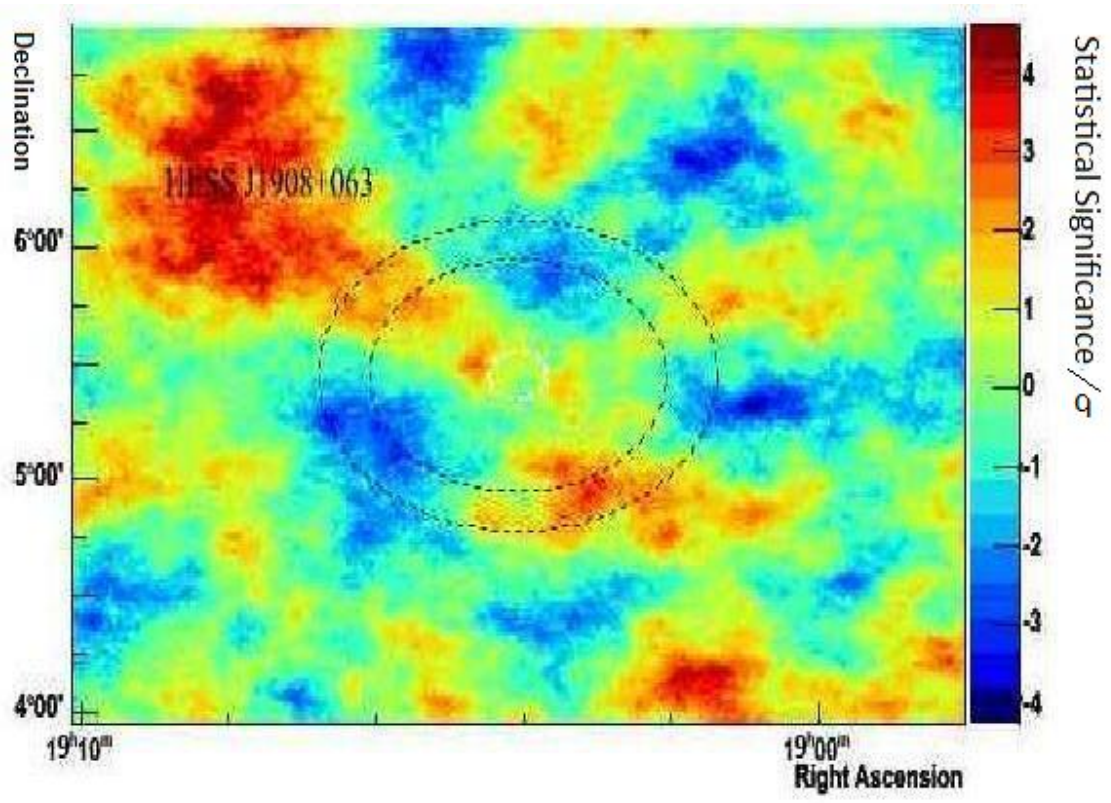


Figure 5.5: A $\gamma$-ray skymap using a ring background for a pointlike emission region surrounding the nebula G39.2-0.3. The position of the nebula corresponds to an area of above average significance but at 3 $\sigma$ this is not enough to claim the detection of this source.

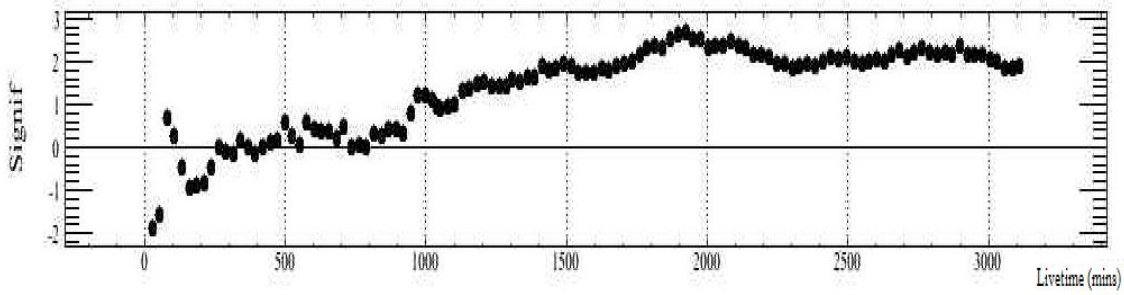


Figure 5.6: The buildup of significance with time of the nebula G39.2-0.3.

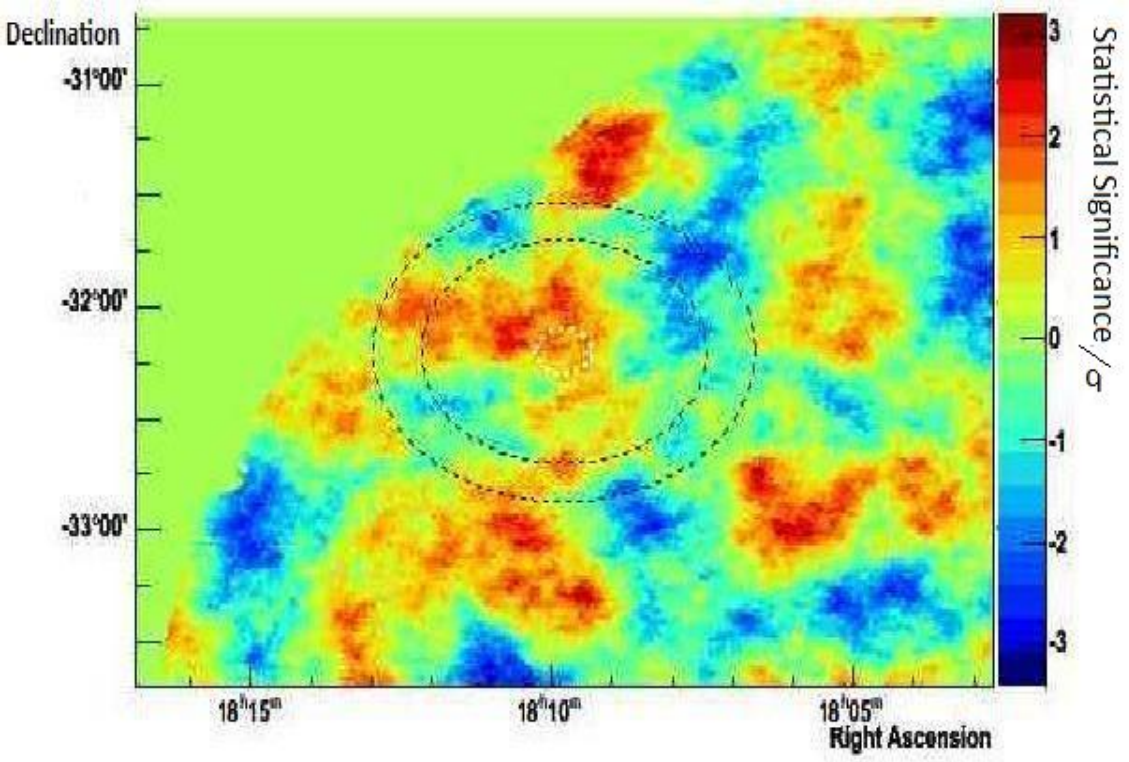


Figure 5.7: A $\gamma$-ray skymap using a ring background for a pointlike emission region surrounding the nebula G7.4-2.0. As the source was at the edge of the camera in the observations the area in the northeast of the skymap is completely smooth as it was not covered in the observation.

the X-ray regime this nebula is small and extended to the southeast of its progenitor pulsar PSR B1046-58 [92], it can be seen in Figure 5.8. The progenitor pulsar has a characteristic age of 20,400 years making this another middle-aged nebula and so an extended nebula should be seen in the TeV $\gamma$-ray regime with a flux of $1.5\times10^{-16}$

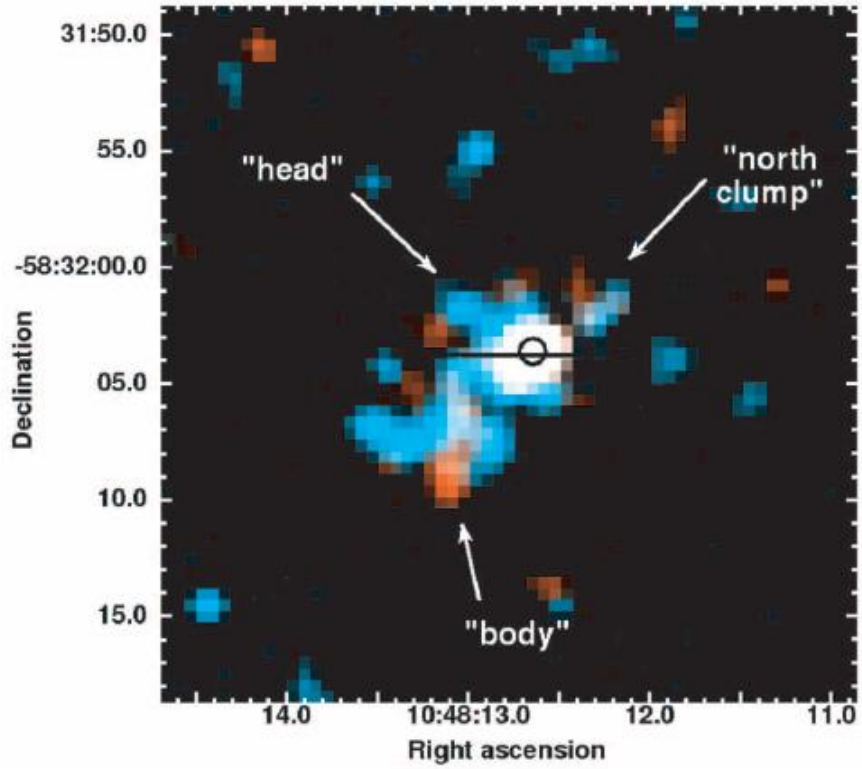


Figure 5.8: The nebula G287.4+0.6 as seen in the 0.5-10 keV X-ray spectrum. The progenitor pulsar is marked with a black circle [92].

photons/s/cm$^2$ expected. This small predicted flux would not be detectable in the 24.5 hours of observations made of this region by the HESS telescopes and indeed no detection is made. The region surrounding the source is shown in Figure 5.9

### 5.5.6 G10.93-45.44

In common with the majority of other sources for which the complete array of X-ray parameters including the magnetic field strength are known G10.93-45.44 is a middle aged pulsar wind nebula surrounding a central progenitor pulsar PSR J2124-3358 [119]. This pulsar has a characteristic age of 5,860,000 years much older than any observed $\gamma$-ray pulsar wind nebula (see Figure 5.10). As a result we might expect to see an extended nebula in the $\gamma$-ray regime to the north of the observed nebula and perhaps a bow-shocked nebula close to it. However, predictions for this nebula based on the de Jager model [67] indicate a predicted flux of $4.59\times10^{-16}$

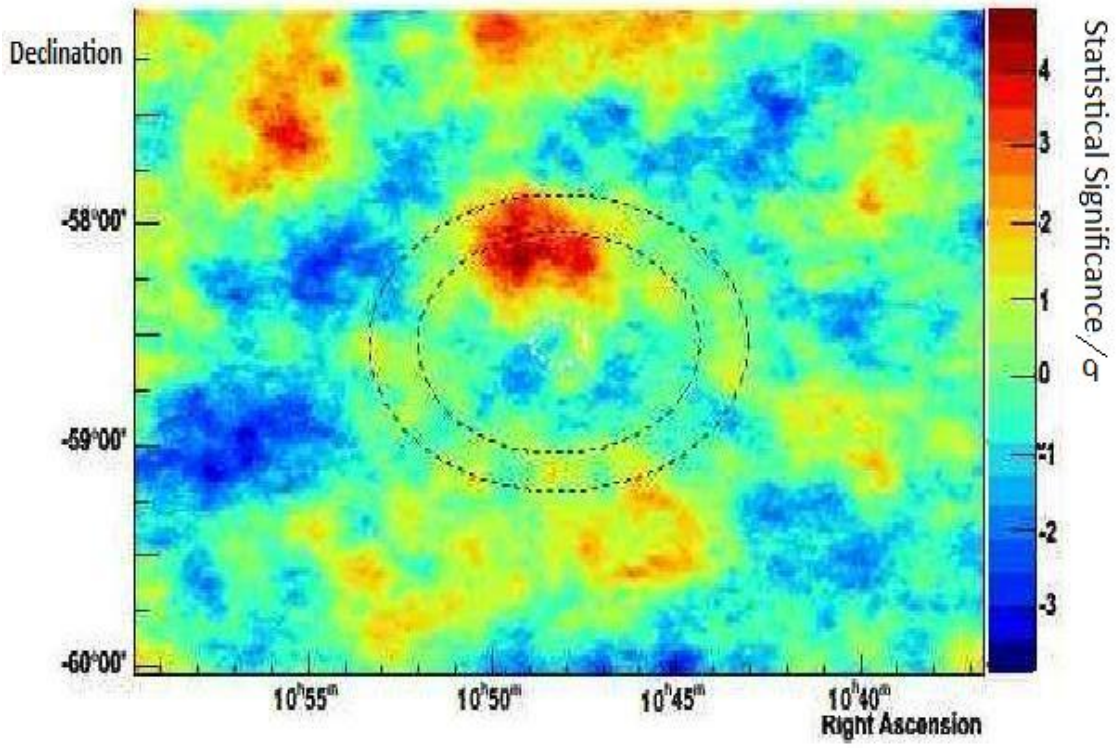


Figure 5.9: A $\gamma$-ray skymap using a ring background for a pointlike emission region surrounding the nebula G287.4+0.6. The nebula was not observed.

photons/s/cm$^2$ above 1 TeV and so detection of this nebula is not expected if the model is correct and indeed the nebula is not seen in the $\gamma$-ray observations seen in Figure 5.11.

### 5.5.7 MSH11-62

Unlike many of the other sources for which X-ray data was available to make predictions of X-ray flux, MSH11-62 is a younger source surrounded by a SNR shell [98]. While the characteristic age of its pulsar is estimated at 20,000 years, observation of the SNR suggests a younger age of closer to 6,500 years placing this nebula somewhere around the time that inverse shock crushing is expected to occur and so may be visible as a point source if seen in the TeV $\gamma$-ray regime. Flux predictions indicate a nebula flux of $7.42\times10^{-15}$ photons/s/cm$^2$ above 1 TeV adjacent to the progenitor pulsar and so it is unlikely to be seen with the current generation of VHE $\gamma$-ray telescopes and indeed is not detected in the 25 hours of observations available (see

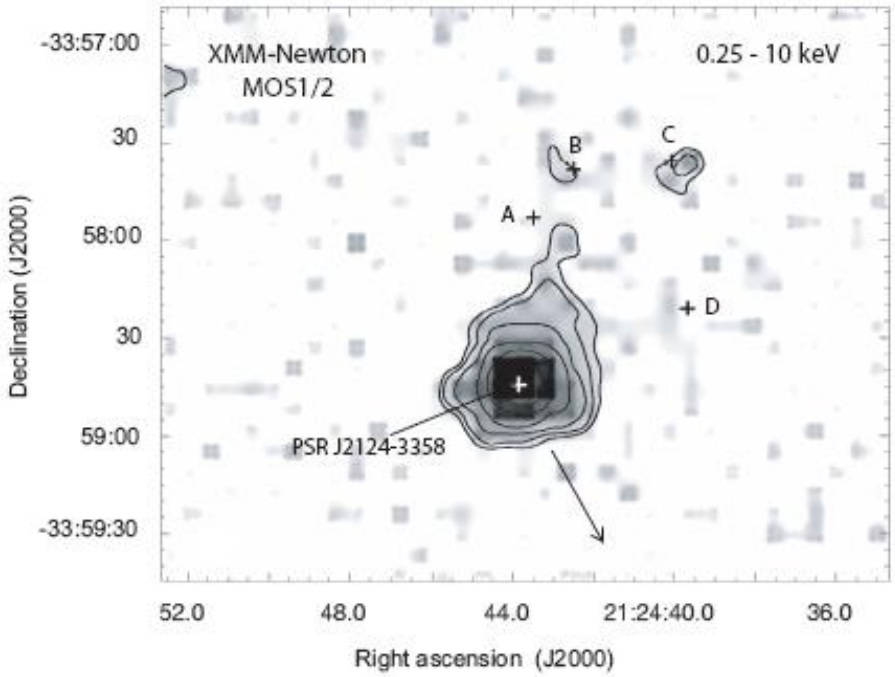


Figure 5.10: An X-ray image of the nebula G10.93-45.44 as seen in [119] produced using the XMM-Newton satellite. It shows extension towards the north of the progenitor pulsar.

Figure 5.12).

### 5.5.8 MSH15-56

The final source for which X-ray data and magnetic field strength are available is also the most distant of the observed X-ray sources under investigation at a distance of at least 17 kPc [118]. As a result it is faint and predictions based on the de Jager model [67] indicate that no emission is expected when its measured magnetic field of 220 $\mu$G [118] is included in the calculation and indeed it is not observed in the 15 hours of observations made in this analysis seen in Figure 5.13. However due to the strength of the magnetic field measured for this nebula SSC effects may make the nebula brighter, but in these circumstances emission is still unlikely to be seen.

### 5.5.9 Other Sources

The remaining nebulae for which upper limits have been calculated have not been observed sufficiently well in the X-ray regime for $\gamma$-ray fluxes for these nebulae to be

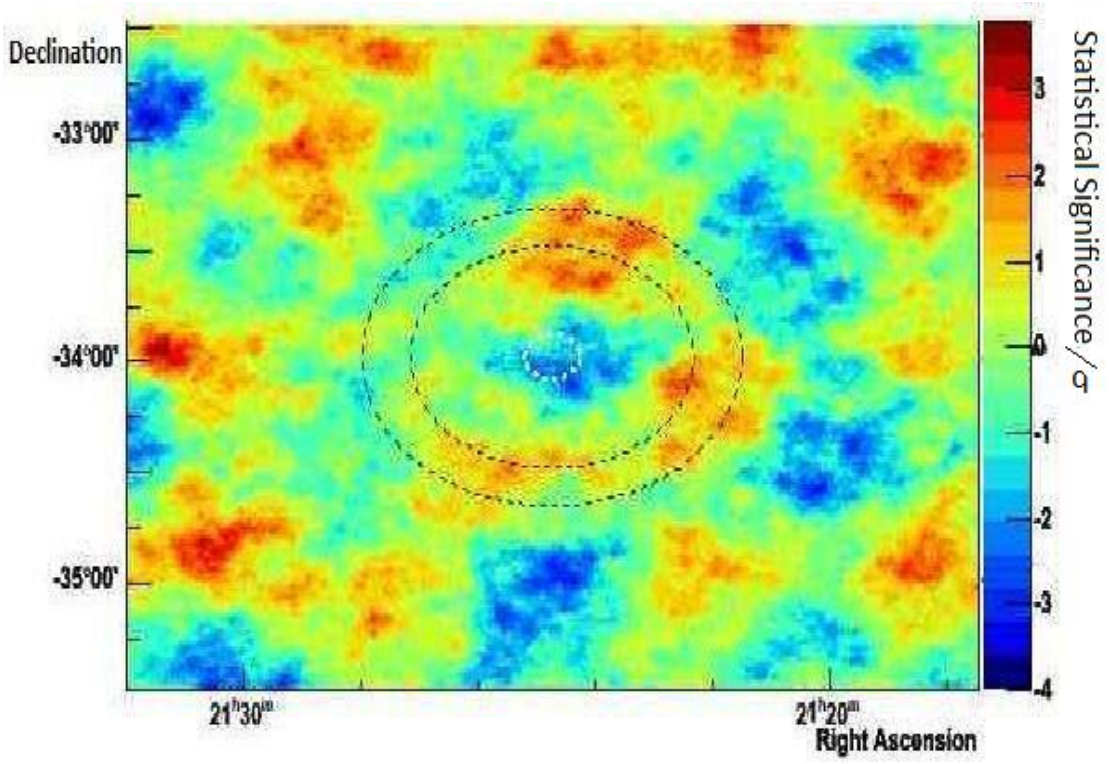


Figure 5.11: A $\gamma$-ray skymap using a ring background for a point-like emission region surrounding the nebula G10.93-45.44. The nebula was not detected.

predicted. None of these nebulae are seen in the TeV $\gamma$-ray regime but the regions observed are shown. MSH 11-54 is shown in Figure 5.14, Geminga in Figure 5.15, G293.8+0.6 in Figure 5.16, G327.1-1.1 in Figure 5.17, G34.01+20.27 in Figure 5.18, G47.38-3.88 in Figure 5.19 and G180.7-1.7 in Figure 5.20.

## 5.6 $\gamma$-ray Upper Limits of Pulsar Wind Nebulae

This Chapter focused on the search for counterpart $\gamma$-ray sources to X-ray selected pulsar wind nebulae using archival HESS data. No new sources were found but some of the sources did have upper limits close to predicted flux estimates and so longer observation times for these sources may result in their detection in the future. In addition to calculating upper limits for these sources in the TeV $\gamma$-ray regime, the data obtained were used to investigate the magnetic field of the pulsar wind nebulae studied. Where $\gamma$-ray upper limits and X-ray fluxes were available magnetic field strength lower limits were calculated and compared to published magnetic field

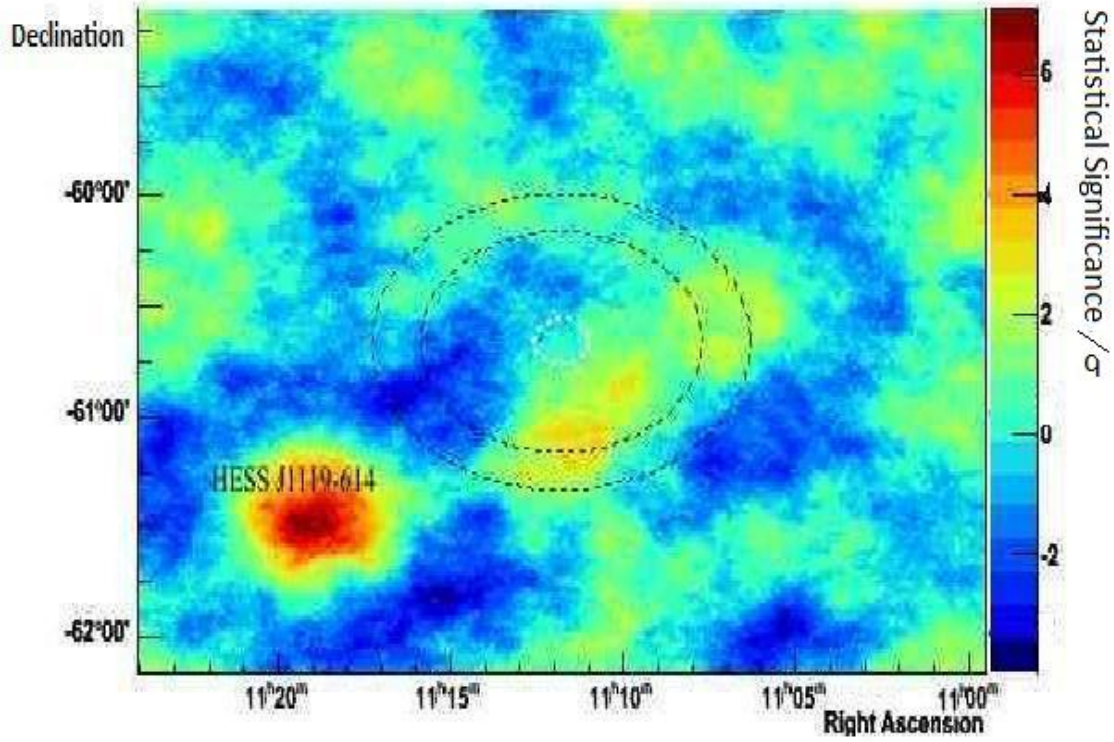


Figure 5.12: A $\gamma$-ray skymap using a ring background for a point-like emission region surrounding the nebula MSH11-62. The nebula was not observed. The HESS source HESS J1119-614 [71] is also seen in the field of view of this source.

strengths. No previously published magnetic field strengths were precluded by this method.

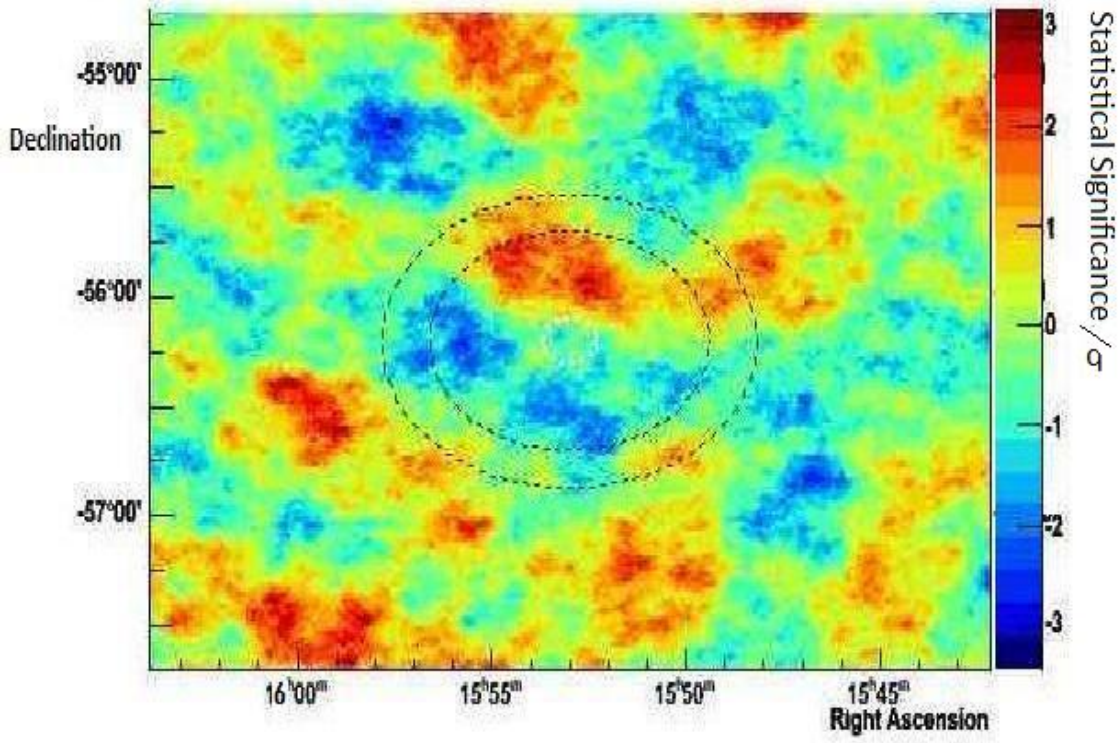


Figure 5.13: A $\gamma$-ray skymap using a ring background for a point-like emission region surrounding the nebula MSH15-56. The nebula was not detected.

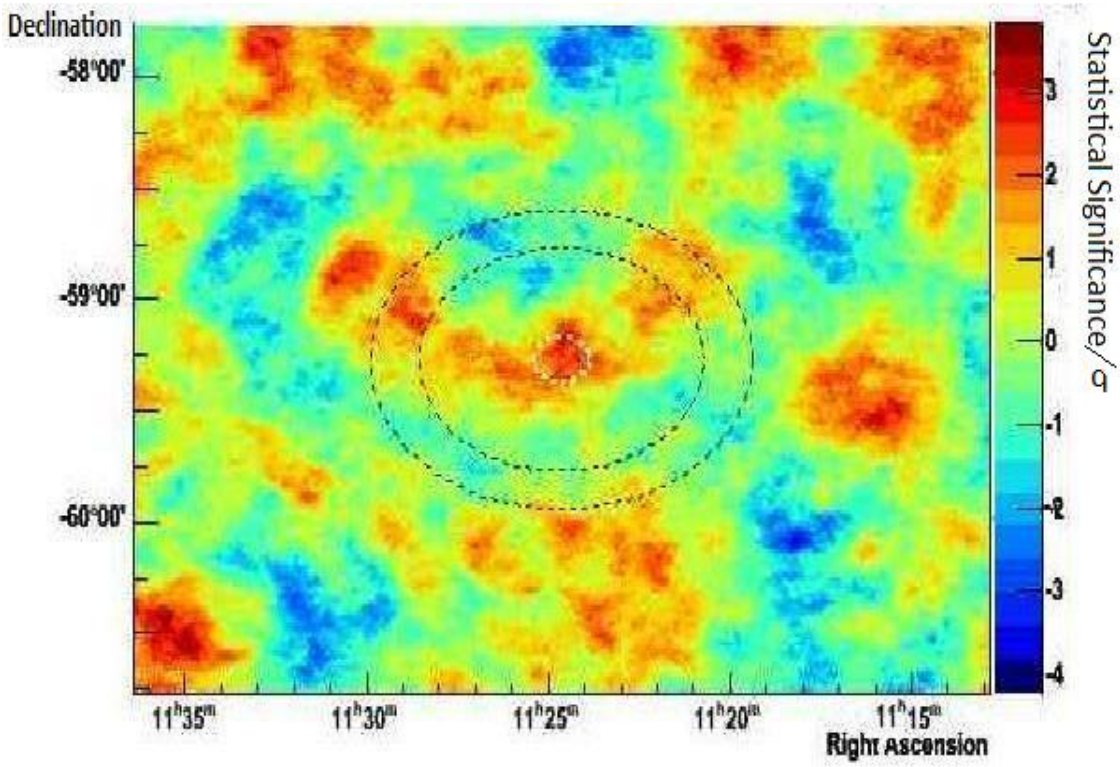


Figure 5.14: A $\gamma$-ray skymap using a ring background for a point-like emission region surrounding the nebula MSH11-54. The nebula was not detected.

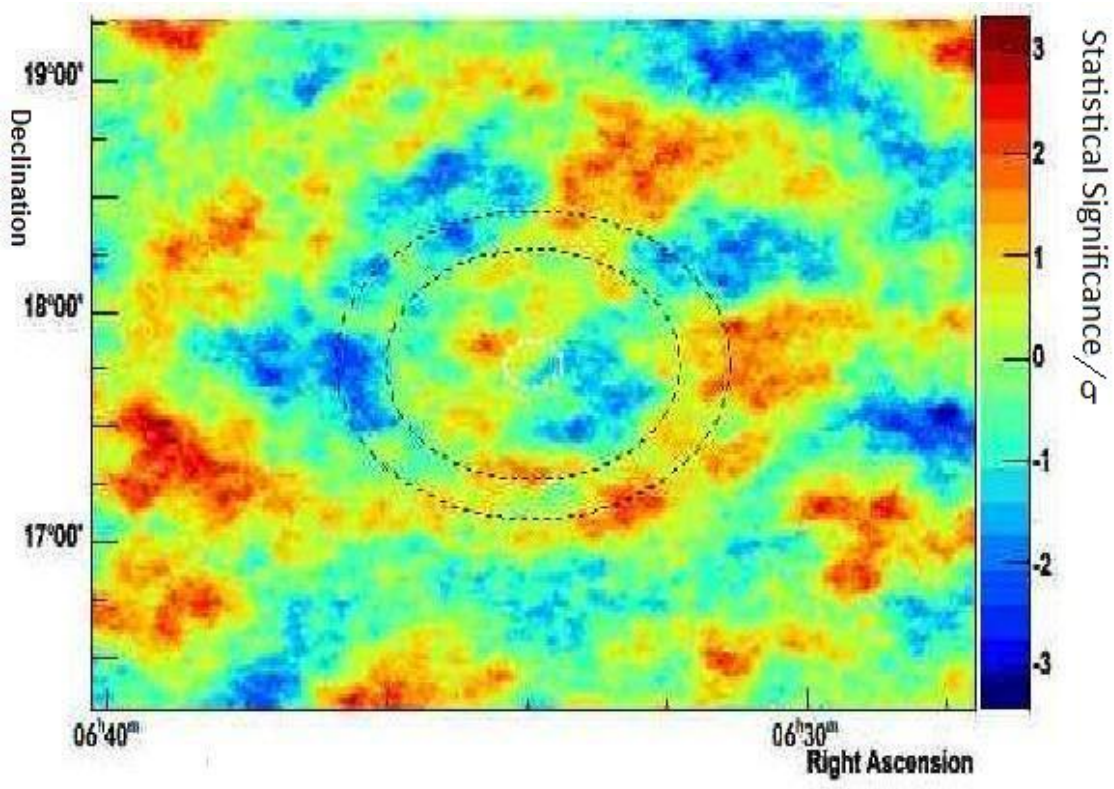


Figure 5.15: A $\gamma$-ray skymap using a ring background for a point-like emission region surrounding the Geminga Nebula. The nebula was not detected.

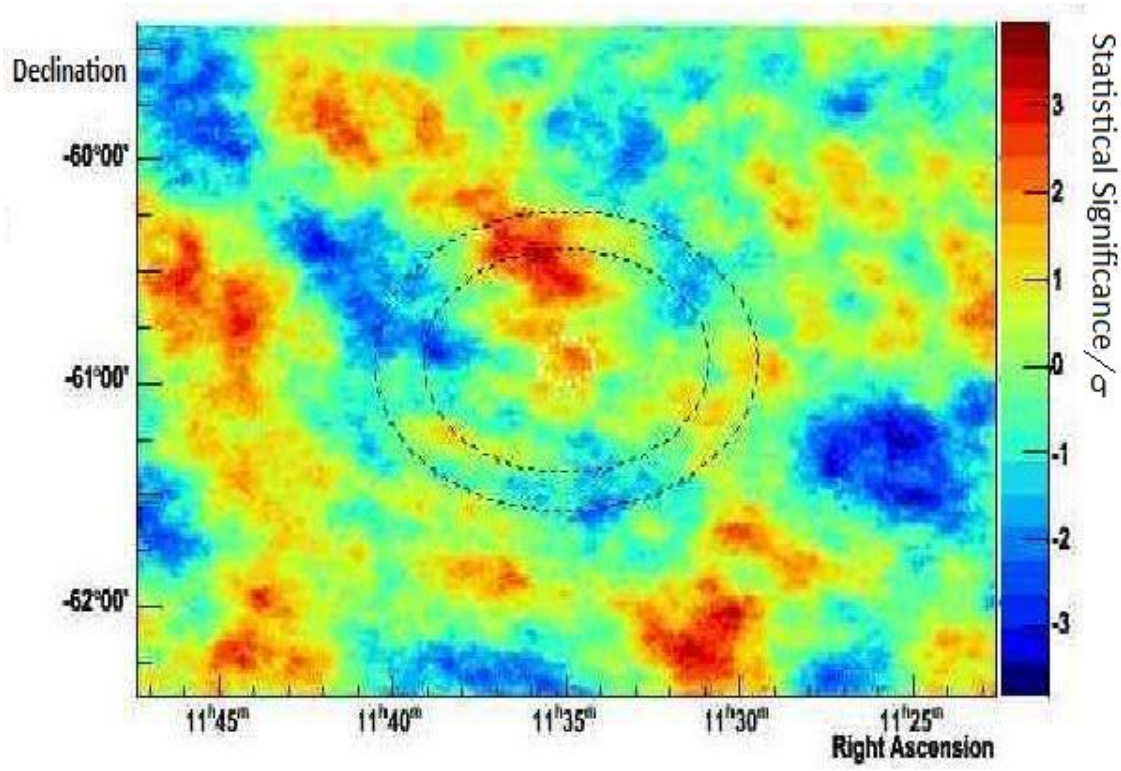


Figure 5.16: A $\gamma$-ray skymap using a ring background for a point-like emission region surrounding the nebula G293.8+0.6. The nebula was not detected.

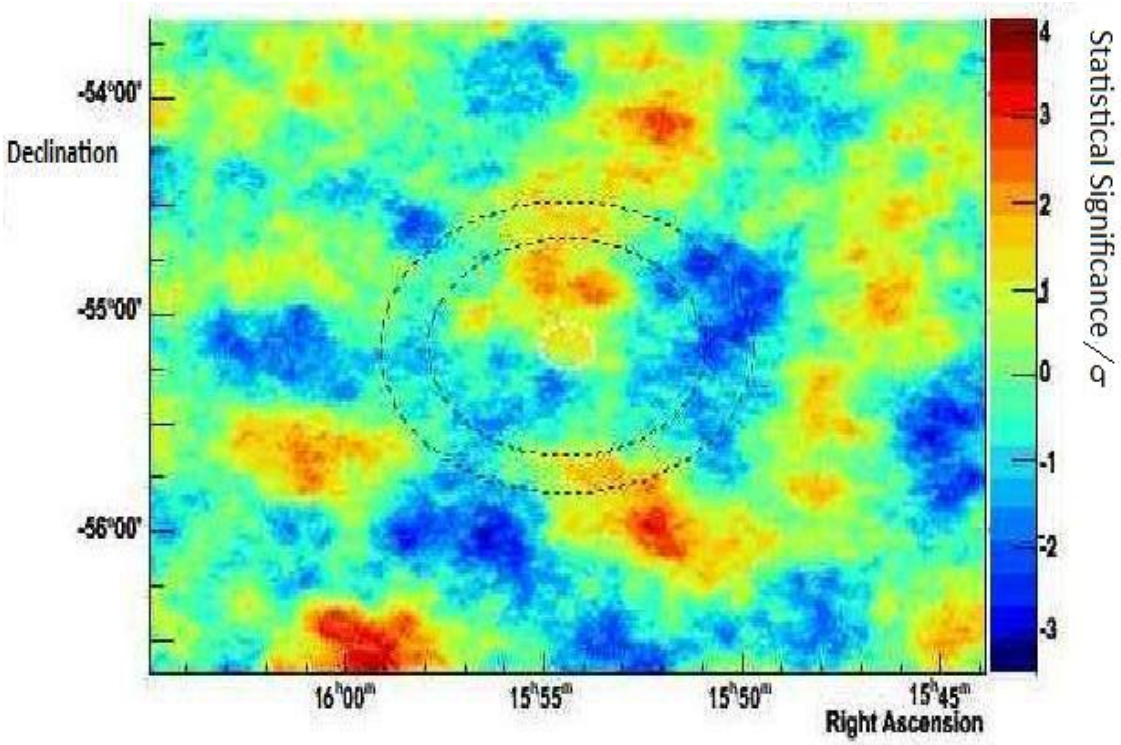


Figure 5.17: A $\gamma$-ray skymap using a ring background for a point-like emission region surrounding the nebula G327.1-1.1. The nebula was not detected.

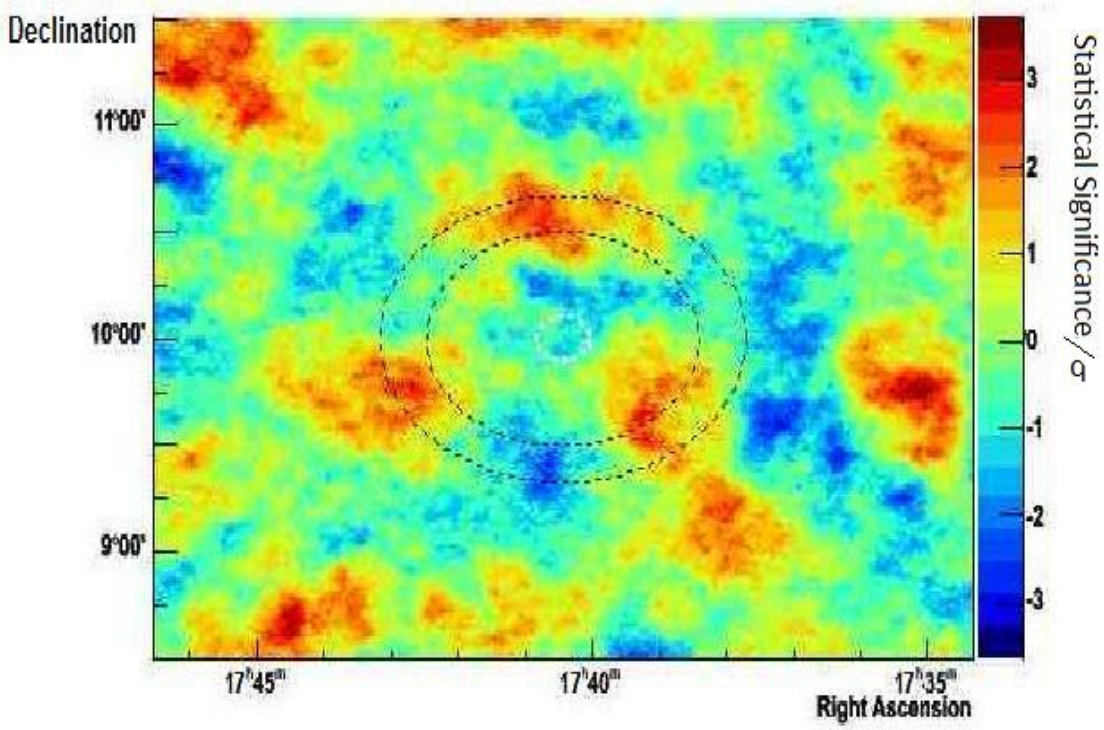


Figure 5.18: A $\gamma$-ray skymap using a ring background for a point-like emission region surrounding the nebula G34.01-20.27. The nebula was not detected.

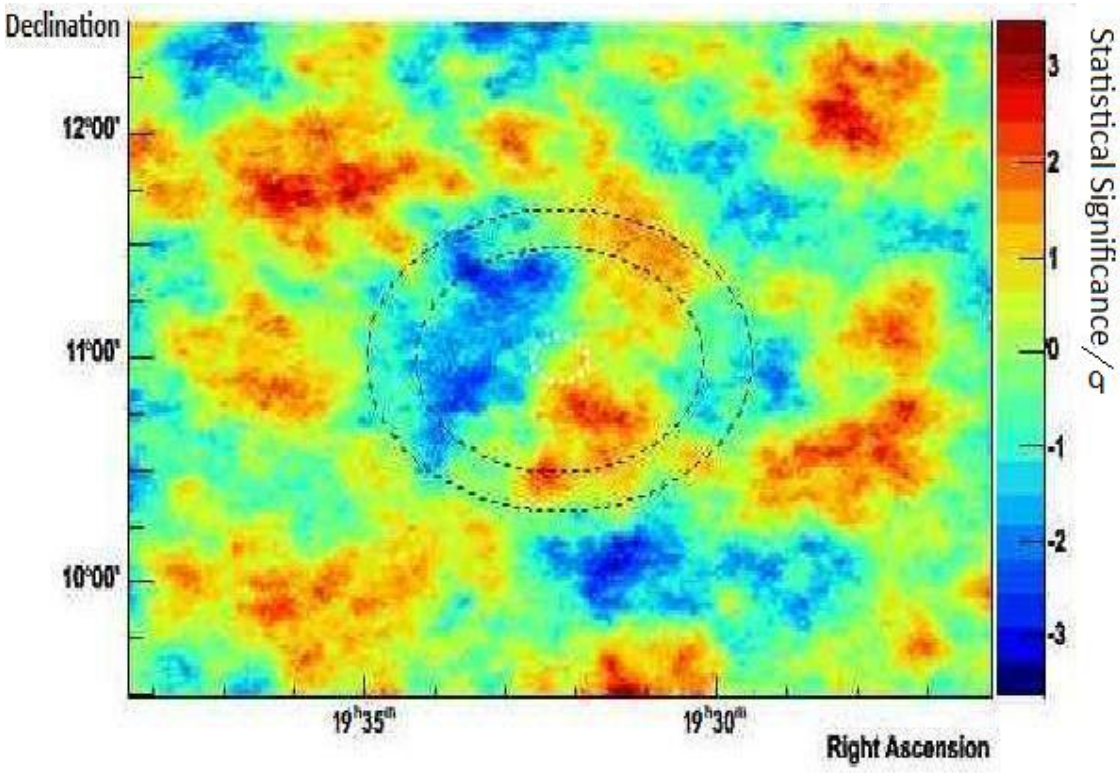


Figure 5.19: A $\gamma$-ray skymap using a ring background for a point-like emission region surrounding the nebula G47.38-3.88. The nebula was not detected.

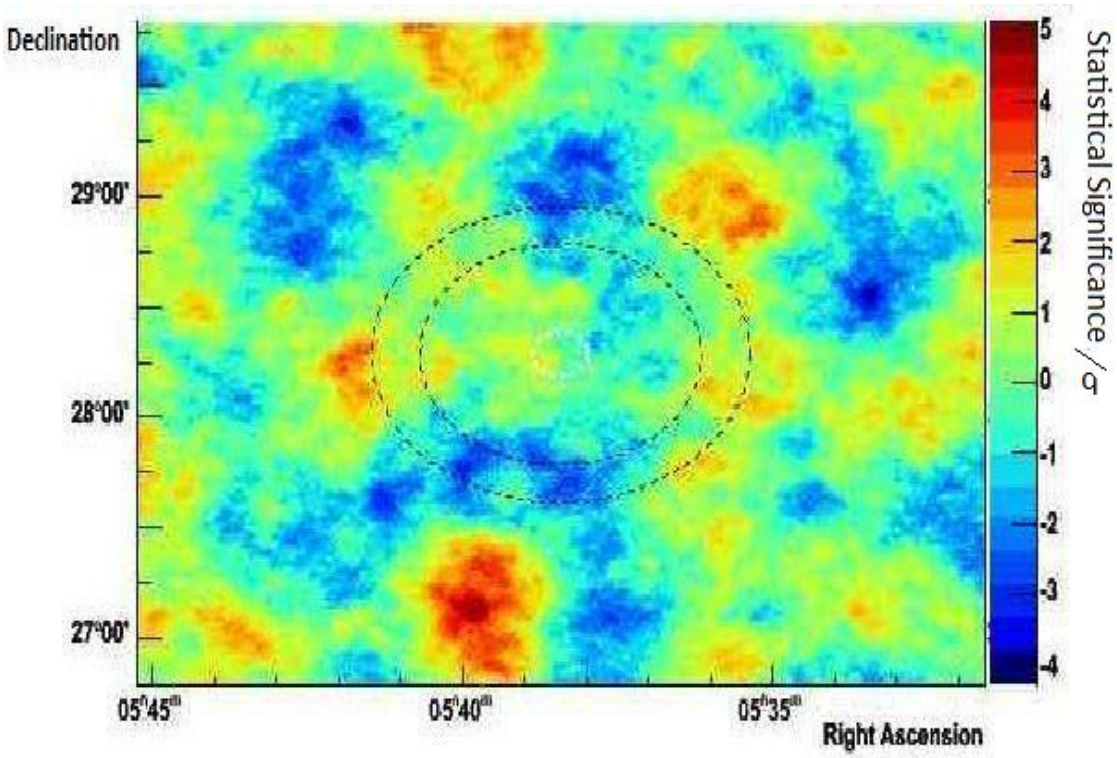


Figure 5.20: A $\gamma$-ray skymap using a ring background for a point-like emission region surrounding the nebula G180.0-1.7. The nebula was not detected.

# Chapter 6

# Disambiguation of Pulsar Wind Nebulae

As has been discussed in Chapter 5 many of the pulsar wind nebulae that are observed in the X-ray regime are difficult to detect in the TeV $\gamma$-ray regime as they are confused with other extended nebulae located adjacent to them. This confusion is largely due to the relative sizes of X-ray and TeV $\gamma$-ray pulsar wind nebulae as discussed in Section 4.4.2. This confusion is due to both the physical extension of the adjacent nebulae and the poor angular resolution of TeV $\gamma$-ray observatories.

This investigation will focus on analysis of the spectra and morphology at high energies of three nebulae which are located at the edges of two larger and brighter $\gamma$-ray pulsar wind nebulae. G11.2-0.3 surrounds the young pulsar PSR J1811-1925 and shows a statistical significance (when treated as a point source) of 3.49 $\sigma$ due to its position in the outer reaches of the extended nebula corresponding to the pulsar wind nebula G11.1-1.0.

The other two sources under investigation are both located in the outer regions of the largest known TeV $\gamma$-ray pulsar wind nebula known, HESS J1825-137, which is discussed in Section 4.2.3. G16.7+0.1 is located southwest of the progenitor pulsar in the outer reaches in its emission, beyond the area analysed in [20]. In contrast G18.5-0.4, otherwise known as the Eel Nebula, is located to the north of HESS J1825-137 closer to its progenitor pulsar but not in the direction in which most of the emission from this source is thought to occur.

In most cases when an attempt is made to separate the observed emission from two sources, it is based on the fitting of expected functions derived from the observational uncertainties of the instrument used to collect the data, as was done in the investigation of CTB 37A [26]. However, in this case the extension of the sources under investigation is not the result of the PSF of the HESS instruments but mainly due to the extension of the sources themselves which appear to overlap in the TeV $\gamma$-ray regime. In order to disentangle these sources we must thus use the physical properties of the sources themselves and so I have chosen to apply an energy threshold to the targets under investigation. By looking at photons with energies greater than 1 TeV it is possible to view only the central portions of the pulsar wind nebula under investigation, the portion of the nebula where young energetic electrons are present. This threshold was chosen as a compromise between the desire to view only the highest energy electrons which are coincident with X-ray emission and the need for adequate data for a morphological analysis.

A 1 TeV threshold was chosen after analysis of the targets considered in this Chapter at four different thresholds, the initial threshold of the observation, 700 GeV, 1 TeV and 5 TeV. A 1 TeV threshold was chosen as it offered the greatest distinction between adjacent nebulae in the observation of the Eel nebula. As can be seen in Section 6.2.2 no distinction is seen between the nebulae at the observation threshold of the HESS telescopes and indeed no distinction is seen at a 700 GeV energy threshold. At a 5 TeV threshold very few events are available to calculate significances and fluxes and as a result the Eel nebula is not seen. Another advantage of using a 1 TeV energy threshold for this analysis is that this threshold is used in lots of published literature and so fluxes quoted about a 1 TeV flux are directly comparable to these values. As a number of thresholds were attempted an adjustment had to be made to the final significance to take these trials into account.

When nebulae were observed adjacent to one another linear cross sections across lines of right ascension or declination were applied to determine the distinction between the nebulae. A cross section analysis was chosen to allow nebulae to be simply modelled in contrast to a more complex analysis model which would be required for a 2D skymap. The cross sections were taken along lines of right ascension

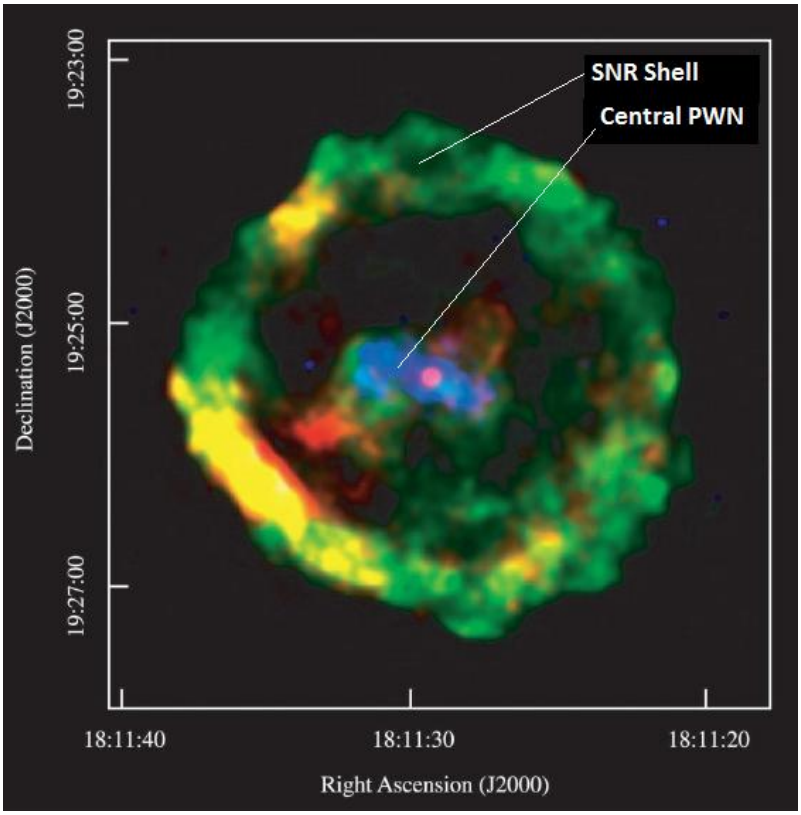


Figure 6.1: Chandra X-ray image of the nebula G11.2-0.3 which consists of a central pulsar wind nebula surrounded by an expanding supernova remnant shell [173].

and declination as this facility was built into the analysis software and did not require additional programming and testing which could not be carried out due to time constraints. The cross section was taken with a width of 0.2° corresponding to the diameter of the HESS point spread function.

## 6.1 G11.2-0.3

Of the sources under investigation, G11.2-0.3 is the closest to another TeV source, HESS J1809-193 (G11.1-1.0), with only 0.4° between the two objects' progenitor pulsars. In other wavelengths, the source under investigation, G11.2-0.3, is the better studied of the two sources as it has been the subject of several X-ray observations, most recently with the *Chandra* [173] and *INTEGRAL* [68] satellites.

The most comprehensive imaging observations of the source in the X-ray regime

were made using the *Chandra* observatory and show a classic plerionic nebula with a central pulsar wind nebula surrounded by supernova shell [173], as shown in Figure 6.1. The shell has a 5' diameter corresponding to a physical size of 7 pc for the nebula given the measured distance to the pulsar of 5 kpc, which implies an age for the nebula of $\approx$ 2000 years. Additionally, this is consistent with an association for this nebula with the historically observed supernova of 386AD, which has been proposed as the progenitor event for this nebula [173].

The central pulsar wind nebula of G11.2-0.3 is clearly detected in the *Chandra* observations, as can be seen in the centre of Figure 6.1. An elongated structure along the east-west axis is seen. As discussed in Chapter 5 the pulsar wind nebula has a flux of $2.77 \times 10^{-3}$ photons/cm$^2$/s at 1 keV with an X-ray spectral index of -1.73 [127] [25]. This allowed a prediction for the flux above 1 TeV to be made at $2.95 \times 10^{-14}$ photons/cm$^2$/s, within an order of magnitude of the observed upper limit of 3.55 $\times 10^{-13}$ photons/cm$^2$/s above 1TeV. However, this prediction assumes that the magnetic field of the nebula is in equipartition and so is likely to be inaccurate.

The source also shows a high statistical significance when observed in the TeV regime of 3.6 $\sigma$ when a point like analysis is used and an even higher 11.4 $\sigma$ when an extended analysis is used, as discussed in Chapter 5. However, this is the result of emission not from G11.2-0.3 itself but from the adjacent source HESS J1809-193 which has also been subject to X-ray observations [127]. HESS J1809-193 is a known middle-aged $\gamma$-ray pulsar wind nebula, shown in Figure 6.2.

Observations of the area surrounding these nebulae in the TeV regime seen in Figure 6.2 show that the observed HESS source is coincident with both X-ray nebulae discussed. The $\gamma$-ray nebula cannot be exclusively associated with the nebula G11.2-0.3 as the area of observed $\gamma$-ray emission is not contained within the observed extent of the surrounding supernova remnant seen in X-rays. Most of the observed emission must be associated with G11.1-1.0 as published. However, a contribution from the G11.2-0.3 nebula cannot be ruled out and so this section will attempt to separate out the two nebulae in order to see if emission is seen from the nebula G11.2-0.3 in the TeV regime.

To determine if G11.2-0.3 can be distinguished from its larger neighbour, HESS

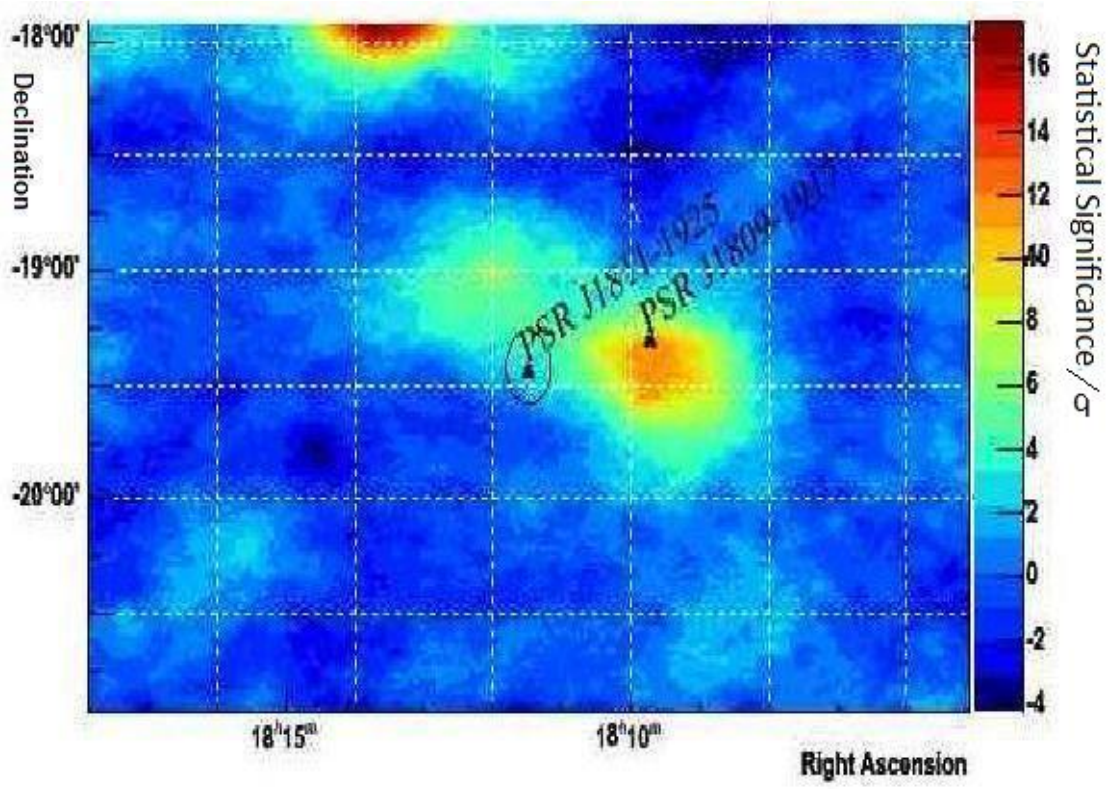


Figure 6.2: A VHE $\gamma$-ray observation of the area of the nebula HESS J1809-193 and G11.2-0.3. The progenitor pulsar of each nebula is marked with a triangle PSR J1809-1917 corresponds to the larger neighbouring nebula, HESS J1809-193 (G11.1-1.0) and PSR J1811-1925 corresponds to the nebula G11.2-0.3 under investigation. The black circle around PSR J1811-1925 indicates the extent of the X-ray SNR G11.2-0.3

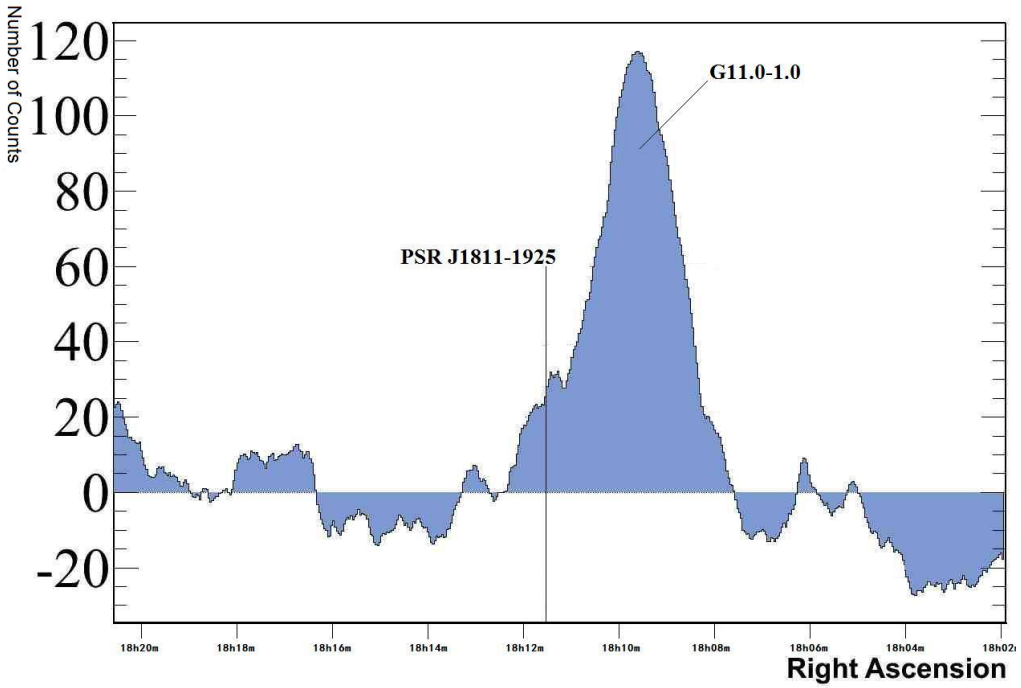


Figure 6.3: Showing the event excess for E < 0.44 TeV along declination of -19.42° through the centre of the nebula G11.2-0.3 showing the position of this source and its larger brighter neighbour HESS J1809-193

J1809-193 in the VHE $\gamma$-ray regime a cross-section was placed along a declination of -19.42°, coincident with the progenitor pulsar of G11.2-0.3, to see if a distinction could be made between the two sources. This is shown in Figure 6.3. A small excess is observed at the point of right ascension corresponding to PSR J1811-1925. The area of the cross-section corresponding to the fall-off in emission from the central G11.1+1.0 nebula was fit by both a second and forth order polynomial in order to determine the presence of emission from the smaller source G11.2-0.3. These were made using a least squares fit with statistical errors on binned points, the analysis is in Figure 6.4. The $\chi^2$ of these polynomial fits were calculated and show due to the poor statistics available neither hypothesis can be excluded. At E > 0.44 TeV, $\chi^2 = 2.26/20$ under the assumption of a single source and $\chi^2 = 1.15/18$ for a double source. A threshold was also applied to the data excluding all events below 1 TeV and the fitting process was repeated, in this case $\chi^2 = 1.03/20$ was calculated for a

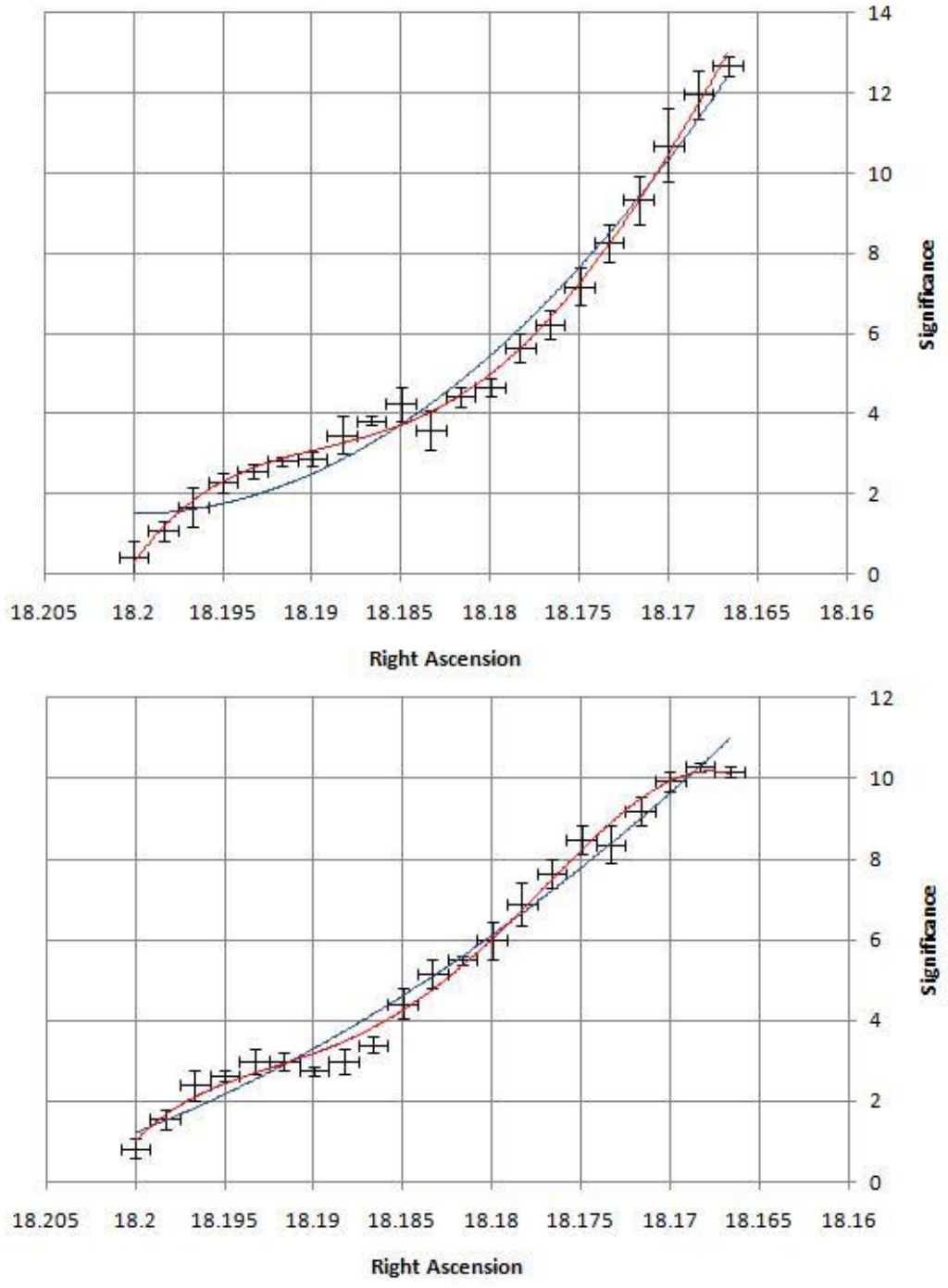


Figure 6.4: Showing the cross-section of the G11.2-0.3 nebula through a declination of -19.42 from a right ascension of 18h10m to 18h12m with a lower energy threshold of 0.44 TeV (above) and 1 TeV (below). A fit for a single (blue) and double (red) source is shown in each case.

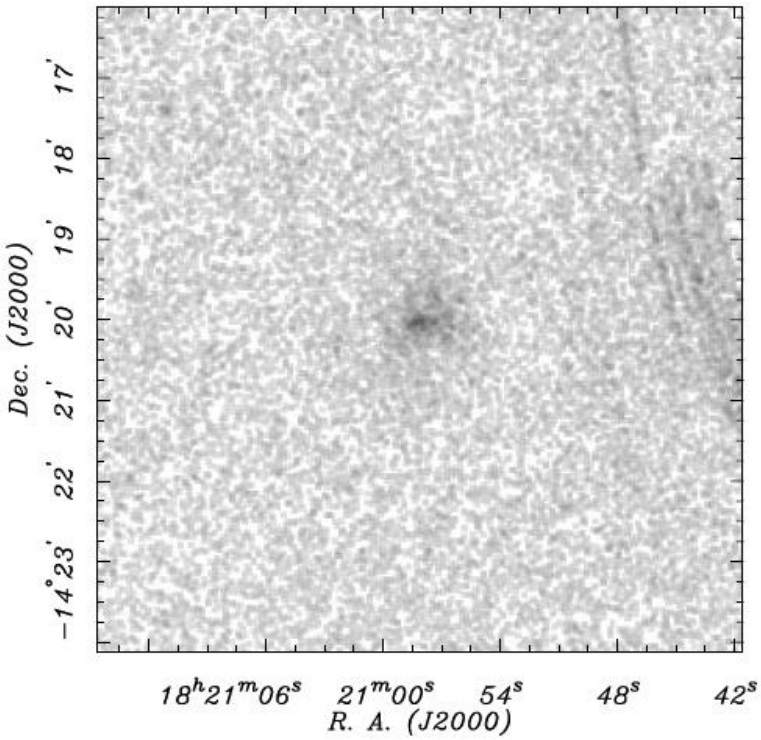


Figure 6.5: XMM-Newton X-ray image of the nebula G16.7+0.1 [99].

single source and $\chi^2 = 0.44/18$ for a double source, this is also seen in Figure 6.4.

## 6.2 HESS J1825-137

The other two nebulae under investigation in this chapter are close to a much larger, better known extended nebula, HESS J1825-137. Discussed in Section 4.2.3, this is the largest and oldest known pulsar wind nebula in the $\gamma$-ray regime and so the two nebulae under investigation are more distant from the centre of the main source and from the progenitor pulsar, PSR B1823-13 than is the case for G11.2-0.3. G16.7+0.1 is located southwest of PSR B1823-13 in the outer reaches in its emission, beyond the area analysed to demonstrate falloff in emission with distance from the progenitor pulsar as shown in Section 4.2.3 [20].

In contrast G18.5-0.4, otherwise known as the Eel nebula, is located to the north of HESS J1825-137, closer to its progenitor pulsar. The direction of emission in the nebula HESS J1825-137 mostly occurs towards the southwest of its progenitor

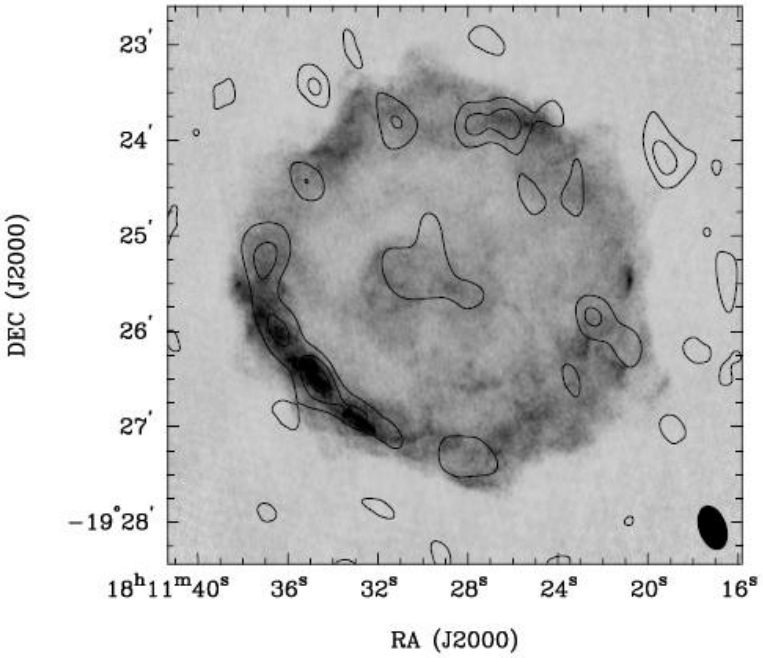


Figure 6.6: Radio image of G16.7+0.1 showing the surrounding SNR, 89 GHz data is shown in contours and 8.6 GHz shown in greyscale, taken from [44].

and so this emission region, although apparently part of the larger nebula, is not explained by the expected morphology of this source and as such represents the most promising candidate of the three to be observed as an independent pulsar wind nebula.

### 6.2.1 G16.7+0.1

The X-ray source G16.7+0.1 was most recently observed by Helfand et al [99] using the XMM-Newton satellite (see Figure 6.5). It is one of the faintest synchrotron nebulae yet detected due to its location at a distance of 10 kpc. As a result of this the nebula has a small angular extent of only 0.07° and it is more distant than the larger HESS J1825-137 nebula which is at 4.12 kpc.

The progenitor associated with G16.7+0.1 is yet to be observed, but a SNR shell is seen in the radio regime confirming the identification of the central nebula as a pulsar wind nebula [44] (see Figure 6.6). The central nebula has a luminosity of 1.1 $\times 10^{34}$ ergs/s and spectral index of 1.17 $\pm$ 0.29 [99] between 0.1 and 8 keV leading

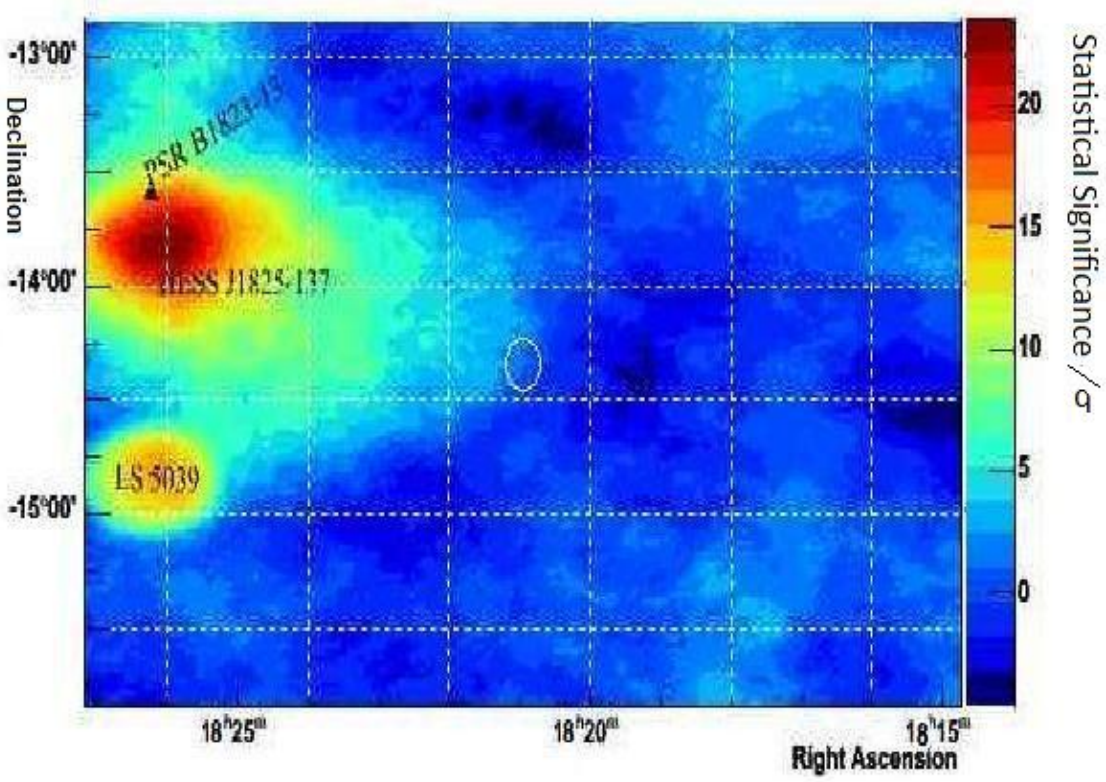


Figure 6.7: Showing the significance plot for the area surrounding the nebula G16.7+0.1 in the TeV $\gamma$-ray regime. The important other sources in the field of view are labelled appropriately and the extent of the on position for this source is marked with a while circle. It shows position of G16.7+0.1 at the edge of the emission region from HESS J1825-137.

to a predicted flux of $1.46 \times 10^{-13}$ ergs/s/cm$^2$ above 1 TeV if the magnetic field of this nebula is assumed to be in equipartition. This is close to the value obtained for the upper limit for this source of $2.12 \times 10^{-13}$ ergs/s/cm$^2$, but this could be an least in part due to the presence of emission from the outer reaches of HESS J1825-137.

To look for the nebula G16.7+0.1, archival HESS data for the region surrounding this nebula was analysed as both a point-like and an extended source, and upper limits obtained from both of these analyses can be seen in Section 5.3. In order to see the effect of being at the edge of the nebula, the point-like analysis for this object is shown in Figure 6.7, a significance of $\approx 3.5\ \sigma$ is obtained, however, as we can see most of this looks likely to be the result of emission from the large HESS

J1825-137 nebula.

By raising the threshold of events included in the analysis, the larger HESS J1825-137 nebula was shrunk, allowing any higher energy emission resulting from the smaller, more distant nebula G16.7+0.1 to be seen independent of the larger source. An analysis of the region surrounding G16.7+0.1 was undertaken with an energy cut of 1 TeV applied (rising from a threshold of 0.35 TeV in the original analysis) and is shown in Figure 6.8. No emission is seen from the area of the G16.7+0.1 nebula at such a threshold, indicating that the observed emission in this region forms part of the emission from the larger extended source HESS J1825-137. This is also shown in the cross-section of this nebula through the pulsar at a declination of -14.34° which is seen in Figure 6.9

The predicted flux of an order of magnitude lower than the derived upper limit for this nebula along with the large background surrounding this source makes it unlikely to be observed with the current generation of TeV Cherenkov observatories. However, this prediction was made by assuming the nebula is in equipartition which as we have seen may not be the case.

### 6.2.2 The Eel Nebula

The Eel Nebula, also known as G18.5-0.4, is the least well-observed at X-ray wavelengths of the three nebulae discussed in this Chapter, the only observations available being from ASCA [172] and Chandra [169]. In the X-ray regime it is separate from the nebula produced by PSR B1825-13 which corresponds to the nebula HESS J1825-137. However, as in the TeV regime this nebula is exceptionally extended, the X-ray emission in this area of the sky has been associated with the larger complex.

In Chapter 5 no prediction for the flux expected from this source was made as no spectral measurements from have been made with the current generation of X-ray telescopes (XMM-Newton and Chandra). However, older ASCA observations do give a power law spectrum of $\Gamma = 2.17 \pm 0.25$ with a integrated flux between 2 and 10 keV of $(8.27 \pm 0.24) \times 10^{-12}$ ergs/s/cm$^2$; the X-ray image is seen in Figure 6.10 [172]. These values can be used to predict a flux in the TeV $\gamma$-ray regime using the de Jager model [67] of $(2.5 \pm 0.5) \times 10^{-13}$ergs/s/cm$^2$ which given the number of

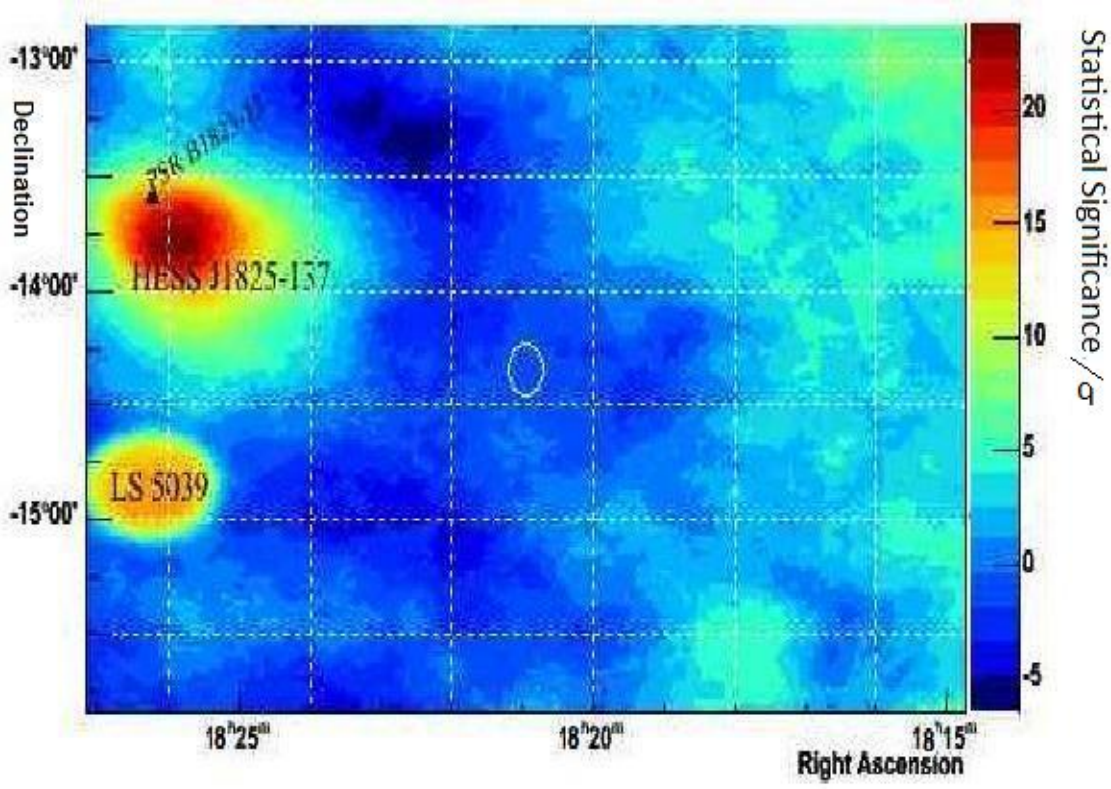


Figure 6.8: The significance plot for the area surrounding the nebula G16.7+0.1 in the TeV $\gamma$-ray regime when a 1 TeV energy cut is applied. The important other sources in the field of view are labelled and the extent of the 'ON' position for this source is marked with a white circle. It shows no evidence for emission corresponding to the position of known X-ray nebula G16.7+0.1.

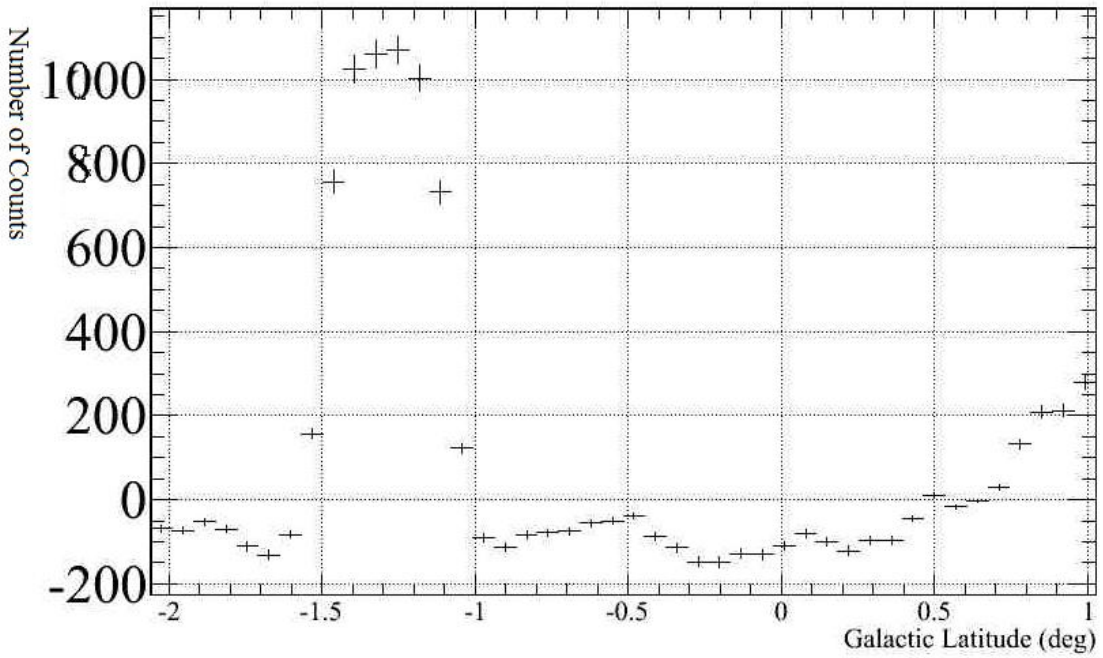


Figure 6.9: A cross-section through the G16.7+0.1 nebula at a Galactic longitude of 16.7° with a 1 TeV minimum energy cut applied. No emission is seen corresponding to the G16.7+0.1 nebula, located at 0.1° Galactic latitude.

observations available in this region implies that emission from this region is likely to be observed. The large error present in the prediction is due to an uncertainty in the distance to this source which is presently unknown, as the progenitor pulsar for this source has not been determined.

By increasing the energy threshold above which events are included in the analysis we hope to shrink the size of the nebula as we have done for the other sources under investigation in this Chapter. In this case we increase the energy threshold to 1 TeV and compare this to the nebula seen when no cut is applied corresponding to a lower energy threshold of 0.37 TeV. As we can see, when the analysis is done using all available VHE $\gamma$-ray data no gap is seen between HESS J1825-137 and the Eel Nebula (see Figure 6.11) while when a raised threshold of 1 TeV (see Figure 6.12) is applied a distinct gap between the nebulae is seen. Thus we show an independent nebula in the TeV $\gamma$-ray regime corresponding to the X-ray Eel nebula. This distinction is best shown in the cross-section through a right ascension of 256.54° as

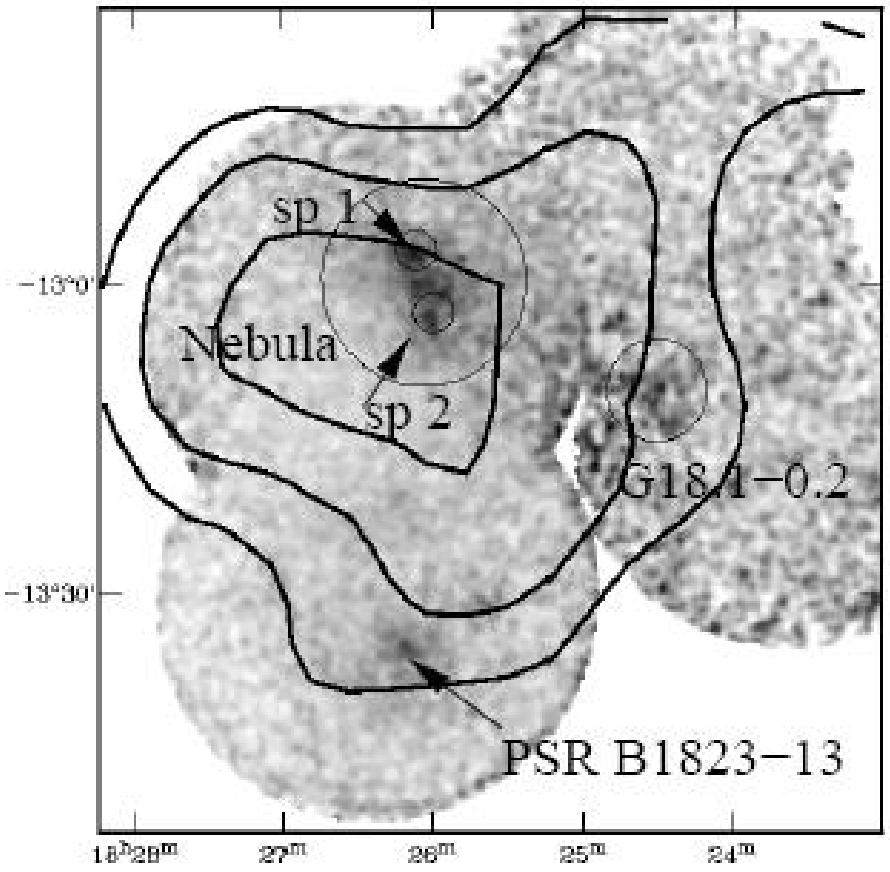


Figure 6.10: An ASCA X-ray image showing the area surrounding the Eel nebula. It shows the Eel (marked 'Nebula') and the nebula surrounding PSR B1823-23 as distinct X-ray nebulae. Black lines show the confidence intervals for the corresponding GeV source GeV1825-1310 [172].

seen in Figure 6.13, this shows a distinct gap, more than half the size of the adjacent Eel nebula between it and the larger HESS J1825-137.

In order to determine if the cross-section obtained from the Eel nebula could be best described as a single or double source the Eel Nebula was fit by both a second and fourth order polynomial. These were made using a least squares fit with statistical errors on binned points, the analysis is shown in Figure 6.14. The $\chi^2$ of these polynomial fits were calculated and a $\chi^2 = 38/14$ was obtained for a single source while $\chi^2 = 17/12$ was calculated for a double source, hence the source is much better described as two sources when seen at energies greater than 1 TeV. The source has a peak significance of 6.3 $\sigma$ for its emission above 1TeV. However,

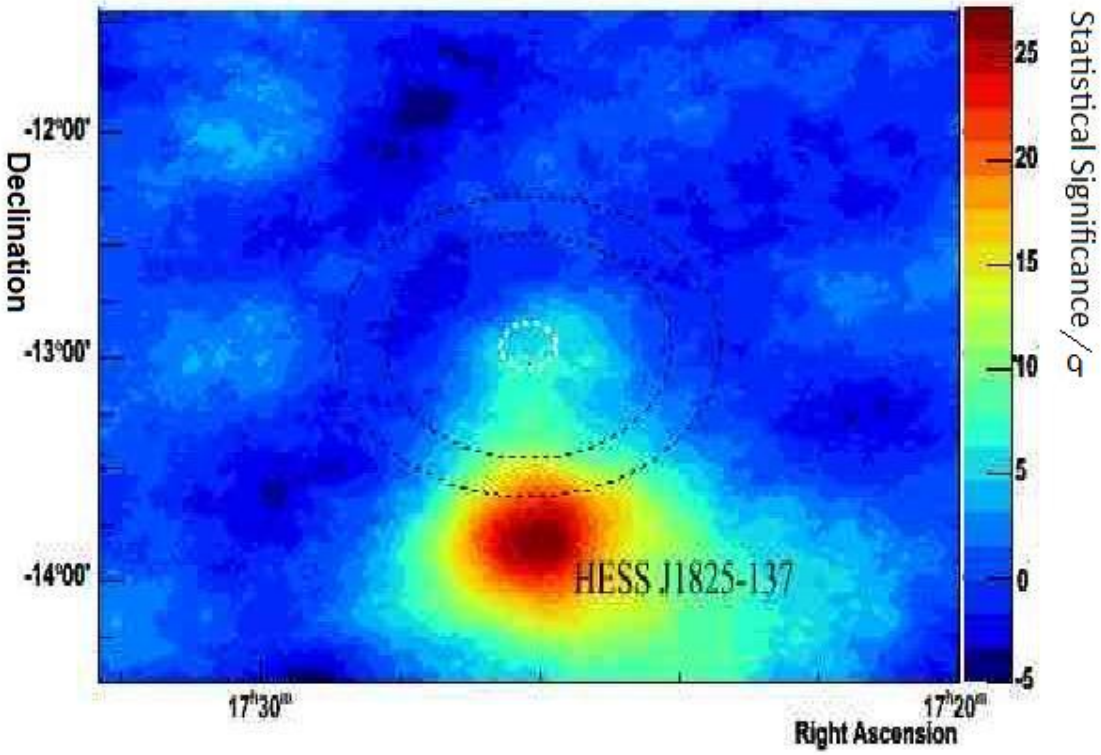


Figure 6.11: A skymap centred on the Eel Nebula with no lower energy cut applied.

as many analysis thresholds were applied to this source and the distinction between it and the larger adjacent nebula could only be seen when a 1 TeV energy threshold was applied a trials factor must be taken into account. This was calculated by using the 4 trials (one where no additional cut was applied and trails with cuts of 700 GeV, 1 TeV and 5 TeV) that were used to investigate the seperation of these nebulae. A seperation between the Eel and the adjacent nebulae was only seen when a 1 TeV energy cut was applied. An adjustment of the significance observed was made based on one successful trial out of a total of four, no other factors were taken into account in the calculation of this trials factor. After this adjustment a 5.9 $\sigma$ significance is seen, comfortably confirming its presence as an independent source in TeV $\gamma$-rays. It has a flux above 1 TeV of (3.9 $\pm$ 0.5) photons/cm$^2$/s.

A spectrum was then obtained from the observed nebula and shows a power law typical of a pulsar wind nebula with a spectral index of -2.33$\pm$0.2. This is somewhat higher than is seen in most pulsar wind nebula, close to the spectral index seen in the Crab nebula of -2.4. The spectrum is shown in Figure 6.15 and includes only data above 1 TeV as below this value the nebula from which these photons are derived cannot be determined due to the extension of HESS J1825-137 at low energies. Using the de Jager model detailed in Chapter 5 and the flux at 1 TeV of this source along with known X-ray data [172] it is possible to calculated the magnetic field strength of 20-30 $\mu$G for this source, typical of nebulae of this type. The uncertainty in this measurement is due to an uncertainty in the spectral index of this nebula in X-rays which is not determined in the ASCA observation used [172].

## 6.3 Untangling Adjacent Pulsar Wind Nebulae

In this Chapter we have attempted to disentangle pulsar wind nebulae from their larger more prominent neighbours and demonstrate that in some cases emission is coming from more than one source. This was attempted for three nebulae but of these, only one (the Eel nebula) was found to show distinct emission from its neighbouring source (HESS J1825-137). The Eel has a significance of 5.9 $\sigma$ and a flux above 1 TeV of (3.9 $\pm$ 0.5) $\times 10^{-13}$ photons/cm$^2$/s.

This source was established as a source independent of the nebula adjacent to it by increasing the analysis threshold. This technique could be used on other extended nebulae to determine if they can be split into separate components and indeed will be recommended to the HESS collaboration for this purpose.

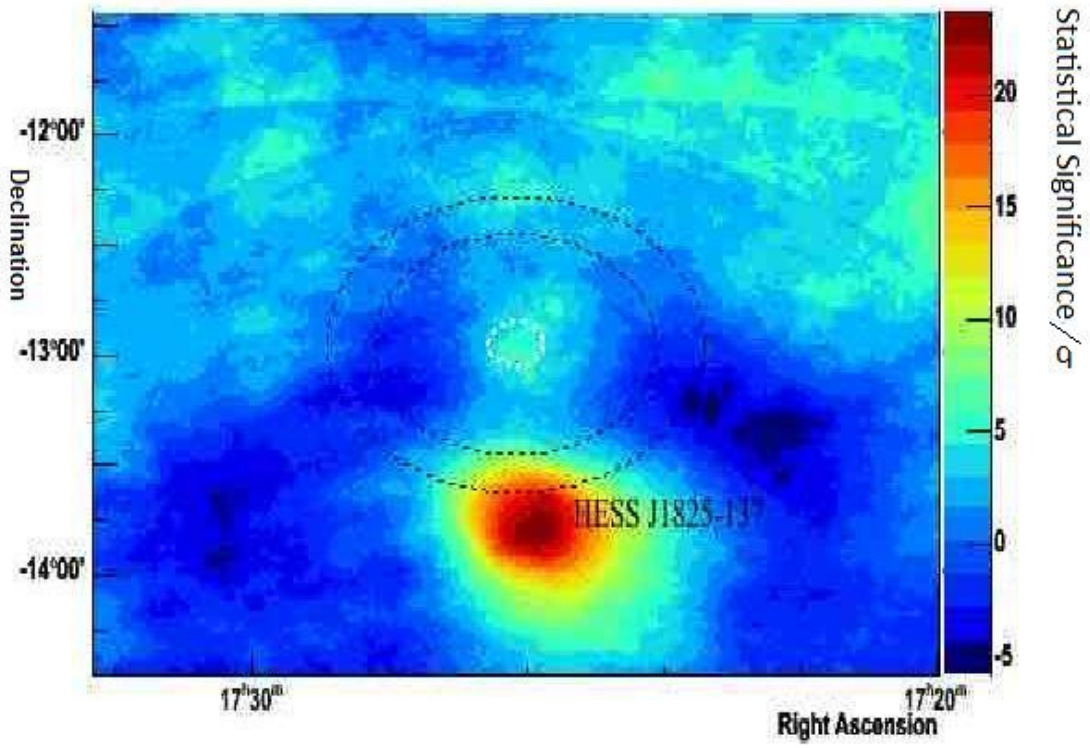


Figure 6.12: A skymap centered on the Eel Nebula with a 1 TeV lower energy cut applied.

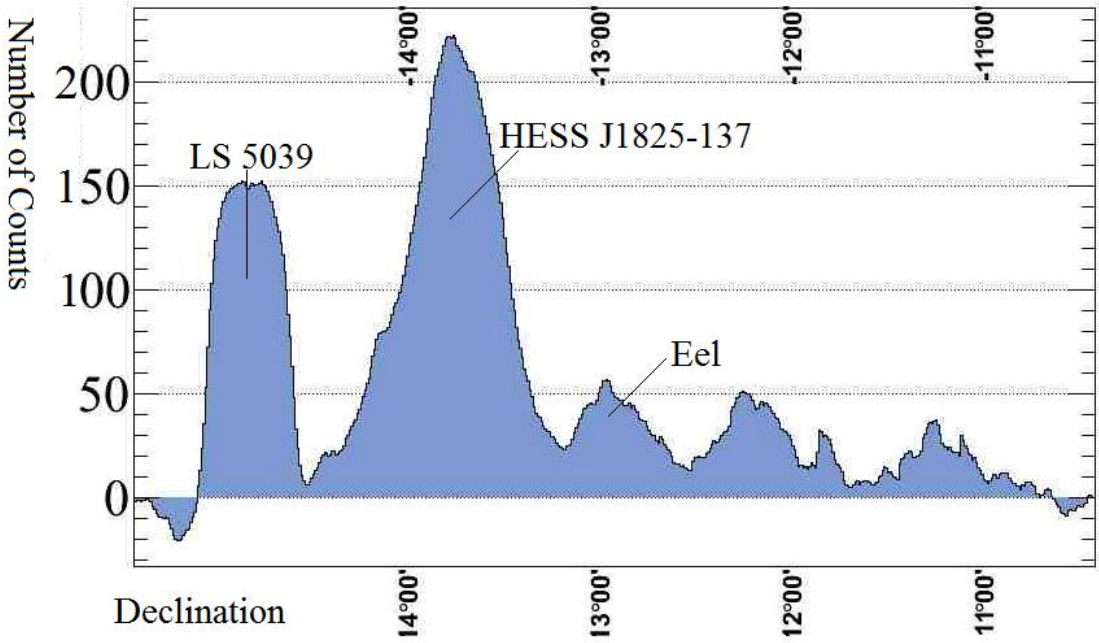


Figure 6.13: A cross-section applied through the Eel Nebula at a right ascension of 256.54° when a 1 TeV cut is applied to the data. In addition to the labelled peaks corresponding the Eel, HESS J1825-137 and LS 5039 there are peaks which show a similar number of counts to the Eel peak at approximately -12° and -11° which do not correspond to any known source. Although a similar count is seen at these points they correspond to an areas of observation with much less data than the area around the Eel peak, as a result there is a much higher error at these points and their significances are consistent with 0.

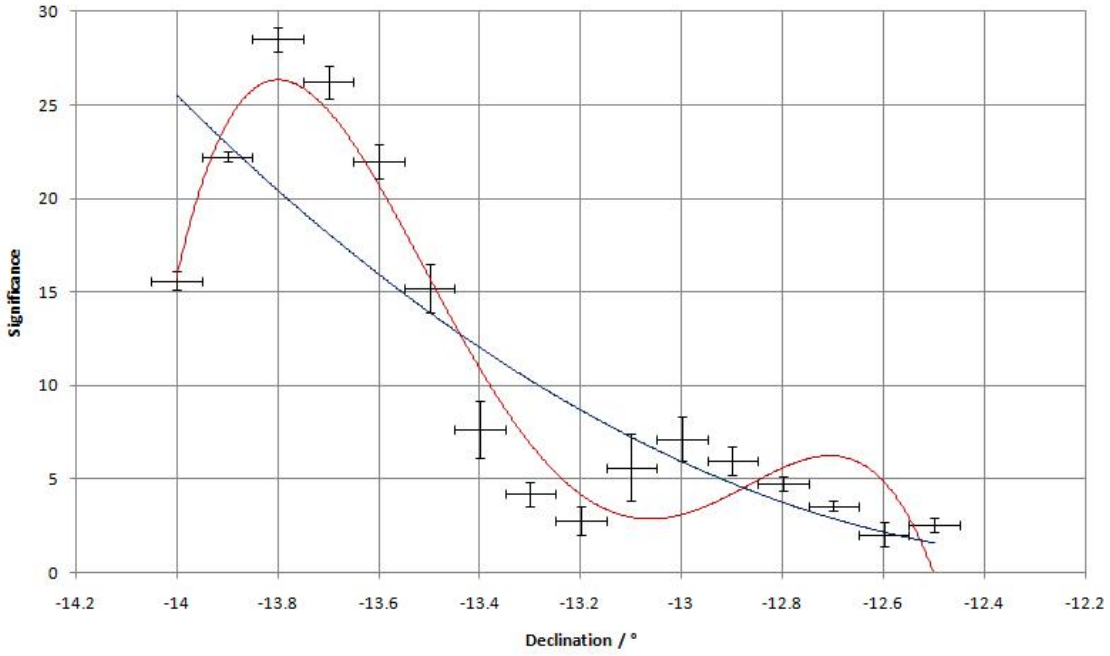


Figure 6.14: The cross-section applied through the Eel Nebula at a right ascension of 256.54° from a declination of -14 ° to -12.5 ° when a 1 TeV lower energy threshold is applied to the data. A fit for a single (blue) and double (red) source is shown.

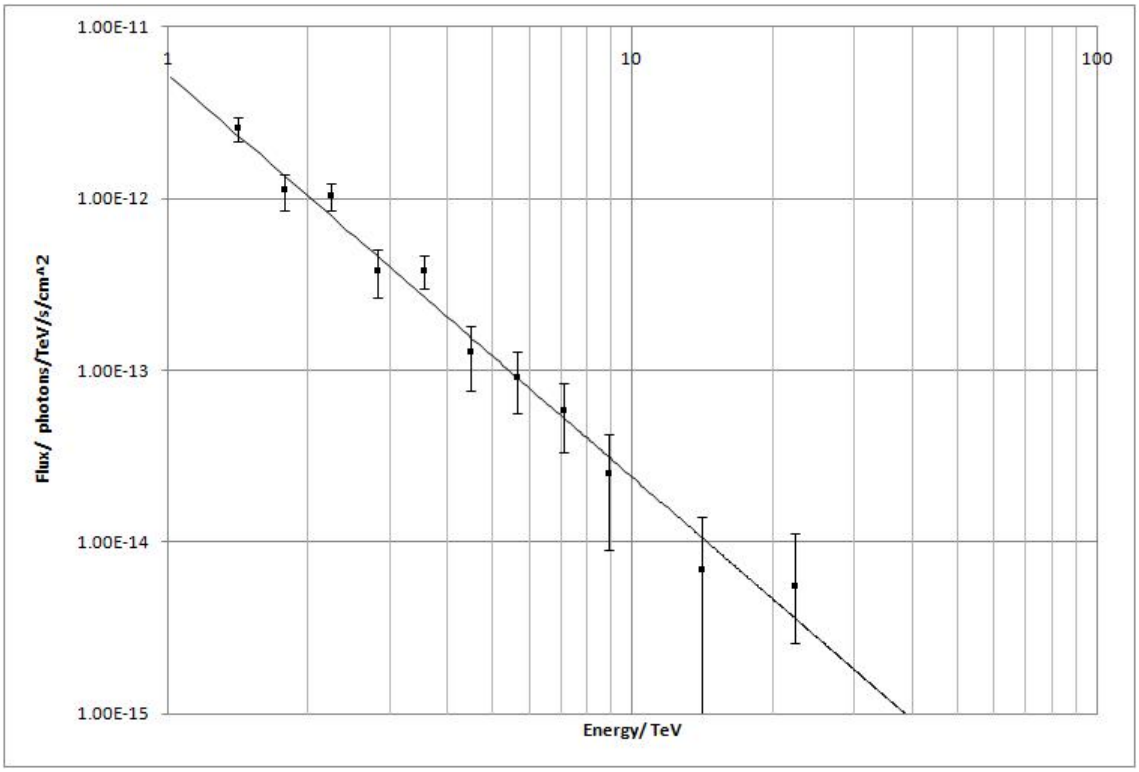


Figure 6.15: Showing the spectrum of the Eel nebula.

# Chapter 7

# Conclusions and Prospects for the Future

In this thesis I have discussed the pulsar wind nebulae of which TeV $\gamma$-ray observations have been made in order to attempt to find some new sources in this regime. This has been complemented by discussion of the theoretical background necessary to understand these observations. I have also tried to draw together all that is known about detected PWN and compare it to theoretical predictions concerning their development. In this Chapter I will summarise the theoretical and observational material presented throughout the thesis and comment on the conclusions that can be drawn from this. Additionally, we investigate the prospects for observing pulsar wind nebulae with the next generation Cherenkov instrument, CTA (The Cherenkov telescope array).

## 7.1 Pulsar Wind Nebulae in the TeV regime

As discussed in Chapter 2, pulsar wind nebulae are formed by the interaction of the relativistic electrons which are streaming out from the magnetic poles of a pulsar with the surrounding medium of a supernova remnant. The nebulae emit in all energy regimes from the radio to VHE $\gamma$-rays, but are largest in the VHE $\gamma$-ray regime; this is due to the nature of the emission observed in this regime. In most wavelengths the emission seen in pulsar wind nebulae is caused by synchrotron emission, while

in the VHE $\gamma$-ray regime the emission is the product of the inverse Compton process. These processes, along with the other methods by which non-thermal radiation can be produced were discussed in Section 1.3. Chapter 2 discussed the theoretical background of the expansion of pulsar wind nebulae into the ambient supernova remnant medium along with discussion of the nature of the development of pulsar wind nebula emission. This led on to Chapter 4 where a discussion of all known $\gamma$-ray pulsar wind nebulae was presented.

### 7.1.1 The Development of TeV Pulsar Wind Nebulae

The discussion of all known pulsar wind nebulae presented in Chapter 4 allowed a population study of the development of pulsar wind nebulae which have been observed at VHE $\gamma$-ray energies to be undertaken. This was however, somewhat limited by the number of sources that have been observed; only 23 are known and thus used in this study. These observations do however allow us to show the basic development of many properties of $\gamma$-ray pulsar wind nebulae.

The study of the development of the properties of focused on three observational properties of TeV pulsar wind nebula. The first to be investigated was the spectra of these objects. As inverse Compton emission and synchrotron emission are both dependent on the underlying electron spectrum, a relationship between the spectra seen from both of these processes is expected. To test this, I investigated the relationship between the X-ray spectrum between 0.5 and 8 keV and the $\gamma$-ray spectrum above 1 TeV. However, due to the errors associated with the measurement of these spectra in the published observations no relationship between the spectra observed in X-ray and the $\gamma$-ray could be observed or refuted. A study of the development of spectra in comparison with the characteristic age of the progenitor pulsar was also undertaken and it was found that the spectra of these objects does not vary with time in either the X-ray or the TeV $\gamma$-ray regime. This is interesting as it tells us that most of the emission observed in a TeV pulsar wind nebula is probably emitted from the central portion of the nebula adjacent to its progenitor pulsar, where the spectrum of the nebula is expected to remain constant.

Another important property of the VHE $\gamma$-ray pulsar wind nebulae that was

investigated in Chapter 4 was the development of the size of these nebulae. While the expansion of pulsar wind nebulae into their surrounding medium is fairly complex due to density variations in the medium into which the expansion occurs, it is interesting to note the general development of the nebulae by studying the change in their size when compared to the characteristic age of these sources. This was done using both the X-ray and $\gamma$-ray extent of the sources and it was shown that the size of the nebulae in X-rays became smaller with age while in $\gamma$-rays they increase with age. This is due to the nature of the underlying electron population which produces the emission in each waveband. The emission seen in the X-ray regime is the product of the highest energy electrons present in the nebula which produces the highest energy synchrotron photons. These electrons cool rapidly and so are not seen at large distances from the progenitor pulsar, which results in smaller nebulae as the pulsar output diminishes with age. In contrast older, cooled electrons are responsible for the emission observed in the VHE $\gamma$-ray regime and so these are seen much further from the progenitor pulsar. In older nebulae they have had more time to travel from the pulsar and so a larger nebula is observed.

The nature of the underlying electron population visible is also a factor in the final property of pulsar wind nebulae that was investigated in this study, the luminosity of the sources observed. In this case no link was seen between the age of the pulsar wind nebulae (again defined by their progenitors' characteristic age) and the luminosity of pulsar wind nebulae in the TeV $\gamma$-ray regime due to a large large number of factors which affect the emission as discussed in Section 4.4.3. In contrast a decay is seen in the luminosity of these nebulae in the X-ray regime due to the diminishing output of the progenitor pulsar. This agrees with the decline in pulsar output expected.

The forthcoming next generation Cherenkov telescope, CTA should allow many more pulsar wind nebulae to be discovered and as such will allow a more accurate population study to be conducted. It will also reduce the influence of selection effects on the study.

### 7.1.2 The Search for New TeV Pulsar Wind Nebulae associated with known X-ray Pulsar Wind Nebulae

Chapter 5 focused on an attempt to find the counterpart sources to known X-ray pulsar wind nebulae. This was conducted using archival HESS data from campaigns focusing on neighbouring known targets as well as from the HESS Galactic Plane survey [23]. Point-like and extended analysis was undertaken on all known X-ray pulsar wind nebulae for which archival HESS data were available and compared to predicted values calculated using the method presented by de Jager [67]. While none of the observations indicated a distinct nebula unequivocally associated with an X-ray source, a number did have upper limits close to predicted fluxes estimated and so a longer observation time may result in the positive detection of these sources in the TeV regime. They may also be good targets for observation with the next generation of Cherenkov telescopes.

In addition to calculating the upper limits for these sources in the TeV regime, the data obtained were used to investigate the magnetic fields of the pulsar wind nebulae studied. Where X-ray data and $\gamma$-ray upper limits were available, lower limits to the magnetic field strength could be obtained and compared to the field strength calculated by other means in the relevant published works. None of the previously published magnetic field predictions were excluded by this analysis.

A number of the sources were however highly significant; these were associated with the edges of neighbouring larger nebulae. An attempt to determine if the emission seen in these areas was associated with the nebula under investigation or the larger adjacent nebula was made in Chapter 6.

### 7.1.3 The Disambiguation of Pulsar Wind Nebulae

During the search for $\gamma$-ray emission from X-ray selected pulsar wind nebulae three targets were identified as having significance indicative of a detection due to their proximity to a larger extended pulsar wind nebula. In order to reduce the size of the larger companion nebulae to see only the young, highly energetic component immediately surrounding the progenitor pulsars, the energy threshold of the analysis

in each case was increased.

No emission was seen from two of the sources under investigation G11.2-0.3 and G16.7+0.1 independent of the larger sources with which they overlap. The third source, the Eel nebula, was observed as was a spectrum and morphology for this source above 1 TeV. It has a significance of 5.9 $\sigma$, a flux above 1 TeV of (3.9 $\pm$ 0.5) $\times 10^{-13}$ photons/cm$^2$/s and a spectral index of (-2.33 $\pm$ 0.2). This allowed the magnetic field strength for this object to be calculated as 20-30 $\mu$G. Further X-ray observations of this source may allow the magnetic field to be more accurately measured.

## 7.2 Future observations of Pulsar Wind Nebulae in the TeV

The work to build the next generation Cherenkov observatory, the Cherenkov Telescope Array (CTA) is underway. The increased sensitivity (a factor of 10), angular resolution ($\approx$ 0.1 arcmin) and several orders of magnitude ($\approx$ 10 GeV - 100 TeV) increase in observable energies compared to current instruments make the forthcoming CTA project an exciting prospect for future observations with detections of $\approx$ 1000 sources expected.

Twenty three pulsar wind nebulae have been observed with the current generation of Cherenkov telescopes, representing approximately a quarter of the known sources visible in the TeV $\gamma$-ray regime. In addition to this, many as yet unidentified dark sources may represent relic PWN and several of the binary systems observed are thought to have a pulsar wind nebula component to their emission, as in the case of LS 5039 [18]. As a consequence of this pulsar wind nebulae should provide a number of interesting CTA sources.

In young plerions such as G21.5-0.9 [50] where the SNR and PWN are still co-located, the angular resolution, which may be up to an order of magnitude better than HESS, will allow us to resolve these very high energy $\gamma$-ray objects for the first time and hence prove which part of the complex is responsible for the emission.

In older PWN, such as HESS J1825-137 [20], which have been the subject of

reverse shock crushing, the investigation of older electron populations could prove even more interesting. CTA observations could detect electron energy dependence as a function of distance from the progenitor pulsar. This would allow the point of inverse shock to be determined, giving a deeper insight into this process. No conclusive observations of these exist with the current generation of Cherenkov instruments, but they are thought to be produced when a PWN created by a fast moving progenitor pulsar is subject to inverse shock crushing [66].

The increased energy range of CTA would also be invaluable in the understanding of the inverse Compton emission mechanism which is thought to dominate pulsar wind nebulae. The broad energy range of CTA will allow the turnover point of many nebulae to be observed. So far this has only been observed in the nebulae Vela X [22] and the Crab [17]. This will allow the electron spectrum to be probed accurately while multiwavelength comparison with synchrotron turnover will allow accurate determination of the magnetic field and the underlying electron energy spectrum. Comparison between magnetic fields of different ages of nebulae will allow the evolution of these fields to be accurately studied.

The factor of 10 increase to sensitivity of the new array of telescopes will allow a much greater number of pulsar wind nebulae to be observed. A typical source of VHE $\gamma$-rays observed with HESS has a flux above 1 TeV in the order of $\approx 10^{-13}$ ergs/s/cm$^2$ and so the more sensitive CTA observatory should be able to see pulsar wind nebulae with fluxes predicted to occur in the $\approx 10^{-14}$ ergs/s/cm$^2$ range. Of the sources under investigation in Chapter 5, 3-5 sources would thus be visible within 30 hours of observation. A sensitivity curve showing the improvement is seen in Figure 7.1.

This includes sources such as G11.2-0.3 and G16.7+0.1 which were discussed in Chapter 5, the observation of which will also benefit from the increased angular resolution of the improved system because it will allow us to determine more accurately the origin of observed $\gamma$-rays in order to identify if they are indeed produced by the larger obscuring nebula near these sources or by these sources themselves. Additionally, sources such as G39.2-0.3 should be visible as it has the highest significance of the sources for which upper limits were calculated in Chapter 5 and is predicted to

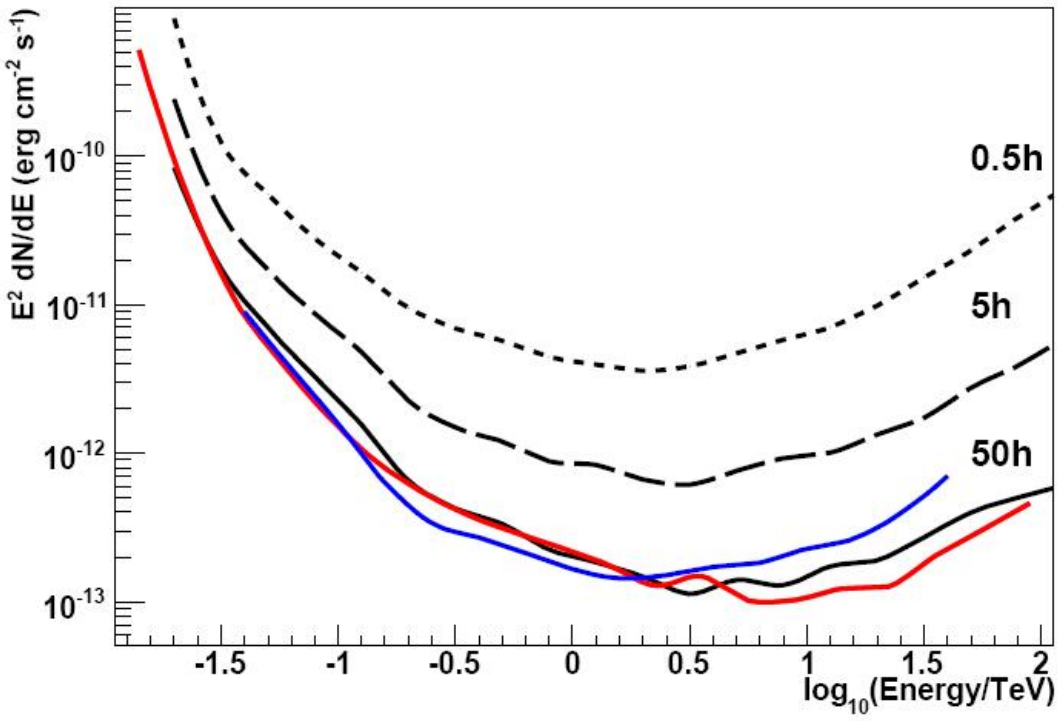


Figure 7.1: The projected sensitvity for a possible configuration of telescopes for CTA after 0.5 hours, 5 hours and 50 hours of observations [60]. For 50 hours of observation two differing analysis methods are shown (red and blue lines). HESS sensitivity after 50 hours is roughly equivalent to 0.5 hours of CTA observations.

have a flux of $2.99 \times 10^{-14}$ergs/s/cm$^2$ if its magnetic field is in equipartition. Some of the sources investigated may be visible depending on their magnetic field strength; an example of this is MSH 11-62 which will be visible if it is in equipartition but probably will not be observed if the higher magnetic field predicted of 70.0 $\mu$G [98] is present. However, as we have seen in Chapter 5 the equipartition derived estimates are not particularly reliable and so it is more likely that nebulae such as MSH 11-62 will not be visible. This demonstrates the need to look at more than one wavelength in order to truly understand the nature of the emission observed in this source.

## 7.3 Conclusion

The aim of this Thesis was to study the development of pulsar wind nebulae in the TeV regime and in so doing to uncover more sources which have as yet not been observed at these wavelengths. It was found that the extent of a pulsar wind nebula in the TeV $\gamma$-ray increased with its age as expected while no developmental relationship was seen concerning the luminosity or spectral index of the nebulae when observed in the TeV $\gamma$-ray regime, largely due to uncertainties in the measurments available.

TeV $\gamma$-ray upper limits were calculated for several nebulae previously observed in the X-ray regime using the *Chandra* satellite. This allowed the strength of their magnetic fields to be constrained but only one new source, which was confused with its companion was made, the Eel nebula.

Predictions of the fluxes of many of these sources were made from observations of their emission in X-rays and some of these sources should be uncovered with the next generation Cherenkov instrument, CTA.

# Bibliography

[1] A. A. Abdo, B. T. Allen, T. Aune, D. Berley, C. Chen, G. E. Christopher, T. DeYoung, B. L. Dingus, R. W. Ellsworth, M. M. Gonzalez, J. A. Goodman, E. Hays, C. M. Hoffman, P. H. Hüntemeyer, B. E. Kolterman, J. T. Linnemann, J. E. McEnery, T. Morgan, A. I. Mincer, P. Nemethy, J. Pretz, J. M. Ryan, P. M. Saz Parkinson, A. Shoup, G. Sinnis, A. J. Smith, V. Vasileiou, G. P. Walker, D. A. Williams, and G. B. Yodh. Milagro Observations of Multi-TeV Emission from Galactic Sources in the Fermi Bright Source List. *Astrophysical Jounal Letters*, 700:L127, August 2009.

[2] A. A. Abdo and the Fermi Collaboration. The Fermi Gamma-Ray Space Telescope Discovers the Pulsar in the Young Galactic Supernova Remnant CTA 1. *Science*, 322:1218–, November 2008.

[3] A. A. Abdo and the Fermi Collaboration. Detection of 16 Gamma-Ray Pulsars Through Blind Frequency Searches Using the Fermi LAT. *Science*, 325:840, August 2009.

[4] A. A. Abdo and The Fermi collaboration. Pulsed Gamma-rays from PSR J2021+3651 with the Fermi Large Area Telescope. *Astrophysical Journal*, 700:1059, August 2009.

[5] A. A. Abdo and The Fermi collaboration. Fermi Large Area Telescope Observations of the Crab Pulsar And Nebula. *Astrophysical Journal*, 708:1254, January 2010.

[6] V. A. Acciari and The VERITAS collaboration. Discovery of Very High Energy $\gamma$-ray Emission from the SNR G54.1+0.3.

[7] V. A. Acciari and The VERITAS collaboration. Observation of Extended Very High Energy Emission from the Supernova Remnant IC 443 with VERITAS. *Astrophysical Jounal Letters*, 698:L133, June 2009.

[8] F. Acero and The HESS Collaboration. Detection of Gamma Rays from a Starburst Galaxy. *Science*, 326:1080, November 2009.

[9] F. Acero and the HESS collaboration. Localizing the VHE $\gamma$-ray source at the Galactic Centre. *Monthly Notices of the Royal Astronomical Society*, page 1915, December 2009.

[10] F. Aharonian, A. Akhperjanian, M. Beilicke, K. Bernlöhr, H.-G. Börst, H. Bojahr, O. Bolz, T. Coarasa, J. L. Contreras, J. Cortina, S. Denninghoff, M. V. Fonseca, M. Girma, N. Götting, G. Heinzelmann, G. Hermann, A. Heusler, W. Hofmann, D. Horns, I. Jung, R. Kankanyan, M. Kestel, A. Kohnle, A. Konopelko, D. Kranich, H. Lampeitl, M. Lopez, E. Lorenz, F. Lucarelli, O. Mang, D. Mazin, H. Meyer, R. Mirzoyan, A. Moralejo, E. Oña-Wilhelmi, M. Panter, A. Plyasheshnikov, G. Pühlhofer, R. de los Reyes, W. Rhode, J. Ripken, G. Rowell, V. Sahakian, M. Samorski, M. Schilling, M. Siems, D. Sobzynska, W. Stamm, M. Tluczykont, V. Vitale, H. J. Völk, C. A. Wiedner, and W. Wittek. The Crab Nebula and Pulsar between 500 GeV and 80 TeV: Observations with the HEGRA Stereoscopic Air Cerenkov Telescopes. *Astrophysical Journal*, 614:897–913, October 2004.

[11] F. Aharonian and the HESS collaboration. A New Population of Very High Energy Gamma-Ray Sources in the Milky Way. *Science*, 307:1938, March 2005.

[12] F. Aharonian and The HESS collaboration. Discovery of extended VHE gamma-ray emission from the asymmetric pulsar wind nebula in MSH 15-52 with HESS. *Astronomy and Astrophysics*, 435:L17, May 2005.

[13] F. Aharonian and the HESS collaboration. H.E.S.S. observations of PKS 2155-304. *Astronomy and Astrophysics*, 430:865, February 2005.

[14] F. Aharonian and The HESS collaboration. Serendipitous discovery of the unidentified extended TeV $\gamma$-ray source HESS J1303-631. *Astronomy and Astrophysics*, 439:1013–1021, September 2005.

[15] F. Aharonian and The HESS collaboration. Very high energy gamma rays from the composite SNR G 0.9+0.1. *Astronomy and Astrophysics*, 432:L25, March 2005.

[16] F. Aharonian and The HESS collaboration. Very high energy gamma rays from the composite SNR G 0.9+0.1. *Astronomy and Astrophysics*, 432:L25, March 2005.

[17] F. Aharonian and the HESS collaboration. *Astronomy and Astrophysics*, 457:899, October 2006.

[18] F. Aharonian and The HESS Collaboration. 3.9 day orbital modulation in the TeV $\gamma$-ray flux and spectrum from the X-ray binary LS 5039. *Astronomy and Astrophysics*, 460:743, December 2006.

[19] F. Aharonian and The HESS collaboration. Discovery of the two "wings" of the Kookaburra complex in VHE $\gamma$-rays with HESS. *Astronomy and Astrophysics*, 456:245, September 2006.

[20] F. Aharonian and The HESS collaboration. Energy dependent $\gamma$-ray morphology in the pulsar wind nebula HESS J1825-137. *Astronomy and Astrophysics*, 460:365, December 2006.

[21] F. Aharonian and The HESS Collaboration. Fast Variability of Tera-Electron Volt $\gamma$ Rays from the Radio Galaxy M87. *Science*, 314:1424, December 2006.

[22] F. Aharonian and the HESS collaboration. First detection of a VHE gamma-ray spectral maximum from a cosmic source: HESS discovery of the Vela X nebula. *Astronomy and Astrophysics*, 448:L43, March 2006.

[23] F. Aharonian and the HESS collaboration. The H.E.S.S. Survey of the Inner Galaxy in Very High Energy Gamma Rays. *Astrophysical Journal*, 636:777, January 2006.

[24] F. Aharonian and the HESS Collaboration. Detection of extended very-high-energy $\gamma$-ray emission towards the young stellar cluster Westerlund 2. *Astronomy and Astrophysics*, 467:1075, June 2007.

[25] F. Aharonian and The HESS collaboration. Discovery of two candidate pulsar wind nebulae in very-high-energy gamma rays. *Astronomy and Astrophysics*, 472:489, September 2007.

[26] F. Aharonian and The HESS collaboration. Discovery of a VHE gamma-ray source coincident with the supernova remnant CTB 37A. *Astronomy and Astrophysics*, 490:685, November 2008.

[27] F. Aharonian and The HESS collaboration. Discovery of very high energy gamma-ray emission coincident with molecular clouds in the W 28 (G6.4-0.1) field. *Astronomy and Astrophysics*, 481:401, April 2008.

[28] F. Aharonian and the HESS collaboration. HESS very-high-energy gamma-ray sources without identified counterparts. *Astronomy and Astrophysics*, 477:353, January 2008.

[29] F. Aharonian and The HESS collaboration. Detection of very high energy radiation from HESS J1908+063 confirms the Milagro unidentified source MGRO J1908+06. *Astronomy and Astrophysics*, 499:723, June 2009.

[30] F. Aharonian and the HESS collaboration. Discovery of Very High Energy $\gamma$-Ray Emission from Centaurus a with H.E.S.S. *Astrophysical Jounal Letters*, 695:L40, April 2009.

[31] F. Aharonian and the HESS collaboration. Simultaneous multiwavelength observations of the second exceptional $\gamma$-ray flare of PKS 2155-304 in July 2006. *Astronomy and Astrophysics*, 502:749, August 2009.

[32] F. A. Aharonian. *Very high energy cosmic gamma radiation : a crucial window on the extreme Universe, World Scientific.* 2004.

[33] J. Albert and the MAGIC collaboration. Discovery of Very High Energy Gamma Radiation from IC 443 with the MAGIC Telescope. *Astrophysical Journal Letters*, 664:L87, August 2007.

[34] J. Albert and the MAGIC collaboration. VHE $\gamma$-Ray Observation of the Crab Nebula and its Pulsar with the MAGIC Telescope. *Astrophysical Journal*, 674:1037, February 2008.

[35] W. B. Atwood and the Fermi collaboration. The Large Area Telescope on the Fermi Gamma-Ray Space Telescope Mission. *Astrophysical Journal*, 697:1071–1102, June 2009.

[36] W. B. Atwood and the GLAST Collaboration. Gamma Large Area Silicon Telescope (GLAST) applying silicon strip detector technology to the detection of gamma rays in space. *Nuclear Instruments and Methods in Physics Research A*, 342:302, March 1994.

[37] W. Baade and F. Zwicky. Remarks on Super-Novae and Cosmic Rays. *Physical Review*, 46:76, July 1934.

[38] D. Berge, S. Funk, and J. Hinton. Background modelling in very-high-energy $\gamma$-ray astronomy. *Astronomy and Astrophysics*, 466:1219, May 2007.

[39] K. Bernlöhr. Private Communication, 2009.

[40] R. M. Bionta, G. Blewitt, C. B. Bratton, D. Caspere, and A. Ciocio. Observation of a neutrino burst in coincidence with supernova 1987A in the Large Magellanic Cloud. *Physical Review Letters*, 58:1494, April 1987.

[41] J. A. Blazek, B. M. Gaensler, S. Chatterjee, E. van der Swaluw, F. Camilo, and B. W. Stappers. The Duck Redux: An Improved Proper-Motion Upper Limit for the Pulsar B1757-24 near the Supernova Remnant G5.4-1.2. *Astrophysical Journal*, 652:1523, December 2006.

[42] J. M. Blondin, R. A. Chevalier, and D. M. Frierson. Pulsar Wind Nebulae in Evolved Supernova Remnants. *Astrophysical Journal*, 563:806, December 2001.

[43] F. Bocchino, E. van der Swaluw, R. Chevalier, and R. Bandiera. The nature of the X-ray halo of the plerion G21.5-0.9 unveiled by XMM-Newton and Chandra. *Astronomy and Astrophysics*, 442:539, November 2005.

[44] D. C.-J. Bock and B. M. Gaensler. Measurement of Spectral Breaks in Pulsar Wind Nebulae with Millimeter-Wave Interferometry. *Astrophysical Journal*, 626:343, June 2005.

[45] T. M. Braje, R. W. Romani, M. S. E. Roberts, and N. Kawai. Chandra Imaging of the Gamma-Ray Source GeV J1809-2327. *Astrophysical Jounal Letters*, 565:L91, February 2002.

[46] D. N. Burrows, J. E. Hill, J. A. Nousek, A. A. Wells, A. D. Short, R. Willingale, O. Citterio, G. Chincarini, and G. Tagliaferri. Swift X-Ray Telescope. In K. A. Flanagan & O. H. Siegmund, editor, *Society of Photo-Optical Instrumentation Engineers (SPIE) Conference Series*, volume 4140 of *Presented at the Society of Photo-Optical Instrumentation Engineers (SPIE) Conference*, page 64, December 2000.

[47] F. Camilo, V. M. Kaspi, A. G. Lyne, R. N. Manchester, J. F. Bell, N. D'Amico, N. P. F. McKay, and F. Crawford. Discovery of Two High Magnetic Field Radio Pulsars. *Astrophysical Journal*, 541:367, September 2000.

[48] F. Camilo, D. R. Lorimer, N. D. R. Bhat, E. V. Gotthelf, J. P. Halpern, Q. D. Wang, F. J. Lu, and N. Mirabal. Discovery of a 136 Millisecond Radio and X-Ray Pulsar in Supernova Remnant G54.1+0.3. *Astrophysical Jounal Letters*, 574:L71, July 2002.

[49] F. Camilo, S. M. Ransom, B. M. Gaensler, and D. R. Lorimer. Discovery of the Energetic Pulsar J1747-2809 in the Supernova Remnant G0.9+0.1. *Astrophysical Jounal Letters*, 700:L34, July 2009.

[50] F. Camilo, S. M. Ransom, B. M. Gaensler, P. O. Slane, D. R. Lorimer, J. Reynolds, R. N. Manchester, and S. S. Murray. PSR J1833-1034: Discovery of the Central Young Pulsar in the Supernova Remnant G21.5-0.9. *Astrophysical Journal*, 637:456, January 2006.

[51] B. W. Carroll and D. A. Ostlie. *An introduction to modern astrophysics and cosmology, Pearson*. July 2006.

[52] O. Celik. Observations of the Crab Nebula and Pulsar with VERITAS. In *International Cosmic Ray Conference*, volume 2 of *International Cosmic Ray Conference*, page 847, 2008.

[53] P. M. Chadwick, K. Lyons, T. J. L. McComb, K. J. Orford, J. L. Osborne, S. M. Rayner, S. E. Shaw, K. E. Turver, and G. J. Wieczorek. Very High Energy Gamma Rays from PKS 2155-304. *Astrophysical Journal*, 513:161, March 1999.

[54] Y. Chen, Q. D. Wang, E. V. Gotthelf, B. Jiang, Y.-H. Chu, and R. Gruendl. Chandra ACIS Spectroscopy of N157B: A Young Composite Supernova Remnant in a Superbubble. *Astrophysical Journal*, 651:237, November 2006.

[55] K. S. Cheng, C. Ho, and M. Ruderman. Energetic radiation from rapidly spinning pulsars. I - Outer magnetosphere gaps. II - VELA and Crab. *Astrophysical Journal*, 300:500, January 1986.

[56] R. A. Chevalier. The interaction of supernovae with the interstellar medium. *Annual Reviews of Astronomy and Astrophysics*, 15:175, 1977.

[57] D. H. Clark, P. Murdin, R. Wood, R. Gilmozzi, J. Danziger, and A. W. Furr. Three-dimensional structure of the Crab Nebula. *Monthly Notices of the Royal Astronomical Society*, 204:415, July 1983.

[58] T. R. Clifton and A. G. Lyne. High-radio-frequency survey for young and millisecond pulsars. *Nature*, 320:43, March 1986.

[59] I. Contopoulos and C. Kalapotharakos. The pulsar synchrotron in 3D: curvature radiation. *Monthly Notices of the Royal Astronomical Society*, page 381, March 2010.

[60] The CTA Consortium. Design Concepts for the Cherenkov Telescope Array. *ArXiv e-prints*, August 2010.

[61] N. D'Amico, V. M. Kaspi, R. N. Manchester, F. Camilo, A. G. Lyne, A. Possenti, I. H. Stairs, M. Kramer, F. Crawford, J. F. Bell, N. P. F. McKay, B. M. Gaensler, and M. S. E. Roberts. Two Young Radio Pulsars Coincident with EGRET Sources. *Astrophysical Jounal Letters*, 552:L45, May 2001.

[62] D. Darling. www.daviddarling.info/encyclopedia/B/binding_energy.html - Binding Energy.

[63] J. K. Daugherty and A. K. Harding. Electromagnetic cascades in pulsars. *Astrophysical Journal*, 252:337, January 1982.

[64] J. M. Davies and E. S. Cotton. Design of the quartermaster solar furnace. *Solar Energy*, 1:16, 1957.

[65] O. C. de Jager, S. E. S. Ferreira, and A. Djannati-Ataï. MHD and Radiation Modelling of G21.5-0.9. In F. A. Aharonian, W. Hofmann, & F. Rieger, editor, *American Institute of Physics Conference Series*, volume 1085 of *American Institute of Physics Conference Series*, page 199, December 2008.

[66] O. C. de Jager, S. E. S. Ferreira, A. Djannati-Ataï, M. Dalton, C. Deil, K. Kosack, M. Renaud, U. Schwanke, and O. Tibolla. Unidentified Gamma-Ray Sources as Ancient Pulsar Wind Nebulae. *ArXiv e-prints*, June 2009.

[67] O. C. de Jager, A. K. Harding, and et al. The Expected Flux of TeV Photons from Plerions. In *International Cosmic Ray Conference*, volume 2 of *International Cosmic Ray Conference*, page 528, 1995.

[68] A. J. Dean, A. de Rosa, V. A. McBride, R. Landi, A. B. Hill, L. Bassani, A. Bazzano, A. J. Bird, and P. Ubertini. INTEGRAL observations of PSR J1811-1925 and its associated pulsar wind nebula. *Monthly Notices of the Royal Astronomical Society*, 384:L29, February 2008.

[69] C. D. Dermer and G. Menon. *High Energy Radiation from Black Holes: Gamma Rays, Cosmic Rays, and Neutrinos*. November 2009.

[70] H. J. Dickinson. PhD Thesis - Very High Energy Gamma-Rays from Binary Systems, 2009.

[71] A. Djannati-Atai. cxc.harvard.edu/cdo/snr09/pres/DjannatiAtai_Arache_v2.pdf.

[72] A. Djannati-Ataĭ, O. C. de Jager, R. Terrier, and et al. New Companions for the lonely Crab? VHE emission from young pulsar wind nebulae revealed by H.E.S.S. In *International Cosmic Ray Conference*, volume 2 of *International Cosmic Ray Conference*, page 823, 2008.

[73] R. Dodson, D. Legge, J. E. Reynolds, and P. M. McCulloch. The Vela Pulsar's Proper Motion and Parallax Derived from VLBI Observations. *Astrophysical Journal*, 596:1137, October 2003.

[74] R. G. Dodson, P. M. McCulloch, and D. R. Lewis. High Time Resolution Observations of the January 2000 Glitch in the Vela Pulsar. *Astrophysical Jounal Letters*, 564:L85, January 2002.

[75] I. Du Plessis, O. C. de Jager, S. Buchner, H. I. Nel, A. R. North, B. C. Raubenheimer, and D. J. van der Walt. The Nonthermal Radio, X-Ray, and TeV Gamma-Ray Spectra of MSH 15-52. *Astrophysical Journal*, 453:746, November 1995.

[76] R. Enomoto. Status of CANGAROO-III. In F. A. Aharonian, W. Hofmann, & F. Rieger, editor, *American Institute of Physics Conference Series*, volume 1085 of *American Institute of Physics Conference Series*, page 661, December 2008.

[77] G. G. Fazio, H. F. Helmken, E. O'Mongain, and T. C. Weekes. Detection of High-Energy Gamma Rays from the Crab Nebula. *Astrophysical Jounal Letters*, 175:L117, August 1972.

[78] G. J. Feldman and R. D. Cousins. Unified approach to the classical statistical analysis of small signals. *Physics Review D*, 57:3873, April 1998.

[79] E. Fermi. Galactic Magnetic Fields and the Origin of Cosmic Radiation. *Astrophysical Journal*, 119:1, January 1954.

[80] The Fermi-LAT Collaboration. Fermi Large Area Telescope First Source Catalog. *ArXiv e-prints*, February 2010.

[81] J. A. Frieman, M. S. Turner, and D. Huterer. Dark Energy and the Accelerating Universe. *Annual Reviews of Astronomy and Astrophysics*, 46:385, September 2008.

[82] C. L. Fryer. Mass Limits For Black Hole Formation. *Asrophysical Journal*, 522:413–418, September 1999.

[83] S. Funk, G. Hermann, J. Hinton, D. Berge, K. Bernlöhr, W. Hofmann, P. Nayman, F. Toussenel, and P. Vincent. The trigger system of the H.E.S.S. telescope array. *Astroparticle Physics*, 22:285, November 2004.

[84] B. M. Gaensler, K. T. S. Brazier, R. N. Manchester, S. Johnston, and A. J. Green. SNR G320.4-01.2 and PSR B1509-58: new radio observations of a complex interacting system. *Monthly Notices of the Royal Astronomical Society*, 305:724, May 1999.

[85] B. M. Gaensler, N. S. Schulz, V. M. Kaspi, M. J. Pivovaroff, and W. E. Becker. XMM-Newton Observations of PSR B1823-13: An Asymmetric Synchrotron Nebula around a Vela-like Pulsar. *Astrophysical Journal*, 588:441, May 2003.

[86] B. M. Gaensler and P. O. Slane. The Evolution and Structure of Pulsar Wind Nebulae. *Annual Reviews of Astronomy and Astrophysics*, 44:17, September 2006.

[87] B. M. Gaensler, E. van der Swaluw, F. Camilo, V. M. Kaspi, F. K. Baganoff, F. Yusef-Zadeh, and R. N. Manchester. The Mouse that Soared: High-Resolution X-Ray Imaging of the Pulsar-powered Bow Shock G359.23-0.82. *Astrophysical Journal*, 616:383, November 2004.

[88] F. P. Gavriil, M. E. Gonzalez, E. V. Gotthelf, V. M. Kaspi, M. A. Livingstone, and P. M. Woods. Magnetar-Like Emission from the Young Pulsar in Kes 75. *Science*, 319:1802, March 2008.

[89] R. Giacconi, G. Branduardi, U. Briel, A. Epstein, D. Fabricant, E. Feigelson, W. Forman, P. Gorenstein, J. Grindlay, H. Gursky, F. R. Harnden, J. P. Henry,

C. Jones, E. Kellogg, D. Koch, S. Murray, E. Schreier, F. Seward, H. Tananbaum, K. Topka, L. Van Speybroeck, S. S. Holt, R. H. Becker, E. A. Boldt, P. J. Serlemitsos, G. Clark, C. Canizares, T. Markert, R. Novick, D. Helfand, and K. Long. The Einstein HEAO 2 X-ray Observatory. *Astrophysical Journal*, 230:540, June 1979.

[90] V. L. Ginzburg and S. I. Syrovatskii. Cosmic Magnetobremsstrahlung (synchrotron Radiation). *Annual Reviews of Astronomy and Astrophysics*, 3:297, 1965.

[91] P. Gondoin, B. Aschenbach, C. Erd, D. H. Lumb, S. Majerowicz, D. Neumann, and J. L. Sauvageot. In-orbit calibration of the XMM-Newton telescopes. In K. A. Flanagan & O. H. Siegmund, editor, *Society of Photo-Optical Instrumentation Engineers (SPIE) Conference Series*, volume 4140 of *Presented at the Society of Photo-Optical Instrumentation Engineers (SPIE) Conference*, page 1, December 2000.

[92] M. E. Gonzalez, V. M. Kaspi, M. J. Pivovaroff, and B. M. Gaensler. Chandra and XMM-Newton Observations of the Vela-like Pulsar B1046-58. *Astrophysical Journal*, 652:569, November 2006.

[93] E. V. Gotthelf and J. P. Halpern. Discovery of a Young, Energetic 70.5 ms Pulsar Associated with the TeV Gamma-Ray Source HESS J1837-069. *Astrophysical Journal*, 681:515, July 2008.

[94] E. V. Gotthelf and J. P. Halpern. Discovery of a Highly Energetic X-Ray Pulsar Powering HESS J1813-178 in the Young Supernova Remnant G12.82-0.02. *Astrophysical Jounal Letters*, 700:L158, August 2009.

[95] Y. Gupta, D. Mitra, D. A. Green, and A. Acharyya. The discovery of PSR J1833-1034 : the pulsar associated with the supernova remnant G21.5-0.9. *Current Science*, 89:853, August 2005.

[96] H. E. S. S. Collaboration: A. Djannati-Atai, O. C. De Jager, R. Terrier, Y. A. Gallant, and S. Hoppe. New Companions for the lonely Crab? VHE emission

from young pulsar wind nebulae revealed by H.E.S.S. *ArXiv e-prints*, October 2007.

[97] J. P. Halpern, F. Camilo, E. V. Gotthelf, D. J. Helfand, M. Kramer, A. G. Lyne, K. M. Leighly, and M. Eracleous. PSR J2229+6114: Discovery of an Energetic Young Pulsar in the Error Box of the EGRET Source 3EG J2227+6122. *Astrophysical Jounal Letters*, 552:L125, May 2001.

[98] I. M. Harrus, J. P. Hughes, K. P. Singh, K. Koyama, and I. Asaoka. Interpretation of the Center-filled Emission from the Supernova Remnant W44. *Astrophysical Journal*, 488:781, October 1997.

[99] D. J. Helfand, M. A. Agüeros, and E. V. Gotthelf. An X-Ray Image of the Composite Supernova Remnant SNR G16.7+0.1. *Astrophysical Journal*, 592:941, August 2003.

[100] D. J. Helfand, B. F. Collins, and E. V. Gotthelf. Chandra X-Ray Imaging Spectroscopy of the Young Supernova Remnant Kesteven 75. *Astrophysical Journal*, 582:783, January 2003.

[101] D. J. Helfand, E. V. Gotthelf, J. P. Halpern, F. Camilo, D. R. Semler, R. H. Becker, and R. L. White. Discovery of the Putative Pulsar and Wind Nebula Associated with the TeV Gamma-Ray Source HESS J1813-178. *Astrophysical Journal*, 665:1297, August 2007.

[102] V. F. Hess. Beobacktungen der durchdringenden Strahlung bei sieben Freiballonfahrten. *Phys. Zeits.*, 12:998, 1911.

[103] J. W. T. Hessels, M. S. E. Roberts, S. M. Ransom, V. M. Kaspi, R. W. Romani, C.-Y. Ng, P. C. C. Freire, and B. M. Gaensler. Observations of PSR J2021+3651 and its X-Ray Pulsar Wind Nebula G75.2+0.1. *Astrophysical Journal*, 612:389, September 2004.

[104] J. J. Hester. The Crab Nebula: An Astrophysical Chimera. *Annual Reviews of Astronomy and Astrophysics*, 46:127, September 2008.

[105] J.J. Hester. apod.nasa.gov/apod/ap080217.html.

[106] J.J. Hester. apod.nasa.gov/apod/ap050326.html.

[107] A. Hewish, S. J. Bell, J. D. H. Pilkington, P. F. Scott, and R. A. Collins. Observation of a Rapidly Pulsating Radio Source. *Nature*, 217:709, February 1968.

[108] A. M. Hillas. Cerenkov light images of EAS produced by primary gamma. In F. C. Jones, editor, *International Cosmic Ray Conference*, volume 3 of *International Cosmic Ray Conference*, page 445, August 1985.

[109] A. M. Hillas. Cosmic Rays: Recent Progress and some Current Questions. *ArXiv Astrophysics e-prints*, July 2006.

[110] J. Hinton. Gamma-ray Astronomy. *ArXiv e-prints*, December 2007.

[111] J. A. Hinton, S. Funk, S. Carrigan, Y. A. Gallant, O. C. de Jager, K. Kosack, A. Lemière, and G. Pühlhofer. Discovery of an X-ray nebula around PSR J1718-3825 and implications for the nature of the $\gamma$-ray source HESS J1718-385. *Astronomy and Astrophysics*, 476:L25, December 2007.

[112] K. Hirata, T. Kajita, M. Koshiba, M. Nakahata, and Y. Oyama. Observation of a neutrino burst from the supernova SN1987A. *Physical Review Letters*, 58:1490, April 1987.

[113] G. Hobbs, A. G. Lyne, M. Kramer, C. E. Martin, and C. Jordan. Long-term timing observations of 374 pulsars. *Monthly Notices of the Royal Astronomical Society*, 353:1311, October 2004.

[114] W. Hofmann, I. Jung, A. Konopelko, H. Krawczynski, H. Lampeitl, and G. Pühlhofer. Comparison of techniques to reconstruct VHE gamma-ray showers from multiple stereoscopic Cherenkov images. *Astroparticle Physics*, 12:135, November 1999.

[115] S. Hoppe, E. de Oña-Wilhemi, B. Khélifi, R. C. G. Chaves, O. C. de Jager, C. Stegmann, R. Terrier, and for the H. E. S. S. Collaboration. Detection of

very-high-energy gamma-ray emission from the vicinity of PSR B1706-44 with H.E.S.S. *ArXiv e-prints*, June 2009.

[116] D. Horan and S. Wakely. TeVCat: An Online Catalog for TeV Astronomy. In *AAS/High Energy Astrophysics Division*, volume 10 of *AAS/High Energy Astrophysics Division*, page 41.06, March 2008.

[117] J. P. Hughes, P. O. Slane, D. N. Burrows, G. Garmire, J. A. Nousek, C. M. Olbert, and J. W. Keohane. A Pulsar Wind Nebula in the Oxygen-rich Supernova Remnant G292.0+1.8. *Astrophysical Journal Letters*, 559:L153, October 2001.

[118] J. P. Hughes, P. O. Slane, and P. P. Plucinsky. Discovery of X-Ray Emission from G328.4+0.2, a Crab-like Supernova Remnant. *Astrophysical Journal*, 542:386, October 2000.

[119] C. Y. Hui and W. Becker. Searches for diffuse X-ray emission around millisecond pulsars: an X-ray nebula associated with PSR J2124-3358. *Astronomy and Astrophysics*, 448:L13, March 2006.

[120] R. A. Hulse and J. H. Taylor. Discovery of a pulsar in a binary system. *Astrophysical Jounal Letters*, 195:L51, January 1975.

[121] T. B. Humensky and The VERITAS Collaboration. VERITAS Observations of Supernova Remnants and Pulsar Wind Nebulae in the Fermi Era. *ArXiv e-prints*, December 2009.

[122] K. Jahoda, J. H. Swank, A. B. Giles, M. J. Stark, T. Strohmayer, W. Zhang, and E. H. Morgan. In-orbit performance and calibration of the Rossi X-ray Timing Explorer (RXTE) Proportional Counter Array (PCA). In O. H. Siegmund & M. A. Gummin, editor, *Society of Photo-Optical Instrumentation Engineers (SPIE) Conference Series*, volume 2808 of *Presented at the Society of Photo-Optical Instrumentation Engineers (SPIE) Conference*, page 59, October 1996.

[123] K. G. Jansky. Radio Waves from Outside the Solar System. *Nature*, 132:66, July 1933.

[124] J. V. Jelley. *Čerenkov Radiation and its applications, Pergamon.* 1958.

[125] S. Johnston, A. G. Lyne, R. N. Manchester, D. A. Kniffen, N. D'Amico, J. Lim, and M. Ashworth. A high-frequency survey of the southern Galactic plane for pulsars. *Monthly Notices of the Royal Astronomical Society*, 255:401, April 1992.

[126] T. Kamae. GLAST large area telescope - daily survey of high energy sky. *Nuclear Physics B Proceedings Supplements*, 122:179, July 2003.

[127] O. Kargaltsev and G. G. Pavlov. X-Ray Emission from PSR J1809-1917 and Its Pulsar Wind Nebula, Possibly Associated with the TeV Gamma-Ray Source HESS J1809-193. *Astrophysical Journal*, 670:655, November 2007.

[128] O. Kargaltsev and G. G. Pavlov. Pulsar Wind Nebulae in the Chandra Era. volume 983 of *American Institute of Physics Conference Series*, page 171, February 2008.

[129] O. Kargaltsev, G. G. Pavlov, and J. A. Wong. Young Energetic PSR J1617-5055, Its Nebula, and TeV Source HESS J1616-508. *Astrophysical Journal*, 690:891, January 2009.

[130] V. M. Kaspi, F. Crawford, R. N. Manchester, A. G. Lyne, F. Camilo, N. D'Amico, and B. M. Gaensler. The 69 Millisecond Radio Pulsar near the Supernova Remnant RCW 103. *Astrophysical Jounal Letters*, 503:L161, August 1998.

[131] V. M. Kaspi, E. V. Gotthelf, B. M. Gaensler, and M. Lyutikov. X-Ray Detection of Pulsar PSR B1757-24 and Its Nebular Tail. *Astrophysical Jounal Letters*, 562:L163, December 2001.

[132] V. M. Kaspi, R. N. Manchester, B. Siegman, S. Johnston, and A. G. Lyne. On the spin-down of PSR B1509-58. *Astrophysical Jounal Letters*, 422:L83, February 1994.

[133] M. Kramer, J. F. Bell, R. N. Manchester, A. G. Lyne, F. Camilo, I. H. Stairs, N. D'Amico, V. M. Kaspi, G. Hobbs, D. J. Morris, F. Crawford, A. Possenti, B. C. Joshi, M. A. McLaughlin, D. R. Lorimer, and A. J. Faulkner. The Parkes Multibeam Pulsar Survey - III. Young pulsars and the discovery and timing of 200 pulsars. *Monthly Notices of the Royal Astronomical Society*, 342:1299, July 2003.

[134] L. Kuiper, W. Hermsen, G. Cusumano, R. Diehl, V. Schönfelder, A. Strong, K. Bennett, and M. L. McConnell. The Crab pulsar in the 0.75-30 MeV range as seen by CGRO COMPTEL. A coherent high-energy picture from soft X-rays up to high-energy gamma-rays. *Astronomy and Astrophysics*, 378:918, November 2001.

[135] H. S. Kumar and S. Safi-Harb. Variability of the High Magnetic Field X-Ray Pulsar PSR J1846-0258 Associated with the Supernova Remnant Kes 75 as Revealed by the Chandra X-Ray Observatory. *Astrophysical Jounal Letters*, 678:L43, May 2008.

[136] M. I. Large, A. E. Vaughan, and B. Y. Mills. A Pulsar Supernova Association? *Nature*, 220:340, October 1968.

[137] D. A. Leahy and W. W. Tian. The distance of the SNR Kes 75 and PWN PSR J1846-0258 system. *Astronomy and Astrophysics*, 480:L25, March 2008.

[138] T.-P. Li and Y.-Q. Ma. Analysis methods for results in gamma-ray astronomy. *Astrophysical Journal*, 272:317–324, September 1983.

[139] M. S. Longair. *High energy astrophysics. Volume 2. Stars, the Galaxy and the interstellar medium. Cambride University Press.* 1994.

[140] E. Lorenz. Status of the 17 m MAGIC telescope. *New Astronomy Review*, 48:339, April 2004.

[141] F. J. Lu, Q. D. Wang, B. Aschenbach, P. Durouchoux, and L. M. Song. Chandra Observation of Supernova Remnant G54.1+0.3: A Close Cousin of the Crab Nebula. *Astrophysical Jounal Letters*, 568:L49, March 2002.

[142] MAGIC Collaboration. Very-High-Energy gamma rays from a Distant Quasar: How Transparent Is the Universe? *Science*, 320:1752, June 2008.

[143] R. N. Manchester, G. B. Hobbs, A. Teoh, and M. Hobbs. ATNF Pulsar Catalog (Manchester+, 2005). *VizieR Online Data Catalog*, 7245:0, August 2005.

[144] R. N. Manchester, G. B. Hobbs, A. Teoh, and M. Hobbs. The Australia Telescope National Facility Pulsar Catalogue. *Astronomical Journal*, 129:1993, April 2005.

[145] R. N. Manchester, A. G. Lyne, F. Camilo, J. F. Bell, V. M. Kaspi, N. D'Amico, N. P. F. McKay, F. Crawford, I. H. Stairs, A. Possenti, M. Kramer, and D. C. Sheppard. The Parkes multi-beam pulsar survey - I. Observing and data analysis systems, discovery and timing of 100 pulsars. *Monthly Notices of the Royal Astronomical Society*, 328:17, November 2001.

[146] V. Mangano, E. Massaro, F. Bocchino, T. Mineo, and G. Cusumano. The extended hard X-ray emission from the Vela Plerion. *Astronomy and Astrophysics*, 436:917, June 2005.

[147] V. Marandon, A. Djannati-Atai, R. Terrier, G. Puehlhofer, D. Hauser, S. Schwarzburg, and D. Horns. A closer look at HESS J1837-069 following the pulsar discovery. In F. A. Aharonian, W. Hofmann, & F. Rieger, editor, *American Institute of Physics Conference Series*, volume 1085 of *American Institute of Physics Conference Series*, page 320, December 2008.

[148] C. B. Markwardt and H. Ögelman. An X-ray jet from the Vela pulsar. *Nature*, 375:40, May 1995.

[149] F. E. Marshall, E. V. Gotthelf, J. Middleditch, Q. D. Wang, and W. Zhang. The Big Glitcher: The Rotation History of PSR J0537-6910. *Astrophysical Journal*, 603:682, March 2004.

[150] F. Mattana, M. Falanga, D. Götz, R. Terrier, P. Esposito, A. Pellizzoni, A. de Luca, V. Marandon, A. Goldwurm, and P. Caraveo. High-energy flux evolution of Pulsar Wind Nebulae. In F. A. Aharonian, W. Hofmann, & F. Rieger, editor,

*American Institute of Physics Conference Series*, volume 1085 of *American Institute of Physics Conference Series*, page 308, December 2008.

[151] T. Mineo, C. Ferrigno, L. Foschini, A. Segreto, G. Cusumano, G. Malaguti, G. Di Cocco, and C. Labanti. INTEGRAL observations of the Crab pulsar. *Astronomy and Astrophysics*, 450:617, May 2006.

[152] Z. Misanovic, G. G. Pavlov, and G. P. Garmire. Chandra Observations of the Pulsar B1929+10 and Its Environment. *Astrophysical Journal*, 685:1129, October 2008.

[153] A. A. Moiseev. Gamma-ray Large Area Space Telescope: Mission overview. *Nuclear Instruments and Methods in Physics Research A*, 588:41, April 2008.

[154] D. J. Morris, G. Hobbs, A. G. Lyne, I. H. Stairs, F. Camilo, R. N. Manchester, A. Possenti, J. F. Bell, V. M. Kaspi, N. D. Amico, N. P. F. McKay, F. Crawford, and M. Kramer. The Parkes Multibeam Pulsar Survey - II. Discovery and timing of 120 pulsars. *Monthly Notices of the Royal Astronomical Society*, 335:275, September 2002.

[155] H. Muraishi, T. Tanimori, S. Yanagita, T. Yoshida, M. Moriya, T. Kifune, S. A. Dazeley, P. G. Edwards, S. Gunji, S. Hara, T. Hara, A. Kawachi, H. Kubo, Y. Matsubara, Y. Mizumoto, M. Mori, Y. Muraki, T. Naito, K. Nishijima, J. R. Patterson, G. P. Rowell, T. Sako, K. Sakurazawa, R. Susukita, T. Tamura, and T. Yoshikoshi. Evidence for TeV gamma-ray emission from the shell type SNR RX J1713.7-3946. *Astronomy and Astrophysics*, 354:L57, February 2000.

[156] C.-Y. Ng, P. O. Slane, B. M. Gaensler, and J. P. Hughes. Deep Chandra Observation of the Pulsar Wind Nebula Powered by Pulsar PSR J1846-0258 in the Supernova Remnant Kes 75. *Astrophysical Journal*, 686:508, October 2008.

[157] C. M. Olbert, J. W. Keohane, K. A. Arnaud, K. K. Dyer, S. P. Reynolds, and S. Safi-Harb. Chandra Detection of a Pulsar Wind Nebula Associated with Supernova Remnant 3C 396. *Astrophysical Jounal Letters*, 592:L45, July 2003.

[158] T. Oosterbroek, I. Cognard, A. Golden, P. Verhoeve, D. D. E. Martin, C. Erd, R. Schulz, J. A. Stüwe, A. Stankov, and T. Ho. Simultaneous absolute timing of the Crab pulsar at radio and optical wavelengths. *Astronomy and Astrophysics*, 488:271, September 2008.

[159] M. Pallavicini. Solar Neutrinos. *ArXiv e-prints*, October 2009.

[160] Q. A. Parker, S. Phillipps, M. J. Pierce, M. Hartley, N. C. Hambly, M. A. Read, H. T. MacGillivray, S. B. Tritton, C. P. Cass, R. D. Cannon, M. Cohen, J. E. Drew, D. J. Frew, E. Hopewell, S. Mader, D. F. Malin, M. R. W. Masheder, D. H. Morgan, R. A. H. Morris, D. Russeil, K. S. Russell, and R. N. F. Walker. The AAO/UKST SuperCOSMOS H$\alpha$ survey. *Monthly Notices of the Royal Astronomical Society*, 362:689, September 2005.

[161] G. G. Pavlov, S. Bhattacharyya, and V. E. Zavlin. New X-ray Observations of the Geminga Pulsar Wind Nebula. *Astrophysical Journal*, 715:66, May 2010.

[162] The Pierre Auger Collaboration. Measurement of the energy spectrum of cosmic rays above 10ˆ18 eV using the Pierre Auger Observatory. *ArXiv e-prints*, February 2010.

[163] P Plailly. Private communication. April 2004.

[164] A. Possenti, R. Cerutti, M. Colpi, and S. Mereghetti. Re-examining the X-ray versus spin-down luminosity correlation of rotation powered pulsars. *Astronomy and Astrophysics*, 387:993, June 2002.

[165] G. Pühlhofer and the HEGRA collaboration. The technical performance of the HEGRA system of imaging air Cherenkov telescopes. *Astroparticle Physics*, 20:267, December 2003.

[166] W. Reich. Radio Observations of Supernova Remnants. In W. Becker, H. Lesch, & J. Trümper, editor, *Neutron Stars, Pulsars, and Supernova Remnants*, page 1, 2002.

[167] M. Renaud, S. Hoppe, N. Komin, E. Moulin, V. Marandon, and A.-C. Clapson. Pulsar Wind Nebula candidates recently discovered by H.E.S.S. In F. A. Aharonian, W. Hofmann, & F. Rieger, editor, *American Institute of Physics Conference Series*, volume 1085 of *American Institute of Physics Conference Series*, page 285, December 2008.

[168] S. P. Reynolds and R. A. Chevalier. Evolution of pulsar-driven supernova remnants. *Astrophysical Journal*, 278:630, March 1984.

[169] M. Roberts, C. Brogan, and M. Lyutikov. The Rabbit and the Eel: Deep Chandra Observations of Two EGRET Pulsar Wind Nebulae. In *Bulletin of the American Astronomical Society*, volume 38 of *Bulletin of the American Astronomical Society*, page 997, December 2007.

[170] M. S. E. Roberts, E. V. Gotthelf, J. P. Halpern, C. L. Brogan, and S. M. Ransom. Recent Observations of EGRET Pulsar Wind Nebulae. In W. Becker & H. H. Huang, editor, *WE-Heraeus Seminar on Neutron Stars and Pulsars 40 years after the Discovery*, page 24, January 2007.

[171] M. S. E. Roberts, R. W. Romani, S. Johnston, and A. J. Green. The "Rabbit": A Potential Radio Counterpart of GEV J1417-6100. *Astrophysical Journal*, 515:712, April 1999.

[172] M. S. E. Roberts, R. W. Romani, and N. Kawai. The ASCA Catalog of Potential X-Ray Counterparts of GEV Sources. *Astrophysical Journal*, 133:451, April 2001.

[173] M. S. E. Roberts, C. R. Tam, V. M. Kaspi, M. Lyutikov, G. Vasisht, M. Pivovaroff, E. V. Gotthelf, and N. Kawai. The Pulsar Wind Nebula in G11.2-0.3. *Astrophysical Journal*, 588:992, May 2003.

[174] R. W. Romani, C.-Y. Ng, R. Dodson, and W. Brisken. The Complex Wind Torus and Jets of PSR B1706-44. *Astrophysical Journal*, 631:480, September 2005.

[175] W. Röntgen. On A New Kind Of X-Rays. *Nature*, 53:274, 1896.

[176] A. H. Rots, K. Jahoda, and A. G. Lyne. Absolute Timing of the Crab Pulsar with the Rossi X-Ray Timing Explorer. *Astrophysical Jounal Letters*, 605:L129, April 2004.

[177] S. Safi-Harb and H. S. Kumar. Using Chandra to Unveil the High-Energy Properties of the High Magnetic Field Radio Pulsar J1119-6127. *Astrophysical Journal*, 684:532, September 2008.

[178] F. D. Seward, P. Gorenstein, and R. K. Smith. Chandra Observations of the X-Ray Halo around the Crab Nebula. *Astrophysical Journal*, 636:873–880, January 2006.

[179] F. D. Seward and F. R. Harnden, Jr. A new, fast X-ray pulsar in the supernova remnant MSH 15-52. *Astrophysical Jounal Letters*, 256:L45, May 1982.

[180] L. Sidoli, S. Mereghetti, G. L. Israel, and F. Bocchino. X-ray emission from the galactic center region supernova remnant G0.9+0.1. *Astronomy and Astrophysics*, 361:719, September 2000.

[181] D. A. Smith, E. Brion, R. Britto, P. Bruel, J. Bussons Gordo, D. Dumora, E. Durand, P. Eschstruth, P. Espigat, J. Holder, A. Jacholkowska, J. Lavalle, R. Le Gallou, B. Lott, H. Manseri, F. Münz, E. Nuss, F. Piron, R. C. Rannot, T. Reposeur, and T. Sako. Mrk 421, Mrk 501, and 1ES 1426+428 at 100 GeV with the CELESTE Cherenkov telescope. *Astronomy and Astrophysics*, 459:453, November 2006.

[182] F. G. Smith. *Pulsars. Moskva.* 1979.

[183] G. Spandre and the GLAST Collaboration. The $\gamma$-ray large-area space telescope: An astro-particle mission to explore the high-energy $\gamma$-ray sky. *Nuclear Instruments and Methods in Physics Research A*, 572:500, March 2007.

[184] F. W. Stecker, O. C. de Jager, and M. H. Salamon. TeV gamma rays from 3C 279 - A possible probe of origin and intergalactic infrared radiation fields. *Astrophysical Jounal Letters*, 390:L49, May 1992.

[185] F. R. Stephenson and D. A. Green. Historical Supernovae. In M. Turatto, S. Benetti, L. Zampieri, & W. Shea, editor, *1604-2004: Supernovae as Cosmological Lighthouses*, volume 342 of *Astronomical Society of the Pacific Conference Series*, page 63, December 2005.

[186] T. Tanimori, K. Sakurazawa, S. A. Dazeley, P. G. Edwards, T. Hara, Y. Hayami, S. Kamei, T. Kifune, T. Konishi, Y. Matsubara, T. Matsuoka, Y. Mizumoto, A. Masaike, M. Mori, H. Muraishi, Y. Muraki, T. Naito, S. Oda, S. Ogio, T. Osaki, J. R. Patterson, M. D. Roberts, G. P. Rowell, A. Suzuki, R. Suzuki, T. Sako, T. Tamura, G. J. Thornton, R. Susukita, S. Yanagita, T. Yoshida, and T. Yoshikoshi. Detection of Gamma Rays of up to 50 TeV from the Crab Nebula. *Astrophysical Jounal Letters*, 492:L33, January 1998.

[187] R. Terrier, A. Djannati-Atai, S. Hoppe, V. Marandon, M. Renaud, and O. de Jager. H.E.S.S. Observations of the Young Composite SNR Kes 75. In F. A. Aharonian, W. Hofmann, & F. Rieger, editor, *American Institute of Physics Conference Series*, volume 1085 of *American Institute of Physics Conference Series*, page 316, December 2008.

[188] A. Van Etten and R. W. Romani. The Extended X-ray Nebula of PSR J1420-6048. *Astrophysical Journal*, 711:1168, March 2010.

[189] VERITAS Collaboration. A connection between star formation activity and cosmic rays in the starburst galaxy M82. *Nature*, 462:770, December 2009.

[190] P. Villard. Contribution a‘ létude du rayonnement du radium. *Séances de la Société française de physique*, page 17, 1900.

[191] N. Wang, R. N. Manchester, R. T. Pace, M. Bailes, V. M. Kaspi, B. W. Stappers, and A. G. Lyne. Glitches in southern pulsars. *Monthly Notices of the Royal Astronomical Society*, 317:843, October 2000.

[192] Q. D. Wang, E. V. Gotthelf, Y.-H. Chu, and J. R. Dickel. Detection of an X-Ray Pulsar Wind Nebula and Tail in SNR N157B. *Astrophysical Journal*, 559:275, September 2001.

[193] T. C. Weekes, M. F. Cawley, D. J. Fegan, K. G. Gibbs, A. M. Hillas, P. W. Kowk, R. C. Lamb, D. A. Lewis, D. Macomb, N. A. Porter, P. T. Reynolds, and G. Vacanti. Observation of TeV gamma rays from the Crab nebula using the atmospheric Cerenkov imaging technique. *Astrophysical Journal*, 342:379, July 1989.

[194] T. C. Weekes and the VERITAS collaboration. VERITAS: the Very Energetic Radiation Imaging Telescope Array System. *Astroparticle Physics*, 17:221–243, May 2002.

[195] K. W. Weiler and N. Panagia. VELA X and the evolution of Plerions. *Astronomy and Astrophysics*, 90:269, October 1980.

[196] M. C. Weisskopf, H. D. Tananbaum, L. P. Van Speybroeck, and S. L. O'Dell. Chandra X-ray Observatory (CXO): overview. In J. E. Truemper & B. Aschenbach, editor, *Society of Photo-Optical Instrumentation Engineers (SPIE) Conference Series*, volume 4012 of *Presented at the Society of Photo-Optical Instrumentation Engineers (SPIE) Conference*, page 2, July 2000.

# Appendix A

# Analysis Dataset Details

This appendix contains the details of the data used in the observations in Chapter 4, Chapter 5 and Chapter 6. In each case the run number of the observation is given along with the time (UTC), date and position of each run is given along with its idenifying run number. All of the data used in this Thesis was taken using all four HESS telescopes.

## A.1 The Crab Nebula

| Run No. | Target | RA | Dec | Offset | Date | Duration |
|---|---|---|---|---|---|---|
| | | ° | ° | ° | dd.mm.yyyy | s |
| 23037 | The Crab | 83.6 | 22.0 | 0.5 | 13.10.2004 | 1567 |
| 23062 | The Crab | 83.6 | 22.0 | 0.5 | 14.10.2004 | 1682 |
| 23063 | The Crab | 83.6 | 22.0 | 0.5 | 14.10.2004 | 1686 |
| 23080 | The Crab | 83.6 | 22.0 | 0.5 | 15.10.2004 | 1686 |
| 23081 | The Crab | 83.6 | 22.0 | 0.5 | 15.10.2004 | 1686 |
| 23114 | The Crab | 83.6 | 22.0 | 0.5 | 16.10.2004 | 1685 |
| 23117 | The Crab | 83.6 | 22.0 | 0.5 | 16.10.2004 | 1686 |
| 23134 | The Crab | 83.6 | 22.0 | 0.5 | 17.10.2004 | 1687 |
| 23155 | The Crab | 83.6 | 22.0 | 0.5 | 21.10.2004 | 1687 |
| 23156 | The Crab | 83.6 | 22.0 | 0.5 | 21.10.2004 | 1572 |

| Run No. | Target | RA | Dec | Offset | Date | Duration |
|---|---|---|---|---|---|---|
| | | ° | ° | ° | dd.mm.yyyy | s |
| 23304 | The Crab | 83.6 | 22.0 | 0.5 | 20.11.2004 | 1613 |
| 23309 | The Crab | 83.6 | 22.0 | 0.5 | 20.11.2004 | 1686 |
| 23310 | The Crab | 83.6 | 22.0 | 0.5 | 20.11.2004 | 1686 |
| 23526 | The Crab | 83.6 | 22.0 | 0.5 | 04.12.2004 | 1687 |
| 23544 | The Crab | 83.6 | 22.0 | 0.5 | 05.12.2004 | 1686 |
| 23545 | The Crab | 83.6 | 22.0 | 0.5 | 05.12.2004 | 1687 |
| 23546 | The Crab | 83.6 | 22.0 | 0.5 | 05.12.2004 | 947 |
| 23547 | The Crab | 83.6 | 22.0 | 0.5 | 05.12.2004 | 950 |
| 23555 | The Crab | 83.6 | 22.0 | 0.0 | 06.12.2004 | 1686 |
| 23556 | The Crab | 83.6 | 22.0 | 0.5 | 06.12.2004 | 1686 |
| 23576 | The Crab | 83.6 | 22.0 | 0.0 | 07.12.2004 | 1686 |
| 23577 | The Crab | 83.6 | 22.0 | 0.5 | 07.12.2004 | 1687 |
| 23579 | The Crab | 83.6 | 22.0 | 0.5 | 07.12.2004 | 972 |
| 23580 | The Crab | 83.6 | 22.0 | 0.0 | 07.12.2004 | 837 |
| 23593 | The Crab | 83.6 | 22.0 | 0.5 | 08.12.2004 | 1687 |
| 23595 | The Crab | 83.6 | 22.0 | 0.5 | 08.12.2004 | 1687 |
| 23600 | The Crab | 83.6 | 22.0 | 0.5 | 09.12.2004 | 1686 |
| 23601 | The Crab | 83.6 | 22.0 | 0.5 | 09.12.2004 | 1686 |
| 23608 | The Crab | 83.6 | 22.0 | 0.5 | 10.12.2004 | 1686 |
| 23611 | The Crab | 83.6 | 22.0 | 0.5 | 10.12.2004 | 1686 |
| 23612 | The Crab | 83.6 | 22.0 | 0.5 | 10.12.2004 | 1687 |
| 23642 | The Crab | 83.6 | 22.0 | 0.5 | 13.12.2004 | 1686 |
| 23662 | The Crab | 83.6 | 22.0 | 0.5 | 15.12.2004 | 1686 |
| 23738 | The Crab | 83.6 | 22.0 | 0.5 | 03.01.2005 | 1679 |
| 23739 | The Crab | 83.6 | 22.0 | 0.5 | 03.01.2005 | 1686 |
| 23740 | The Crab | 83.6 | 22.0 | 0.5 | 03.01.2005 | 1686 |
| 23741 | The Crab | 83.6 | 22.0 | 0.5 | 03.01.2005 | 1686 |
| 23753 | The Crab | 83.6 | 22.0 | 0.5 | 04.01.2005 | 1686 |

| Run No. | Target | RA | Dec | Offset | Date | Duration |
|---|---|---|---|---|---|---|
| | | ° | ° | ° | dd.mm.yyyy | s |
| 23754 | The Crab | 83.6 | 22.0 | 0.5 | 04.01.2005 | 1686 |
| 23755 | The Crab | 83.6 | 22.0 | 0.5 | 04.01.2005 | 1687 |
| 23756 | The Crab | 83.6 | 22.0 | 0.5 | 04.01.2005 | 1687 |
| 23937 | The Crab | 83.6 | 22.0 | 0.5 | 29.01.2005 | 1645 |
| 23939 | The Crab | 83.6 | 22.0 | 0.5 | 29.01.2005 | 1688 |
| 23968 | The Crab | 83.6 | 22.0 | 0.5 | 30.01.2005 | 1688 |
| 23969 | The Crab | 83.6 | 22.0 | 0.5 | 30.01.2005 | 1553 |
| 23978 | The Crab | 83.6 | 22.0 | 0.0 | 31.01.2005 | 611 |
| 23981 | The Crab | 83.6 | 22.0 | 0.5 | 31.01.2005 | 1691 |
| 24116 | The Crab | 83.6 | 22.0 | 0.5 | 10.02.2005 | 1688 |
| 24138 | The Crab | 83.6 | 22.0 | 0.5 | 11.02.2005 | 907 |
| 24139 | The Crab | 83.6 | 22.0 | 0.5 | 11.02.2005 | 1688 |
| 24411 | The Crab | 83.6 | 22.0 | 0.5 | 04.03.2005 | 1687 |
| 24412 | The Crab | 83.6 | 22.0 | 0.5 | 04.03.2005 | 1687 |
| 29873 | The Crab | 83.6 | 22.0 | 0.5 | 07.12.2005 | 1690 |
| 29874 | The Crab | 83.6 | 22.0 | 0.5 | 07.12.2005 | 1694 |
| 30013 | The Crab | 83.6 | 22.0 | 0.5 | 28.12.2005 | 1690 |
| 30014 | The Crab | 83.6 | 22.0 | 0.5 | 28.12.2005 | 1690 |
| 30141 | The Crab | 83.6 | 22.0 | 0.5 | 23.01.2006 | 109 |
| 35941 | The Crab | 83.6 | 22.0 | 0.7 | 13.11.2006 | 1688 |
| 35956 | The Crab | 83.6 | 22.0 | 0.7 | 14.11.2006 | 1689 |
| 35957 | The Crab | 83.6 | 22.0 | 0.7 | 14.11.2006 | 1689 |
| 35992 | The Crab | 83.6 | 22.0 | 0.7 | 16.11.2006 | 1688 |
| 36012 | The Crab | 83.6 | 22.0 | 0.7 | 17.11.2006 | 1689 |
| 36013 | The Crab | 83.6 | 22.0 | 0.7 | 17.11.2006 | 1689 |
| 36066 | The Crab | 83.6 | 22.0 | 0.7 | 20.11.2006 | 1689 |
| 36174 | The Crab | 83.6 | 22.0 | 0.7 | 24.11.2006 | 1688 |
| 36361 | The Crab | 83.6 | 22.0 | 0.7 | 12.12.2006 | 1688 |

| Run No. | Target | RA | Dec | Offset | Date | Duration |
|---|---|---|---|---|---|---|
| | | ° | ° | ° | dd.mm.yyyy | s |
| 36380 | The Crab | 83.6 | 22.0 | 0.7 | 14.12.2006 | 1688 |
| 41647 | The Crab | 83.6 | 22.0 | 0.5 | 11.09.2007 | 1289 |
| 41648 | The Crab | 83.6 | 22.0 | 0.5 | 11.09.2007 | 959 |
| 41678 | The Crab | 83.6 | 22.0 | 0.5 | 12.09.2007 | 1309 |
| 41712 | The Crab | 83.6 | 22.0 | 0.5 | 13.09.2007 | 1689 |
| 41713 | The Crab | 83.6 | 22.0 | 0.5 | 13.09.2007 | 1160 |
| 41753 | The Crab | 83.6 | 22.0 | 0.5 | 14.09.2007 | 1687 |
| 41808 | The Crab | 83.6 | 22.0 | 0.5 | 15.09.2007 | 1688 |
| 42317 | The Crab | 83.6 | 22.0 | 0.5 | 11.10.2007 | 1208 |
| 42342 | The Crab | 83.6 | 22.0 | 0.5 | 12.10.2007 | 911 |
| 42364 | The Crab | 83.6 | 22.0 | 0.5 | 13.10.2007 | 1689 |
| 42365 | The Crab | 83.6 | 22.0 | 0.5 | 13.10.2007 | 1688 |
| 42383 | The Crab | 83.6 | 22.0 | 0.5 | 14.10.2007 | 1688 |
| 42415 | The Crab | 83.6 | 22.0 | 0.5 | 15.10.2007 | 1688 |
| 42556 | The Crab | 83.6 | 22.0 | 0.5 | 21.10.2007 | 1690 |
| 42557 | The Crab | 83.6 | 22.0 | 0.5 | 21.10.2007 | 733 |
| 43038 | The Crab | 83.6 | 22.0 | 0.5 | 19.11.2007 | 1688 |
| 43039 | The Crab | 83.6 | 22.0 | 0.5 | 19.11.2007 | 1688 |
| 43424 | The Crab | 83.6 | 22.0 | 0.5 | 07.12.2007 | 1689 |
| 43447 | The Crab | 83.6 | 22.0 | 0.5 | 08.12.2007 | 1687 |
| 43471 | The Crab | 83.6 | 22.0 | 0.5 | 09.12.2007 | 1687 |
| 43472 | The Crab | 83.6 | 22.0 | 0.5 | 09.12.2007 | 1688 |
| 43489 | The Crab | 83.6 | 22.0 | 0.5 | 10.12.2007 | 1689 |
| 43490 | The Crab | 83.6 | 22.0 | 0.5 | 10.12.2007 | 1688 |
| 48399 | The Crab | 83.6 | 22.0 | 0.5 | 25.09.2008 | 655 |
| 48476 | The Crab | 83.6 | 22.0 | 0.5 | 28.09.2008 | 1687 |
| 48525 | The Crab | 83.6 | 22.0 | 0.5 | 30.09.2008 | 1445 |
| 48552 | The Crab | 83.6 | 22.0 | 0.5 | 01.10.2008 | 1009 |

| Run No. | Target | RA | Dec | Offset | Date | Duration |
|---|---|---|---|---|---|---|
| | | ° | ° | ° | dd.mm.yyyy | s |
| 48570 | The Crab | 83.6 | 22.0 | 0.5 | 02.10.2008 | 1507 |
| 48602 | The Crab | 83.6 | 22.0 | 0.5 | 04.10.2008 | 1688 |
| 48630 | The Crab | 83.6 | 22.0 | 0.5 | 06.10.2008 | 1688 |
| 48646 | The Crab | 83.6 | 22.0 | 0.5 | 07.10.2008 | 1687 |
| 48647 | The Crab | 83.6 | 22.0 | 0.5 | 07.10.2008 | 1217 |
| 48682 | The Crab | 83.6 | 22.0 | 0.5 | 08.10.2008 | 1688 |
| 48683 | The Crab | 83.6 | 22.0 | 0.5 | 08.10.2008 | 1109 |
| 48717 | The Crab | 83.6 | 22.0 | 0.5 | 09.10.2008 | 1688 |
| 48734 | The Crab | 83.6 | 22.0 | 0.5 | 10.10.2008 | 1688 |
| 48750 | The Crab | 83.6 | 22.0 | 0.5 | 11.10.2008 | 1402 |
| 54354 | The Crab | 83.6 | 22.0 | 0.5 | 26.10.2009 | 1693 |
| 54390 | The Crab | 83.6 | 22.0 | 0.5 | 28.10.2009 | 1689 |
| 54391 | The Crab | 83.6 | 22.0 | 0.5 | 28.10.2009 | 1689 |
| 54392 | The Crab | 83.6 | 22.0 | 0.5 | 28.10.2009 | 1628 |
| 54404 | The Crab | 83.6 | 22.0 | 0.5 | 29.10.2009 | 1688 |
| 54566 | The Crab | 83.6 | 22.0 | 0.5 | 11.11.2009 | 1688 |
| 54588 | The Crab | 83.6 | 22.0 | 0.5 | 12.11.2009 | 1688 |
| 54589 | The Crab | 83.6 | 22.0 | 0.5 | 12.11.2009 | 1689 |
| 54603 | The Crab | 83.6 | 22.0 | 0.5 | 13.11.2009 | 1688 |
| 54604 | The Crab | 83.6 | 22.0 | 0.5 | 13.11.2009 | 1689 |
| 54623 | The Crab | 83.6 | 22.0 | 0.5 | 14.11.2009 | 1688 |
| 54624 | The Crab | 83.6 | 22.0 | 0.5 | 14.11.2009 | 1692 |
| 54653 | The Crab | 83.6 | 22.0 | 0.5 | 15.11.2009 | 1691 |
| 54706 | The Crab | 83.6 | 22.0 | 0.5 | 18.11.2009 | 1688 |
| 54707 | The Crab | 83.6 | 22.0 | 0.5 | 18.11.2009 | 1690 |
| 54734 | The Crab | 83.6 | 22.0 | 0.5 | 19.11.2009 | 1688 |
| 54735 | The Crab | 83.6 | 22.0 | 0.5 | 19.11.2009 | 1689 |
| 54748 | The Crab | 83.6 | 22.0 | 0.5 | 20.11.2009 | 1688 |

| Run No. | Target | RA | Dec | Offset | Date | Duration |
|---|---|---|---|---|---|---|
| | | ° | ° | ° | dd.mm.yyyy | s |
| 54749 | The Crab | 83.6 | 22.0 | 0.5 | 20.11.2009 | 1688 |
| 54771 | The Crab | 83.6 | 22.0 | 0.5 | 21.11.2009 | 1691 |
| 54772 | The Crab | 83.6 | 22.0 | 0.5 | 21.11.2009 | 1688 |
| 54789 | The Crab | 83.6 | 22.0 | 0.5 | 22.11.2009 | 1689 |
| 54809 | The Crab | 83.6 | 22.0 | 0.5 | 23.11.2009 | 1689 |

## A.2 G180.0-1.7

| Run No. | Target | RA | Dec | Offset | Date | Duration |
|---|---|---|---|---|---|---|
| | | ° | ° | ° | dd.mm.yyyy | s |
| 35518 | PSR J0538+2817 | 83.8 | 28.3 | 0.7 | 22.10.2006 | 1689 |
| 35519 | PSR J0538+2817 | 85.4 | 28.3 | 0.7 | 22.10.2006 | 1688 |
| 35520 | PSR J0538+2817 | 84.6 | 28.9 | 0.7 | 22.10.2006 | 1189 |
| 35521 | PSR J0538+2817 | 83.8 | 28.3 | 0.7 | 22.10.2006 | 1359 |
| 36334 | PSR J0538+2817 | 84.6 | 27.6 | 0.7 | 10.12.2006 | 1155 |
| 36347 | PSR J0538+2817 | 84.6 | 29.0 | 0.7 | 11.12.2006 | 1368 |
| 36363 | PSR J0538+2817 | 85.4 | 28.3 | 0.7 | 12.12.2006 | 1687 |
| 36364 | PSR J0538+2817 | 84.6 | 27.6 | 0.7 | 12.12.2006 | 1688 |
| 36396 | PSR J0538+2817 | 84.6 | 27.6 | 0.7 | 15.12.2006 | 1688 |

## A.3 Geminga

| Run No. | Target | RA | Dec | Offset | Date | Duration |
|---|---|---|---|---|---|---|
| | | ° | ° | ° | dd.mm.yyyy | s |
| 36046 | Geminga | 98.5 | 17.8 | 0.7 | 19.11.2006 | 1689 |
| 36136 | Geminga | 98.5 | 17.8 | 0.7 | 23.11.2006 | 1688 |
| 36140 | Geminga | 98.5 | 17.8 | 0.7 | 23.11.2006 | 1689 |
| 36177 | Geminga | 98.5 | 17.8 | 0.7 | 24.11.2006 | 1688 |
| 36178 | Geminga | 98.5 | 17.8 | 0.7 | 24.11.2006 | 622 |
| 36181 | Geminga | 98.5 | 17.8 | 0.7 | 24.11.2006 | 1689 |
| 36182 | Geminga | 98.5 | 17.8 | 0.7 | 24.11.2006 | 1600 |
| 36190 | Geminga | 98.5 | 17.8 | 0.7 | 25.11.2006 | 807 |
| 36191 | Geminga | 98.5 | 17.8 | 0.7 | 25.11.2006 | 1688 |
| 36192 | Geminga | 98.5 | 17.8 | 0.7 | 25.11.2006 | 1688 |
| 36193 | Geminga | 98.5 | 17.8 | 0.7 | 25.11.2006 | 2168 |
| 36215 | Geminga | 98.5 | 17.8 | 0.7 | 28.11.2006 | 1688 |
| 43658 | Geminga | 98.5 | 17.8 | 1.0 | 02.01.2008 | 1687 |
| 43766 | Geminga | 98.5 | 17.8 | 1.0 | 06.01.2008 | 1688 |
| 43809 | Geminga | 98.5 | 17.8 | 1.0 | 07.01.2008 | 1487 |
| 43810 | Geminga | 98.5 | 17.8 | 1.0 | 07.01.2008 | 1689 |
| 43830 | Geminga | 98.5 | 17.8 | 1.0 | 09.01.2008 | 1688 |
| 43831 | Geminga | 98.5 | 17.8 | 1.0 | 09.01.2008 | 1487 |
| 43858 | Geminga | 98.5 | 17.8 | 1.0 | 10.01.2008 | 1688 |
| 43883 | Geminga | 98.5 | 17.8 | 1.0 | 11.01.2008 | 1689 |
| 43884 | Geminga | 98.5 | 17.8 | 1.0 | 11.01.2008 | 1687 |
| 43958 | Geminga | 98.5 | 17.8 | 1.0 | 13.01.2008 | 1687 |
| 43998 | Geminga | 98.5 | 17.8 | 1.0 | 14.01.2008 | 1688 |

## A.4 G287.4+0.6

| Run No. | Target | RA | Dec | Offset | Date | Duration |
|---|---|---|---|---|---|---|
| | | ° | ° | ° | dd.mm.yyyy | s |
| 20105 | Eta Carinae | 161.3 | -59.7 | 0.5 | 24.03.2004 | 1683 |
| 20106 | Eta Carinae | 161.3 | -59.7 | 0.5 | 24.03.2004 | 602 |
| 20107 | Eta Carinae | 161.3 | -59.7 | 1.4 | 24.03.2004 | 1683 |
| 20108 | Eta Carinae | 161.3 | -59.7 | 0.5 | 24.03.2004 | 1682 |
| 30531 | WR 20 A | 156.0 | -57.8 | 2.7 | 03.03.2006 | 1964 |
| 30555 | WR 20 A | 156.0 | -57.8 | 2.7 | 03.03.2006 | 1691 |
| 31044 | G290.4+0.2 | 167.0 | -60.1 | 2.9 | 04.04.2006 | 1689 |
| 31660 | G284.8+0.2 | 157.4 | -57.6 | 2.7 | 02.05.2006 | 1689 |
| 32314 | PSR J1048-5832 | 160.7 | -58.5 | 0.7 | 23.05.2006 | 1687 |
| 32319 | PSR J1048-5832 | 162.0 | -57.8 | 1.0 | 23.05.2006 | 1691 |
| 32320 | PSR J1048-5832 | 162.0 | -59.2 | 0.4 | 23.05.2006 | 1689 |
| 32340 | PSR J1048-5832 | 163.4 | -58.5 | 0.8 | 24.05.2006 | 1689 |
| 32344 | PSR J1048-5832 | 160.7 | -58.5 | 0.8 | 24.05.2006 | 1684 |
| 32348 | PSR J1048-5832 | 162.1 | -57.8 | 1.0 | 24.05.2006 | 1689 |
| 32366 | WR 20 A | 156.0 | -57.8 | 2.7 | 25.05.2006 | 1689 |
| 32450 | WR 20 A | 156.0 | -57.8 | 2.7 | 28.05.2006 | 1689 |
| 32483 | WR 20 A | 156.0 | -57.8 | 2.7 | 29.05.2006 | 1688 |
| 32890 | WR 20 A | 156.0 | -57.8 | 2.7 | 16.06.2006 | 1689 |
| 44747 | G290.3+0.4 | 167.0 | -59.9 | 2.8 | 04.06.2008 | 1689 |
| 45121 | G284.7+0.2 | 157.2 | -57.5 | 2.8 | 27.04.2008 | 1464 |
| 45122 | G284.7+0.2 | 157.2 | -57.5 | 2.8 | 27.04.2008 | 1687 |
| 45282 | G284.7+0.2 | 157.2 | -57.5 | 2.8 | 04.05.2008 | 1688 |
| 45283 | G284.7+0.2 | 157.2 | -57.5 | 2.8 | 04.05.2008 | 1687 |
| 45713 | G290.3+0.4 | 167.0 | -59.9 | 2.8 | 28.05.2008 | 1688 |
| 45740 | G290.3+0.4 | 167.0 | -59.9 | 2.8 | 30.05.2008 | 1688 |
| 45882 | G290.3+0.4 | 167.0 | -59.9 | 2.8 | 04.06.2008 | 1688 |
| 50164 | Eta Carinae | 161.3 | -59.7 | 0.6 | 01.02.2009 | 1688 |
| 50175 | Eta Carinae | 161.3 | -59.7 | 1.2 | 04.02.2009 | 1687 |

| Run No. | Target | RA | Dec | Offset | Date | Duration |
|---|---|---|---|---|---|---|
| | | ° | ° | ° | dd.mm.yyyy | s |
| 50177 | Eta Carinae | 161.3 | -59.7 | 0.6 | 04.02.2009 | 787 |
| 50180 | Eta Carinae | 161.3 | -59.7 | 1.2 | 04.02.2009 | 633 |
| 50181 | Eta Carinae | 161.3 | -59.7 | 0.6 | 04.02.2009 | 633 |
| 50192 | Eta Carinae | 161.3 | -59.7 | 0.6 | 06.02.2009 | 460 |
| 55598 | Eta Carinae | 161.3 | -59.7 | 1.2 | 19.01.2010 | 1689 |
| 55600 | Eta Carinae | 161.3 | -58.5 | 0.5 | 19.01.2010 | 1513 |
| 55885 | Eta Carinae | 161.3 | -59.7 | 0.6 | 09.02.2010 | 1689 |
| 55887 | Eta Carinae | 161.3 | -59.7 | 1.2 | 09.02.2010 | 1688 |
| 55901 | Eta Carinae | 161.3 | -59.7 | 0.6 | 10.02.2010 | 1688 |
| 55917 | Eta Carinae | 161.3 | -59.7 | 1.2 | 11.02.2010 | 140 |
| 55918 | Eta Carinae | 161.3 | -59.7 | 1.2 | 11.02.2010 | 1688 |
| 55960 | Eta Carinae | 161.3 | -59.7 | 1.2 | 14.02.2010 | 1688 |
| 55962 | Eta Carinae | 161.3 | -59.7 | 1.2 | 14.02.2010 | 1688 |
| 55985 | Eta Carinae | 161.3 | -59.7 | 0.6 | 15.02.2010 | 1690 |
| 55987 | Eta Carinae | 161.3 | -59.7 | 1.2 | 15.02.2010 | 1688 |
| 56008 | Eta Carinae | 161.3 | -59.7 | 1.2 | 16.02.2010 | 1689 |
| 56010 | Eta Carinae | 161.3 | -59.7 | 0.6 | 16.02.2010 | 1688 |
| 56078 | Eta Carinae | 161.3 | -59.7 | 0.6 | 19.02.2010 | 1688 |
| 56094 | Eta Carinae | 161.3 | -59.7 | 0.2 | 20.02.2010 | 1689 |
| 56095 | Eta Carinae | 161.3 | -59.7 | 0.6 | 20.02.2010 | 1689 |
| 56111 | Eta Carinae | 161.3 | -59.7 | 1.2 | 21.02.2010 | 1445 |
| 56120 | Eta Carinae | 161.3 | -59.7 | 1.2 | 22.02.2010 | 1688 |
| 56122 | Eta Carinae | 161.3 | -59.7 | 0.6 | 22.02.2010 | 1688 |
| 56139 | Eta Carinae | 161.3 | -59.7 | 1.2 | 23.02.2010 | 750 |
| 56347 | Eta Carinae | 161.3 | -59.7 | 0.6 | 09.03.2010 | 1688 |
| 56365 | Eta Carinae | 161.3 | -59.7 | 1.2 | 10.03.2010 | 1688 |
| 56460 | Eta Carinae | 161.3 | -59.7 | 0.6 | 13.03.2010 | 1689 |
| 56488 | Eta Carinae | 161.3 | -59.7 | 1.2 | 14.03.2010 | 1688 |

| Run No. | Target | RA | Dec | Offset | Date | Duration |
|---|---|---|---|---|---|---|
| | | ° | ° | ° | dd.mm.yyyy | s |
| 56525 | Eta Carinae | 161.3 | -59.7 | 0.6 | 15.03.2010 | 1688 |
| 56556 | Eta Carinae | 161.3 | -59.7 | 1.2 | 16.03.2010 | 1689 |
| 56589 | Eta Carinae | 161.3 | -59.7 | 0.6 | 17.03.2010 | 1689 |
| 56635 | Eta Carinae | 161.3 | -59.7 | 1.2 | 18.03.2010 | 1695 |
| 56637 | Eta Carinae | 161.3 | -59.7 | 0.6 | 18.03.2010 | 1697 |
| 56774 | Eta Carinae | 161.3 | -59.7 | 1.2 | 22.03.2010 | 1695 |

## A.5 MSH11-62

| Run No. | Target | RA | Dec | Offset | Date | Duration |
|---|---|---|---|---|---|---|
| | | ° | ° | ° | dd.mm.yyyy | s |
| 20003 | Centaurus X-3 | 170.3 | -60.6 | 1.3 | 21.03.2004 | 1683 |
| 20049 | Centaurus X-3 | 170.3 | -60.6 | 1.3 | 22.03.2004 | 1683 |
| 20050 | Centaurus X-3 | 170.3 | -60.6 | 1.3 | 22.03.2004 | 1571 |
| 20078 | Centaurus X-3 | 170.3 | -60.6 | 1.3 | 23.03.2004 | 1683 |
| 20080 | Centaurus X-3 | 170.3 | -60.6 | 1.3 | 23.03.2004 | 1682 |
| 30600 | G293.6+0.2 | 173.2 | -61.2 | 2.6 | 05.03.2006 | 1693 |
| 30602 | G293.2-0.8 | 171.7 | -62.1 | 2.3 | 05.03.2006 | 1693 |
| 30603 | G292.8+0.2 | 171.6 | -61.0 | 1.8 | 05.03.2006 | 1693 |
| 30924 | MSH 11-62 | 168.0 | -60.6 | 0.7 | 28.03.2006 | 1688 |
| 30969 | G291.6-0.8 | 168.5 | -61.5 | 0.9 | 31.03.2006 | 1689 |
| 31025 | G292.0-1.8 | 168.5 | -62.6 | 2.0 | 03.04.2006 | 1688 |

| Run No. | Target | RA | Dec | Offset | Date | Duration |
|---|---|---|---|---|---|---|
| | | ° | ° | ° | dd.mm.yyyy | s |
| 31026 | G291.2+0.2 | 168.5 | -60.4 | 0.4 | 03.04.2006 | 1688 |
| 31027 | G291.2-1.8 | 167.0 | -62.3 | 1.7 | 03.04.2006 | 1688 |
| 31044 | G290.4+0.2 | 167.0 | -60.1 | 0.7 | 04.04.2006 | 1689 |
| 31045 | G290.4-1.8 | 165.4 | -62.0 | 1.8 | 04.04.2006 | 1688 |
| 36755 | PSR J1124-5916 | 171.2 | -58.6 | 2.6 | 16.01.2007 | 1688 |
| 36756 | PSR J1124-5916 | 171.2 | -60.0 | 1.7 | 16.01.2007 | 1693 |
| 36777 | PSR J1124-5916 | 172.5 | -59.3 | 2.6 | 17.01.2007 | 1689 |
| 36778 | PSR J1124-5916 | 169.8 | -59.3 | 1.7 | 17.01.2007 | 1689 |
| 36803 | PSR J1124-5916 | 171.2 | -58.6 | 2.6 | 18.01.2007 | 1688 |
| 36804 | PSR J1124-5916 | 171.2 | -60.0 | 1.7 | 18.01.2007 | 1688 |
| 38699 | Centaurus X-3 | 170.3 | -60.6 | 0.5 | 09.05.2007 | 1688 |
| 38700 | Centaurus X-3 | 170.3 | -60.6 | 1.9 | 09.05.2007 | 1671 |
| 38701 | Centaurus X-3 | 170.3 | -60.6 | 1.3 | 09.05.2007 | 1689 |
| 38738 | Centaurus X-3 | 170.3 | -60.6 | 1.9 | 10.05.2007 | 1688 |
| 38917 | Centaurus X-3 | 170.3 | -60.6 | 1.4 | 16.05.2007 | 1688 |
| 38918 | Centaurus X-3 | 170.3 | -60.6 | 1.3 | 16.05.2007 | 1687 |
| 38919 | Centaurus X-3 | 170.3 | -60.6 | 1.9 | 16.05.2007 | 1688 |
| 38921 | Centaurus X-3 | 170.3 | -60.6 | 0.5 | 16.05.2007 | 1688 |
| 38947 | Centaurus X-3 | 170.3 | -60.6 | 1.4 | 17.05.2007 | 1690 |
| 38949 | Centaurus X-3 | 170.3 | -60.6 | 1.3 | 17.05.2007 | 465 |
| 38950 | Centaurus X-3 | 170.3 | -60.6 | 1.9 | 17.05.2007 | 1689 |
| 43771 | IGR J11215-5952 | 170.5 | -60.6 | 1.2 | 06.01.2008 | 1689 |
| 43772 | IGR J11215-5952 | 170.5 | -59.2 | 1.9 | 06.01.2008 | 1688 |
| 43773 | IGR J11215-5952 | 169.0 | -59.9 | 1.0 | 06.01.2008 | 1688 |
| 43774 | IGR J11215-5952 | 161.8 | -59.9 | 2.1 | 06.01.2008 | 1028 |
| 44686 | G292.9-1.0 | 171.0 | -62.2 | 2.1 | 03.04.2008 | 1688 |
| 44747 | G290.3+0.4 | 167.0 | -59.9 | 0.9 | 06.04.2008 | 1689 |
| 44778 | G290.3-1.1 | 165.8 | -61.3 | 1.2 | 07.04.2008 | 1689 |

| Run No. | Target | RA | Dec | Offset | Date | Duration |
|---|---|---|---|---|---|---|
| | | ° | ° | ° | dd.mm.yyyy | s |
| 44779 | G291.2-0.9 | 167.7 | -61.5 | 0.8 | 07.04.2008 | 1688 |
| 44780 | G291.2+0.0 | 168.4 | -60.6 | 0.2 | 07.04.2008 | 1689 |
| 44781 | G292.1-1.2 | 169.2 | -62.1 | 1.5 | 07.04.2008 | 1688 |
| 44782 | G293.5-0.9 | 172.3 | -62.3 | 2.6 | 07.04.2008 | 1688 |
| 44807 | G292.1+0.3 | 170.3 | -60.7 | 1.2 | 08.04.2008 | 1688 |
| 44809 | G292.1+0.3 | 170.3 | -60.7 | 1.2 | 08.04.2008 | 1597 |
| 45691 | G291.2-0.9 | 167.7 | -61.5 | 0.8 | 27.05.2008 | 1688 |
| 45692 | G291.2-0.9 | 167.7 | -61.5 | 0.8 | 27.05.2008 | 1688 |
| 45693 | G291.2-0.9 | 167.7 | -61.5 | 0.8 | 27.05.2008 | 1688 |
| 45713 | G290.3+0.4 | 167.0 | -59.9 | 0.9 | 28.05.2008 | 1688 |
| 45740 | G290.3+0.4 | 167.0 | -59.9 | 0.9 | 30.05.2008 | 1688 |
| 45741 | G290.3-1.1 | 165.8 | -61.3 | 1.2 | 30.05.2008 | 1689 |
| 45742 | G290.3-1.1 | 165.8 | -61.3 | 1.2 | 30.05.2008 | 1687 |
| 45766 | G291.2+0.0 | 167.7 | -61.5 | 0.8 | 31.05.2008 | 1689 |
| 45767 | G291.2-0.9 | 167.7 | -61.5 | 0.8 | 31.05.2008 | 1679 |
| 45792 | G293.5-0.9 | 172.3 | -62.3 | 2.6 | 01.06.2008 | 1688 |
| 45825 | G292.1+0.3 | 170.3 | -60.7 | 1.2 | 02.06.2008 | 1688 |
| 45826 | G292.1-1.2 | 169.2 | -62.1 | 1.5 | 02.06.2008 | 1688 |
| 45882 | G290.3+0.4 | 167.0 | -59.9 | 0.9 | 04.06.2008 | 1688 |
| 45883 | G290.3-1.1 | 165.8 | -61.3 | 1.2 | 04.06.2008 | 1687 |
| 50327 | Eta Carinae | 161.3 | -59.7 | 2.8 | 19.03.2009 | 1687 |
| 50395 | Eta Carinae | 161.3 | -59.7 | 2.8 | 23.03.2005 | 1687 |
| 50477 | PSR J1124-5916 | 171.2 | -59.3 | 2.6 | 26.03.2005 | 1204 |

## A.6 MSH11-54

| Run No. | Target | RA | Dec | Offset | Date | Duration |
|---|---|---|---|---|---|---|
| | | ° | ° | ° | dd.mm.yyyy | s |
| 20003 | Centaurus X-3 | 170.3 | -60.6 | 1.0 | 21.03.2004 | 1683 |
| 20049 | Centaurus X-3 | 170.3 | -60.6 | 1.0 | 22.03.2004 | 1683 |
| 20050 | Centaurus X-3 | 170.3 | -60.6 | 1.9 | 22.03.2004 | 1571 |
| 20078 | Centaurus X-3 | 170.3 | -60.6 | 1.0 | 23.03.2004 | 1683 |
| 20080 | Centaurus X-3 | 170.3 | -60.6 | 1.0 | 23.03.2004 | 1682 |
| 30600 | G293.6+0.2 | 173.2 | -61.2 | 2.2 | 05.03.2006 | 1693 |
| 30602 | G293.2-0.8 | 171.7 | -62.1 | 2.8 | 05.03.2006 | 1693 |
| 30603 | G292.8+0.2 | 171.6 | -61.0 | 1.7 | 05.03.2006 | 1693 |
| 30924 | MSH 11-62 | 168.0 | -60.6 | 2.6 | 28.03.2006 | 1688 |
| 30969 | G291.6-0.8 | 168.5 | -61.5 | 2.6 | 31.03.2006 | 1689 |
| 31026 | G291.2+0.2 | 168.5 | -60.4 | 1.8 | 03.04.2006 | 1688 |
| 31044 | G290.4+0.2 | 167.0 | -60.1 | 2.3 | 04.04.2006 | 1689 |
| 36755 | PSR J1124-5916 | 171.2 | -58.6 | 0.7 | 16.01.2007 | 1688 |
| 36756 | PSR J1124-5916 | 171.2 | -60.0 | 0.7 | 16.01.2007 | 1693 |
| 36777 | PSR J1124-5916 | 172.5 | -59.3 | 0.7 | 17.01.2007 | 1689 |
| 36778 | PSR J1124-5916 | 169.8 | -59.3 | 0.7 | 17.01.2007 | 1689 |
| 36803 | PSR J1124-5916 | 171.2 | -58.6 | 0.7 | 18.01.2007 | 1688 |
| 36804 | PSR J1124-5916 | 171.2 | -60.0 | 0.7 | 18.01.2007 | 1688 |
| 38699 | Centaurus X-3 | 170.3 | -60.6 | 1.8 | 09.05.2007 | 1688 |
| 38700 | Centaurus X-3 | 170.3 | -60.6 | 1.4 | 09.05.2007 | 1671 |
| 38701 | Centaurus X-3 | 170.3 | -60.6 | 2.1 | 09.05.2007 | 1689 |
| 38738 | Centaurus X-3 | 170.3 | -60.6 | 1.4 | 10.05.2007 | 1688 |
| 38917 | Centaurus X-3 | 170.3 | -60.6 | 0.8 | 16.05.2007 | 1688 |
| 38918 | Centaurus X-3 | 170.3 | -60.6 | 2.1 | 16.05.2007 | 1687 |
| 38919 | Centaurus X-3 | 170.3 | -60.6 | 1.4 | 16.05.2007 | 1688 |
| 38921 | Centaurus X-3 | 170.3 | -60.6 | 1.8 | 16.05.2007 | 1688 |
| 38947 | Centaurus X-3 | 170.3 | -60.6 | 0.8 | 17.05.2007 | 1690 |
| 38949 | Centaurus X-3 | 170.3 | -60.6 | 1.4 | 17.05.2007 | 465 |

| Run No. | Target | RA | Dec | Offset | Date | Duration |
|---|---|---|---|---|---|---|
| | | ° | ° | ° | dd.mm.yyyy | s |
| 38950 | Centaurus X-3 | 170.3 | -60.6 | 1.8 | 17.05.2007 | 1689 |
| 43771 | IGR J11215-5952 | 170.5 | -60.6 | 1.3 | 06.01.2008 | 1689 |
| 43772 | IGR J11215-5952 | 170.5 | -59.2 | 0.4 | 06.01.2008 | 1688 |
| 43773 | IGR J11215-5952 | 169.0 | -59.9 | 1.2 | 06.01.2008 | 1688 |
| 43774 | IGR J11215-5952 | 161.8 | -59.9 | 0.7 | 06.01.2008 | 1028 |
| 44686 | G292.9-1.0 | 171.0 | -62.2 | 2.9 | 03.04.2008 | 1688 |
| 44747 | G290.3+0.4 | 167.0 | -59.9 | 2.2 | 06.04.2008 | 1689 |
| 44779 | G291.2-0.9 | 167.7 | -61.5 | 2.8 | 07.04.2008 | 1688 |
| 44780 | G291.2+0.0 | 168.4 | -60.6 | 2.0 | 07.04.2008 | 1689 |
| 44781 | G292.1-1.2 | 169.2 | -62.1 | 3.0 | 07.04.2008 | 1688 |
| 44807 | G292.1+0.3 | 170.3 | -60.7 | 1.5 | 08.04.2008 | 1688 |
| 44809 | G292.1+0.3 | 170.3 | -60.7 | 1.5 | 08.04.2008 | 1597 |
| 45691 | G291.2-0.9 | 167.7 | -61.5 | 2.8 | 27.05.2008 | 1688 |
| 45692 | G291.2-0.9 | 167.7 | -61.5 | 2.8 | 27.05.2008 | 1688 |
| 45693 | G291.2-0.9 | 167.7 | -61.5 | 2.8 | 27.05.2008 | 1688 |
| 45713 | G290.3+0.4 | 167.0 | -59.9 | 2.2 | 28.05.2008 | 1688 |
| 45740 | G290.3+0.4 | 167.0 | -59.9 | 2.2 | 30.05.2008 | 1688 |
| 45766 | G291.2+0.0 | 167.7 | -61.5 | 2.0 | 31.05.2008 | 1689 |
| 45767 | G291.2-0.9 | 167.7 | -61.5 | 2.8 | 31.05.2008 | 1679 |
| 45825 | G292.1+0.3 | 170.3 | -60.7 | 1.5 | 02.06.2008 | 1688 |
| 45826 | G292.1-1.2 | 169.2 | -62.1 | 3.0 | 02.06.2008 | 1688 |
| 45882 | G290.3+0.4 | 167.0 | -59.9 | 2.2 | 04.06.2008 | 1688 |
| 50454 | PSR J1124-5916 | 171.2 | -59.3 | 0.7 | 25.03.2009 | 1689 |
| 50479 | PSR J1124-5916 | 171.2 | -59.3 | 0.7 | 26.03.2009 | 1688 |
| 50557 | PSR J1124-5916 | 171.2 | -59.3 | 0.7 | 29.03.2009 | 1688 |
| 50558 | PSR J1124-5916 | 171.2 | -59.3 | 0.7 | 29.03.2009 | 1688 |
| 50577 | PSR J1124-5916 | 171.2 | -59.3 | 0.7 | 30.03.2009 | 1689 |
| 50616 | PSR J1124-5916 | 171.2 | -59.3 | 0.7 | 01.04.2009 | 1689 |

## A.7 G293.8+0.6

| Run No. | Target | RA | Dec | Offset | Date | Duration |
|---|---|---|---|---|---|---|
| | | ° | ° | ° | dd.mm.yyyy | s |
| 20003 | Centaurus X-3 | 170.3 | -60.6 | 1.8 | 21.03.2004 | 1683 |
| 20049 | Centaurus X-3 | 170.3 | -60.6 | 1.8 | 22.03.2004 | 1683 |
| 20050 | Centaurus X-3 | 170.3 | -60.6 | 1.7 | 22.03.2004 | 1571 |
| 20051 | Centaurus X-3 | 170.3 | -60.6 | 1.8 | 22.03.2004 | 1682 |
| 20078 | Centaurus X-3 | 170.3 | -60.6 | 1.8 | 23.03.2004 | 1683 |
| 20079 | Centaurus X-3 | 170.3 | -60.6 | 1.7 | 23.03.2004 | 1682 |
| 20080 | Centaurus X-3 | 170.3 | -60.6 | 1.0 | 23.03.2004 | 1682 |
| 30598 | G294.4-1.8 | 173.5 | -63.4 | 2.5 | 05.03.2006 | 1694 |
| 30599 | G294.0-0.8 | 173.3 | -62.3 | 1.4 | 05.03.2006 | 1690 |
| 30600 | G293.6+0.2 | 173.2 | -61.2 | 0.4 | 05.03.2006 | 1693 |
| 30602 | G293.2-0.8 | 171.7 | -62.1 | 1.5 | 05.03.2006 | 1693 |
| 30603 | G292.8+0.2 | 171.6 | -61.0 | 1.1 | 05.03.2006 | 1693 |
| 36756 | PSR J1124-5916 | 171.2 | -60.0 | 1.6 | 16.01.2007 | 1693 |
| 36777 | PSR J1124-5916 | 172.5 | -59.3 | 1.7 | 17.01.2007 | 1689 |
| 36804 | PSR J1124-5916 | 171.2 | -60.0 | 1.6 | 18.01.2007 | 1688 |
| 38699 | Centaurus X-3 | 170.3 | -60.6 | 2.4 | 09.05.2007 | 1688 |
| 38700 | Centaurus X-3 | 170.3 | -60.6 | 1.0 | 09.05.2007 | 1671 |
| 38701 | Centaurus X-3 | 170.3 | -60.6 | 1.7 | 09.05.2007 | 1689 |
| 38736 | Centaurus X-3 | 170.3 | -60.6 | 1.9 | 10.05.2007 | 1688 |
| 38738 | Centaurus X-3 | 170.3 | -60.6 | 1.0 | 10.05.2007 | 1688 |
| 38917 | Centaurus X-3 | 170.3 | -60.6 | 1.9 | 16.05.2007 | 1688 |
| 38918 | Centaurus X-3 | 170.3 | -60.6 | 1.7 | 16.05.2007 | 1687 |
| 38919 | Centaurus X-3 | 170.3 | -60.6 | 1.0 | 16.05.2007 | 1688 |
| 38947 | Centaurus X-3 | 170.3 | -60.6 | 1.9 | 17.05.2007 | 1690 |
| 38949 | Centaurus X-3 | 170.3 | -60.6 | 1.0 | 17.05.2007 | 465 |
| 43771 | IGR J11215-5952 | 170.5 | -60.6 | 1.6 | 06.01.2008 | 1689 |
| 43774 | IGR J11215-5952 | 161.8 | -59.9 | 1.4 | 06.01.2008 | 1028 |
| 44686 | G292.9-1.0 | 171.0 | -62.2 | 1.8 | 03.04.2008 | 1688 |
| 44782 | G293.5-0.9 | 172.3 | -62.3 | 1.5 | 07.04.2008 | 1688 |

| Run No. | Target | RA | Dec | Offset | Date | duration |
|---|---|---|---|---|---|---|
| | | ° | ° | ° | dd.mm.yyyy | s |
| 44807 | G292.1+0.3 | 170.3 | -60.7 | 1.7 | 08.04.2008 | 1688 |
| 44809 | G292.1+0.3 | 170.3 | -60.7 | 1.7 | 08.04.2008 | 1597 |
| 45792 | G293.5-0.9 | 172.3 | -62.3 | 2.5 | 01.06.2008 | 1688 |
| 45825 | G292.1+0.3 | 170.3 | -60.7 | 1.7 | 02.06.2008 | 1688 |

## A.8 MSH15-56

| Run No. | Target | RA | Dec | Offset | Date | duration |
|---|---|---|---|---|---|---|
| | | ° | ° | ° | dd.mm.yyyy | s |
| 25378 | G328.3-0.7 | 239.7 | -54.1 | 2.3 | 05.05.2005 | 1670 |
| 25400 | G327.1-0.7 | 238.2 | -54.8 | 1.4 | 06.05.2005 | 1539 |
| 25594 | G328.9-0.7 | 240.5 | -53.7 | 2.8 | 17.05.2005 | 1678 |
| 25979 | G324.1-0.7 | 234.0 | -56.7 | 2.5 | 02.06.2005 | 1684 |
| 25980 | G324.7-0.7 | 234.8 | -56.3 | 1.9 | 02.06.2005 | 1684 |
| 25981 | G325.0+0.7 | 233.8 | -55.0 | 2.8 | 02.06.2005 | 1683 |
| 25982 | G325.3-0.7 | 235.7 | -55.9 | 1.5 | 02.06.2005 | 1683 |
| 25984 | G325.9-0.7 | 236.5 | -55.6 | 1.1 | 02.06.2005 | 1684 |
| 25985 | G326.5-0.7 | 237.3 | -55.2 | 1.1 | 02.06.2005 | 1684 |
| 25986 | G326.2+0.7 | 235.4 | -54.3 | 2.5 | 02.06.2005 | 1684 |
| 25987 | G326.8+0.7 | 236.3 | -53.9 | 2.5 | 02.06.2005 | 1683 |
| 25988 | G327.7-0.7 | 239.0 | -54.4 | 1.8 | 02.06.2005 | 1688 |
| 25989 | G327.4+0.7 | 237.1 | -53.6 | 2.7 | 02.06.2005 | 1683 |
| 26175 | G327.1-0.7 | 238.2 | -54.8 | 1.4 | 08.06.2005 | 1683 |
| 27179 | G328.9-0.7 | 240.5 | -53.7 | 2.8 | 12.07.2005 | 1682 |
| 27180 | G327.4+0.7 | 237.1 | -53.6 | 2.7 | 12.07.2005 | 1683 |
| 27198 | G324.1-0.7 | 233.9 | -56.7 | 2.4 | 13.07.2005 | 1686 |
| 27199 | G325.6+0.7 | 234.6 | -54.6 | 2.5 | 13.07.2005 | 1682 |
| 46798 | G327.5+0.7 | 237.2 | -53.5 | 2.8 | 20.07.2008 | 1688 |
| 46823 | G328.5+0.0 | 239.2 | -53.4 | 2.9 | 21.07.2008 | 1688 |
| 46869 | G328.5+0.0 | 239.2 | -53.4 | 2.9 | 22.07.2008 | 1687 |
| 46893 | G327.5+0.7 | 237.2 | -53.5 | 2.8 | 23.07.2008 | 1688 |

| Run No. | Target | RA | Dec | Offset | Date | Duration |
|---|---|---|---|---|---|---|
| | | ° | ° | ° | dd.mm.yyyy | s |
| 46894 | G328.5+0.0 | 239.2 | -53.4 | 2.9 | 23.07.2008 | 1688 |
| 46895 | G328.5+0.0 | 239.2 | -53.4 | 2.9 | 23.07.2008 | 1693 |
| 46919 | G328.5+0.0 | 239.2 | -53.4 | 2.9 | 24.07.2008 | 1688 |
| 47025 | G327.5+0.7 | 237.2 | -53.5 | 2.8 | 26.07.2008 | 1688 |
| 47026 | G328.5+0.0 | 239.2 | -53.4 | 2.9 | 26.07.2008 | 1688 |
| 51587 | G326.7-1.1 | 237.8 | -55.5 | 0.7 | 26.05.2009 | 1687 |
| 51588 | G326.7-1.1 | 237.8 | -55.5 | 0.7 | 26.05.2009 | 1689 |
| 51589 | G327.2-1.8 | 239.5 | -55.6 | 0.9 | 26.05.2009 | 1688 |
| 51614 | G326.7-0.6 | 327.5 | -55.1 | 1.3 | 28.05.2009 | 1533 |
| 51637 | G326.7-0.6 | 327.5 | -55.1 | 1.3 | 29.05.2009 | 1689 |
| 51638 | G326.7-0.6 | 327.5 | -55.1 | 1.3 | 29.05.2009 | 1688 |
| 51658 | G326.5-1.1 | 327.8 | -55.5 | 0.7 | 30.05.2009 | 1688 |
| 51659 | G326.7-0.6 | 237.5 | -55.0 | 1.3 | 30.05.2009 | 272 |
| 52356 | G326.4-1.0 | 237.5 | -55.5 | 0.8 | 12.07.2009 | 1689 |
| 52372 | G325.6-1.0 | 236.4 | -56.0 | 1.0 | 13.07.2009 | 1690 |

## A.9 G327.1-1.1

| Run No. | Target | RA | Dec | Offset | Date | Duration |
|---|---|---|---|---|---|---|
| | | ° | ° | ° | dd.mm.yyyy | s |
| 25378 | G328.3-0.7 | 239.7 | -54.1 | 1.3 | 05.05.2005 | 1670 |
| 25400 | G327.1-0.7 | 238.2 | -54.8 | 0.4 | 06.05.2005 | 1539 |
| 25984 | G325.9-0.7 | 236.5 | -55.6 | 1.8 | 02.06.2005 | 1684 |
| 25985 | G326.5-0.7 | 237.3 | -55.2 | 0.7 | 02.06.2005 | 1684 |
| 25988 | G327.7-0.7 | 239.0 | -54.4 | 0.7 | 02.06.2005 | 1688 |
| 25989 | G327.4+0.7 | 237.1 | -53.6 | 1.8 | 02.06.2005 | 1683 |
| 26175 | G327.1-0.7 | 238.2 | -54.8 | 0.4 | 08.06.2005 | 1683 |
| 51454 | G327.9-1.1 | 239.7 | -54.6 | 0.8 | 21.05.2009 | 1085 |
| 51456 | G327.9-1.1 | 239.7 | -54.6 | 0.8 | 21.05.2009 | 1688 |
| 51587 | G326.7-1.1 | 237.8 | -55.5 | 0.7 | 26.05.2009 | 1687 |
| 51588 | G326.7-1.1 | 237.8 | -55.5 | 0.7 | 26.05.2009 | 1689 |
| 51589 | G327.2-1.8 | 239.5 | -55.6 | 0.9 | 26.05.2009 | 1688 |
| 51614 | G326.7-0.6 | 327.5 | -55.1 | 1.3 | 28.05.2009 | 1533 |
| 51638 | G326.7-0.6 | 327.5 | -55.1 | 1.3 | 29.05.2009 | 1688 |
| 51658 | G326.5-1.1 | 327.8 | -55.5 | 0.7 | 30.05.2009 | 1688 |
| 51661 | G327.9-1.1 | 239.7 | -54.6 | 0.8 | 30.05.2009 | 1688 |
| 52356 | G326.4-1.0 | 237.5 | -55.5 | 0.8 | 12.07.2009 | 1689 |

## A.10 G34.01+20.27

| Run No. | Target | RA | Dec | Offset | Date | Duration |
|---|---|---|---|---|---|---|
| | | ° | ° | ° | dd.mm.yyyy | s |
| 34241 | PSR J1740+1000 | 265.1 | 10.7 | 0.7 | 21.08.2006 | 1690 |
| 34283 | PSR J1740+1000 | 265.1 | 9.3 | 0.7 | 22.08.2006 | 1679 |
| 34288 | PSR J1740+1000 | 265.8 | 10.0 | 0.7 | 22.08.2006 | 1689 |
| 34315 | PSR J1740+1000 | 264.4 | 10.0 | 0.7 | 23.08.2006 | 1688 |
| 34367 | PSR J1740+1000 | 265.1 | 9.3 | 0.7 | 25.08.2006 | 1689 |
| 34368 | PSR J1740+1000 | 265.8 | 10.0 | 0.7 | 25.08.2006 | 1689 |
| 34369 | PSR J1740+1000 | 264.4 | 10.0 | 0.7 | 25.08.2006 | 1688 |
| 34393 | PSR J1740+1000 | 265.1 | 10.7 | 0.7 | 26.08.2006 | 1688 |
| 34398 | PSR J1740+1000 | 265.1 | 9.3 | 0.7 | 26.08.2006 | 1688 |
| 34441 | PSR J1740+1000 | 265.8 | 10.0 | 0.7 | 27.08.2006 | 1689 |

## A.11 The Duck Nebula

| Run No. | Target | RA | Dec | Offset | Date | Duration |
|---|---|---|---|---|---|---|
| | | ° | ° | ° | dd.mm.yyyy | s |
| 20902 | G7.8+0.0 | 270.8 | -22.2 | 2.7 | 21.05.2004 | 1682 |
| 20963 | G5.0+0.0 | 269.3 | -24.6 | 0.7 | 24.05.2004 | 1682 |
| 20993 | G4.3+0.0 | 268.9 | -25.2 | 1.1 | 26.05.2004 | 1683 |
| 20994 | G3.6+0.0 | 268.5 | -25.8 | 1.7 | 26.05.2004 | 1683 |
| 20995 | G2.9+0.0 | 268.1 | -26.4 | 2.4 | 26.05.2004 | 1683 |
| 21122 | G5.7+0.0 | 269.7 | -24.0 | 0.9 | 11.06.2004 | 1683 |
| 21124 | G6.4+0.0 | 270.0 | -23.4 | 1.4 | 11.06.2004 | 1683 |
| 21125 | G7.1+0.0 | 270.4 | -22.8 | 2.1 | 11.06.2004 | 1682 |
| 21183 | W28 | 270.3 | -23.2 | 1.8 | 14.06.2004 | 1683 |
| 21184 | W28 | 270.3 | -23.2 | 1.6 | 14.06.2004 | 1682 |
| 21185 | W28 | 270.3 | -23.2 | 2.2 | 14.06.2004 | 604 |
| 21189 | W28 | 270.3 | -23.2 | 1.2 | 14.06.2004 | 1683 |
| 21219 | G2.2-1.0 | 268.7 | -27.6 | 3.0 | 15.06.2004 | 1682 |
| 21234 | W28 | 270.3 | -23.2 | 1.8 | 16.06.2004 | 1683 |
| 21244 | G2.9-1.0 | 269.1 | -27.0 | 2.3 | 16.06.2004 | 1683 |
| 21267 | W28 | 270.3 | -23.2 | 1.8 | 17.06.2004 | 1682 |
| 21293 | W28 | 270.3 | -23.2 | 1.8 | 18.06.2004 | 1683 |
| 21294 | W28 | 270.3 | -23.2 | 1.8 | 18.06.2004 | 1683 |
| 21297 | W28 | 270.3 | -23.2 | 1.8 | 18.06.2004 | 1683 |
| 21317 | W28 | 270.3 | -23.2 | 1.8 | 19.06.2004 | 1683 |
| 21320 | W28 | 270.3 | -23.2 | 1.8 | 19.06.2004 | 1502 |
| 21345 | G3.6-1.0 | 269.5 | -26.4 | 1.6 | 20.06.2004 | 1682 |
| 21395 | G4.3-1.0 | 269.8 | -25.7 | 0.9 | 22.06.2004 | 1683 |
| 21407 | G2.9+0.1 | 267.1 | -25.9 | 2.8 | 23.06.2004 | 1683 |
| 21439 | G3.6+0.1 | 267.5 | -25.4 | 2.3 | 25.06.2004 | 1683 |
| 21440 | G5.7-1.0 | 270.6 | -24.5 | 0.6 | 25.06.2004 | 1683 |
| 21451 | G4.3+1.0 | 267.9 | -24.7 | 1.9 | 26.06.2004 | 1682 |
| 21546 | G8.4+0.0 | 270.8 | -22.1 | 2.8 | 11.07.2004 | 1687 |

| Run No. | Target | RA | Dec | Offset | Date | Duration |
|---|---|---|---|---|---|---|
| | | ° | ° | ° | dd.mm.yyyy | s |
| 21562 | G8.4+0.0 | 270.8 | -22.1 | 2.8 | 12.07.2004 | 1683 |
| 21583 | G3.6+0.0 | 268.5 | -25.8 | 1.7 | 13.07.2004 | 1682 |
| 21584 | G4.3+0.0 | 268.9 | -25.2 | 1.1 | 13.07.2004 | 1682 |
| 21585 | G5.0+0.0 | 269.3 | -24.6 | 0.7 | 13.07.2004 | 1683 |
| 21586 | G7.8+0.0 | 270.8 | -22.2 | 2.7 | 13.07.2004 | 1681 |
| 21600 | G5.7+0.0 | 269.7 | -24.0 | 0.9 | 14.07.2004 | 1683 |
| 24917 | W28 | 270.3 | -23.2 | 2.4 | 06.04.2005 | 1678 |
| 24918 | W28 | 270.3 | -23.2 | 1.0 | 06.04.2005 | 1677 |
| 24919 | W28 | 270.3 | -23.2 | 1.9 | 06.04.2005 | 1678 |
| 24920 | W28 | 270.3 | -23.2 | 1.7 | 06.04.2005 | 1683 |
| 24921 | W28 | 270.3 | -23.2 | 2.4 | 06.04.2005 | 1678 |
| 24936 | W28 | 270.3 | -23.2 | 1.7 | 07.04.2005 | 1678 |
| 24937 | W28 | 270.3 | -23.2 | 1.9 | 07.04.2005 | 1677 |
| 24938 | W28 | 270.3 | -23.2 | 1.0 | 07.04.2005 | 1679 |
| 24939 | W28 | 270.3 | -23.2 | 1.0 | 07.04.2005 | 1674 |
| 24940 | W28 | 270.3 | -23.2 | 1.7 | 07.04.2005 | 1678 |
| 24960 | W28 | 270.3 | -23.2 | 1.9 | 08.04.2005 | 1678 |
| 24961 | W28 | 270.3 | -23.2 | 1.7 | 08.04.2005 | 1677 |
| 24962 | W28 | 270.3 | -23.2 | 2.4 | 08.04.2005 | 1678 |
| 24963 | W28 | 270.3 | -23.2 | 1.7 | 08.04.2005 | 1678 |
| 24990 | W28 | 270.3 | -23.2 | 1.7 | 09.04.2005 | 1677 |
| 24991 | W28 | 270.3 | -23.2 | 1.9 | 09.04.2005 | 1677 |
| 24992 | W28 | 270.3 | -23.2 | 1.0 | 09.04.2005 | 1674 |
| 24993 | W28 | 270.3 | -23.2 | 1.0 | 09.04.2005 | 860 |
| 31030 | G3.0+0.7 | 267.5 | -26.0 | 2.6 | 03.04.2006 | 1689 |
| 31105 | G3.4+0.7 | 267.7 | -25.7 | 2.2 | 05.04.2006 | 1688 |
| 31107 | G3.8+0.7 | 267.9 | -25.3 | 2.0 | 05.04.2006 | 1688 |
| 31467 | G3.2-0.7 | 268.9 | -26.5 | 2.0 | 26.04.2006 | 1688 |

| Run No. | Target | RA | Dec | Offset | Date | Duration |
|---|---|---|---|---|---|---|
| | | ◦ | ◦ | ◦ | dd.mm.yyyy | s |
| 31508 | G2.6+0.7 | 267.2 | -26.3 | 2.9 | 27.04.2006 | 1688 |
| 31509 | G3.8+0.7 | 267.9 | -25.3 | 1.9 | 27.04.2006 | 1688 |
| 31510 | G3.4+0.7 | 267.7 | -25.7 | 2.2 | 27.04.2006 | 1688 |
| 31511 | G3.0+0.7 | 267.5 | -26.0 | 2.6 | 27.04.2006 | 1173 |
| 31623 | W28 | 270.3 | -23.7 | 1.5 | 01.05.2006 | 1689 |
| 31624 | W28 | 270.3 | -23.7 | 1.2 | 01.05.2006 | 1688 |
| 31625 | W28 | 270.3 | -23.7 | 1.5 | 01.05.2006 | 1688 |
| 31671 | W28 | 270.3 | -23.7 | 1.5 | 02.05.2006 | 1689 |
| 31672 | W28 | 270.3 | -23.7 | 1.2 | 02.05.2006 | 1688 |
| 31673 | W28 | 270.3 | -23.7 | 1.5 | 02.05.2006 | 1021 |
| 31701 | W28 | 270.3 | -23.7 | 1.2 | 03.05.2006 | 1688 |
| 31702 | W28 | 270.3 | -23.7 | 1.5 | 03.05.2006 | 1689 |
| 31703 | W28 | 270.3 | -23.7 | 1.2 | 03.05.2006 | 1689 |
| 31704 | W28 | 270.3 | -23.7 | 1.5 | 03.05.2006 | 1688 |
| 31705 | W28 | 270.3 | -23.7 | 1.2 | 03.05.2006 | 827 |
| 31727 | W28 | 270.3 | -23.7 | 1.2 | 04.05.2006 | 1689 |
| 31728 | W28 | 270.3 | -23.7 | 1.5 | 04.05.2006 | 1689 |
| 31729 | W28 | 270.3 | -23.7 | 1.2 | 04.05.2006 | 1687 |
| 31730 | W28 | 270.3 | -23.7 | 1.5 | 04.05.2006 | 1688 |
| 31731 | W28 | 270.3 | -23.7 | 1.2 | 04.05.2006 | 1386 |
| 31757 | W28 | 270.3 | -23.7 | 1.5 | 05.05.2006 | 1688 |
| 31786 | W28 | 270.3 | -23.7 | 1.2 | 05.05.2006 | 1689 |
| 31787 | W28 | 270.3 | -23.7 | 1.5 | 05.05.2006 | 1689 |
| 31788 | W28 | 270.3 | -23.7 | 1.2 | 05.05.2006 | 1689 |
| 31789 | W28 | 270.3 | -23.7 | 1.5 | 05.05.2006 | 1688 |
| 31790 | W28 | 270.3 | -23.7 | 1.2 | 05.05.2006 | 1688 |
| 31801 | W28 | 270.3 | -23.7 | 1.2 | 05.05.2006 | 1688 |
| 31802 | W28 | 270.3 | -23.7 | 1.5 | 05.05.2006 | 1689 |

| Run No. | Target | RA | Dec | Offset | Date | Duration |
|---|---|---|---|---|---|---|
| | | ° | ° | ° | dd.mm.yyyy | s |
| 31803 | W28 | 270.3 | -23.7 | 1.2 | 05.05.2006 | 1689 |
| 31804 | W28 | 270.3 | -23.7 | 1.5 | 05.05.2006 | 966 |
| 31839 | W28 | 270.3 | -23.7 | 1.5 | 08.05.2006 | 1689 |
| 31840 | W28 | 270.3 | -23.7 | 1.2 | 08.05.2006 | 1688 |
| 31841 | W28 | 270.3 | -23.7 | 1.5 | 08.05.2006 | 1688 |
| 31842 | W28 | 270.3 | -23.7 | 1.2 | 08.05.2006 | 1688 |
| 31897 | W28 | 270.3 | -23.7 | 1.8 | 09.05.2006 | 1688 |
| 32321 | W28 | 270.3 | -23.7 | 1.2 | 23.05.2006 | 1689 |
| 32323 | W28 | 270.3 | -23.7 | 1.2 | 23.05.2006 | 1689 |
| 32324 | W28 | 270.3 | -23.7 | 1.5 | 23.05.2006 | 1688 |
| 32325 | W28 | 270.3 | -23.7 | 1.5 | 23.05.2006 | 1689 |
| 32330 | W28 | 270.3 | -23.7 | 1.2 | 23.05.2006 | 1688 |
| 32331 | W28 | 270.3 | -23.7 | 1.5 | 23.05.2006 | 1689 |
| 32384 | W28 | 270.3 | -23.7 | 1.2 | 25.05.2006 | 1689 |
| 32385 | G3.0+0.7 | 267.5 | -26.0 | 2.6 | 25.05.2006 | 1689 |
| 32413 | G4.0-0.7 | 269.4 | -25.9 | 1.2 | 26.05.2006 | 1689 |
| 32414 | G3.6-0.7 | 269.2 | -26.2 | 1.6 | 26.05.2006 | 1689 |
| 32416 | G3.6-0.7 | 269.2 | -26.2 | 1.6 | 26.05.2006 | 1690 |
| 32443 | G3.0+0.7 | 268.9 | -26.5 | 2.0 | 27.05.2006 | 1689 |
| 32444 | G4.0-0.7 | 269.4 | -26.9 | 2.4 | 27.05.2006 | 1688 |
| 32462 | G2.8-0.7 | 268.7 | -26.9 | 2.4 | 28.05.2006 | 1688 |
| 32469 | G2.4-0.7 | 268.5 | -27.2 | 2.8 | 28.05.2006 | 1688 |
| 32497 | G2.8-0.7 | 268.7 | -26.9 | 2.4 | 29.05.2006 | 1688 |
| 32585 | G2.6+0.7 | 267.2 | -26.3 | 2.9 | 01.06.2006 | 1688 |
| 32659 | G3.4+0.7 | 267.7 | -25.6 | 2.2 | 02.06.2006 | 1690 |
| 32660 | G3.4+0.7 | 267.7 | -25.6 | 2.2 | 02.06.2006 | 1690 |
| 32661 | G3.8+0.7 | 267.9 | -25.3 | 1.9 | 02.06.2006 | 1689 |
| 32662 | G3.8+0.7 | 267.9 | -25.3 | 1.9 | 02.06.2006 | 1689 |
| 32663 | G3.2-0.7 | 268.9 | -26.5 | 2.0 | 02.06.2006 | 1689 |

| Run No. | Target | RA | Dec | Offset | Date | Duration |
|---|---|---|---|---|---|---|
| | | ° | ° | ° | dd.mm.yyyy | s |
| 32664 | G3.2-0.7 | 268.9 | -26.5 | 2.0 | 02.06.2006 | 1689 |
| 32665 | G2.4-0.7 | 268.4 | -27.2 | 2.8 | 02.06.2006 | 856 |
| 32680 | G2.4-0.7 | 268.5 | -27.2 | 2.8 | 03.06.2006 | 1690 |
| 32681 | G2.4-0.7 | 268.5 | -27.2 | 2.8 | 03.06.2006 | 1689 |
| 44820 | Terzan 5 | 267.0 | -24.8 | 2.8 | 08.04.2008 | 1688 |
| 44849 | Terzan 5 | 267.0 | -24.8 | 2.8 | 10.04.2008 | 1690 |
| 45257 | Terzan 5 | 267.0 | -24.8 | 2.8 | 03.05.2008 | 1689 |
| 45258 | Terzan 5 | 267.0 | -24.8 | 2.0 | 03.05.2008 | 1688 |
| 46282 | Terzan 5 | 267.0 | -24.8 | 2.0 | 26.06.2008 | 1689 |
| 46285 | Terzan 5 | 267.0 | -24.8 | 2.1 | 26.06.2008 | 1254 |
| 46325 | Terzan 5 | 267.0 | -24.8 | 2.4 | 28.06.2008 | 1688 |
| 46326 | Terzan 5 | 267.0 | -24.8 | 2.1 | 28.06.2008 | 1688 |
| 46345 | Terzan 5 | 267.0 | -24.8 | 2.4 | 29.06.2008 | 1688 |
| 46347 | Terzan 5 | 267.0 | -24.8 | 2.4 | 29.06.2008 | 1687 |
| 46373 | Terzan 5 | 267.0 | -24.8 | 2.1 | 30.06.2008 | 1687 |
| 46376 | Terzan 5 | 267.0 | -24.8 | 2.1 | 30.06.2008 | 1688 |

## A.12 G7.4-2.0

| Run No. | Target | RA | Dec | Offset | Date | Duration |
|---|---|---|---|---|---|---|
| | | ° | ° | ° | dd.mm.yyyy | s |
| 34190 | V4234 Sgr | 270.5 | -33.8 | 2.3 | 19.08.2006 | 1690 |
| 34244 | V4234 Sgr | 269.7 | -33.1 | 2.5 | 21.08.2006 | 1688 |
| 34286 | V4234 Sgr | 270.5 | -33.8 | 2.3 | 22.08.2006 | 1688 |
| 34366 | V4234 Sgr | 269.7 | -33.1 | 2.5 | 25.08.2006 | 1688 |
| 34440 | V4234 Sgr | 270.5 | -33.8 | 2.3 | 27.08.2006 | 1689 |

## A.13 G11.2-0.3

| Run No. | Target | RA | Dec | Offset | Date | Duration |
|---|---|---|---|---|---|---|
| | | ° | ° | ° | dd.mm.yyyy | s |
| 20877 | G9.9+0.0 | 271.9 | -20.4 | 1.3 | 20.05.2004 | 1682 |
| 20949 | G14.1+0.0 | 274.1 | -16.7 | 2.9 | 23.05.2004 | 1682 |
| 20964 | G13.4+0.0 | 273.7 | -17.3 | 2.2 | 24.05.2004 | 1682 |
| 20965 | G12.7+0.0 | 273.3 | -17.9 | 1.6 | 24.05.2004 | 1683 |
| 20966 | G12.0+0.0 | 273.0 | -18.5 | 0.9 | 24.05.2004 | 1682 |
| 20969 | G11.3+0.0 | 272.6 | -19.2 | 0.4 | 24.05.2004 | 1682 |
| 20982 | G9.2+0.0 | 271.5 | -20.9 | 2.0 | 25.05.2004 | 1682 |
| 20983 | G8.5+0.0 | 271.2 | -21.5 | 2.7 | 25.05.2004 | 1682 |
| 21171 | G11.3-1.0 | 273.6 | -19.6 | 0.7 | 13.06.2004 | 1688 |
| 21528 | G12.8-0.0 | 273.7 | -17.4 | 2.2 | 10.07.2004 | 1682 |
| 21544 | G8.4+0.0 | 271.4 | -21.3 | 2.4 | 11.07.2004 | 1682 |
| 21545 | G12.8-0.0 | 273.2 | -18.3 | 1.2 | 11.07.2004 | 1682 |
| 21547 | G8.4+0.0 | 271.4 | -21.3 | 2.4 | 11.07.2004 | 1681 |
| 21548 | G12.8-0.0 | 273.2 | -18.3 | 1.2 | 11.07.2004 | 1682 |
| 21550 | G9.2-1.0 | 272.5 | -21.5 | 2.1 | 11.07.2004 | 1682 |
| 21563 | G12.8-0.0 | 273.2 | -18.3 | 1.2 | 12.07.2004 | 1682 |
| 21564 | G12.8-0.0 | 273.7 | -17.4 | 2.2 | 12.07.2004 | 1682 |
| 21565 | G8.4+0.0 | 271.4 | -21.3 | 2.3 | 12.07.2004 | 1682 |
| 21570 | G9.9-1.0 | 272.8 | -20.9 | 1.4 | 12.07.2004 | 1682 |
| 21571 | G13.4-1.0 | 274.6 | -17.8 | 2.3 | 12.07.2004 | 1682 |
| 21587 | G8.5+0.0 | 271.2 | -21.6 | 2.7 | 13.07.2004 | 1681 |
| 21588 | G9.2+0.0 | 271.5 | -21.0 | 2.0 | 13.07.2004 | 1682 |
| 21590 | G12.8-0.0 | 273.9 | -18.1 | 1.6 | 13.07.2004 | 1684 |
| 21601 | G9.9+0.0 | 271.9 | -20.4 | 1.3 | 13.07.2004 | 1680 |
| 21602 | G8.4+0.0 | 270.6 | -21.4 | 2.9 | 13.07.2004 | 1682 |
| 21603 | G8.4+0.0 | 271.6 | -21.93 | 2.8 | 13.07.2004 | 1682 |
| 21604 | G12.8-0.0 | 273.0 | -17.6 | 1.8 | 13.07.2004 | 1682 |
| 21605 | G12.8-0.0 | 273.0 | -17.6 | 1.8 | 13.07.2004 | 1682 |

| Run No. | Target | RA | Dec | Offset | Date | Duration |
|---|---|---|---|---|---|---|
| | | ° | ° | ° | dd.mm.yyyy | s |
| 21606 | G8.4+0.0 | 271.6 | -21.9 | 2.8 | 13.07.2004 | 1682 |
| 21607 | G8.4+0.0 | 270.6 | -21.4 | 2.9 | 13.07.2004 | 1682 |
| 21609 | G9.9+0.0 | 271.9 | -20.4 | 2.3 | 13.07.2004 | 1682 |
| 21624 | G12.8-0.0 | 273.9 | -18.1 | 1.6 | 15.07.2004 | 1682 |
| 21626 | G9.2+1.0 | 270.6 | -20.5 | 2.4 | 15.07.2004 | 1682 |
| 21627 | G10.6-1.0 | 273.2 | -20.2 | 0.9 | 15.07.2004 | 1682 |
| 21628 | G9.9+1.0 | 271.0 | -19.9 | 1.9 | 15.07.2004 | 1685 |
| 21697 | G12.7-1.0 | 274.2 | -18.4 | 1.7 | 18.07.2004 | 1682 |
| 21717 | G12.0+1.0 | 272.0 | -18.1 | 1.6 | 19.07.2004 | 1031 |
| 21718 | G12.7+1.0 | 272.4 | -17.4 | 2.0 | 19.07.2004 | 1332 |
| 21720 | G14.1-1.0 | 274.9 | -17.2 | 3.0 | 19.07.2004 | 1682 |
| 21743 | G13.4+1.0 | 272.8 | -16.8 | 2.6 | 20.07.2004 | 1682 |
| 22352 | G12.8-0.0 | 273.4 | -17.8 | 1.8 | 08.09.2004 | 1682 |
| 22353 | G12.8-0.0 | 273.4 | -17.8 | 1.6 | 08.09.2004 | 1681 |
| 22354 | G8.4+0.0 | 271.1 | -21.7 | 2.9 | 08.09.2004 | 1681 |
| 22355 | G8.4+0.0 | 271.1 | -21.7 | 2.7 | 08.09.2004 | 1682 |
| 22370 | G12.8-0.0 | 273.4 | -17.8 | 1.2 | 09.09.2004 | 1681 |
| 22371 | G12.8-0.0 | 273.4 | -17.8 | 2.2 | 09.09.2004 | 1682 |
| 22373 | G8.4+0.0 | 271.1 | -21.7 | 2.3 | 09.09.2004 | 1432 |
| 22387 | G8.4+0.0 | 271.1 | -21.7 | 2.3 | 10.09.2004 | 1542 |
| 26155 | J1809-193 | 272.5 | -19.4 | 0.8 | 07.06.2005 | 1690 |
| 26156 | J1809-193 | 272.5 | -19.4 | 0.7 | 07.06.2005 | 1690 |
| 26202 | J1809-193 | 272.5 | -19.4 | 0.3 | 09.06.2005 | 1691 |
| 26235 | J1809-193 | 272.5 | -19.4 | 0.7 | 10.06.2005 | 1690 |
| 26236 | J1809-193 | 272.5 | -19.4 | 0.8 | 10.06.2005 | 1690 |
| 26420 | J1809-193 | 272.5 | -19.4 | 0.7 | 14.06.2005 | 1690 |
| 26932 | J1809-193 | 272.5 | -19.4 | 0.3 | 03.07.2005 | 1695 |
| 26933 | J1809-193 | 272.5 | -19.4 | 1.1 | 03.07.2005 | 1690 |

| Run No. | Target | RA | Dec | Offset | Date | Duration |
|---|---|---|---|---|---|---|
| | | ° | ° | ° | dd.mm.yyyy | s |
| 26961 | J1809-193 | 272.5 | -19.4 | 0.7 | 04.07.2005 | 1691 |
| 26962 | J1809-193 | 272.5 | -19.4 | 0.8 | 04.07.2005 | 1691 |
| 33520 | J18100-1920 | 272.5 | -19.3 | 0.7 | 18.07.2006 | 1689 |
| 33560 | J18100-1920 | 272.5 | -19.3 | 1.0 | 20.07.2006 | 1678 |
| 33561 | J18100-1920 | 272.5 | -19.3 | 0.4 | 20.07.2006 | 1689 |
| 33562 | J18100-1920 | 272.5 | -19.3 | 0.7 | 20.07.2006 | 1689 |
| 33563 | J18100-1920 | 272.5 | -19.3 | 0.9 | 20.07.2006 | 1688 |
| 33564 | J18100-1920 | 272.5 | -19.3 | 1.0 | 20.07.2006 | 1689 |
| 33580 | J18100-1920 | 272.5 | -19.3 | 0.9 | 21.07.2006 | 1689 |
| 33581 | J18100-1920 | 272.5 | -19.3 | 0.7 | 21.07.2006 | 1689 |
| 33582 | J18100-1920 | 272.5 | -19.3 | 0.4 | 21.07.2006 | 1689 |
| 33583 | J18100-1920 | 272.5 | -19.3 | 1.0 | 21.07.2006 | 1688 |
| 33584 | J18100-1920 | 272.5 | -19.3 | 0.9 | 21.07.2006 | 1688 |
| 33605 | J18100-1920 | 272.5 | -19.3 | 0.7 | 22.07.2006 | 1689 |
| 33606 | J18100-1920 | 272.5 | -19.3 | 0.9 | 22.07.2006 | 1689 |
| 33607 | J18100-1920 | 272.5 | -19.3 | 1.0 | 22.07.2006 | 1689 |
| 33629 | J18100-1920 | 272.5 | -19.3 | 0.4 | 23.07.2006 | 1689 |
| 33630 | J18100-1920 | 272.5 | -19.3 | 1.0 | 23.07.2006 | 783 |
| 33631 | J18100-1920 | 272.5 | -19.3 | 0.4 | 23.07.2006 | 1688 |
| 33632 | J18100-1920 | 272.5 | -19.3 | 1.0 | 23.07.2006 | 1689 |
| 33633 | J18100-1920 | 272.5 | -19.3 | 0.9 | 23.07.2006 | 1689 |
| 33656 | J18100-1920 | 272.5 | -19.3 | 1.0 | 24.07.2006 | 1688 |
| 33657 | J18100-1920 | 272.5 | -19.3 | 0.4 | 24.07.2006 | 1689 |
| 33659 | J18100-1920 | 272.5 | -19.3 | 1.0 | 24.07.2006 | 1688 |
| 33660 | J18100-1920 | 272.5 | -19.3 | 0.4 | 24.07.2006 | 1689 |
| 33685 | J18100-1920 | 272.5 | -19.3 | 0.9 | 25.07.2006 | 1689 |
| 33686 | J18100-1920 | 272.5 | -19.3 | 0.9 | 25.07.2006 | 1688 |
| 33687 | J18100-1920 | 272.5 | -19.3 | 0.7 | 25.07.2006 | 1689 |

| Run No. | Target | RA | Dec | Offset | Date | Duration |
|---|---|---|---|---|---|---|
| | | ° | ° | ° | dd.mm.yyyy | s |
| 33688 | J18100-1920 | 272.5 | -19.3 | 1.0 | 25.07.2006 | 1689 |
| 33689 | J18100-1920 | 272.5 | -19.3 | 0.9 | 25.07.2006 | 1688 |
| 33690 | J18100-1920 | 272.5 | -19.3 | 0.7 | 25.07.2006 | 1688 |
| 41347 | HESS J1809-193 | 272.3 | -19.45 | 1.2 | 31.08.2007 | 1689 |
| 41348 | HESS J1809-193 | 272.3 | -19.45 | 0.8 | 31.08.2007 | 1689 |
| 41935 | HESS J1809-193 | 272.3 | -19.45 | 0.9 | 29.09.2007 | 1691 |
| 41955 | HESS J1809-193 | 272.3 | -19.45 | 1.2 | 30.09.2007 | 1689 |
| 41975 | HESS J1809-193 | 272.3 | -19.45 | 0.2 | 01.10.2007 | 1687 |
| 41976 | HESS J1809-193 | 272.3 | -19.45 | 0.8 | 01.10.2007 | 1688 |
| 41992 | HESS J1809-193 | 272.3 | -19.45 | 0.9 | 02.10.2007 | 1688 |
| 41993 | HESS J1809-193 | 272.3 | -19.45 | 0.2 | 02.10.2007 | 1689 |
| 42076 | HESS J1809-193 | 272.3 | -19.45 | 1.2 | 04.10.2007 | 1688 |
| 42077 | HESS J1809-193 | 272.3 | -19.45 | 0.8 | 04.10.2007 | 1688 |
| 42117 | HESS J1809-193 | 272.3 | -19.45 | 0.9 | 05.10.2007 | 1688 |
| 42147 | HESS J1809-193 | 272.3 | -19.45 | 0.2 | 06.10.2007 | 1689 |
| 42170 | HESS J1809-193 | 272.3 | -19.45 | 1.2 | 07.10.2007 | 1688 |
| 42210 | HESS J1809-193 | 272.3 | -19.45 | 0.8 | 08.10.2007 | 1689 |
| 42237 | HESS J1809-193 | 272.3 | -19.45 | 0.9 | 09.10.2007 | 1688 |
| 52498 | Sgr 1806-20 | 272.2 | -20.4 | 1.0 | 18.07.2009 | 1687 |
| 52552 | Sgr 1806-20 | 272.2 | -20.4 | 0.7 | 20.07.2009 | 1687 |
| 52578 | Sgr 1806-20 | 272.2 | -20.4 | 0.9 | 21.07.2009 | 1689 |
| 52580 | Sgr 1806-20 | 272.2 | -20.4 | 0.7 | 21.07.2009 | 1689 |
| 52604 | Sgr 1806-20 | 272.2 | -20.4 | 1.0 | 22.07.2009 | 1688 |
| 52628 | Sgr 1806-20 | 272.2 | -20.4 | 1.7 | 23.07.2009 | 1688 |
| 52655 | Sgr 1806-20 | 272.2 | -20.4 | 1.0 | 24.07.2009 | 1688 |
| 52675 | Sgr 1806-20 | 272.2 | -20.4 | 0.7 | 25.07.2009 | 1688 |
| 52698 | Sgr 1806-20 | 272.2 | -20.4 | 1.0 | 26.07.2009 | 1688 |
| 52716 | Sgr 1806-20 | 272.2 | -20.4 | 1.0 | 27.07.2009 | 1691 |

| Run No. | Target | RA | Dec | Offset | Date | Duration |
|---|---|---|---|---|---|---|
| | | ° | ° | ° | dd.mm.yyyy | s |
| 52954 | Sgr 1806-20 | 272.2 | -20.4 | 1.0 | 11.08.2009 | 1693 |
| 52956 | Sgr 1806-20 | 272.2 | -20.4 | 0.7 | 11.08.2009 | 1688 |
| 52969 | Sgr 1806-20 | 272.2 | -20.4 | 1.0 | 12.08.2009 | 1687 |
| 53008 | Sgr 1806-20 | 272.2 | -20.4 | 0.7 | 13.08.2009 | 1689 |
| 53010 | Sgr 1806-20 | 272.2 | -20.4 | 1.0 | 13.08.2009 | 1689 |
| 53027 | Sgr 1806-20 | 272.2 | -20.4 | 0.7 | 14.08.2009 | 1688 |
| 53048 | Sgr 1806-20 | 272.2 | -20.4 | 1.0 | 15.08.2009 | 1689 |
| 53074 | Sgr 1806-20 | 272.2 | -20.4 | 1.0 | 16.08.2009 | 1687 |
| 53076 | Sgr 1806-20 | 272.2 | -20.4 | 0.7 | 16.08.2009 | 1688 |
| 53125 | Sgr 1806-20 | 272.2 | -20.4 | 1.0 | 18.08.2009 | 1688 |
| 53146 | Sgr 1806-20 | 272.2 | -20.4 | 0.7 | 18.08.2009 | 1688 |
| 53206 | Sgr 1806-20 | 272.2 | -20.4 | 1.0 | 21.08.2009 | 1688 |

## A.14 G16.7+0.1

| Run No. | Target | RA | Dec | Offset | Date | Duration |
|---|---|---|---|---|---|---|
| | | ° | ° | ° | dd.mm.yyyy | s |
| 20858 | G18.3+0.0 | 276.1 | -13.0 | 1.6 | 18.05.2004 | 1683 |
| 20927 | G16.9+0.0 | 275.4 | -14.2 | 0.2 | 22.05.2004 | 1683 |
| 20947 | G15.5+0.0 | 274.7 | -15.5 | 1.2 | 23.05.2004 | 1683 |
| 21195 | G16.9-0.0 | 274.0 | -16.7 | 1.1 | 14.06.2004 | 1683 |
| 21220 | G17.6-1.0 | 276.6 | -14.1 | 1.4 | 15.06.2004 | 1682 |
| 21301 | G16.2-1.0 | 276.0 | -15.3 | 1.2 | 18.06.2004 | 1683 |
| 22325 | G17.4-1.1 | 276.1 | -14.3 | 0.9 | 06.09.2004 | 1683 |
| 22336 | G17.4-1.1 | 276.1 | -14.3 | 0.9 | 07.09.2004 | 1682 |
| 22338 | G17.4-1.1 | 276.1 | -14.3 | 0.9 | 07.09.2004 | 1682 |
| 22340 | G17.4-1.1 | 276.1 | -14.3 | 0.9 | 07.09.2004 | 1682 |
| 22359 | G17.4-1.1 | 276.1 | -14.3 | 0.9 | 08.09.2004 | 1682 |
| 25016 | LS 5039 | 276.6 | -14.8 | 1.3 | 11.04.2005 | 1670 |
| 25020 | LS 5039 | 276.6 | -14.8 | 1.3 | 11.04.2005 | 1459 |
| 25036 | LS 5039 | 276.6 | -14.8 | 1.3 | 12.04.2005 | 1670 |
| 25038 | LS 5039 | 276.6 | -14.8 | 0.8 | 12.04.2005 | 1670 |
| 25050 | LS 5039 | 276.6 | -14.8 | 0.8 | 13.04.2005 | 1670 |
| 25053 | LS 5039 | 276.6 | -14.8 | 1.3 | 13.04.2005 | 1671 |
| 25096 | LS 5039 | 276.6 | -14.8 | 1.3 | 17.04.2005 | 1669 |
| 25104 | LS 5039 | 276.6 | -14.8 | 0.8 | 18.04.2005 | 1669 |
| 25354 | LS 5039 | 276.6 | -14.8 | 1.3 | 04.05.2005 | 1286 |
| 25381 | LS 5039 | 276.6 | -14.8 | 0.8 | 05.05.2005 | 1670 |
| 25427 | LS 5039 | 276.6 | -14.8 | 1.3 | 07.05.2005 | 1670 |
| 25428 | LS 5039 | 276.6 | -14.8 | 0.8 | 07.05.2005 | 1674 |
| 25432 | LS 5039 | 276.6 | -14.8 | 1.3 | 07.05.2005 | 1057 |
| 25455 | LS 5039 | 276.6 | -14.8 | 0.8 | 08.05.2005 | 1670 |
| 25456 | LS 5039 | 276.6 | -14.8 | 1.3 | 08.05.2005 | 1669 |
| 25477 | LS 5039 | 276.6 | -14.8 | 0.8 | 09.05.2005 | 897 |
| 25480 | LS 5039 | 276.6 | -14.8 | 1.3 | 09.05.2005 | 1198 |

| Run No. | Target | RA | Dec | Offset | Date | Duration |
|---|---|---|---|---|---|---|
| | | ◦ | ◦ | ◦ | dd.mm.yyyy | s |
| 25481 | LS 5039 | 276.6 | -14.8 | 0.8 | 09.05.2005 | 1669 |
| 25499 | LS 5039 | 276.6 | -14.8 | 1.3 | 10.05.2005 | 1671 |
| 25547 | LS 5039 | 276.6 | -14.8 | 1.3 | 14.05.2005 | 1674 |
| 25578 | LS 5039 | 276.6 | -14.8 | 1.3 | 16.05.2005 | 1670 |
| 25592 | LS 5039 | 276.6 | -14.8 | 1.3 | 16.05.2005 | 1678 |
| 25598 | LS 5039 | 276.6 | -14.8 | 1.3 | 17.05.2005 | 576 |
| 25679 | LS 5039 | 276.6 | -14.8 | 1.3 | 18.05.2005 | 1671 |
| 26130 | HESS J1825-137 | 276.5 | -14.5 | 1.2 | 06.06.2005 | 1671 |
| 26179 | HESS J1825-137 | 276.5 | -14.5 | 1.2 | 08.06.2005 | 1687 |
| 26182 | LS 5039 | 276.6 | -14.8 | 0.9 | 08.06.2005 | 1683 |
| 26184 | LS 5039 | 276.6 | -14.8 | 0.9 | 08.06.2005 | 1687 |
| 26209 | LS 5039 | 276.6 | -14.8 | 0.9 | 09.06.2005 | 1682 |
| 26237 | HESS J1825-137 | 276.5 | -14.5 | 1.2 | 10.06.2005 | 1682 |
| 26239 | HESS J1825-137 | 276.5 | -14.5 | 1.2 | 10.06.2005 | 1682 |
| 26883 | LS 5039 | 276.6 | -14.8 | 0.9 | 01.07.2005 | 1686 |
| 26885 | LS 5039 | 276.6 | -14.8 | 0.9 | 01.07.2005 | 1682 |
| 26916 | LS 5039 | 276.6 | -14.8 | 0.9 | 02.07.2005 | 1690 |
| 26918 | LS 5039 | 276.6 | -14.8 | 0.9 | 02.07.2005 | 1692 |
| 26920 | LS 5039 | 276.6 | -14.8 | 0.9 | 02.07.2005 | 1680 |
| 26922 | LS 5039 | 276.6 | -14.8 | 0.9 | 02.07.2005 | 1690 |
| 26937 | LS 5039 | 276.6 | -14.8 | 0.9 | 03.07.2005 | 1686 |
| 26939 | LS 5039 | 276.6 | -14.8 | 0.9 | 03.07.2005 | 1682 |
| 26941 | LS 5039 | 276.6 | -14.8 | 0.9 | 03.07.2005 | 1686 |
| 26943 | LS 5039 | 276.6 | -14.8 | 0.9 | 03.07.2005 | 1682 |
| 26965 | LS 5039 | 276.6 | -14.8 | 0.9 | 04.07.2005 | 1687 |
| 26967 | LS 5039 | 276.6 | -14.8 | 0.9 | 04.07.2005 | 1683 |
| 26969 | LS 5039 | 276.6 | -14.8 | 0.9 | 04.07.2005 | 1686 |
| 26971 | LS 5039 | 276.6 | -14.8 | 0.9 | 04.07.2005 | 1655 |
| 26985 | HESS J1825-137 | 276.5 | -14.5 | 1.2 | 05.07.2005 | 1682 |
| 26987 | LS 5039 | 276.6 | -14.8 | 0.9 | 05.07.2005 | 1682 |

| Run No. | Target | RA | Dec | Offset | Date | duration |
|---|---|---|---|---|---|---|
| | | ° | ° | ° | dd.mm.yyyy | s |
| 26989 | LS 5039 | 276.6 | -14.8 | 0.9 | 05.07.2005 | 1687 |
| 26991 | LS 5039 | 276.6 | -14.8 | 0.9 | 05.07.2005 | 1683 |
| 26993 | LS 5039 | 276.6 | -14.8 | 0.9 | 05.07.2005 | 1686 |
| 27156 | HESS J1825-137 | 276.5 | -14.5 | 1.2 | 11.07.2005 | 1680 |
| 27158 | HESS J1825-137 | 276.5 | -14.5 | 1.2 | 11.07.2005 | 1681 |
| 28385 | LS 5039 | 276.6 | -14.8 | 0.8 | 02.09.2005 | 1680 |
| 28386 | LS 5039 | 276.6 | -14.8 | 1.3 | 02.09.2005 | 1682 |
| 28389 | LS 5039 | 276.6 | -14.8 | 0.8 | 02.09.2005 | 1682 |
| 28417 | LS 5039 | 276.6 | -14.8 | 1.3 | 04.09.2005 | 1686 |
| 28420 | LS 5039 | 276.6 | -14.8 | 0.8 | 04.09.2005 | 1682 |
| 28421 | LS 5039 | 276.6 | -14.8 | 1.3 | 04.09.2005 | 1682 |
| 28441 | LS 5039 | 276.6 | -14.8 | 0.8 | 05.09.2005 | 1687 |
| 28442 | LS 5039 | 276.6 | -14.8 | 1.3 | 05.09.2005 | 1682 |
| 28468 | LS 5039 | 276.6 | -14.8 | 0.8 | 06.09.2005 | 1694 |
| 29362 | LS 5039 | 276.6 | -14.8 | 1.3 | 20.10.2005 | 1690 |
| 29372 | LS 5039 | 276.6 | -14.8 | 1.3 | 21.10.2005 | 1690 |
| 29383 | LS 5039 | 276.6 | -14.8 | 0.8 | 22.10.2005 | 1690 |
| 29425 | LS 5039 | 276.6 | -14.8 | 1.3 | 24.10.2005 | 1690 |
| 34647 | LS 5039 | 276.6 | -14.8 | 0.9 | 10.09.2006 | 1689 |
| 34648 | LS 5039 | 276.6 | -14.8 | 1.3 | 10.09.2006 | 1689 |
| 34822 | LS 5039 | 276.6 | -14.8 | 1.3 | 17.09.2006 | 1688 |
| 34823 | LS 5039 | 276.6 | -14.8 | 0.9 | 17.09.2006 | 1688 |
| 34923 | LS 5039 | 276.6 | -14.8 | 1.3 | 21.09.2006 | 1689 |
| 34924 | LS 5039 | 276.6 | -14.8 | 0.9 | 21.09.2006 | 1689 |
| 35490 | LS 5039 | 276.6 | -14.8 | 1.3 | 19.10.2006 | 1688 |
| 39577 | LS 5039 | 276.6 | -14.8 | 0.9 | 11.06.2007 | 1689 |
| 39578 | LS 5039 | 276.6 | -14.8 | 1.3 | 11.06.2007 | 1689 |

| Run No. | Target | RA | Dec | Offset | Date | Duration |
|---|---|---|---|---|---|---|
| | | ° | ° | ° | dd.mm.yyyy | s |
| 39684 | LS 5039 | 276.6 | -14.8 | 0.9 | 14.06.2007 | 1690 |
| 39687 | LS 5039 | 276.6 | -14.8 | 1.3 | 14.06.2007 | 1688 |
| 39688 | LS 5039 | 276.6 | -14.8 | 0.9 | 14.06.2007 | 1688 |
| 39802 | LS 5039 | 276.6 | -14.8 | 0.9 | 18.06.2007 | 1689 |
| 39805 | LS 5039 | 276.6 | -14.8 | 1.3 | 18.06.2007 | 1688 |
| 39806 | LS 5039 | 276.6 | -14.8 | 0.9 | 18.06.2007 | 1689 |
| 39881 | LS 5039 | 276.6 | -14.8 | 0.9 | 22.06.2007 | 1689 |
| 39884 | LS 5039 | 276.6 | -14.8 | 1.3 | 22.06.2007 | 1688 |
| 39885 | LS 5039 | 276.6 | -14.8 | 0.9 | 22.06.2007 | 1688 |
| 41350 | LS 5039 | 276.6 | -14.8 | 1.3 | 31.08.2007 | 1688 |
| 41371 | LS 5039 | 276.6 | -14.8 | 0.8 | 01.09.2007 | 1689 |
| 41406 | LS 5039 | 276.6 | -14.8 | 1.3 | 02.09.2007 | 1688 |
| 41422 | LS 5039 | 276.6 | -14.8 | 0.8 | 03.09.2007 | 1688 |
| 41445 | LS 5039 | 276.6 | -14.8 | 1.3 | 04.09.2007 | 1688 |
| 41465 | LS 5039 | 276.6 | -14.8 | 0.8 | 05.09.2007 | 1688 |
| 41490 | LS 5039 | 276.6 | -14.8 | 1.3 | 06.09.2007 | 1688 |
| 41514 | LS 5039 | 276.6 | -14.8 | 0.8 | 07.09.2007 | 1688 |
| 41542 | LS 5039 | 276.6 | -14.8 | 1.3 | 08.09.2007 | 1688 |
| 41566 | LS 5039 | 276.6 | -14.8 | 1.3 | 09.09.2007 | 1688 |
| 41569 | LS 5039 | 276.6 | -14.8 | 0.8 | 09.09.2007 | 1688 |
| 41570 | LS 5039 | 276.6 | -14.8 | 1.3 | 09.09.2007 | 1689 |
| 41573 | LS 5039 | 276.6 | -14.8 | 0.8 | 09.09.2007 | 1688 |
| 41598 | LS 5039 | 276.6 | -14.8 | 1.3 | 10.09.2007 | 1688 |
| 41601 | LS 5039 | 276.6 | -14.8 | 0.8 | 10.09.2007 | 1689 |
| 41602 | LS 5039 | 276.6 | -14.8 | 1.3 | 10.09.2007 | 1689 |
| 41628 | LS 5039 | 276.6 | -14.8 | 0.8 | 11.09.2007 | 1688 |
| 41629 | LS 5039 | 276.6 | -14.8 | 1.3 | 11.09.2007 | 1688 |
| 41635 | LS 5039 | 276.6 | -14.8 | 0.8 | 11.09.2007 | 1688 |

| Run No. | Target | RA | Dec | Offset | Date | Duration |
|---|---|---|---|---|---|---|
| | | ° | ° | ° | dd.mm.yyyy | s |
| 41636 | LS 5039 | 276.6 | -14.8 | 1.3 | 11.09.2007 | 1688 |
| 41696 | LS 5039 | 276.6 | -14.8 | 1.3 | 13.09.2007 | 1688 |
| 41699 | LS 5039 | 276.6 | -14.8 | 0.8 | 13.09.2007 | 1689 |
| 41700 | LS 5039 | 276.6 | -14.8 | 1.3 | 13.09.2007 | 1688 |
| 41740 | LS 5039 | 276.6 | -14.8 | 0.8 | 14.09.2007 | 1689 |
| 41741 | LS 5039 | 276.6 | -14.8 | 1.3 | 14.09.2007 | 1689 |
| 45325 | LS 5039 | 276.6 | -14.8 | 0.8 | 05.05.2008 | 1689 |
| 45327 | LS 5039 | 276.6 | -14.8 | 1.3 | 05.05.2008 | 1688 |
| 45426 | LS 5039 | 276.6 | -14.8 | 1.3 | 09.05.2008 | 1690 |
| 45427 | LS 5039 | 276.6 | -14.8 | 0.8 | 09.05.2008 | 1688 |
| 45429 | LS 5039 | 276.6 | -14.8 | 1.3 | 09.05.2008 | 1689 |
| 45719 | LS 5039 | 276.6 | -14.8 | 0.8 | 28.05.2008 | 1688 |
| 45720 | LS 5039 | 276.6 | -14.8 | 1.3 | 28.05.2008 | 1687 |
| 45798 | LS 5039 | 276.6 | -14.8 | 2.0 | 01.06.2008 | 1689 |
| 45799 | LS 5039 | 276.6 | -14.8 | 0.8 | 01.06.2008 | 1689 |
| 45800 | LS 5039 | 276.6 | -14.8 | 1.3 | 01.06.2008 | 1047 |
| 45801 | LS 5039 | 276.6 | -14.8 | 1.3 | 01.06.2008 | 1687 |
| 46261 | LS 5039 | 276.6 | -14.8 | 0.8 | 25.06.2008 | 1688 |
| 46262 | LS 5039 | 276.6 | -14.8 | 1.3 | 25.06.2008 | 1688 |
| 46301 | LS 5039 | 276.6 | -14.8 | 1.3 | 27.06.2008 | 1688 |
| 46304 | LS 5039 | 276.6 | -14.8 | 0.8 | 27.06.2008 | 1011 |
| 46396 | LS 5039 | 276.6 | -14.8 | 1.3 | 01.07.2008 | 1688 |
| 46399 | LS 5039 | 276.6 | -14.8 | 0.8 | 01.07.2008 | 1687 |
| 46512 | LS 5039 | 276.6 | -14.8 | 1.3 | 05.07.2008 | 1690 |
| 47763 | LS 5039 | 276.6 | -14.8 | 1.3 | 26.08.2008 | 1689 |
| 48385 | LS 5039 | 276.6 | -14.8 | 0.8 | 25.09.2008 | 1689 |

## A.15 G18.5-0.4

| Run No. | Target | RA | Dec | Offset | Date | Duration |
|---|---|---|---|---|---|---|
| | | ◦ | ◦ | ◦ | dd.mm.yyyy | s |
| 20905 | G21.1+0.0 | 276.1 | -13.0 | 0.5 | 21.05.2004 | 1682 |
| 20907 | G19.7+0.0 | 276.7 | -11.8 | 1.2 | 21.05.2004 | 1683 |
| 20926 | G19.0+0.0 | 276.4 | -12.4 | 0.6 | 22.05.2004 | 1682 |
| 20927 | G16.9+0.0 | 275.4 | -14.2 | 1.7 | 22.05.2004 | 1683 |
| 21195 | G16.9-0.0 | 274.0 | -16.7 | 1.8 | 14.06.2004 | 1683 |
| 21220 | G17.6-1.0 | 276.6 | -14.1 | 1.1 | 15.06.2004 | 1682 |
| 21301 | G16.2-1.0 | 276.0 | -15.3 | 2.4 | 18.06.2004 | 1683 |
| 21425 | G21.1-1.0 | 278.3 | -11.0 | 2.6 | 24.06.2004 | 1683 |
| 21700 | G19.7-1.0 | 277.6 | -12.2 | 1.3 | 18.07.2004 | 1675 |
| 21747 | G19.0-1.0 | 277.3 | -12.8 | 0.8 | 20.07.2004 | 1683 |
| 21768 | G18.3-1.0 | 277.0 | -13.5 | 0.7 | 21.07.2004 | 1683 |
| 22168 | G17.8-0.7 | 276.1 | -14.4 | 1.5 | 20.08.2004 | 1622 |
| 22169 | G17.8-0.7 | 276.7 | -13.2 | 0.3 | 20.08.2004 | 1626 |
| 22170 | G17.8-0.7 | 277.1 | -14.1 | 1.3 | 20.08.2004 | 985 |
| 22182 | G17.8-0.7 | 276.7 | -12.2 | 0.3 | 21.08.2004 | 1503 |
| 22324 | G17.4-1.1 | 277.2 | -14.3 | 1.5 | 06.09.2004 | 1683 |
| 22325 | G17.4-1.1 | 276.1 | -14.3 | 1.4 | 06.09.2004 | 1683 |
| 22336 | G17.4-1.1 | 276.1 | -14.3 | 1.4 | 07.09.2004 | 1682 |
| 22337 | G17.4-1.1 | 277.2 | -14.3 | 1.5 | 07.09.2004 | 1682 |
| 22338 | G17.4-1.1 | 276.1 | -14.3 | 1.4 | 07.09.2004 | 1682 |
| 22339 | G17.4-1.1 | 277.2 | -14.3 | 1.5 | 07.09.2004 | 1683 |
| 22340 | G17.4-1.1 | 276.1 | -14.3 | 1.4 | 07.09.2004 | 1682 |
| 22341 | G17.4-1.1 | 277.2 | -14.3 | 1.5 | 07.09.2004 | 1685 |
| 22358 | G17.4-1.1 | 277.2 | -14.3 | 1.5 | 08.09.2004 | 1684 |
| 22359 | G17.4-1.1 | 276.1 | -14.3 | 1.4 | 08.09.2004 | 1682 |
| 25015 | LS 5039 | 276.6 | -14.8 | 2.6 | 11.04.2005 | 1670 |
| 25016 | LS 5039 | 276.6 | -14.8 | 1.2 | 11.04.2005 | 1670 |
| 25019 | LS 5039 | 276.6 | -14.8 | 2.6 | 11.04.2005 | 1670 |

| Run No. | Target | RA | Dec | Offset | Date | Duration |
|---|---|---|---|---|---|---|
| | | ° | ° | ° | dd.mm.yyyy | s |
| 25020 | LS 5039 | 276.6 | -14.8 | 1.2 | 11.04.2005 | 1459 |
| 25035 | LS 5039 | 276.6 | -14.8 | 2.0 | 12.04.2005 | 1670 |
| 25036 | LS 5039 | 276.6 | -14.8 | 2.0 | 12.04.2005 | 1670 |
| 25037 | LS 5039 | 276.6 | -14.8 | 2.0 | 12.04.2005 | 1669 |
| 25038 | LS 5039 | 276.6 | -14.8 | 2.0 | 12.04.2005 | 1670 |
| 25039 | LS 5039 | 276.6 | -14.8 | 1.2 | 12.04.2005 | 1798 |
| 25040 | LS 5039 | 276.6 | -14.8 | 2.6 | 12.04.2005 | 1764 |
| 25050 | LS 5039 | 276.6 | -14.8 | 2.0 | 13.04.2005 | 1670 |
| 25051 | LS 5039 | 276.6 | -14.8 | 2.0 | 13.04.2005 | 1669 |
| 25052 | LS 5039 | 276.6 | -14.8 | 2.6 | 13.04.2005 | 1670 |
| 25053 | LS 5039 | 276.6 | -14.8 | 1.2 | 13.04.2005 | 1671 |
| 25095 | LS 5039 | 276.6 | -14.8 | 2.6 | 17.04.2005 | 1674 |
| 25096 | LS 5039 | 276.6 | -14.8 | 1.2 | 17.04.2005 | 1669 |
| 25103 | LS 5039 | 276.6 | -14.8 | 2.0 | 18.04.2005 | 1669 |
| 25104 | LS 5039 | 276.6 | -14.8 | 2.0 | 18.04.2005 | 1669 |
| 25426 | LS 5039 | 276.6 | -14.8 | 2.6 | 07.05.2005 | 1678 |
| 25427 | LS 5039 | 276.6 | -14.8 | 1.2 | 07.05.2005 | 1670 |
| 25428 | LS 5039 | 276.6 | -14.8 | 2.0 | 07.05.2005 | 1674 |
| 25429 | LS 5039 | 276.6 | -14.8 | 2.0 | 07.05.2005 | 1670 |
| 26130 | LS 5039 | 276.6 | -14.8 | 1.5 | 06.06.2005 | 1676 |
| 26131 | LS 5039 | 276.6 | -14.8 | 0.1 | 06.06.2005 | 1682 |
| 25432 | LS 5039 | 276.6 | -14.8 | 1.2 | 06.06.2005 | 1057 |
| 25454 | LS 5039 | 276.6 | -14.8 | 2.0 | 08.05.2005 | 1670 |
| 25455 | LS 5039 | 276.6 | -14.8 | 2.0 | 08.05.2005 | 1670 |
| 25456 | LS 5039 | 276.6 | -14.8 | 1.2 | 08.05.2005 | 1669 |
| 25477 | LS 5039 | 276.6 | -14.8 | 2.0 | 09.05.2005 | 897 |
| 25478 | LS 5039 | 276.6 | -14.8 | 2.0 | 09.05.2005 | 1199 |
| 25479 | LS 5039 | 276.6 | -14.8 | 2.6 | 09.05.2005 | 1198 |

| Run No. | Target | RA | Dec | Offset | Date | Duration |
|---|---|---|---|---|---|---|
| | | ° | ° | ° | dd.mm.yyyy | s |
| 25480 | LS 5039 | 276.6 | -14.8 | 1.2 | 09.05.2005 | 1198 |
| 25481 | LS 5039 | 276.6 | -14.8 | 2.0 | 09.05.2005 | 1669 |
| 25483 | LS 5039 | 276.6 | -14.8 | 2.0 | 09.05.2005 | 1475 |
| 25499 | LS 5039 | 276.6 | -14.8 | 1.4 | 10.05.2005 | 1671 |
| 25500 | LS 5039 | 276.6 | -14.8 | 2.4 | 10.05.2005 | 1670 |
| 25547 | LS 5039 | 276.6 | -14.8 | 1.4 | 14.05.2005 | 1674 |
| 25548 | LS 5039 | 276.6 | -14.8 | 2.4 | 14.05.2005 | 1674 |
| 25577 | LS 5039 | 276.6 | -14.8 | 2.4 | 16.05.2005 | 1669 |
| 25578 | LS 5039 | 276.6 | -14.8 | 1.4 | 16.05.2005 | 1670 |
| 25592 | LS 5039 | 276.6 | -14.8 | 1.4 | 16.05.2005 | 1678 |
| 25593 | LS 5039 | 276.6 | -14.8 | 2.4 | 16.05.2005 | 1677 |
| 25679 | LS 5039 | 276.6 | -14.8 | 1.2 | 18.05.2005 | 1671 |
| 25680 | LS 5039 | 276.6 | -14.8 | 2.6 | 18.05.2005 | 1671 |
| 26161 | LS 5039 | 276.6 | -14.8 | 2.0 | 07.06.2005 | 1683 |
| 26179 | HESS J1825-137 | 276.5 | -14.5 | 1.5 | 08.06.2005 | 1687 |
| 26180 | HESS J1825-137 | 276.5 | -14.5 | 0.1 | 08.06.2005 | 1680 |
| 26182 | LS 5039 | 276.6 | -14.8 | 2.0 | 08.06.2005 | 1070 |
| 26183 | LS 5039 | 276.6 | -14.8 | 2.0 | 08.06.2005 | 1061 |
| 26184 | LS 5039 | 276.6 | -14.8 | 2.0 | 08.06.2005 | 1072 |
| 26185 | LS 5039 | 276.6 | -14.8 | 2.0 | 08.06.2005 | 1682 |
| 26206 | LS 5039 | 276.6 | -14.8 | 2.0 | 09.06.2005 | 1677 |
| 26208 | LS 5039 | 276.6 | -14.8 | 2.0 | 09.06.2005 | 1683 |
| 26209 | LS 5039 | 276.6 | -14.8 | 2.0 | 09.06.2005 | 1682 |
| 26237 | HESS J1825-137 | 276.5 | -14.5 | 1.5 | 10.06.2005 | 1682 |
| 26238 | HESS J1825-137 | 276.5 | -14.5 | 0.1 | 10.06.2005 | 1682 |
| 26239 | HESS J1825-137 | 276.5 | -14.5 | 1.5 | 10.06.2005 | 1682 |
| 26240 | HESS J1825-137 | 276.5 | -14.5 | 0.1 | 10.06.2005 | 1686 |
| 26882 | LS 5039 | 276.6 | -14.8 | 2.0 | 01.07.2005 | 1686 |
| 26883 | LS 5039 | 276.6 | -14.8 | 2.0 | 01.07.2005 | 1686 |

| Run No. | Target | RA | Dec | Offset | Date | Duration |
|---|---|---|---|---|---|---|
| | | ° | ° | ° | dd.mm.yyyy | s |
| 26885 | LS 5039 | 276.6 | -14.8 | 2.0 | 01.07.2005 | 1682 |
| 26916 | LS 5039 | 276.6 | -14.8 | 2.0 | 02.07.2005 | 1690 |
| 26917 | LS 5039 | 276.6 | -14.8 | 2.0 | 02.07.2005 | 1690 |
| 26918 | LS 5039 | 276.6 | -14.8 | 2.0 | 02.07.2005 | 1692 |
| 26919 | LS 5039 | 276.6 | -14.8 | 2.0 | 02.07.2005 | 1681 |
| 26920 | LS 5039 | 276.6 | -14.8 | 2.0 | 02.07.2005 | 1680 |
| 26921 | LS 5039 | 276.6 | -14.8 | 2.0 | 02.07.2005 | 1691 |
| 26922 | LS 5039 | 276.6 | -14.8 | 2.0 | 02.07.2005 | 1690 |
| 26923 | LS 5039 | 276.6 | -14.8 | 2.0 | 02.07.2005 | 1680 |
| 26936 | LS 5039 | 276.6 | -14.8 | 2.0 | 03.07.2005 | 1683 |
| 26937 | LS 5039 | 276.6 | -14.8 | 2.0 | 03.07.2005 | 1680 |
| 26938 | LS 5039 | 276.6 | -14.8 | 2.0 | 03.07.2005 | 1683 |
| 26939 | LS 5039 | 276.6 | -14.8 | 2.0 | 03.07.2005 | 1682 |
| 26940 | LS 5039 | 276.6 | -14.8 | 2.0 | 03.07.2005 | 1686 |
| 26941 | LS 5039 | 276.6 | -14.8 | 2.0 | 03.07.2005 | 1687 |
| 26942 | LS 5039 | 276.6 | -14.8 | 2.0 | 03.07.2005 | 1686 |
| 26943 | LS 5039 | 276.6 | -14.8 | 2.0 | 03.07.2005 | 1682 |
| 26965 | LS 5039 | 276.6 | -14.8 | 2.0 | 04.07.2005 | 1687 |
| 26966 | LS 5039 | 276.6 | -14.8 | 2.0 | 04.07.2005 | 1682 |
| 26967 | LS 5039 | 276.6 | -14.8 | 2.0 | 04.07.2005 | 1680 |
| 26968 | LS 5039 | 276.6 | -14.8 | 2.0 | 04.07.2005 | 1683 |
| 26969 | LS 5039 | 276.6 | -14.8 | 2.0 | 04.07.2005 | 1686 |
| 26970 | LS 5039 | 276.6 | -14.8 | 2.0 | 04.07.2005 | 1686 |
| 26971 | LS 5039 | 276.6 | -14.8 | 2.0 | 04.07.2005 | 1682 |
| 26984 | HESS J1825-137 | 276.5 | -14.5 | 0.1 | 05.07.2005 | 1683 |
| 26985 | HESS J1825-137 | 276.5 | -14.5 | 1.5 | 05.07.2005 | 1682 |
| 26986 | LS 5039 | 276.6 | -14.8 | 2.0 | 05.07.2005 | 1686 |
| 26987 | LS 5039 | 276.6 | -14.8 | 2.0 | 05.07.2005 | 1682 |
| 26988 | LS 5039 | 276.6 | -14.8 | 2.0 | 05.07.2005 | 1683 |

| Run No. | Target | RA | Dec | Offset | Date | Duration |
|---|---|---|---|---|---|---|
| | | ° | ° | ° | dd.mm.yyyy | s |
| 26989 | LS 5039 | 276.6 | -14.8 | 2.0 | 05.07.2005 | 1687 |
| 26990 | LS 5039 | 276.6 | -14.8 | 2.0 | 05.07.2005 | 1682 |
| 26991 | LS 5039 | 276.6 | -14.8 | 2.0 | 05.07.2005 | 1683 |
| 26992 | LS 5039 | 276.6 | -14.8 | 2.0 | 05.07.2005 | 1682 |
| 26993 | LS 5039 | 276.6 | -14.8 | 2.0 | 05.07.2005 | 1686 |
| 27155 | HESS J1825-137 | 276.5 | -14.5 | 0.1 | 11.07.2005 | 1691 |
| 27156 | HESS J1825-137 | 276.5 | -14.5 | 1.5 | 11.07.2005 | 1680 |
| 27157 | HESS J1825-137 | 276.5 | -14.5 | 0.1 | 11.07.2005 | 1691 |
| 27158 | HESS J1825-137 | 276.5 | -14.5 | 1.5 | 11.07.2005 | 1681 |
| 28417 | LS 5039 | 276.6 | -14.8 | 1.2 | 04.09.2005 | 1686 |
| 28418 | LS 5039 | 276.6 | -14.8 | 2.6 | 04.09.2005 | 1682 |
| 28419 | LS 5039 | 276.6 | -14.8 | 2.0 | 04.09.2005 | 1684 |
| 28420 | LS 5039 | 276.6 | -14.8 | 2.0 | 04.09.2005 | 1682 |
| 28421 | LS 5039 | 276.6 | -14.8 | 1.2 | 04.09.2005 | 1588 |
| 28439 | LS 5039 | 276.6 | -14.8 | 2.6 | 05.09.2005 | 1682 |
| 28440 | LS 5039 | 276.6 | -14.8 | 2.0 | 05.09.2005 | 1685 |
| 28441 | LS 5039 | 276.6 | -14.8 | 2.0 | 05.09.2005 | 1687 |
| 28442 | LS 5039 | 276.6 | -14.8 | 1.2 | 05.09.2005 | 1682 |
| 28443 | LS 5039 | 276.6 | -14.8 | 2.6 | 05.09.2005 | 1686 |
| 29361 | LS 5039 | 276.6 | -14.8 | 2.6 | 20.10.2005 | 1690 |
| 29362 | LS 5039 | 276.6 | -14.8 | 1.2 | 20.10.2005 | 1690 |
| 29370 | LS 5039 | 276.6 | -14.8 | 2.0 | 21.10.2005 | 1690 |
| 29371 | LS 5039 | 276.6 | -14.8 | 2.6 | 21.10.2005 | 1690 |
| 29383 | LS 5039 | 276.6 | -14.8 | 2.0 | 22.10.2005 | 1690 |
| 29425 | LS 5039 | 276.6 | -14.8 | 1.2 | 24.10.2005 | 1690 |
| 29440 | LS 5039 | 276.6 | -14.8 | 2.0 | 25.10.2005 | 1690 |
| 29441 | LS 5039 | 276.6 | -14.8 | 2.6 | 25.10.2005 | 1690 |
| 34821 | LS 5039 | 276.6 | -14.8 | 2.4 | 17.09.2006 | 1689 |

| Run No. | Target | RA | Dec | Offset | Date | Duration |
|---|---|---|---|---|---|---|
| | | ° | ° | ° | dd.mm.yyyy | s |
| 34822 | LS 5039 | 276.6 | -14.8 | 1.4 | 17.09.2006 | 1688 |
| 34824 | LS 5039 | 276.6 | -14.8 | 1.0 | 17.09.2006 | 1363 |
| 34922 | LS 5039 | 276.6 | -14.8 | 2.4 | 21.09.2006 | 1689 |
| 34923 | LS 5039 | 276.6 | -14.8 | 1.4 | 21.09.2006 | 1689 |
| 34924 | LS 5039 | 276.6 | -14.8 | 2.0 | 21.09.2006 | 1689 |
| 34925 | LS 5039 | 276.6 | -14.8 | 2.0 | 21.09.2006 | 1689 |
| 34926 | LS 5039 | 276.6 | -14.8 | 2.4 | 21.09.2006 | 1689 |
| 35362 | LS 5039 | 276.6 | -14.8 | 2.4 | 11.10.2006 | 1686 |
| 38228 | SNR 21.5-0.9 | 277.8 | -10.3 | 2.9 | 17.04.2007 | 1688 |
| 38229 | SNR 21.5-0.9 | 278.1 | -11.2 | 2.3 | 17.04.2007 | 1688 |
| 38260 | SNR 21.5-0.9 | 277.8 | -10.3 | 2.9 | 18.04.2007 | 1688 |
| 38264 | SNR 21.5-0.9 | 277.8 | -10.3 | 2.9 | 18.04.2007 | 1688 |
| 38265 | SNR 21.5-0.9 | 277.8 | -10.3 | 2.9 | 18.04.2007 | 1274 |
| 38280 | SNR 21.5-0.9 | 278.1 | -11.2 | 2.3 | 19.04.2007 | 637 |
| 38446 | SNR 21.5-0.9 | 277.8 | -10.3 | 2.9 | 26.04.2007 | 1687 |
| 39576 | LS 5039 | 276.6 | -14.8 | 2.0 | 11.06.2007 | 1689 |
| 39577 | LS 5039 | 276.6 | -14.8 | 2.0 | 11.06.2007 | 1689 |
| 39578 | LS 5039 | 276.6 | -14.8 | 1.4 | 11.06.2007 | 1689 |
| 39579 | LS 5039 | 276.6 | -14.8 | 2.4 | 11.06.2007 | 1688 |
| 39684 | LS 5039 | 276.6 | -14.8 | 2.0 | 14.06.2007 | 1690 |
| 39685 | LS 5039 | 276.6 | -14.8 | 2.0 | 14.06.2007 | 1688 |
| 39686 | LS 5039 | 276.6 | -14.8 | 2.4 | 14.06.2007 | 1688 |
| 39687 | LS 5039 | 276.6 | -14.8 | 1.4 | 14.06.2007 | 1688 |
| 39688 | LS 5039 | 276.6 | -14.8 | 2.0 | 14.06.2007 | 1688 |
| 39689 | LS 5039 | 276.6 | -14.8 | 2.0 | 14.06.2007 | 1689 |
| 39802 | LS 5039 | 276.6 | -14.8 | 2.0 | 18.06.2007 | 1689 |
| 39803 | LS 5039 | 276.6 | -14.8 | 2.0 | 18.06.2007 | 1689 |
| 39804 | LS 5039 | 276.6 | -14.8 | 2.4 | 18.06.2007 | 1687 |

| Run No. | Target | RA | Dec | Offset | Date | Duration |
|---|---|---|---|---|---|---|
| | | ° | ° | ° | dd.mm.yyyy | s |
| 39805 | LS 5039 | 276.6 | -14.8 | 1.4 | 18.06.2007 | 1688 |
| 39806 | LS 5039 | 276.6 | -14.8 | 2.0 | 18.06.2007 | 1689 |
| 39807 | LS 5039 | 276.6 | -14.8 | 2.0 | 18.06.2007 | 1688 |
| 39881 | LS 5039 | 276.6 | -14.8 | 2.0 | 22.06.2007 | 1689 |
| 39882 | LS 5039 | 276.6 | -14.8 | 2.0 | 22.06.2007 | 1689 |
| 39883 | LS 5039 | 276.6 | -14.8 | 2.4 | 22.06.2007 | 1688 |
| 39884 | LS 5039 | 276.6 | -14.8 | 1.4 | 22.06.2007 | 1688 |
| 39885 | LS 5039 | 276.6 | -14.8 | 2.0 | 22.06.2007 | 1688 |
| 40141 | G21.5-0.9 | 278.1 | -11.2 | 2.3 | 08.07.2007 | 1689 |
| 40227 | G21.5-0.9 | 278.1 | -11.2 | 2.9 | 11.07.2007 | 1689 |
| 40262 | G21.5-0.9 | 278.1 | -11.2 | 2.3 | 12.07.2007 | 1689 |
| 40294 | G21.5-0.9 | 278.1 | -11.2 | 2.3 | 13.07.2007 | 1688 |
| 40295 | G21.5-0.9 | 278.1 | -11.2 | 2.9 | 13.07.2007 | 1689 |
| 40324 | G21.5-0.9 | 278.1 | -11.2 | 2.9 | 14.07.2007 | 1689 |
| 40325 | G21.5-0.9 | 278.1 | -11.2 | 2.3 | 14.07.2007 | 1021 |
| 40357 | G21.5-0.9 | 278.1 | -11.2 | 2.9 | 15.07.2007 | 1689 |
| 40382 | G21.5-0.9 | 278.1 | -11.2 | 2.3 | 16.07.2007 | 1688 |
| 40385 | G21.5-0.9 | 278.1 | -11.2 | 2.9 | 16.07.2007 | 1689 |
| 40412 | G21.5-0.9 | 278.1 | -11.2 | 2.3 | 17.07.2007 | 1689 |
| 40413 | G21.5-0.9 | 278.1 | -11.2 | 2.9 | 17.07.2007 | 1689 |
| 41349 | LS 5039 | 276.6 | -14.8 | 2.6 | 31.08.2007 | 1688 |
| 41350 | LS 5039 | 276.6 | -14.8 | 1.2 | 31.08.2007 | 1688 |
| 45324 | LS 5039 | 276.6 | -14.8 | 2.6 | 05.05.2008 | 952 |
| 45325 | LS 5039 | 276.6 | -14.8 | 2.0 | 05.05.2008 | 1689 |
| 45326 | LS 5039 | 276.6 | -14.8 | 2.0 | 05.05.2008 | 1689 |
| 45327 | LS 5039 | 276.6 | -14.8 | 1.2 | 05.05.2008 | 1688 |
| 45328 | LS 5039 | 276.6 | -14.8 | 2.6 | 05.05.2008 | 1089 |
| 45425 | LS 5039 | 276.6 | -14.8 | 2.6 | 09.05.2008 | 1688 |

| Run No. | Target | RA | Dec | Offset | Date | Duration |
|---|---|---|---|---|---|---|
| | | ° | ° | ° | dd.mm.yyyy | s |
| 45426 | LS 5039 | 276.6 | -14.8 | 1.2 | 09.05.2008 | 1690 |
| 45427 | LS 5039 | 276.6 | -14.8 | 2.0 | 09.05.2008 | 1688 |
| 45429 | LS 5039 | 276.6 | -14.8 | 1.2 | 09.05.2008 | 1689 |
| 45430 | LS 5039 | 276.6 | -14.8 | 2.6 | 09.05.2008 | 1689 |
| 45718 | LS 5039 | 276.6 | -14.8 | 2.0 | 28.05.2008 | 1688 |
| 45719 | LS 5039 | 276.6 | -14.8 | 2.0 | 28.05.2008 | 1688 |
| 45720 | LS 5039 | 276.6 | -14.8 | 1.2 | 28.05.2008 | 1687 |
| 45798 | LS 5039 | 276.6 | -14.8 | 2.0 | 01.06.2008 | 1689 |
| 45799 | LS 5039 | 276.6 | -14.8 | 2.0 | 01.06.2008 | 1689 |
| 46260 | LS 5039 | 276.6 | -14.8 | 2.0 | 25.06.2008 | 1688 |
| 46261 | LS 5039 | 276.6 | -14.8 | 2.0 | 25.06.2008 | 1688 |
| 46262 | LS 5039 | 276.6 | -14.8 | 1.2 | 25.06.2008 | 1688 |
| 46263 | LS 5039 | 276.6 | -14.8 | 2.6 | 25.06.2008 | 1688 |
| 46264 | LS 5039 | 276.6 | -14.8 | 2.0 | 25.06.2008 | 1263 |
| 46301 | LS 5039 | 276.6 | -14.8 | 1.2 | 27.06.2008 | 1688 |
| 46302 | LS 5039 | 276.6 | -14.8 | 2.6 | 27.06.2008 | 1688 |
| 46303 | LS 5039 | 276.6 | -14.8 | 2.0 | 27.06.2008 | 1688 |
| 46304 | LS 5039 | 276.6 | -14.8 | 2.0 | 27.06.2008 | 1011 |
| 46396 | LS 5039 | 276.6 | -14.8 | 1.2 | 01.07.2008 | 1688 |
| 46397 | LS 5039 | 276.6 | -14.8 | 2.6 | 01.07.2008 | 1687 |
| 46398 | LS 5039 | 276.6 | -14.8 | 2.0 | 01.07.2008 | 1688 |
| 46399 | LS 5039 | 276.6 | -14.8 | 2.0 | 01.07.2008 | 1687 |
| 46512 | LS 5039 | 276.6 | -14.8 | 1.2 | 05.07.2008 | 1690 |
| 47763 | LS 5039 | 276.6 | -14.8 | 1.2 | 26.08.2008 | 1689 |
| 48202 | G20.5+1.0 | 276.2 | -10.6 | 2.4 | 18.09.2008 | 1688 |
| 48203 | G18.9+1.0 | 275.5 | -12.0 | 1.4 | 18.09.2008 | 1494 |
| 48256 | G18.5+2.0 | 274.4 | -11.9 | 2.4 | 19.09.2008 | 1688 |

| Run No. | Target | RA | Dec | Offset | Date | Duration |
|---|---|---|---|---|---|---|
| | | ° | ° | ° | dd.mm.yyyy | s |
| 48257 | G16.9+2.0 | 273.6 | -13.3 | 2.9 | 19.09.2008 | 1687 |
| 48289 | G20.1+2.0 | 275.1 | -10.5 | 2.8 | 21.09.2008 | 1688 |
| 48310 | G18.1+1.0 | 275.1 | -12.7 | 1.5 | 22.09.2008 | 1688 |
| 48311 | G18.1+1.0 | 275.1 | -12.7 | 1.5 | 22.09.2008 | 1687 |
| 48384 | LS 5039 | 276.6 | -14.8 | 2.0 | 25.09.2008 | 1688 |
| 48385 | LS 5039 | 276.6 | -14.8 | 2.0 | 25.09.2008 | 1689 |

## A.16 G39.2-0.3

| Run No. | Target | RA | Dec | Offset | Date | Duration |
|---|---|---|---|---|---|---|
| | | ° | ° | ° | dd.mm.yyyy | s |
| 26033 | G36.6-0.9 | 285.3 | 2.9 | 2.7 | 03.06.2005 | 1691 |
| 26038 | G36.6-0.9 | 285.3 | 2.9 | 2.7 | 03.06.2005 | 1692 |
| 26158 | G36.6-0.2 | 284.7 | 3.2 | 2.7 | 07.06.2005 | 1690 |
| 28203 | G36.6-0.9 | 285.3 | 2.9 | 2.7 | 24.08.2005 | 1691 |
| 32521 | G40.0-1.0 | 288.1 | 5.8 | 1.0 | 30.05.2006 | 1689 |
| 32522 | G39.7-2.4 | 288.1 | 4.9 | 2.1 | 30.05.2006 | 887 |
| 32523 | G40.3-2.4 | 288.4 | 5.4 | 2.3 | 30.05.2006 | 1688 |
| 32524 | G40.3+0.4 | 285.9 | 6.7 | 1.3 | 30.05.2006 | 1689 |
| 32525 | G39.4-0.9 | 286.6 | 5.3 | 0.6 | 30.05.2006 | 1688 |
| 32526 | G40.6-1.0 | 287.2 | 6.4 | 1.5 | 30.05.2006 | 1688 |
| 32553 | G36.7+0.6 | 284.0 | 3.6 | 2.7 | 31.05.2006 | 1689 |
| 32554 | G37.3+0.6 | 284.3 | 4.2 | 2.1 | 31.05.2006 | 1689 |
| 32593 | G40.9+0.4 | 286.2 | 7.3 | 1.8 | 01.06.2006 | 1689 |
| 32685 | G41.8-1.0 | 287.8 | 7.4 | 2.7 | 03.06.2006 | 1689 |
| 32686 | G41.2-1.0 | 287.5 | 6.9 | 2.1 | 03.06.2006 | 1689 |
| 32698 | G38.8-0.9 | 286.3 | 4.8 | 0.7 | 04.06.2006 | 1689 |
| 32700 | G38.2-0.8 | 286.0 | 4.3 | 1.1 | 04.06.2006 | 1689 |
| 32767 | G41.5+0.4 | 286.4 | 7.8 | 2.4 | 05.06.2006 | 1689 |
| 32768 | G37.6-0.8 | 285.7 | 3.8 | 1.7 | 05.06.2006 | 1688 |
| 32769 | G37.0-0.8 | 285.4 | 3.3 | 2.3 | 05.06.2006 | 1689 |
| 32779 | G39.1+0.5 | 285.2 | 5.7 | 0.8 | 06.06.2006 | 1688 |
| 32780 | G38.5+0.5 | 285.0 | 5.2 | 1.0 | 06.06.2006 | 1689 |
| 32781 | G37.9+0.6 | 284.6 | 4.7 | 1.6 | 06.06.2006 | 1688 |
| 33358 | G40.3-2.4 | 288.4 | 5.4 | 2.3 | 05.07.2006 | 1688 |
| 34073 | SS 433 | 288.0 | 5.0 | 1.0 | 15.08.2006 | 1689 |
| 34074 | SS 433 | 288.0 | 5.0 | 3.0 | 15.08.2006 | 1689 |
| 34107 | SS 433 | 288.0 | 5.0 | 1.0 | 16.08.2006 | 1689 |
| 34108 | SS 433 | 288.0 | 5.0 | 3.0 | 16.08.2006 | 1689 |

| Run No. | Target | RA | Dec | Offset | Date | Duration |
|---|---|---|---|---|---|---|
| | | ° | ° | ° | dd.mm.yyyy | s |
| 34128 | SS 433 | 288.0 | 5.0 | 1.0 | 17.08.2006 | 1688 |
| 34129 | SS 433 | 288.0 | 5.0 | 3.0 | 17.08.2006 | 1688 |
| 34130 | SS 433 | 288.0 | 5.0 | 1.0 | 17.08.2006 | 1688 |
| 34927 | G41.3-0.6 | 287.2 | 7.2 | 2.1 | 21.09.2006 | 1688 |
| 38994 | HESS J1908+062 | 287.1 | 6.3 | 2.0 | 18.05.2007 | 1688 |
| 38995 | HESS J1908+062 | 287.1 | 6.3 | 0.8 | 18.05.2007 | 1688 |
| 39026 | HESS J1908+062 | 287.1 | 6.3 | 1.8 | 19.05.2007 | 1687 |
| 39027 | HESS J1908+062 | 287.1 | 6.3 | 1.2 | 19.05.2007 | 1687 |
| 39085 | HESS J1908+062 | 287.1 | 6.3 | 0.8 | 21.05.2007 | 1689 |
| 39086 | HESS J1908+062 | 287.1 | 6.3 | 0.8 | 21.05.2007 | 1688 |
| 39112 | HESS J1908+062 | 287.1 | 6.3 | 2.0 | 22.05.2007 | 1684 |
| 39113 | HESS J1908+062 | 287.1 | 6.3 | 0.8 | 22.05.2007 | 1688 |
| 39137 | HESS J1908+062 | 287.1 | 6.3 | 1.7 | 23.05.2007 | 1688 |
| 39138 | HESS J1908+062 | 287.1 | 6.3 | 1.2 | 23.05.2007 | 1688 |
| 39161 | HESS J1908+062 | 287.1 | 6.3 | 1.2 | 24.05.2007 | 1688 |
| 39163 | HESS J1908+062 | 287.1 | 6.3 | 1.7 | 24.05.2007 | 1689 |
| 39216 | HESS J1908+062 | 287.1 | 6.3 | 2.0 | 26.05.2007 | 1688 |
| 39502 | HESS J1908+062 | 287.1 | 6.3 | 1.2 | 09.06.2007 | 941 |
| 39503 | HESS J1908+062 | 287.1 | 6.3 | 1.7 | 09.06.2007 | 733 |
| 39616 | HESS J1908+062 | 287.1 | 6.3 | 1.7 | 12.06.2007 | 1688 |
| 39617 | HESS J1908+062 | 287.1 | 6.3 | 1.2 | 12.06.2007 | 1687 |
| 39618 | HESS J1908+062 | 287.1 | 6.3 | 0.8 | 12.06.2007 | 1689 |
| 39662 | HESS J1908+062 | 287.1 | 6.3 | 1.2 | 13.06.2007 | 1688 |
| 39663 | HESS J1908+062 | 287.1 | 6.3 | 1.7 | 13.06.2007 | 1688 |
| 39664 | HESS J1908+062 | 287.1 | 6.3 | 1.2 | 13.06.2007 | 1689 |
| 39849 | HESS J1908+062 | 287.1 | 6.3 | 1.7 | 20.06.2007 | 1688 |
| 39850 | HESS J1908+062 | 287.1 | 6.3 | 1.2 | 20.06.2007 | 1689 |
| 41936 | HESS J1908+062 | 287.1 | 6.3 | 1.8 | 29.09.2007 | 1688 |

| Run No. | Target | RA | Dec | Offset | Date | Duration |
|---|---|---|---|---|---|---|
| | | ° | ° | ° | dd.mm.yyyy | s |
| 41937 | HESS J1908+062 | 287.1 | 6.3 | 0.9 | 29.09.2007 | 1181 |
| 41956 | HESS J1908+062 | 287.1 | 6.3 | 1.9 | 30.09.2007 | 1688 |
| 41957 | HESS J1908+062 | 287.1 | 6.3 | 1.0 | 30.09.2007 | 1689 |
| 41977 | HESS J1908+062 | 287.1 | 6.3 | 1.8 | 01.10.2007 | 1689 |
| 41994 | HESS J1908+062 | 287.1 | 6.3 | 0.9 | 02.10.2007 | 1689 |
| 42078 | HESS J1908+062 | 287.1 | 6.3 | 1.9 | 04.10.2007 | 1372 |
| 42118 | HESS J1908+062 | 287.1 | 6.3 | 1.1 | 05.10.2007 | 1689 |
| 42119 | HESS J1908+062 | 287.1 | 6.3 | 1.8 | 05.10.2007 | 1689 |
| 42148 | HESS J1908+062 | 287.1 | 6.3 | 0.9 | 06.10.2007 | 1688 |
| 42149 | HESS J1908+062 | 287.1 | 6.3 | 1.9 | 06.10.2007 | 1689 |
| 42171 | HESS J1908+062 | 287.1 | 6.3 | 1.1 | 07.10.2007 | 1687 |
| 42211 | HESS J1908+062 | 287.1 | 6.3 | 1.8 | 08.10.2007 | 1688 |
| 42238 | HESS J1908+062 | 287.1 | 6.3 | 0.9 | 09.10.2007 | 1688 |
| 42272 | HESS J1908+062 | 287.1 | 6.3 | 1.9 | 10.10.2007 | 1688 |
| 42300 | HESS J1908+062 | 287.1 | 6.3 | 1.1 | 11.10.2007 | 1688 |
| 42325 | HESS J1908+062 | 287.1 | 6.3 | 1.1 | 12.10.2007 | 1688 |
| 42326 | HESS J1908+062 | 287.1 | 6.3 | 1.8 | 12.10.2007 | 1689 |
| 53032 | G39.2-0.3 | 286.0 | 5.5 | 0.7 | 14.08.2009 | 1503 |
| 53033 | G39.2-0.3 | 286.0 | 5.5 | 0.7 | 14.08.2009 | 1688 |
| 53081 | G39.2-0.3 | 286.0 | 5.5 | 0.7 | 16.08.2009 | 1688 |
| 53104 | G39.2-0.3 | 286.0 | 5.5 | 0.7 | 17.08.2009 | 1687 |
| 53130 | G39.2-0.3 | 286.0 | 5.5 | 0.7 | 18.08.2009 | 1691 |
| 53152 | G39.2-0.3 | 286.0 | 5.5 | 0.7 | 19.08.2009 | 1688 |
| 53153 | G39.2-0.3 | 286.0 | 5.5 | 0.7 | 19.08.2009 | 1688 |
| 53179 | G39.2-0.3 | 286.0 | 5.5 | 0.7 | 20.08.2009 | 1688 |
| 53180 | G39.2-0.3 | 286.0 | 5.5 | 0.7 | 20.08.2009 | 1688 |
| 53181 | G39.2-0.3 | 286.0 | 5.5 | 0.7 | 20.08.2009 | 1688 |
| 53182 | G39.2-0.3 | 286.0 | 5.5 | 0.7 | 20.08.2009 | 1688 |

| Run No. | Target | RA | Dec | Offset | Date | Duration |
|---|---|---|---|---|---|---|
| | | ° | ° | ° | dd.mm.yyyy | s |
| 53210 | G39.2-0.3 | 286.0 | 5.5 | 0.7 | 21.08.2009 | 1689 |
| 53211 | G39.2-0.3 | 286.0 | 5.5 | 0.7 | 21.08.2009 | 1687 |
| 53213 | G39.2-0.3 | 286.0 | 5.5 | 0.7 | 21.08.2009 | 1688 |
| 53233 | G39.2-0.3 | 286.0 | 5.5 | 0.7 | 22.08.2009 | 1688 |
| 53234 | G39.2-0.3 | 286.0 | 5.5 | 0.7 | 22.08.2009 | 1689 |
| 53235 | G39.2-0.3 | 286.0 | 5.5 | 0.7 | 22.08.2009 | 1688 |
| 53236 | G39.2-0.3 | 286.0 | 5.5 | 0.7 | 22.08.2009 | 1688 |
| 53258 | G39.2-0.3 | 286.0 | 5.5 | 0.7 | 23.08.2009 | 1688 |
| 53259 | G39.2-0.3 | 286.0 | 5.5 | 0.7 | 23.08.2009 | 1688 |
| 53260 | G39.2-0.3 | 286.0 | 5.5 | 0.7 | 23.08.2009 | 1689 |
| 53279 | G39.2-0.3 | 286.0 | 5.5 | 0.7 | 24.08.2009 | 1689 |
| 53299 | G39.2-0.3 | 286.0 | 5.5 | 0.7 | 25.08.2009 | 1688 |
| 53300 | G39.2-0.3 | 286.0 | 5.5 | 0.7 | 25.08.2009 | 1688 |
| 53548 | G39.2-0.3 | 286.0 | 5.5 | 0.7 | 10.09.2009 | 1688 |
| 53560 | G39.2-0.3 | 286.0 | 5.5 | 0.7 | 11.09.2009 | 1689 |
| 53561 | G39.2-0.3 | 286.0 | 5.5 | 0.7 | 11.09.2009 | 1689 |
| 53605 | G39.2-0.3 | 286.0 | 5.5 | 0.7 | 14.09.2009 | 1690 |
| 53628 | G39.2-0.3 | 286.0 | 5.5 | 0.7 | 15.09.2009 | 1689 |
| 53629 | G39.2-0.3 | 286.0 | 5.5 | 0.7 | 15.09.2009 | 1688 |
| 53648 | G39.2-0.3 | 286.0 | 5.5 | 0.7 | 16.09.2009 | 1688 |
| 53673 | G39.2-0.3 | 286.0 | 5.5 | 0.7 | 17.09.2009 | 1689 |
| 53674 | G39.2-0.3 | 286.0 | 5.5 | 0.7 | 17.09.2009 | 1689 |
| 53701 | G39.2-0.3 | 286.0 | 5.5 | 0.7 | 18.09.2009 | 1688 |
| 53702 | G39.2-0.3 | 286.0 | 5.5 | 0.7 | 18.09.2009 | 1688 |
| 53725 | G39.2-0.3 | 286.0 | 5.5 | 0.7 | 19.09.2009 | 1689 |
| 53726 | G39.2-0.3 | 286.0 | 5.5 | 0.7 | 19.09.2009 | 1688 |
| 53727 | G39.2-0.3 | 286.0 | 5.5 | 0.7 | 19.09.2009 | 1688 |
| 53728 | G39.2-0.3 | 286.0 | 5.5 | 0.7 | 19.09.2009 | 1689 |

| Run No. | Target | RA | Dec | Offset | Date | Duration |
|---|---|---|---|---|---|---|
| | | ° | ° | ° | dd.mm.yyyy | s |
| 53759 | G39.2-0.3 | 286.0 | 5.5 | 0.7 | 20.09.2009 | 1689 |
| 53762 | G39.2-0.3 | 286.0 | 5.5 | 0.7 | 20.09.2009 | 1689 |
| 53798 | G39.2-0.3 | 286.0 | 5.5 | 0.7 | 21.09.2009 | 1688 |
| 53937 | G39.2-0.3 | 286.0 | 5.5 | 0.7 | 06.10.2009 | 1688 |
| 53938 | G39.2-0.3 | 286.0 | 5.5 | 0.7 | 06.10.2009 | 1689 |
| 53988 | G39.2-0.3 | 286.0 | 5.5 | 0.7 | 07.10.2009 | 1688 |
| 53989 | G39.2-0.3 | 286.0 | 5.5 | 0.7 | 07.10.2009 | 1688 |
| 53990 | G39.2-0.3 | 286.0 | 5.5 | 0.7 | 07.10.2009 | 1689 |
| 54033 | G39.2-0.3 | 286.0 | 5.5 | 0.7 | 11.10.2009 | 1688 |
| 54051 | G39.2-0.3 | 286.0 | 5.5 | 0.7 | 12.10.2009 | 1689 |
| 54052 | G39.2-0.3 | 286.0 | 5.5 | 0.7 | 12.10.2009 | 1689 |
| 54077 | G39.2-0.3 | 286.0 | 5.5 | 0.7 | 13.10.2009 | 1690 |

## A.17 G47.38-3.88

| Run No. | Target | RA | Dec | Offset | Date | Duration |
|---|---|---|---|---|---|---|
| | | ◦ | ◦ | ◦ | dd.mm.yyyy | s |
| 51622 | G46.1-3.5 | 292.1 | 10.1 | 1.3 | 25.05.2009 | 1688 |
| 51751 | G47.1-3.5 | 292.6 | 10.9 | 0.5 | 02.06.2009 | 1689 |
| 51785 | G46.1-3.5 | 292.1 | 10.1 | 1.3 | 04.06.2009 | 1689 |
| 52475 | G47.1-3.5 | 292.6 | 10.9 | 0.5 | 17.07.2009 | 1688 |

## A.18 G10.93-45.44

| Run No. | Target | RA | Dec | Offset | Date | Duration |
|---|---|---|---|---|---|---|
| | | ° | ° | ° | dd.mm.yyyy | s |
| 33117 | PSR J2124-3358 | 322.0 | -34.0 | 0.7 | 25.06.2006 | 1688 |
| 33147 | PSR J2124-3358 | 321.2 | -33.0 | 0.7 | 26.06.2006 | 1689 |
| 33296 | PSR J2124-3358 | 321.2 | -34.7 | 0.7 | 02.07.2006 | 1688 |
| 33315 | PSR J2124-3358 | 322.0 | -34.0 | 0.7 | 03.07.2006 | 1688 |
| 33316 | PSR J2124-3358 | 320.3 | -34.0 | 0.7 | 03.07.2006 | 1689 |
| 33360 | PSR J2124-3358 | 321.2 | -34.0 | 0.7 | 05.07.2006 | 1689 |
| 33377 | PSR J2124-3358 | 321.8 | -34.7 | 0.7 | 06.07.2006 | 1689 |
| 33378 | PSR J2124-3358 | 322.0 | -34.0 | 0.7 | 06.07.2006 | 1689 |
| 33379 | PSR J2124-3358 | 320.3 | -34.0 | 0.7 | 06.07.2006 | 1688 |
| 33390 | PSR J2124-3358 | 321.2 | -33.3 | 0.7 | 07.07.2006 | 1689 |